Light or Darkness

Luminescence and quenching of phosphors for LEDs and sensing

Author: Juriaan Willem de Wit
Title: Light or Darkness
Doi: 10.33540/2326
Printed by: Ridderprint

Light or Darkness

Luminescence and quenching of phosphors for LEDs and sensing

Licht of Donker

Luminescentie en doving van fosforen voor LEDs en sensoren

(met een samenvatting in het Nederlands)

Proefschrift

ter verkrijging van de graad van doctor aan de Universiteit Utrecht op gezag van de rector magnificus, prof. dr. H.R.B.M. Kummeling, ingevolge het besluit van het college voor promoties in het openbaar te verdedigen op

woensdag 12 juni 2024 des middags te 16:15

door

Jurriaan Willem de Wit

geboren op 22 mei 1993 te Eindhoven

Promotor:
Prof. dr. A. Meijerink

Copromotor:
Dr. F.T. Rabouw

Beoordelingscommissie:
Dr. E.M. Hutter
Prof. dr. P.E. de Jongh
Prof. dr. P. Smet
Prof. dr. W.K. Kegel
Prof. dr. D.A.M. Vanmaekelbergh

Dit proefschrift is mede gefinancierd uit de Toeslag voor Topconsortia voor Kennis en Innovatie (TKI's) van het Ministerie van Economische Zaken en Klimaat

Voor Papa

Contents

Chapter 1	Introduction	8
Chapter 2	Theory	16
Chapter 3	Increasing the power: Absorption bleach, thermal quenching, and Auger quenching of the red-emitting phosphor $K_2TiF_6:Mn^{4+}$	36
Chapter 4	Luminescence and formation of cubic and hexagonal $(K,Rb)_2SiF_6:Mn^{4+}$	56
Chapter 5	Shedding light on host-to-Yb^{3+} energy transfer in $Cs_2AgBiBr_6:Yb^{3+}$ (nano)crystals	80
Chapter 6	New insights in luminescence and quenching mechanisms of Ag_2S nanocrystals through temperature-dependent spectroscopy	102
Chapter 7	Summary & outlook	118
Chapter 8	Nederlandse Samenvatting	128
Appendix	Acknowledgements	136
	List of publications and conference contributions	
	About the author	

Chapter 1

Introduction

Luminescent materials play a pivotal role in various technological domains, serving as crucial components not only in light-emitting devices (lamps, displays) but in medical imaging, data communication and storage, optical sensing, healthcare, weapons, and navigation.[1] The core function involves converting electromagnetic radiation from one wavelength to another, with an emphasis on efficiency. However, a perpetual challenge lies in the competition between desired photon emission and the often undesirable conversion to heat. This thesis focuses on microcrystalline red phosphors for displays and both doped and undoped nanocrystalline semiconductors, examining their implications for displays, imaging, and sensing applications. **Chapter 2** delves into the theoretical background of optical processes within these different categories of luminescent materials, offering the context for a better understanding of subsequent chapters.

Red-emitting Mn^{4+}-doped phosphors

From the lamps you effortlessly switch on, to the smartphone screen you routinely glance or stare at, artificial lighting plays a crucial role in our lives. The majority of contemporary lighting sources depend on a combination of blue LEDs and photoluminescent materials, known as phosphors. These phosphors partially absorb the blue LED light and convert it to different colors, ultimately producing (warm) white light. Traditional phosphors are typically made of inorganic crystalline materials, wherein a small fraction of lattice ions is replaced with an optically active dopant. In the past two decades these phosphor-converted white LEDs have become the norm as backlights for displays and consumer lighting because of the high efficiency, durability, compactness and low cost of fabrication.[2] Workhorses in consumer lighting are lanthanide-doped $Si_{6-z}Al_zO_zN_{8-z}:Eu^{2+}$ (β-sialon, green), $Y_3Al_5O_{12}:Ce^{3+}$ (YAG, yellow/green) and $CaAlSiN_3:Eu^{2+}$ (CASN, orange), while transition-metal-doped $K_2SiF_6:Mn^{4+}$ (KSF, red) has become a common red phosphor for display technologies (**Figure 1.1**)

How humans perceive light dictates the basic principles for designing lighting devices and displays. In **Figure 1.2a** we plot the general eye sensitivity curve (black dashed) along with the color response of the human eye.[3,4] Above 675 nm, the human eye hardly registers red light anymore and photons emitted around this region reduce the efficiency of light sources. This efficiency of lamps is quantified in terms of luminous efficacy (lumen/watt) and is commonly displayed on the packaging of a lamp, which is a measure of light emitted corrected for the eye sensitivity curve (lumen) per watt consumed. The broad emission band of the red phosphor CASN:Eu^{2+} stretches into this region, contrary to $K_2SiF_6:Mn^{4+}$ with sharp emission lines around 630 nm.

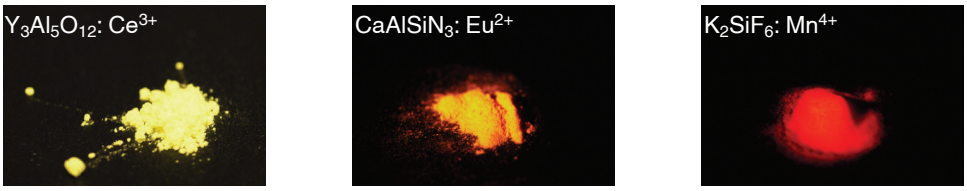

Figure 1.1 | Appearance of some commonly used phosphors under UV illumination. Workhorses in consumer lighting are $Y_3Al_5O_{12}:Ce^{3+}$ (yellow/green) and $CaAlSiN_3:Eu^{2+}$ (orange), while $K_2SiF_6:Mn^{4+}$ (red) has become a common red phosphor for display technologies.

To delve into what further makes KSF:Mn^{4+} a unique commercial display phosphor, we zoom in on human color perception and display technology. Human color perception can be described by the CIE1931 color diagram (**Figure 1.2b**), which encompasses all colors an (average) human can perceive. It provides a quantitative link between the physiologically perceived color and wavelengths in the electromagnetic spectrum. Inside the CIE1931 diagram in **Figure 1.2b** is a dashed triangle that encloses all the colors that can be obtained with a spectrum composed of a blue LED with green-emitting β-SiAlON:Eu^{2+} and red-emitting KSF:Mn^{4+}.[5] A white-light spectrum of these combined materials is provided in **Figure 1.2c**. The sharp lines on the red side of the spectrum originate from KSF:Mn^{4+}. In addition to stimulating the eye's red receptor cells without emitting in the near infrared, narrow emission bands ensure a pure color mixing, resulting in more vibrant colors. White-light LEDs serve as backlight in liquid-crystal displays (LCDs) and the

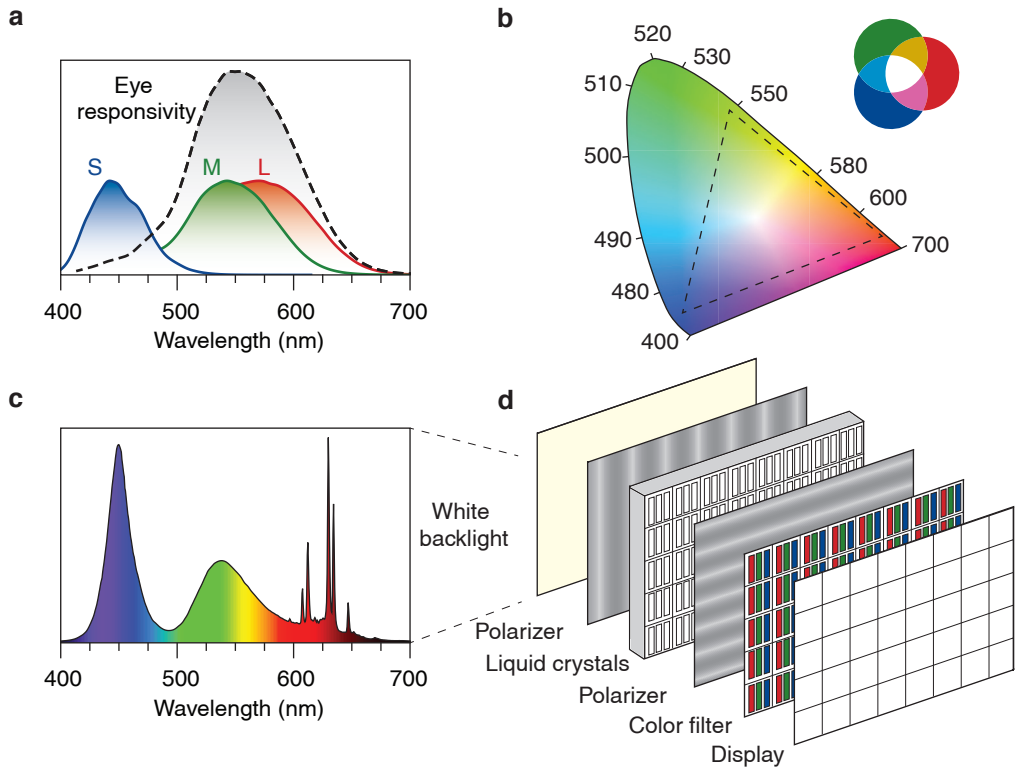

Figure 1.2 | Colors perception of the human eye and phosphor emission in LCD displays. (**a**) The human eye has color receptors for blue (S), green (M), and red (L). Together these form the eye responsivity curve *V* (dashed line). (**b**) All colors an average human can perceive are summarized in the CIE 1931 color space chromaticity diagram Here the curved edge corresponds to monochromatic light. In order to realistically reproduce colors on a display, a white backlight is used in LCD displays. An example spectrum is shown in panel (**c**) for a blue LED coated with β-SiAlON:Eu^{2+} (green) and K_2SiF_6:Mn^{4+} (red). A schematic of the display is shown in panel (**d**). Here the white light first passes through a vertical polarizer. For each pixel (divided into three color subpixels), light passes through an individually controlled liquid-crystal cell. The polarization added in this layer determines whether the light will pass (bright) or be blocked (black) by the next polarization plate. Finally, the light goes through a color filter plate to create a color image with high color purity on the display.

blue, green and red emission colors are the building blocks for color images in a display consisting of millions of pixels, each pixel divided into RGB subpixels. In **Figure 1.2d** a simplified lay-out of a screen is shown, where the white backlight originates from the spectrum in **Figure 1.2c**. Between crossed polarizers a TFT (thin-film transistor) can apply a voltage to a liquid crystal behind a subpixel color filter. If no voltage is applied the crossed polarizers block transmission of light and the pixel is black. If a voltage is applied the liquid crystal organizes in a helix that rotates the polarization direction of light by 90°, white light is transmitted and the desired color passes through the filter behind the TFT contact. In modern 4K displays (3840 × 2160 pixels) this process takes place in ~8.3 million pixels to create a color image that can be refreshed 50 to 100 times per second.

The characteristics that make $K_2SiF_6:Mn^{4+}$ a good display phosphor should also make it an efficient lamp phosphor. However, the application of KSF:Mn^{4+} in higher power applications like consumer lighting is limited because of stability issues and also an effect called saturation i.e. the process where the emission intensity increases sub-linearly with blue excitation power.[6] In **Chapter 3**, we study the saturation characteristics of the K_2TiF_6: Mn^{4+} phosphor at varying blue excitation powers. During these measurements, we monitored the light-induced temperature increase by employing the temperature-dependent emission spectrum of K_2TiF_6: Mn^{4+} as an in situ luminescent thermometer. By combining continuous-wave and pulsed excitation spectroscopy with dynamic Monte Carlo simulations we provide a unified and quantitative picture of all factors that contribute to the saturation of $K_2TiF_6:Mn^{4+}$: thermal quenching, absorption bleach and Auger quenching. Based on the new insights we provide suggestions for improvements, but also find that the long radiative lifetime of Mn^{4+} emission is one of the main causes for saturation in Mn^{4+} doped fluorides that makes application in (high-power) lighting challenging.

Considering that the (inherent) long radiative lifetime of Mn^{4+}-doped fluorides lies at the heart of saturation effects in these materials, we attempted to shorten the lifetime by creating disorder through mixing different alkaline ions in one crystal. In this process, we serendipitously discovered the red-emitting, hexagonal $(K,Rb)_2SiF_6:Mn^{4+}$ phosphor, a polymorph of the cubic KSF:Mn^{4+}. In **Chapter 4**, we discuss the optical properties, thermal stability, and formation process of this novel phosphor material. Because of the lower symmetry around the Mn^{4+} ion in this host, the absorption strength and luminous efficacy increase in addition to a 25% reduction of the excited-state lifetime in comparison with cubic KSF:Mn^{4+} while retaining the high thermal-quenching temperature around 500 K. The shorter emission lifetime is beneficial as it helps to reduce saturation effects.

Moving to the nanoscale

With the demand for smaller and smaller light sources in e.g. next-generation microLED displays, the absorption strength of the phosphor layer must also increase. A small amount of (green or red) phosphor on a microLED pixel must fully convert the incoming blue light, so high material absorption is necessary (**Figure 1.3a**).[7] Most traditional phosphors, when grains are reduced to sub-micron size, lack the required absorption strength while also the efficiency drops as a result of quenching at surface defects.[8] Semiconductor nanocrystals (NCs) doped with lanthanides can be used to kill two birds with one stone: they typically have very strong (tunable) absorption while lanthanides have very narrow emission bands, ideal for achieving the desired high color purity in displays. In recent years semiconductor halide perovskite and elpasolite nanocrystals have emerged as promising candidates for lanthanide incorporation, with various reports

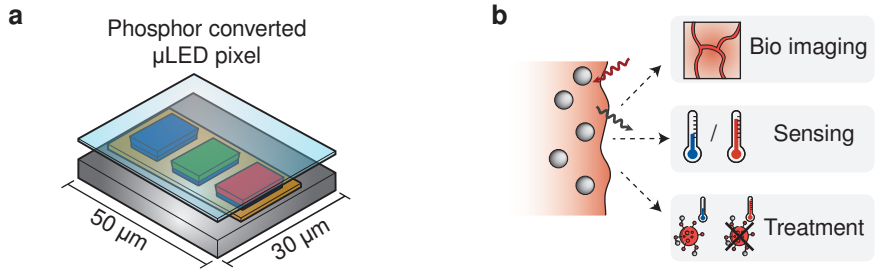

Figure 1.3 | The application of nanoscale phosphors. (**a**) Schematic image of a phosphor-converted µLED display.[13] The µLEDs are located on a substrate (grey) and can be operated with a TFT (yellow). On top of the µLED for the green and red subpixel, a green- and red-emitting nanophosphor are added. Usually a color filter is added to ensure high color purity, but this is not shown here. On top a glass plate is added. The benefit of µLED technology is that each pixel can be turned off completely, which allows for higher contrast, and the simpler design means that thinner and lighter screens can be realized. (**b**) Schematic illustration of luminescent nanocrystals embedded in organic tissue. With Ag_2S NCs for example, excitation results in NIR emission around 1200 nm with which one could perform bioimaging, and luminescence thermometry. Upon binding, the heat generated from light absorption can result in localized heating, enabling precise and targeted destruction of cancerous cells.

highlighting lanthanide luminescence being sensitized through the host absorption.[9,10] However, in literature there are only a few reports that provide evidence for and discuss the host-to-lanthanide energy-transfer mechanism.[11,12]

In this context, we investigated energy transfer in $Cs_2AgBiBr_6$ nanocrystals and microcrystals doped with the near-infrared-emitting lanthanide ion Yb^{3+} and discuss our findings in **Chapter 5**. Temperature-dependent and time-resolved photoluminescence studies on undoped and Yb-doped $Cs_2AgBiBr_6$ reveal that the energy transfer does not take place through the red emissive state of the $Cs_2AgBiBr_6$ host. Instead, there is a competition between relaxation to the red-emitting state and trapping of photoexcited charge carriers on Yb^{3+}. Trapping on Yb^{3+} subsequently results in a charge-transfer state that relaxes to the $^2F_{5/2}$ excited state of Yb^{3+}, followed by NIR narrow f–f emission to the $^2F_{7/2}$ ground state.

In **Chapter 6** we study the temperature dependence of luminescence for bright near-infrared-emitting Ag_2S nanocrystals. There is an ongoing debate about the origin of the photoluminescence. Temperature-dependent studies reveal strong and reversible thermal quenching above 200 K for differently capped Ag_2S, based on both intensity and luminescence lifetime measurements. The intrinsic thermal quenching indicates that the optical transition responsible for the NIR emission involves strong electron–phonon coupling. Also, the temperature-dependent intensity and lifetime used for temperature sensing rely on this quenching process while the quenching limits the maximum quantum efficiency at room temperature to about 15%. Cooling the material down from room temperature reveals that the average lifetime first lengthens because of reduced thermal quenching. Below 200 K the average lifetime shortens down to 50 K, after which it lengthens again below 50 K. We explain this behavior using a model that includes several thermally coupled exciton states with different recombination lifetimes and degeneracies. Based on the temperature-dependent optical properties a mechanism for the emission of Ag_2S is proposed to involve recombination of a hole trapped on Ag^+ with a delocalized conduction-band electron.

References

[1] D. F. Vanderwerf, *The Story of Light Science*, Springer, **2017**.
[2] J. Cho, J. H. Park, J. K. Kim, E. F. Schubert, *Laser Photon. Rev.* **2017**, 11, 1600147.
[3] A. Stockman, L. T. Sharpe, *Vision Res.* **2000**, 40, 1711.
[4] L. T. Sharpe, A. Stockman, W. Jagla, H. Jägle, J. Vis. *Vision Res.* **2005**, 5, 3.
[5] L. Wang, X. Wang, T. Kohsei, K. Yoshimura, M. Izumi, N. Hirosaki, R.-J. Xie, *Opt. Express* **2015**, 23, 28707.
[6] M. A. Van De Haar, M. Tachikirt, A. C. Berends, M. R. Krames, A. Meijerink, F. T. Rabouw, *ACS Photonics* **2021**, 8, 1784.
[7] T. Wu, C. W. Sher, Y. Lin, C. F. Lee, S. Liang, Y. Lu, S. W. H. Chen, W. Guo, H. C. Kuo, Z. Chen, *Appl. Sci.* **2018**, 8.
[8] Z. Liu, C.-H. Lin, B.-R. Hyun, C.-W. Sher, Z. Lv, B. Luo, F. Jiang, T. Wu, C.-H. Ho, H.-C. Kuo, *Light Sci. Appl.* **2020**, 9, 83.
[9] R. Marin, D. Jaque, *Chem. Rev.* **2021**, 121, 1425.
[10] H. Tang, Y. Xu, X. Hu, Q. Hu, T. Chen, W. Jiang, L. Wang, W. Jiang, *Adv. Sci.* **2021**, 3, 1.
[11] S. Jin, R. Li, H. Huang, N. Jiang, J. Lin, S. Wang, Y. Zheng, X. Chen, D. Chen, *Light Sci. Appl.* **2022**, 11, 52.
[12] F. Schmitz, K. Guo, J. Horn, R. Sorrentino, G. Conforto, F. Lamberti, R. Brescia, F. Drago, M. Prato, Z. He, U. Giovanella, F. Cacialli, D. Schlettwein, D. Meggiolaro, T. Gatti, *J. Phys. Chem. Lett.* **2020**, 11.
[13] Y. Wu, J. Ma, P. Su, L. Zhang, B. Xia, *Nanomaterials* **2020**, 10, 2482.
[14] I. Z. Gutierrez, C. Gerke, Y. Shen, E. Ximendes, M. M. Silvan, R. Marin, D. Jaque, O. G. Calderón, S. Melle, J. Rubio-Retama, *ACS Appl. Mater. Interfaces* **2022**, 14, 4871.
[15] J. Zhao, Q. Zhang, W. Liu, G. Shan, X. Wang, *Colloids Surface B* **2022**, 211, 112295.
[16] M. Gao, H. Zhao, Z. Wang, Y. Zhao, X. Zou, L. Sun, *Adv. Powder Technol.* **2021**, 32, 1972.
[17] L. Ming, I. Zabala-Gutierrez, O. G. Calderon, S. Melle, E. Ximendes, J. Rubio-Retama, R. Marin, *Opt. Mater.* **2023**, 141, 113940.
[18] E. Hemmer, A. Benayas, F. Légaré, F. Vetrone, *Nanoscale Horizons* **2016**, 1, 168.
[19] Y. Zhang, G. Hong, Y. Zhang, G. Chen, F. Li, H. Dai, Q. Wang, *ACS Nano* **2012**, 6, 3695.
[20] O. E. Semonin, J. C. Johnson, J. M. Luther, A. G. Midgett, A. J. Nozik, M. C. Beard, *J. Phys. Chem. Lett.* **2010**, 1, 2445.

Chapter 2

Theory

The photoluminescence (PL) properties of very different types of emitters are discussed in this thesis, but they have one thing in common: it all starts in a crystalline solid. The absorption and emission of light studied here either originate from energy levels related to the electronic structure of high purity crystals as in semiconductors, or it involves optically active dopants that are incorporated into a wide bandgap host crystal. We start this chapter by explaining the process of luminescence and the selection rules that govern the rate at which it takes place. Throughout the rest of this chapter, we will discuss the theoretical concepts that lie at the basis of luminescence in semiconductors, transition metal ions, and lanthanide ions.

2.1 Photoluminescence and selection rules

Photoluminescence is the process where a material first absorbs a photon to create an electronic excited state, followed by emission of a photon to return to the ground state. In semiconductors, excitation involves the redistribution of electrons over several crystal unit cells, while in transition metal and lanthanide ions, electrons are redistributed over localized atomic orbitals. The pathway back to the ground state, and the rate at which this occurs can be studied with (time-resolved) luminescence spectroscopy. In many cases photoexcitation results in the emission of phonons (heat) instead of photons (light), a decay pathway we generally try to combat in the field of luminescence. If the system does show luminescence, the rate at which it takes place may span many orders of magnitude, from roughly 10^9 s^{-1} to 10^2 s^{-1}, and is essentially determined by a set of optical selection rules which govern the rate of transitions from one electronic state to another and follow from the laws of quantum mechanics.

What actually happens in a material during absorption and emission of a photon? To understand this, let us consider a two-level system like in **Figure 2.1a**, where the system is either in the ground state or excited state. Each state is described by an electronic wavefunction. When interacting with light, the system experiences an oscillating electromagnetic (EM) field that is approximately homogeneous as the wavelength of a (visible) photon is much larger (hundreds of nm) than the dimension of the electronic wavefunction. The excitation process involves the mixing of the ground state and excited state, where the transition state has mixed ground-state and excited-state character. The oscillating EM field can induce the transition to the excited state, if the mixed state has an electric dipole moment. Transitions that fulfill this requirement are called allowed electric-dipole transitions.

To evaluate if there is a change in electric dipole moment for the transition between the ground and excited state we consider the wavefunctions of these states. Here, the square modulus of the wavefunction $|\Psi|^2$ reflects the probability of finding an electron in a certain position. **Figure 2.1b** provides a schematic illustration of a maximally mixed transition state from one orbital with s character to another with p character. The resulting $|\Psi|^2$ shows an asymmetric electron distribution that gives rise to an oscillating electric transition dipole moment. An s–s transition, e.g. from a 1s to 2s orbital (**Figure 2.1c**) always results in a symmetrical $|\Psi|^2$ probability density distribution that does not result in a dipole moment. This is summarized in the parity selection rule for electric dipole transitions $\Delta l = \pm 1$, where l is the orbital angular momentum.

Transitions are experimentally characterized by the rate at which they absorb and emit light. In a two-level system (absorption or emission), the transition rate from one state to another is proportional to the square of the transition dipole moment, as defined by Fermi's golden rule. Hence, a

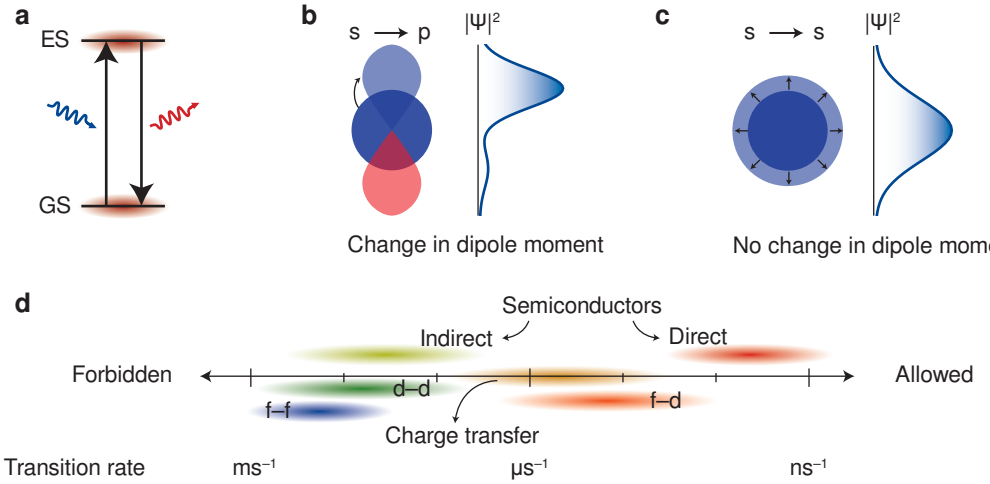

Figure 2.1 | Photoluminescence and the impact of the parity selection rule. (**a**) Absorption (blue) and emission (red) of a photon in a 2-level system involve the mixing of two quantum states, here denoted with ground state (GS) and excited state (ES). (**b**) Schematic representation of a one-electron transition from an s to p orbital, with red and blue denoting different phases. $|\Psi|^2$ is the probability density of locating an electron in a specific volume surrounding the core during the transition, thereby indicating the presence or absence of a dipole moment in the mixed state. (**c**) Similar as in panel **b** but now for a transition from a 1s to 2s orbital. Because of the symmetric expansion of the wavefunction such a transition lacks a change dipole moment and is parity forbidden. (**d**) Overview of several well-known types of transitions in inorganic emitters placed on a scale from "allowed" to "forbidden" electric dipole transitions.[1,2] An important consideration for photoluminescence applications is the rate at which a material emits photons.

large transition dipole moment signifies an allowed transition, leading to strong absorption and a fast emission rate. Furthermore, the most intense transitions are characterized by conservation of the electron spin, as the oscillating electromagnetic (EM) field of light has no direct interaction with the electron spin. This is summarized in the spin selection rule $\Delta S = 0$, where S is the total magnetic spin moment of a state. **Figure 2.1d** offers an overview of typical transition rates for various types of electric dipole transitions. These transition span a wide range from "forbidden" f–f, d–d and indirect semiconductor transitions to "allowed" charge transfer, f–d and direct semiconductor transitions. In the figure they are placed on a scale from allowed to forbidden. The influence of the spin selection rule and conservation of momentum on optical transitions is not addressed here but will be discussed in the following chapters.

2.2 The electronic structure of semiconductors and insulators

The energy level structure of crystals can be examined from the both the chemist's and physicist's perspective. From the chemist's viewpoint, chemical bonding in solids generates bonding and antibonding molecular orbitals made up of linear combinations of atomic orbitals (LCAO). In this approximation, energy gap formation in crystals intuitively arises from the separation between bands consisting of bonding and antibonding configurations of molecular orbitals. However, the LCAO approximation is less intuitive in explaining the movement of charge carriers within a crystal. To gain a better understanding of charge carrier movement, especially in semiconductor crystals, the physicist's approach is employed. Here, the crystal lattice is treated as a medium that

imposes periodic boundary conditions on the potential experienced by electrons, (also) leading to the emergence of energy bands and bandgaps. From this perspective, the movement of charge carriers through a crystal is defined by their effective mass. We will first examine crystals based on their chemical bonding and then delve into how a periodic potential in a one-dimensional "crystal" leads to an energy band diagram, extending this understanding to 3D materials.

Chemist's approach – bonds

As atoms are closely packed in crystalline solids, their atomic orbitals overlap and hybridize into molecular orbitals with different energies. The closer packed they are, the stronger the interaction. With the addition of more and more orbitals, each discrete energy level splits into as many energy levels as there are atomic orbitals in a solid. These large numbers of energy levels have infinitesimally small energy separations between them and effectively form continuous energy bands. Core atomic orbitals do not overlap and thus do not contribute to bonding and form narrow bands, while the valence electron orbitals are strongly hybridized and determine most of the optoelectronic properties of crystals. The energy bands are filled with the electrons from the constituent elements and the highest occupied bands form the valence band (VB), where the highest occupied molecular orbital (HOMO) makes up the top of the VB. In semiconductors and insulators there is an energy gap above the valence band that is followed by a continuum of empty levels forming the conduction band (CB), where the CB minimum consists of the lowest unoccupied molecular orbital (LUMO). Which atomic orbitals contribute to the CB and which to the VB depends largely on the type of bonding and the elements in the material.

Let us first consider a strongly ionic crystal like NaCl. In this case, Na donates one 3s electron to the highly electronegative Cl in order to fully fill the 3p orbital (**Figure 2.2a**).[3] The conversion of Na to Na^+ and Cl to Cl^- is unfavorable in the gas phase, as the ionization potential of Na exceeds the energy gained through the electron affinity of Cl. In NaCl (and solids in general), two other factors need to be taken into account. First, the electrostatic potential around the ions makes a transfer of charge from one (electropositive) ion to another (electronegative) ion energetically much more favorable. The Coulomb energy gain depends on the charge of the ions, distances

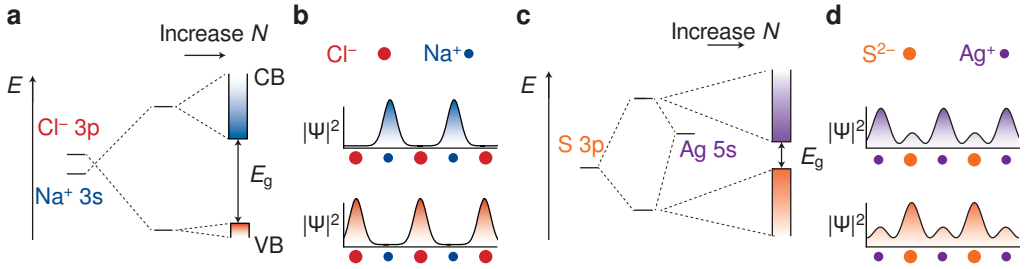

Figure 2.2 | How does the chemical bond between ions lead to band formation in ionic and covalent crystals? (**a**) Simplified energy-level diagram of Na^+ and Cl^- in the gas phase (left side) and in a NaCl crystal. The chemical bonding between Na 3s and Cl 3p orbitals in a crystal results in the formation of a VB and CB separated by an energy gap E_g of ~9 eV (**b**) Schematic representation of the electronic character at the CB minimum (top) and VB maximum (bottom) using LCAO (**c**) A similar energy diagram as in panel **a** for the more covalent bonding between Ag and S in Ag_2S, resulting in bonding and antibonding orbitals. These hybridized orbitals make up the VB and CB. (**d**) Schematic representation of the electronic character of Ag_2S at the VB maximum and CB minimum using LCAO.

between ions and the lattice symmetry. A second factor is the level of orbital overlap between neighboring ions. Because of the large number of ions in a crystal, energy bands form. For the strongly ionic bonding in NaCl, the VB is dominated by Cl^- 3p orbitals whereas the CB is formed by empty Na^+ 3s orbitals. NaCl has a large bandgap of ~9 eV between the VB and CB. If we describe the electron distribution with a linear combination of atomic orbitals (LCAO), the VB maximum electron states have almost complete Cl^- 3p character while at the CB minimum all electron states have 3s Na^+ character. This is schematically depicted in **Figure 2.2b**.

If we now consider a more covalent crystal, like Ag_2S, there is a smaller difference between the atoms in terms of electronegativity. It is not a purely covalent compound like crystalline carbon (diamond), so the bonding has ionic as well as covalent character. It is convenient to introduce the hybridization of Ag and S orbitals by considering the (simplified) bonding between Ag 5s and S 3p orbitals. The combined valence orbitals give rise to hybridized orbitals with bonding and antibonding character, where the antibonding orbitals have predominantly Ag 5s character and the bonding orbital S 3p character (**Figure 2.2c**). The energy gap between the bonding and antibonding orbitals depends on the energy difference between the Ag and S orbitals and the distance between the atoms. In a solid, the VB is formed by (filled) bonding orbitals, the CB by (empty) antibonding orbitals, and the bandgap is defined by the energy difference between the CB minimum and the VB maximum. For Ag_2S the experimentally observed bandgap energy is roughly 1.1 eV. Using the LCAO description again, the VB maximum now has mostly S 3p character, while the CB minimum consists of mostly Ag 5s orbitals. (**Figure 2.2d**).

Physicist's approach – bands

So far we have approached the electronic structure of crystals by looking at the bonds between atoms, or from the chemist's perspective. The physicist's approach facilitates a more intuitive understanding of the optoelectronic properties of semiconductors. Here, we will explain the origin of the formation of energy bands and bandgaps using an infinite 1 dimensional (1D) chain consisting of positive ions.[4]

In this model, the wavefunctions of free electrons form the starting point. In a vacuum, a free electron has a continuum of energy levels. The dispersion relation follows from solving the Schrödinger equation for a free electron:

$$E(k) = \frac{\hbar^2 k^2}{2m_0} \tag{2.1}$$

where the wavevector k is inversely proportional to the wavelength of an electron by $k = 2\pi/\lambda$ and m_0 is the free electron mass in a vacuum. The $E(k)$ relation of a free electron is plotted in **Figure 2.3a**. The dispersion relation changes in a 1D chain because of the periodic potential created by the positively charged atomic cores separated by distance a (**Figure 2.3b**). Electrons that have a wavelength similar to the interatomic spacing a will experience a stronger perturbation, in agreement with Bragg's law for diffraction. The scattering of plane waves on the periodic chain results in two standing waves that describe the electron density throughout the entire chain: one creates a high electron density near the attractive ions (lowering the energy), while the other has a high electron density between the ions (increasing the energy). The energy difference between the two plane waves results in the formation of an energy gap in the dispersion relation at $k = n\pi/a$, where n is an integer number (**Figure 2.3c**). We can use the property that wavefunctions described by k-values that are offset by $n2\pi/a$ are equivalent due to the periodicity of the chain. As a result, the

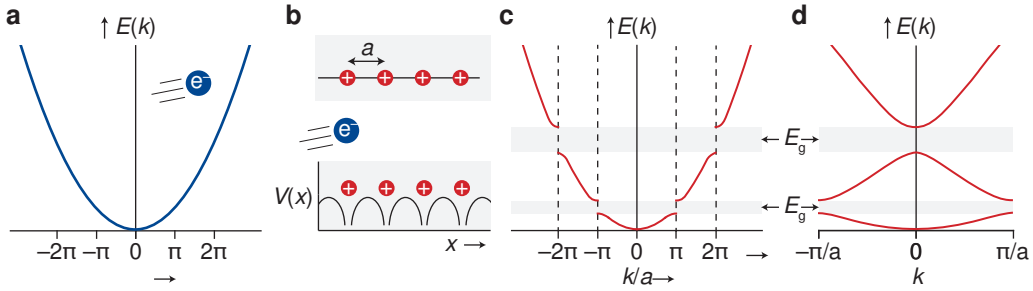

Figure 2.3 | The formation of energy bandgaps in the dispersion relation for a 1D potential. (**a**) Dispersion relation for a free electron in vacuum. There are no restrictions on which energies electrons can have. (**b**) Schematic representation of an electron in a 1D atomic periodic chain consisting of positive charges at distance a (top). The positive charges create a periodic potential which influences the properties of electrons (bottom). (**c**) Dispersion relation for an electron in the 1D chain presented in panel **b**. At k values of $n\pi/a$ scattering of the electron results in "forbidden" energies. (**d**) Reduced zone representation of the dispersion relation depicted in panel **c**.

dispersion relation in **Figure 2.3c** can be fully described by only taking into account values of k between $-\pi/a$ and $+\pi/a$. In the reduced zone representation, all possible electron states in the 1D chain are described by a k-value between $-\pi/a$ and $+\pi/a$ and is shown in **Figure 2.3d**. This region is called the first Brillouin zone.

The principle of energy band formation is the same for 3D crystals, but the energy of the bandgap varies depending on the crystal structure and the direction. The Brillouin zone of a 3D crystal will also be in 3D and plotting the full dispersion relation like in **Figure 2.3d** becomes difficult. Instead, a common way to visualize the band structure of 3D semiconductors is to plot the energy at several high symmetry points in the first Brillouin zone. These symmetry points follow from the (symmetry of the) crystal structure and are denoted by capital Greek letters. The periodic potential electrons experience in different directions will be different. This results in energy landscapes like the one plotted for $Cs_2AgBiBr_6$ in **Figure 2.4a**.[5] Note that in such a diagram not all k-values of the Brillouin zone are presented but only those at high symmetry points as denoted on the x-axis. The band diagram of cubic $Cs_2AgBiBr_6$ will be used to explain excitonic absorption and emission observed in many semiconductors. Note that at the X point, the top of the VB (dashed line) is at lower energy than the bottom of the CB at the L point indicating that this is a semiconductor with a bandgap E_g. The computations for this band structure were performed using density functional theory.[5]

Exciton states

When a semiconductor material absorbs a photon with an energy equal to or higher than the bandgap energy (E_g), a VB electron is excited into the empty CB. The behavior of the "missing" electron in the VB can be modelled as a quasiparticle called a hole (h^+). Both the electron and hole carry a net charge and are therefore called charge carriers. The ability of charge carriers to move through a lattice is reflected by their effective masses. In the context of a band structure diagram, the effective mass of electrons and holes is inversely related to the curvature of the bands, as dictated by the dispersion relation $E(k)$. So a high (low) band curvature corresponds to a low (high) effective mass and thus a high (low) carrier mobility. By approximation, the dispersion relation is

parabolic at the valence band (VB) and conduction band (CB) extrema, resembling that of a free electron but with a different mass. In the band structure diagram of $Cs_2AgBiBr_6$ the dispersion relation around the CB minimum van VB maximum are far from symmetrical reflecting differences in charge mobility in different directions. Usually, one side of the extrema is then selected to represent the effective carrier mass. A broad parabolic shape in the resulting curve indicates a higher effective mass for the charge carrier and a narrow curve reflects a lower effective mass (see **Figure 2.4b**). Ionic compounds typically exhibit larger effective masses for electrons and holes due to a heightened concentration of charge near the nuclei, leading to increased scattering.

After photoexcitation, the electron and hole experience Coulomb attraction and can form a bound state that is called an exciton. The movement of the electron orbiting the hole can be compared to that of an electron orbiting the nucleus of a hydrogen atom. The exciton energy is then:[6]

$$E_X = E_g - \frac{Ry_X}{n^2} + \frac{\hbar^2 K^2}{2(m_e^* + m_h^*)} \tag{2.2}$$

Where, E_g represents the energy gap between the CB and VB, and the Ry_X/n^2 term describes the hydrogen-like set of energy levels of the exciton. Here, Ry_X is essentially the hydrogen Rydberg energy adjusted for a material's relative permittivity and effective electron and hole mass. Note that when $n = \infty$, it denotes the free exciton state, indicating that electrons and holes are no longer bound but move freely within the CB and VB. The third term describes the translational motion of the exciton in the lattice with wavevector K and corrected for combined effective electron (m_e^*) and hole (m_h^*) mass. The resulting exciton dispersion relations for several different n (=1, 2, 3 and ∞) are plotted in **Figure 2.4c**. Exciton formation following light absorption leads to almost vertical transitions ($\Delta K \approx 0$) in this figure because of the negligible momentum of photons compared to excitons.

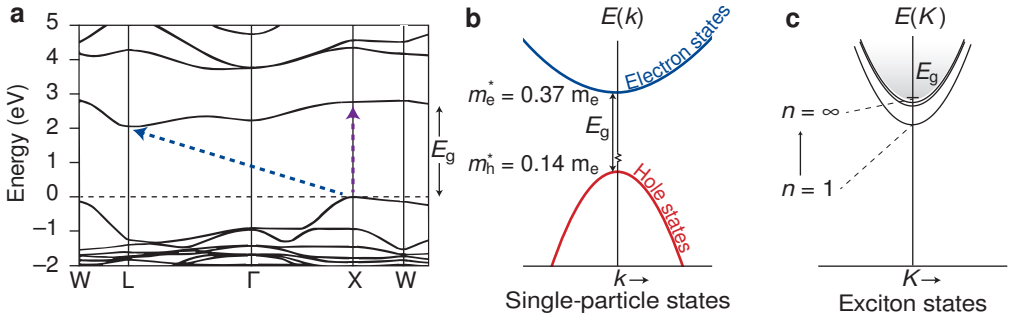

Figure 2.4 | Energy band diagram of $Cs_2AgBiBr_6$ and excitonic transitions observed in semiconductors. (**a**) Band structure diagram of cubic $Cs_2AgBiBr_6$ with high symmetry points denoted on the *x*-axis and the energy on the *y*-axis.[5] (**b**) Schematic representation of electron and hole dispersion relation in $Cs_2AgBiBr_6$ at the X-point. The effective masses of the hole and electron are expressed in terms of the electron mass in vacuum m_e. The wider top curve reflects the larger effective electron mass (m_e^* = 0.37 m_e), whereas the narrower lower curve corresponds to the hole dispersion with a smaller effective mass (m_h^* =0.14 m_e). (**c**) Exciton states plotted with different discrete sets of exciton Rydberg energies *n*, with $n = 1$ as the lowest energy exciton state. Exciton creation leads to discrete absorption bands with an energy lower than E_g. For $E_{abs} \geq E_g$ the absorption intensity increases with the number of energy states available, as indicated by the grey shaded area. Figure adapted from ref. [6].

Optical transitions between the VB and CB in semiconductors and insulators typically involve transitions between bands with different orbital character. Excitation thus results in a transition dipole moment, which satisfies the parity selection rule. In addition, transitions need to conserve total momentum and this conservation law leads to two types of excitonic absorption: direct and indirect bandgap transitions. In $Cs_2AgBiBr_6$ for example, this selection rule is obeyed for the direct transition from the VB maximum to the CB minimum at the X point and gives rise to a strong absorption feature (vertical arrow, **Figure 2.4a**). In some semiconductors (e.g. Si and $Cs_2AgBiBr_6$) the lowest-energy transition from the VB to the CB involves a transition between different *k*-values in the Brillouin zone, which does not conserve total momentum. In such cases, it is called an indirect semiconductor and absorption requires the absorption or emission of phonons (vibrations) to satisfy momentum conservation and results in very weak absorption bands (diagonal arrow, **Figure 2.4a**) and long radiative lifetimes.

In semiconductors, high energy photogenerated charge carriers rapidly (< ps) relax to the edges of the CB and VB, "find" each other and form an exciton with an energy according to Equation 2.2 (**Figure 2.5a**). These excitons can be considered to be delocalized over several unit cells. Electron–hole recombination across the bandgap results in the emission of a photon with energy E_X. This type of emission is characterized by a small energy difference between the absorption onset

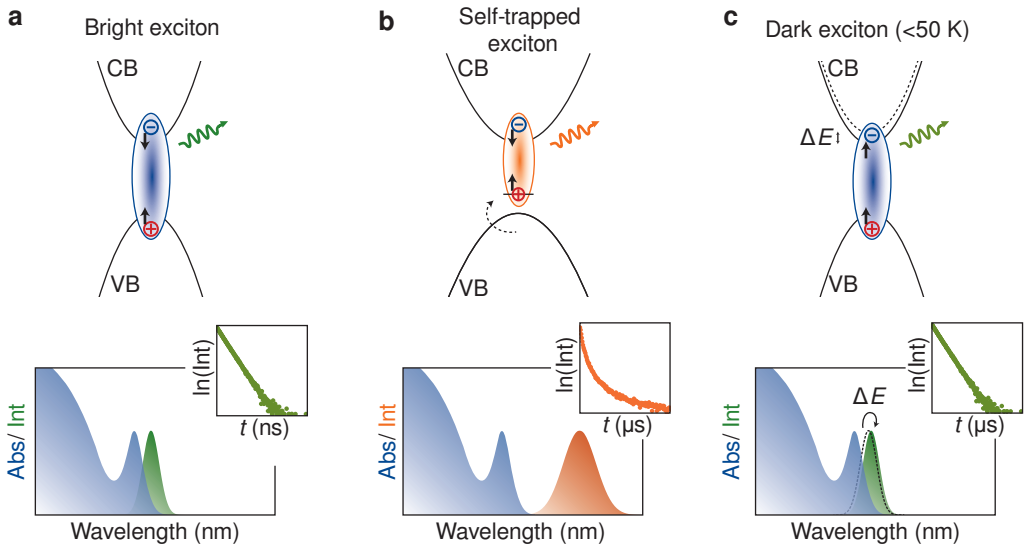

Figure 2.5 | Different types of excitonic transitions and their photoluminescence characteristics (**a**) Bright exciton transitions are typically dipole and spin allowed and result in emission with a small Stokes shift and narrow bandwidth and luminescence decay on the ns timescale. (**b**) Self-trapped excitons form very fast after photoexcitation as a result of (in this example) hole trapping. The emission has a large Stokes shift and broad bandwidth as a result of strong electron-phonon coupling, which arises as a consequence of the lattice reorganization. Luminescence decay curves are multi-exponential and slower, on a µs time scale. (**c**) At low temperatures (< 50 K), an exciton can be "frozen in" an energetically lower lying dark-exciton state. Transition from this state are spin-forbidden and result in emission that takes place on the µs timescale. Given the small energy difference ΔE this is typically not observed in the emission spectrum as it only results in a small shift (dashed line emission at higher temperature, green emission band at low temperatures).

and the emission peak. The emission bandwidth is small because of the limited coupling to lattice vibrations. As the transition is an allowed electric dipole transition the decay rates are high, on the order of ns^{-1}.

In other semiconductors there is a large lattice reorganization around photoexcited charge carriers which stabilizes and subsequently localizes it. Usually this phenomenon is found in more ionic semiconductors. (**Figure 2.5b**).[7] For example, if a hole creates a local lattice distortion it is bound to the location in the perturbed crystal lattice. Here it can attract an electron and form an exciton, hence the name self-trapped exciton. The emission band is redshifted with respect to the exciton energy described in **Equation 2.1** because of the lattice stabilization as well as strong coupling to vibrations during recombination. The vibrationally assisted recombination gives rise to broad emission bands. Depending on the nature of the self-trapped state, the transition rate can vary widely but is typically μs^{-1}.[8] The semiconductors displaying self-trapped emission investigated in this thesis display ~μs^{-1} decay rates and will be discussed in more detail in **Chapter 5** ($Cs_2AgBiBr_6$) and **Chapter 6** (Ag_2S).

At low temperature the spin orientation of the electron and hole become relevant in the emission process. In a simple approximation (ignoring spin-orbit coupling) exchange coupling of the electron and hole spins result in the splitting into a singlet (S=0) and triplet (S=1) excited state, separated by a small energy ΔE which depends on the strength of the exchange coupling. The energetically more favorable triplet state, has a spin-forbidden transition to the ground state because of the spin selection rule $\Delta S = 0$ (**Figure 2.5c**). If the temperature is low enough (typically < 50 K) ΔE is higher than $k_B T$ and the system is "frozen" into the lowest energy excited state after relaxation, resulting in emission originating from a spin-forbidden transition. Because of the small energy difference (few meV) between the high spin and low spin state this is usually not noticeable in the emission spectrum. However, the transition rate decreases by roughly 2 to 3 orders of magnitude because of the forbidden nature of the transition. In view of the forbidden character the triplet excited state is also known as dark state, while the singlet state is known as bright state.[9] Taking spin-orbit coupling into account leads to a more complex situation in which excited states are characterized by their total angular momentum J and selection rules apply to transitions between the ground state and various excited states which are called bright or dark depending on transitions being allowed or forbidden.

Optically active dopants

The incorporation of optically active dopants, such as transition metal or lanthanide ions, into wide bandgap crystals form the basis of most traditional phosphors. Unlike semiconductors, where optical properties arise from transitions between energy levels of the host crystal, these phosphors derive their optical characteristics from energy levels of the dopants due to electron interactions within the dopants' partly filled atomic d (transition metals) and f (lanthanides) orbitals. In this section, we address how these electron–electron interactions shape the energy level structure of transition metal and lanthanide ions. It further explores how the optical properties of transition metal ions are shaped by the surrounding crystal field, contrasting this with the remarkable independence of energy levels observed in lanthanides within a host material.

Transition metal ions

The transition metals can be found in the heart of the periodic table, spanning the groups 3 to 11.

Their electrons occupy the *n*d orbitals (with n = 3, 4, 5), which can at most hold 10 electrons. Transition metal ions often display vibrant colors and in several cases photoluminescence. These phenomena are related to Coulomb interactions between the electrons in partially filled d orbitals that results in a rich energy level structure and absorption and emission of specific wavelengths of light. Such transitions are known as d–d transitions. Both the oxidation state of a metal ion and the nature of its surrounding ligands (in a host crystal) have a large impact on the color. A beautiful example is how the color of an aqueous Cu^{2+} solution changes when different coordinating ligands are added to the solution (**Figure 2.6**). In this section, we will discuss how the d orbital configuration and (octahedral) crystal environment give rise to the optical properties of transition metal ions.

To understand the optical properties of transition metal ions, we will first consider a "free ion", where Coulomb interactions between d orbital electrons play a role and the electrons feel no influence of the environment. The repulsion between negatively charged electrons causes the splitting of d^n configurations into distinct energy levels. In the case of the d^3 configuration for example, the energy levels can be determined by placing the 3 electrons in the 10 available d orbitals with different quantum numbers m_l (varying from −2 to 2) and m_s (−½ or +½). Subsequently, we can determine the total orbital angular M_L ($\Sigma_i m_l$) and total spin angular momentum M_S ($\Sigma_i m_s$) for all $\binom{10}{3} = 120$ possible configurations called microstates. The M_L and M_S values can then be used to determine the *LS*-terms for the energy levels of the d^3 configuration. These *LS*-terms (also known as Russell-Saunders term symbols) are labelled ^{2S+1}L, where the superscript describes the spin-multiplicity and the L value is represented with a letter value analogous to the description of atomic orbitals, but now capital letters are used to reflect that the angular momenta refer to a multi-electron system (L = 0 gives an S, L = 1 a P, L = 2 a D, L = 3 an F, etc.). The ground state is

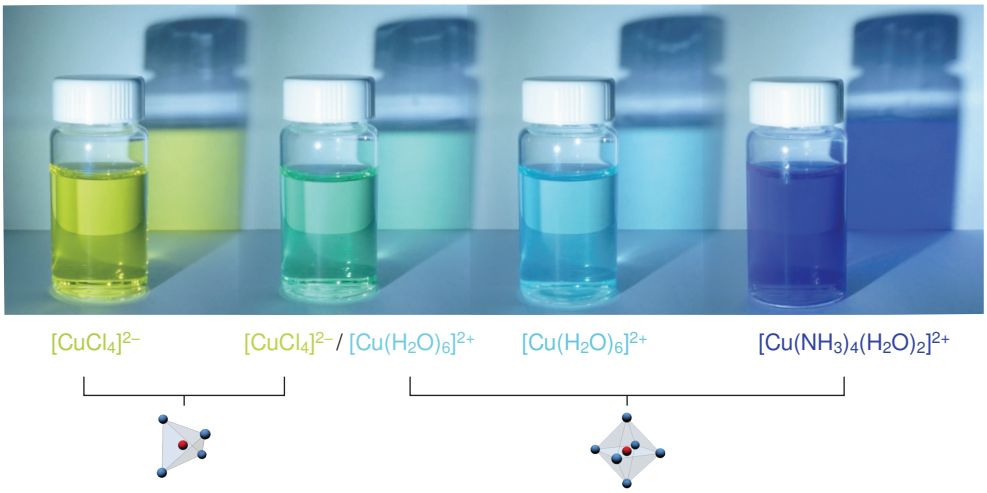

Figure 2.6 | Cu^{2+} coordinated by different ligands in an aqueous solution showing remarkably different optical properties. Going from left to right, Cu^{2+} in the presence of a large excess of Cl^- adopts a tetrahedral coordination which transmits yellow light. Lowering the Cl^- concentration results in a green, mixed $[CuCl_4]^{2-}$ and octahedrally coordinated $[Cu(H_2O)_6]^{2+}$ solution. In pure water all Cu^{2+} is coordinated by H_2O and gives rise to a light blue solution. When ammonia is added to the solution, it replaces part of the water molecules and causes the absorption band to blueshift. A blueish-white LED-YAG:Ce^{3+} lamp was used for illumination.

determined using Hunds' rules: 1) the spin multiplicity (represented by $2S + 1$) is the highest and 2) the angular momentum quantum number (L) reach their maximum values. For d^3 configurations, this corresponds to the ^4F term symbol.

Electron configurations with different LS term symbols possess differing energies due to Coulomb repulsion between electrons in d orbitals. A common way of quantifying the energy of each free-ion term is by the Racah parameters A, B and C. Here A contributes the same energy for each term symbol, whereas the contributions of B and C vary for different LS energy levels. As we consider transitions between different states in optical spectroscopy, we are interested in energy differences between the levels. Therefore, the offset energy created by A is not relevant. The energy of the levels can then be expressed in terms of B and C. Typical values for the B/C ratio for d^n in many host materials are known based on experiments, which means the term symbol energies can be determined based on the experimentally found value of B.[10] For example, for the d^3 configuration in fluoride hosts relevant for this thesis, a B/C ratio that is roughly around 4.5 has been found.

Crystal Field splitting

As demonstrated in **Figure 2.6**, the optical properties of transition metal ions are shaped not only by interactions within the d-electron shell but also by their environment. The influence of the coordinating anions, known as ligands, is of a similar magnitude as that of electron–electron repulsion and can be described with crystal field theory. After reviewing the effect of an octahedral crystal field, the combined impact of electron–electron repulsion and the crystal field will be discussed.

The crystal field theory explains how the arrangement of different types of ligands around the metal ion results in the splitting of the d orbitals. In **Figure 2.7a** the contour plots of the d orbital wavefunctions (blue and red) are shown with negatively charged ligands (black dots) surrounding them in an octahedral symmetry (denoted with O_h). In octahedral complexes, the $d_{x^2-y^2}$ and d_{z^2} orbitals are spatially closer to the coordinating ligands than the d_{xy}, d_{yz} and d_{xz} orbitals and therefore experience more electronic repulsion. The resulting energy separation between the two sets of orbitals is called the crystal-field splitting Δ_O. We can consider the Δ_O value with respect to the theoretical energy of the five degenerate d orbitals when they are surrounded by a uniformly distributed charge. This average energy is called the barycenter. In octahedral symmetry, two e_g orbitals lie 3/5 Δ_O above the barycenter, while three t_{2g} orbitals are positioned 2/5 Δ_O below the barycenter (**Figure 2.7b**).

The value of Δ_O varies systematically depending on the ligands and the metal ion they coordinate. The crystal field splitting increases for higher negative charge of the coordinating ligand and with decreasing distance to the ligands. Based on these considerations they can be ordered in the spectrochemical series:

$$I^- < Br^- < Cl^- < F^- < OH^- < H_2O < NH_3 < CN^-$$

In the series, ligands that cause a large crystal field splitting are on the right. Note that the charge that determines the crystal field splitting is that of the atom coordinating to the transition metal ion, which is −2 for oxygen and −3 for nitrogen. The crystal field strength is also influenced by the size and oxidation state of the central cation. Typically, the higher the charge on the cation and the further down a group, the stronger the crystal field splitting Δ_O will be. The larger splitting observed in heavier transition metal ions is a consequence of the comparatively larger spatial

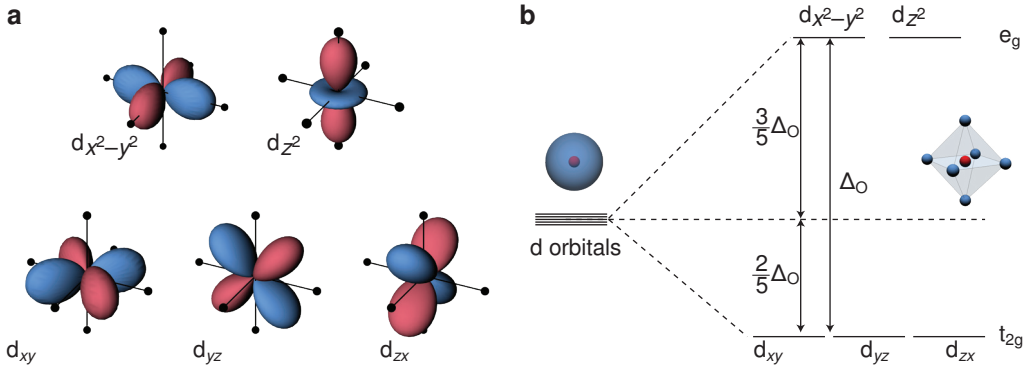

Figure 2. 7 | The transition metal ion d orbitals in octahedral symmetry. (**a**) Contour plots of the real part of the hydrogen-like d orbital wavefunctions, which are obtained by taking linear combinations of the spherical harmonics with $l = 2$. The different colors represent negative (red) and positive (blue) phases of the wavefunction. The black dots represent the positions of negative charges (point charges) in a crystal field with octahedral symmetry. (**b**) The effect of a (theoretical) spherical negative potential around the metal ion defines the barycenter of the five d orbitals. The splitting Δ_O as a result of the octahedral ligand coordination causes the d_{xy}, d_{yz} and d_{zx} orbitals to be lowered in energy, while the $d_{x^2-y^2}$ and d_{z^2} become higher in energy. The t_{2g} and e_g labels come from group theory and define the symmetry properties and indicate the degeneracy of the states, 3 and 2 respectively.

extension of the 4d and 5d orbitals compared to 3d orbitals. Hence, the interaction with ligands increases as one progresses down the periodic table. For highly charged cations the large positive charge draws the negative ligands in closer proximity to the ion. Consequently, the same metal ion with the same ligands experiences a stronger crystal field splitting as the positive charge increases.

With the addition of the crystal field effect, the *LS* terms alone do not accurately describe the electronic states of transition metals incorporated in host crystals anymore. Each (degenerate) *LS* term contains contributions from different d orbitals (like in **Figure 2.7a)** which have the same energy for the free ion. These orbitals split in an octahedral crystal field and, as a result, *LS* terms can split up in several crystal field terms. Another (smaller) effect of the crystal field comes from the changing shape and expansion of the d orbitals as they hybridize with the ligand electrons. Hence, the values of the *B* and *C* parameters change with respect to the free ion values. The splitting of term symbols into crystal field terms is achieved by using their symmetry and applying group theory.[10] The new energy levels arising from the crystal splitting are identified by irreducible representation labels of the octahedral symmetry group. The splitting can be determined from the value of *L* using group theory or can be found in text books for each term symbol.[11] In the d^3 configuration for example, the lowest energy ^4F term symbol splits into the $^4A_2$ ground level and the $^4T_2$ and $^4T_1$ higher energy levels. The letter again indicates the degeneracy of the level (A, B = 1, E = 2 and T = 3), while the subscript reflects the symmetry properties of the level. The spin multiplicity is unaffected by the crystal field and is always the same as that of the term symbol from which the crystal field levels arise. Upon increasing the crystal field strength i.e. by changing the ligands, distance or oxidation state, the levels will be increasingly separated in energy.

In 1954, the energy of the crystal field levels were plotted as function of the crystal field strength for all d^n configuration (n = 2 to 8) by Tanabe and Sugano, in the aptly named

Tanabe–Sugano (TS) diagrams.[12] Since the publication, TS-diagrams have become instrumental in explaining the optical properties of transition metal ions for each d^n configuration. In TS diagrams the energy is plotted as E/B (y-axis) as a function of the the crystal field strength as Δ_O/B, which allows us to use the diagram for any transition metal ion (independent of B). **Figure 2.8a** shows the d^3 TS diagram, which is computed using $B/C = 4.5$ as is common for the d^3 configuration. Note that the energies of all crystal field levels are relative with respect to the lowest energy state ($^4A_2$ for d^3 ions) that as a rule coincides with the x-axis. In the diagram some lines are curved as a result of the anti-crossing rule for states of the same symmetry by mixing under the influence of the crystal field. The two $^4T_1$ states are a good example of this effect. Furthermore, the energy of certain states, such as the ^2E state, is practically independent of the crystal field strength Δ_O. This can be understood by considering that their orbital occupation is t_{2g}^3, the same as the ground state $^4A_2$ (**Figure 2.8d**). Nevertheless, the energy of the $^2E \rightarrow {}^4A_2$ transition can vary between hosts (e.g. 15000 cm^{-1} in oxides and 16000 cm^{-1} in fluorides). These variations stem from differences in electronegativity between ligands, affecting the degree of mixing between transition metal and ligand orbitals and thus the B parameter. For more covalent hosts the mixing increases and causes an expansion of d orbitals, known as the nephelauxetic ('cloud expanding') effect, which reduces the inter-electron repulsion and thus the Racah parameters B and C.

It is important to remember that the transition rates depend on the optical selection rules. In the case of transition metal ions, transitions between the various d^n orbital energy levels do not involve a change in electron configuration or parity. Hence, these $3d^n \rightarrow 3d^n$ (d–d) transitions are

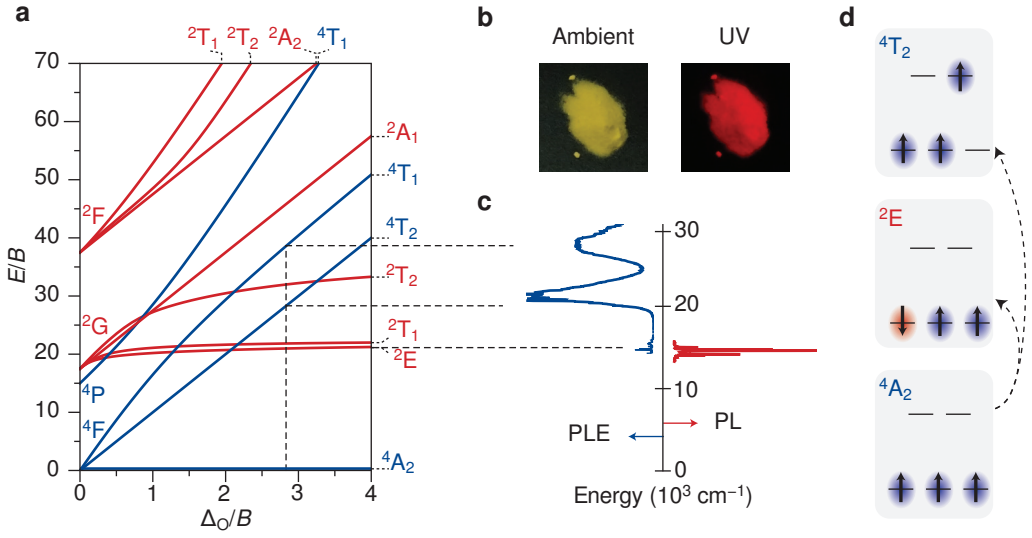

Figure 2.8 | Transitions in the d^3 Tanabe-Sugano diagram and optical properties of $K_2SiF_6:Mn^{4+}$. (**a**) The d^3 Tanabe-Sugano diagram computed using $B/C = 4.5$. Blue lines indicate crystal field levels with a spin multiplicity of 4, while red lines have a spin multiplicity of 2. (**b**) Photographs of K_2SiF_6:7.5 Mn^{4+} powder under ambient and UV illumination. (**c**) Excitation (blue) and emission (red) spectra of $K_2SiF_6:Mn^{4+}$ aligned with the transitions in the Tanabe-Sugano diagram responsible for these bands (λ_{exc} = 460 nm, λ_{em} = 631 nm). (**d**) Electron configuration of the $^4A_2$ ground state and the ^2E and $^4T_2$ excited states in the different d orbitals. The dashed arrows correspond to spin-allowed ($^4A_2 \rightarrow {}^4T_2$) and spin-forbidden ($^4A_2 \rightarrow {}^2E$) transitions.

parity forbidden and have weak absorbance. The corresponding emission rates are similarly slower (μs^{-1}–ms^{-1}). In addition, some transitions are also spin-forbidden if the spin multiplicity changes. In **Figure 2.8a**, these are all the transitions from a level with $S = 3/2$ (blue lines) to a level with $S = 1/2$ (red level) or vice versa. The absorbance of spin-forbidden transitions is even weaker than spin-allowed transitions and the emission rate is on the sub ms^{-1} timescale. The parity selection rule can be relaxed by admixing energy levels with opposite parity states by static odd parity crystal field component (not present in perfect octahedral symmetry!) or by coupling to ungerade (odd parity) lattice vibrations.

With the selection rules and the d^3 TS diagram in mind, we can now interpret which transitions are responsible for the optical properties of the commercial phosphor K_2SiF_6: Mn^{4+}. The primary absorption bands in the blue and UV part of the spectrum give this material a yellow hue, while excitation in these bands results in a deep red emission (**Figure 2.8b**). The broad absorption bands stem from parity-forbidden, but spin-allowed transitions from the $^4A_2$ ground state to the $^4T_2$ and $^4T_1$ excited states (blue spectrum, **Figure 2.8c**). Given that both the $^4T_2$ and $^4T_1$ energies experience a strong change with crystal field strength and that vibrations can cause small changes in ligand to d-electron distance and thus Δ_O, this explains that broad absorption bands are observed. Absorption to the $^4T_2$ and $^4T_1$ levels is followed by fast phonon-mediated relaxation to the lowest excited state, the ^2E level. The emission resulting from the $^2E \rightarrow {}^4A_2$ transition has very narrow emission lines because the ^2E energy hardly varies with crystal field strength Δ_O as is clear from the ^2E level running parallel to the $^4A_2$ ground state in the TS diagram. An alternative way to grasp this concept is to consider that in the $^4A_2 \rightarrow {}^4T_2$ transition an electron is excited from a non-bonding t_{2g} orbital to an anti-bonding e_g orbital (**Figure 2.8d**). This affects the ion–ligand distance and causes strong electron–phonon coupling. In contrast, the $^2E \rightarrow {}^4A_2$ transition involves no change in electron configuration (only spin reorientation). Because the $^2E \rightarrow {}^4A_2$ transition is parity-forbidden and the coordination is octahedral in K_2SiF_6, the emission predominantly arises from coupling to asymmetric lattice vibrations (no zero-phonon line) and will be discussed in more detail in **Chapters 3** and **4**.

Lanthanides

The lanthanides are usually displayed at the bottom of the periodic table and comprise a group of 15 elements ranging from La to Lu. The most common oxidation state for lanthanides is Ln^{3+}, which involves the removal of two 6s electrons and a 4f or 5d electron from the neutral atom. In this state, the electron configuration is $[Xe]4f^n$, with n ranging from 0 to 14. Electronic interactions within the partially filled 4f orbitals give rise to a rich energy level structure that varies per lanthanide. Transitions between the $4f^n$ energy levels (f–f transition) occur through the absorption and emission of ultraviolet (UV), visible, or infrared (IR) light. In addition, also transitions between the 4f and 5d orbitals (f-d) transitions can give rise to efficient luminescence. As a result, luminescent lanthanide-doped materials are used in numerous applications varying from almost outdated (compact) fluorescent tube lamps (Tb^{3+}, Eu^{3+}) and modern LED lighting and displays (Eu^{2+}, Ce^{3+}) [13] to less known but important applications in medical x-ray imaging and homeland security (Ce^{3+}, Tm^{3+}, Pr^{3+}, Eu^{2+}),[14] data storage and communication (Er^{3+}),[15] glow-in-the-dark phosphors (Eu^{2+}, Dy^{3+})[16] and even Euro banknotes (Eu^{2+}, Eu^{3+}, Yb^{3+}, Er^{3+})[17,18] and emerging applications such as high resolution optical thermometry (Yb^{3+} and Er^{3+}).[19]

In contrast to the transition metals discussed before, the optical properties of the trivalent lanthanides are hardly affected by the host material. The 4f-electrons are located in orbitals close

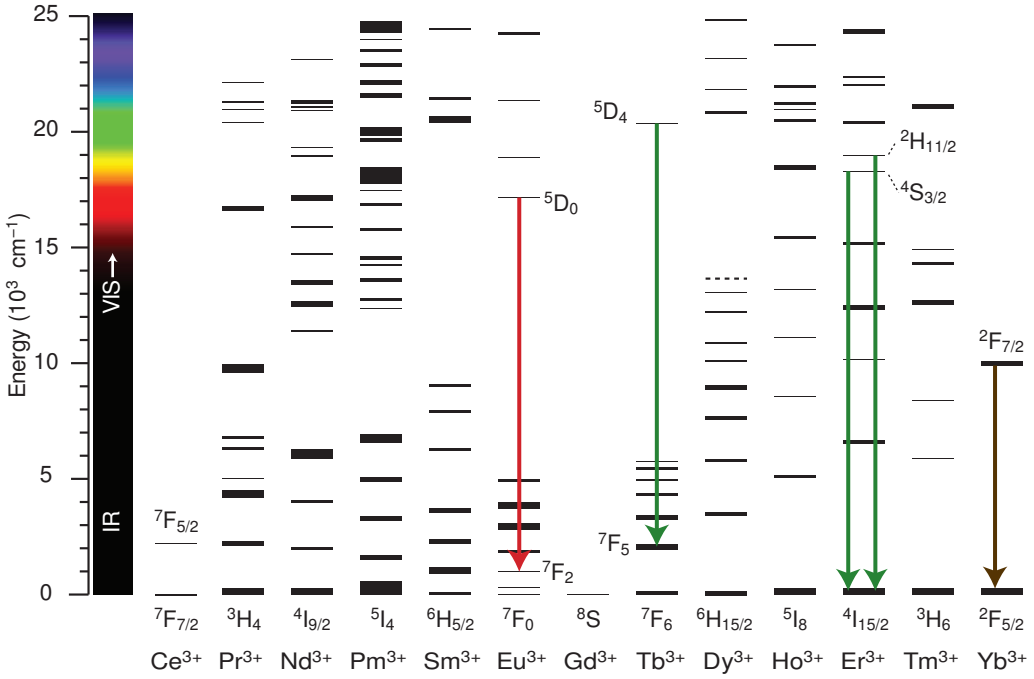

Figure 2.9 | The Dieke diagram containing the energy levels of trivalent lanthanides up to 25 000 cm^{-1} (400 nm) with some important transitions marked with arrows corresponding to the emission color.[21] Each bar in the diagram represents an energy level with a corresponding term symbol. The ground states are labeled and the width of the bar indicates the crystal field splitting. The strong red (λ_{em} = 625 nm) $^5D_0$ to $^7F_2$ transition in Eu^{3+} is used extensively in fluorescent lamps, often in combination with the typical $^5D_4 \rightarrow {}^7F_5$ green emission (λ_{em} = 543 nm) from Tb^{3+}. In recent years, the green emitting levels ($^2H_{11/2}$ and $^4S_{3/2}$) of Er^{3+} have gained a lot of attention for luminescence thermometry applications.[21] The ion investigated in this thesis is Yb^{3+} (which is often used as strong upconversion absorber for green emitting Er^{3+}) and typically absorbs and emits around 1000 nm.

to the nucleus and are therefore shielded from the environment by the more extended 5s and 5p orbitals. The limited interaction of the f orbitals with the surroundings give the f–f transitions very narrow absorption and emission bands with negligible Stokes shift. In addition, the shielding of the f-electrons gives rise to a constant energy level structure regardless of the host material. In the 1950s and 1960s, the energy levels of trivalent lanthanides in $LaCl_3$ were measured and the Dieke diagram was constructed (see **Figure 2.9**).[20] In this diagram the energy levels correspond to different distributions of electrons over the orbitals in the 4f shell. Similar to the determination of d-electron energies, the computation of f-electron energy levels involves accounting for electron–electron interactions, giving rise to *LS* term symbols. An additional interaction important for the energy level structure of lanthanides is spin-orbit coupling. For heavy elements like the lanthanides, fast moving electrons around the nucleus experience a strong magnetic field from the positively charged core.

All the transitions between energy levels described in the Dieke diagram are intra-configurational $4f^n$–$4f^n$ (f–f) transitions and therefore parity forbidden. Some transitions occur through coupling with the magnetic field of photons and are magnetic dipole allowed, for example the $^5D_0 \rightarrow {}^7F_1$

transition in Eu^{3+}. However, most f–f transitions involve forced electric dipole transitions. These are transitions that are weakly allowed due to the crystal field admixing of opposite parity higher energy states, such as $4f^{n-1}5d^1$ states, into the $4f^n$ states. This induces a small change in dipole moment for the f–f transitions and therefore the absorbance is typically weak (or "forbidden", recall **Figure 2.1d**). Emission resulting from transitions between lanthanide $4f^n$ energy levels is equally forbidden and typically takes place on the ms timescale. Note that forbidden does not mean that the emission is weak. The radiative decay rate is slow but the competing process of transferring the excited state energy to lattice vibrations (quenching the luminescence) is even slower when the energy gap to the next lower level is large and this gives rise to highly efficient lanthanide luminescence, for example for the green Tb^{3+} and red Eu^{3+} emissions depicted in **Figure 2.9**.

Trivalent Ytterbium

The Yb^{3+} ion is especially relevant to this thesis and will be discussed in more detail. Yb^{3+} has 13 electrons in its 4f shell, which are distributed over seven 4f hydrogen-like orbitals (**Figure 2.10**). The configuration of 13 electrons can be regarded as a configuration with a single hole in the 4f subshell. Because a single hole does not experience Coulomb interaction it results in only one *LS* term symbol with $L = +3$ and $S = +½$. The corresponding term symbol can be constructed using ^{2S+1}L and yields the ^2F term symbol which is 14-fold degenerate.

If Yb^{3+} contained only one 14-fold degenerate ground state, no optical transitions would be possible. However, spin–orbital coupling creates an energy difference between the configurations with the hole spin parallel or anti-parallel to the orbital angular moment, described by *J* values of 5/2 and 7/2 and term symbols $^2F_{7/2}$ and $^2F_{5/2}$ (**Figure 2.11a**). Note that as we move across the lanthanide series, the influence of spin–orbit coupling increases by a factor of 4 to 5. Spin–orbit coupling increases with the atomic number Z^4 and this is a result of the higher nuclear charge and the lanthanide contraction, which brings the electrons into closer proximity to the core. The effect is clearly visible in **Figure 2.9** by comparing the energy difference between the $^2F_{7/2}$ and $^2F_{5/2}$ levels of Ce^{3+} (a light lanthanide) and Yb^{3+} (a heavy lanthanide).

The resulting states are each $(2J+1)$-fold degenerate and can be further split by the crystal field caused by surrounding ligands. As mentioned earlier, this effect is limited in comparison to electron–electron interaction and spin–orbit coupling but can provide useful information about the coordination of a lanthanide ion in a host material. The effect of an octahedral crystal field for Yb^{3+} in $Cs_2NaYbCl_6$ is shown in **Figure 2.11b**. In such a high-symmetry environment only part of the degeneracy is lifted by the crystal field and the $^2F_{5/2}$ and $^2F_{7/2}$ energy levels are split into 2 and 3 crystal field components, respectively.[22] This results in a final splitting of the energy levels on the order of a few 100 cm^{-1}.

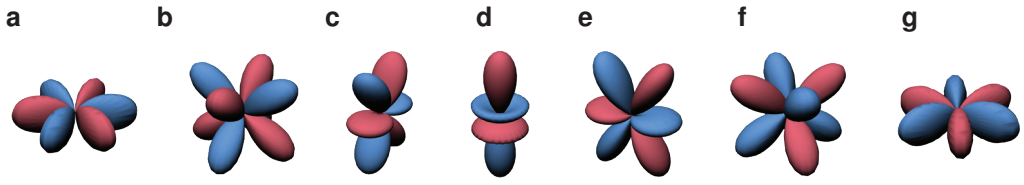

Figure 2.10 | Hydrogen-like 4f orbitals. Contour plots of the real part of the 4f wave functions are plotted by taking linear combinations of complex spherical harmonics with $l = 3$.

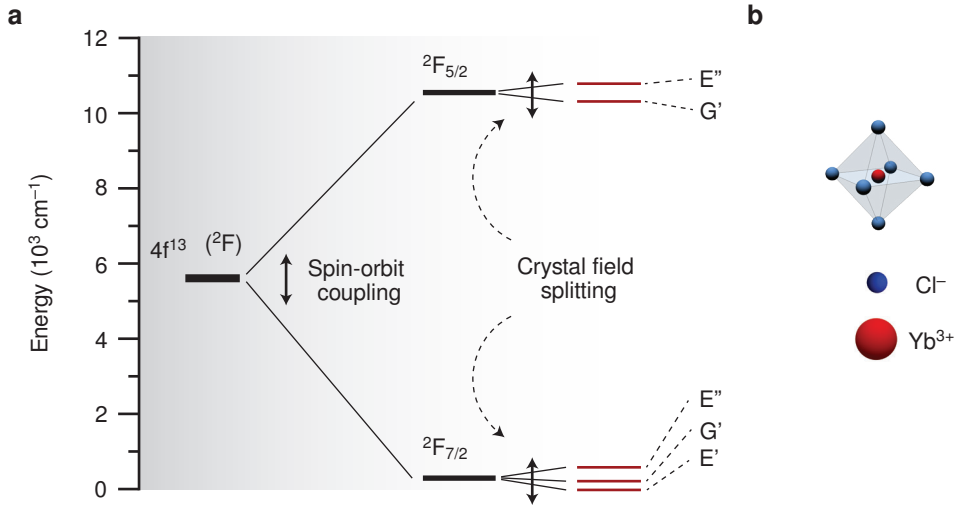

Figure 2.11 | Splitting of the $4f^{13}$ energy levels of Yb^{3+}. (**a**) The degeneracy of the $4f^{13}$ electron configuration of Yb^{3+} is not lifted by electron–electron interaction, because it is a configuration with one hole. The 14-fold degenerate energy level has the ^2F term symbol. This degeneracy is lifted by the effect of spin–orbit coupling, resulting in the ground state configuration $^2F_{7/2}$ and the first and only $^2F_{5/2}$ excited state. If Yb^{3+} is incorporated in a crystalline host, the degeneracy is further lifted by the (small) effect of the crystal field. The crystal field levels are labeled with Mulliken symbols, where ' (prime) means symmetric with respect to σ_h and " (double prime) antisymmetric.[22] (**b**) In an octahedral coordination the crystal field effect for Yb^{3+} in $Cs_2NaYbCl_6$ results in the 3-fold splitting of the $^2F_{7/2}$ and 2-fold splitting of the $^2F_{5/2}$ state.

Charge transfer states

The weak absorbance of lanthanide and transition metal ions poses a problem in some applications. Stronger absorbing transitions to higher energy states are often utilized. A typical example is a charge transfer transition from a ligand to the luminescent ion (ligand-to-metal charge transfer, LMCT). This transition involves a redistribution of electron density between the ion and ligand and requires more energy than redistribution of electrons in the $3d^n$ or $4f^n$ shell. Theyv are usually situated in the UV spectral region. In the LMCT process, the electron density shifts from the ligand to the ion, effectively resulting in the photoreduction of the ion. These transitions are highly intense due to the significant charge distribution difference between the initial and final states, resulting in a large transition dipole moment. Following strong charge-transfer absorption, the system relaxes to lower energy $3d^n$ or $4f^n$ excited states to give the characteristic 3d or 4f transition metal luminescence.

Analogous to the LMCT described above, a VB to CB electron transition in a semiconductor can be followed by energy transfer to a 3d or 4f dopant incorporated in the semiconductor. This transfer process is more complex as the excitation energy is not absorbed by a transition involving the luminescent ion. Energy transfer can occur via subsequent capture of the CB electron and VB hole by the lanthanide (or d-metal) ion, leaving the luminescent ion behind in an excited state. Alternatively, energy transfer may occur via a (trapped) exciton state of the semiconductor to a high excited state of the lanthanide or d-metal ion. This process enables the strong absorption of semiconductors to be used for sensitizing efficient optical emitters.

References

[1] M. A. Van De Haar, M. Tachikirt, A. C. Berends, M. R. Krames, A. Meijerink, F. T. Rabouw, *ACS Photonics* **2021**, 8, 1784.
[2] R. Marin, D. Jaque, *Chem. Rev.* **2021**, 121, 1425.
[3] P. A. Cox, *The Electronic Structure and Chemistry of Solids*, Oxford University Press, **1987**.
[4] J. R. Hook, H. E. Hall, *Solid State Physics*, John Wiley & Sons, **2013**.
[5] E. T. McClure, M. R. Ball, W. Windl, P. M. Woodward, *Chem. Mater.* **2016**, 28, 1348.
[6] S. V Gaponenko, *Introduction to Nanophotonics*, Cambridge University Press, **2010**.
[7] R. T. Williams, K. S. Song, *J. Phys. Chem. Solids* **1990**, 51, 679.
[8] K. I. Kan'no, T. Matsumoto, Y. Kayanuma, *Pure Appl. Chem.* **1997**, 69, 1227.
[9] K. E. Knowles, H. D. Nelson, T. B. Kilburn, D. R. Gamelin, *J. Am. Chem. Soc.* **2015**, 137, 13138.
[10] B. Henderson, G. F. Imbusch, *Optical Spectroscopy of Inorganic Solids*, Oxford University Press, **2006**.
[11] P. Atkins, *Shriver and Atkins' Inorganic Chemistry*, Oxford University Press, USA, **2010**.
[12] Y. K. Xu, S. Adachi, *J. Appl. Phys.* **2009**, 105.
[13] C. Feldmann, T. Jüstel, C. R. Ronda, P. J. Schmidt, *Adv. Funct. Mater.* **2003**, 13, 511.
[14] M. Nikl, *Meas. Sci. Technol.* **2006**, 17, R37.
[15] M. Nakazawa, Y. Kimura, K. Suzuki, *Appl. Phys. Lett.* **1989**, 54, 295.
[16] D. Van der Heggen, J. J. Joos, A. Feng, V. Fritz, T. Delgado, N. Gartmann, B. Walfort, D. Rytz, H. Hagemann, D. Poelman, *Adv. Funct. Mater.* **2022**, 32, 2208809.
[17] J. F. Suyver, A. Meijerink, *Chemisch2Weekblad* **2002**, 98, 12.
[18] J. Mutanen, T. Jaaskelainen, J. P. S. Parkkinen, in *IS&T's PICS Conf.*, **2003**, pp. 421–424.
[19] T. P. Van Swieten, T. Van Omme, D. J. Van Den Heuvel, S. J. W. Vonk, R. G. Spruit, F. Meirer, H. H. P. Garza, B. M. Weckhuysen, A. Meijerink, F. T. Rabouw, *ACS Appl. Nano Mater.* **2021**, 4, 4208.
[20] G. H. Dieke, H. M. Crosswhite, *Appl. Opt.* **1963**, 2, 675.
[21] R. G. Geitenbeek, P. T. Prins, W. Albrecht, A. van Blaaderen, B. M. Weckhuysen, A. Meijerink, *J. Phys. Chem. C* **2017**, 121, 3503.
[22] P. A. Tanner, *Mol. Phys.* **1986**, 58, 317.

Chapter 3

Increasing the Power: Absorption Bleach, Thermal Quenching, and Auger Quenching of the Red-Emitting Phosphor $K_2TiF_6:Mn^{4+}$

Based on:

J.W. de Wit, T.P. van Swieten, M.A. van de Haar, A. Meijerink, F.T. Rabouw, Increasing the power: absorption bleach, thermal quenching, and Auger quenching of the red-emitting phosphor K_2TiF_6: Mn^{4+} *Advanced Optical Materials* 11(9), 2202974, **2023**

Abstract

Mn^{4+}-doped fluorides are popular phosphors for warm-white lighting, converting blue light from light-emitting diodes (LEDs) into red light. However, they suffer from droop, i.e. decreasing performance at increasing power, limiting their applicability for high-power applications. Previous studies have highlighted different causes of droop. Here, we provide a unified picture of droop of Mn^{4+}-doped K_2TiF_6, accounting for all previously proposed mechanisms. By combining continuous wave and pulsed experiments on samples of different Mn^{4+} concentrations we quantify the contributions of absorption bleach, thermal quenching, and Auger quenching at different excitation densities. Our work contributes to understanding the fundamental limitations of these materials, and may inspire strategies to make Mn^{4+}-doped fluorides more efficient in high-power applications.

Introduction

Phosphor-converted white light-emitting diodes (w-LEDs) play a crucial role in many lighting applications. A blue-emitting (In,Ga)N chip and a color-converting phosphor layer together produce white light. Ce^{3+}-doped yttrium aluminum garnet (YAG:Ce^{3+}) is a common phosphor used to convert blue to yellow light.[1,2] A blue LED combined with YAG:Ce^{3+} produces bluish or "cold" white light, while warm white light is often desired for indoor lighting.[3] Currently, warm white light is obtained by the addition of Eu^{2+}-doped $CaAlSiN_3$ (CASN:Eu^{2+}) to the phosphor layer, which introduces a broadband emission ranging from orange to infrared.[4] This does not only create a warmer white color, but also generally raises the color rendering index, thereby making the color of the lamp more pleasant to the human eye.[5] However, it comes with the downside of decreased luminous efficacy due to emission at wavelengths where the eye is less sensitive.[6]

An alternative class of red-emitting materials with higher luminous efficacy than CASN:Eu^{2+}, are the Mn^{4+}-doped fluorides.[7–9] These materials have absorption bands in the ultraviolet (UV) and blue due to spin-allowed transitions. Their room-temperature wet-chemical synthesis is relatively simple and the narrow emission lines around 630 nm give rise to a red color with a high luminous efficacy.[10,11] These properties make Mn^{4+}-doped fluorides excellent blue-to-red converting phosphors for low-power applications such as displays. However, for lighting applications where the light powers are generally orders of magnitude higher, the use of Mn^{4+}-doped fluorides is complicated by droop: at increasing blue illumination powers the output of the phosphor increases sub-linearly, approaches a maximum, and may eventually even drop.[12–14] These phenomena can occur already at excitation densities of 100 W cm^{-2} that are typical in (home) lighting w-LEDs and negatively affect the energy efficiency and the perceived color of Mn^{4+}-containing w-LEDs.[15]

The origin of luminescence droop of Mn^{4+}-doped fluorides is not entirely clear and various mechanisms have been proposed. For example, Mn^{4+}-doped fluorides are known to suffer from temperature quenching above temperatures of 400–500 K.[16] Illumination-induced heating may hence lead to an efficiency drop at high excitation powers.[17] Additionally, the long 5–10 ms lifetime of the ^2E excited state of Mn^{4+} could contribute to droop, as it results in a high steady-state population of excited Mn^{4+} ions. Excited Mn^{4+} ions bleach the $^4A_2 \rightarrow {}^4T_2$ absorption, which ultimately limits the photon conversion rate per Mn^{4+} dopant to an amount equal to the inverse of the lifetime. More indirectly, the high steady-state population of excited Mn^{4+} at high excitation powers may lead to additional losses through excited-state absorption of the blue excitation light or through Auger energy transfer.[18] These losses could be remedied in part by gentle illumination-

induced heating up to 400 K, because the radiative lifetime and hence the steady-state ^2E excited state population decrease with temperature without the loss of light output.[19] While the various possible saturation and quenching mechanisms have been highlighted separately in previous studies, an overarching understanding of their relative contributions and of the potential avenues to alleviate droop has been missing.

In this chapter, we quantify the contributions of thermal quenching, absorption bleach and Auger quenching to droop of the red-emitting phosphor K_2TiF_6:Mn^{4+}. We perform our experiments and modeling on a set of samples with increasing Mn^{4+} doping concentration. Under blue continuous-wave (CW) illumination at increasing intensity, different samples show droop to a different extent. With a combination of luminescence thermometry based on the intensity ratio between anti-Stokes and Stokes emission lines of Mn^{4+}, reference measurements under pulsed excitation, and kinetic Monte Carlo modelling, we explain the different droop behaviors quantitatively.

Results and discussion

Figure 3.1 gives an overview of the temperature-dependent optical properties of K_2TiF_6 (KTF) doped with 0.1 mol% Mn^{4+} with respect to Ti^{4+}. The measurements are done at low excitation power to avoid illumination-induced heating. The emission spectrum upon blue excitation (**Figure 3.1a**) shows a set of sharp emission lines due to the transition from the ^2E lowest excited state to the $^4A_2$ ground state. By elevating the temperature, the high-energy emission bands increase in intensity compared to the low-energy emission bands. The photoluminescence decay (**Figure 3.1b**) is single-exponential in all cases and accelerates for increasing temperatures. The $^2E \rightarrow {}^4A_2$ transition is forbidden by both the spin and the parity selection rule, which explains the long lifetime of 5.8 ms at room temperature. The parity selection rule is relaxed by coupling to three distinct odd-parity vibrations, which are visible as three vibronic lines on either side of the zero-phonon line at 624 nm.

The temperature dependencies of the emission spectra (**Figure 3.1a**) and excited-state lifetime (**Figure 3.1b**) are both a consequence of the vibronic nature of the emission. The rate of emission through

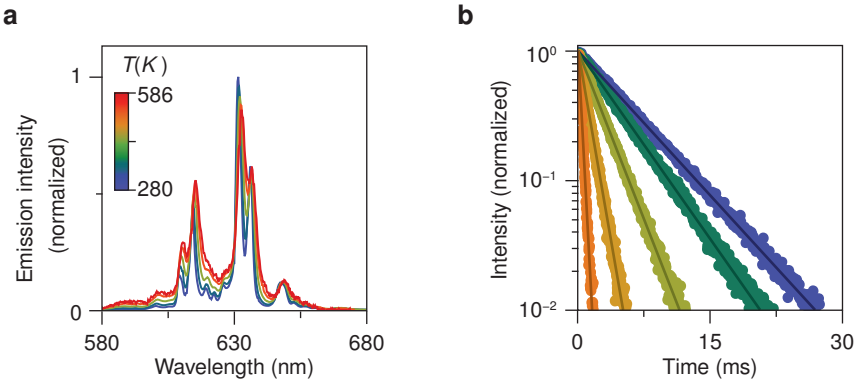

Figure 3.1 | Temperature-dependent spectroscopy of K_2TiF_6:Mn^{4+}. (**a**) Temperature-dependent emission spectra of KTF:0.1% Mn^{4+} upon 460 nm excitation. With increasing temperature, the relative intensity of anti-Stokes emission bands increases compared to the Stokes emission bands. (**b**) Temperature-dependent photoluminescence decay of the red emission, using the same color coding as in panel **a**. Excitation wavelength is 450 nm and detection wavelength is 631 nm.

a vibronic transition is proportional to the phonon occupation $n(T)$ for anti-Stokes emission or to $n(T) + 1$ for Stokes emission. Here, n(T) of a mode with phonon energy $h\nu$ increases with temperature T as

$$n(T) = \frac{1}{e^{h\nu/k_B T} - 1} \tag{3.1}$$

where k_B is the Boltzmann constant. Indeed, we observe that the anti-Stokes/Stokes intensity ratio increases (**Figure 3.2a**) and the excited-state lifetime decreases (**Figure 3.2b**) with increasing temperature. The decrease in lifetime between room temperature and 430 K is due to temperature-dependent vibronic coupling, while the sharp drop at 430 K is due to thermal quenching by nonradiative crossover through the $^4T_2$ state.[20]

For our further analysis and modeling, we model the temperature dependencies of the anti-Stokes/Stokes ratio and the excited-state lifetime by approximating the combined contribution of the vibrational modes of energies $h\nu_6$ = 216 cm^{-1}, $h\nu_4$ = 325 cm^{-1} and $h\nu_3$ = 630 cm^{-1} (see spectrum; **Figure 3.1a**) as if it were due to a single phonon mode of effective energy $h\nu_{eff}$. Details of the model and parameters are provided in Section S3.2 of the Supporting Information. The experimental anti-Stokes/Stokes ratios show an approximately exponential dependence on the inverse temperature,

$$\frac{I_{aS}}{I_S} = ce^{-h\nu_{eff}/k_B T}, \tag{3.2}$$

where c = 1.14 is a prefactor that accounts for effects such as differences in the density of optical states at the anti-Stokes and Stokes emission energies, and $h\nu_{eff}$ = 283 cm^{-1} (**Figure 3.2a**).[21] The excited-state lifetime $\tau(T)$ is determined by a combination of vibronic emission and thermal quenching:[20]

$$\tau(T) = [k_{rad}(0) + \coth(h\nu_{eff}/2k_B T) + k_{nonrad}(0)e^{-E_{act}/k_B T}]^{-1} \tag{3.3}$$

where $k_{rad}(0)$ and $k_{nonrad}(0)$ are the vibronic emission and nonradiative crossover rates at 0 K, respectively, and E_{act} is the activation energy for crossover.[20] We fit the experimental

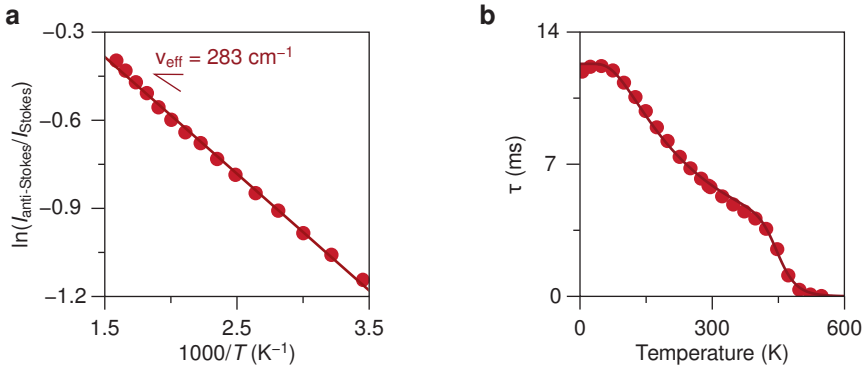

Figure 3.2 | Temperature-dependent optical properties of K_2TiF_6:Mn^{4+}. (**a**) Logarithm of the anti-Stokes/Stokes ratio as a function of inverse temperature. Solid line: fit to Equation 3.2. (**b**) Fitted excited-state lifetime as a function of temperature. Solid line: fit to Equation 3.3. The errors on the data points in panels **a** and **b** are estimated to be <0.3%, by propagating Poisson counting noise on the spectral measurement to an estimated error in the intensity ratios, and considering the standard error on the lifetime value from a single-exponential fit.

temperature-dependent lifetimes to Equation 3.3, yielding $k_{rad}(0)=1/(12.3\ ms)$, $k_{nonrad}(0)=1.5\times10^9\ ms^{-1}$, $h\nu_{eff} = 216\ cm^{-1}$, and $E_{act} = 7100\ cm^{-1}$.

We characterize the saturation behavior of our phosphors under CW excitation with blue light using the custom-built set-up shown in **Figure 3.3a**. The power of the excitation light is controlled with a calibrated motorized attenuator. Then an objective weakly focuses the blue excitation light to a spot of 167 µm at full-width-half-maximum (fwhm) onto the sample. The same objective collects the luminescence and a dichroic mirror (500 nm) separates the blue excitation from the red emitted light. The luminescence image of the sample is magnified by a factor 10 onto a 600-µm-diameter pinhole that transmits only the luminescence originating from the center of the excitation spot. This ensures that the detected signal originates from an area that experiences an approximately uniform excitation intensity. The luminescence is either imaged on a CCD camera or sent to a fiber-coupled spectrometer (**Figure 3.3b** and **c**). For our measurements below, the reported excitation intensities are the excitation intensities averaged over the area from which signal is detected (Section S3.3, Supporting Information).

Figure 3.3d shows the emission spectra of KTF:Mn^{4+} (0.1%) with blue excitation intensity I_{exc} increasing from 0.04 to 1000 W cm^{-2}. Figure S3.3 in the Supporting Information shows the corresponding data for doping concentrations of 0.8, 1.3, and 5.4%. To rule out material degradation, return measurements from high I_{exc} back to lower I_{exc} were always performed. Our maximum excitation intensities of I_{exc} = 1000 W cm^{-2} are intensities encountered in practical applications such as projectors and automotive headlights. The temperature-dependent emission spectrum makes Mn^{4+}-doped fluoride phosphors uniquely suitable to distinguish the temperature contributions to droop behavior.

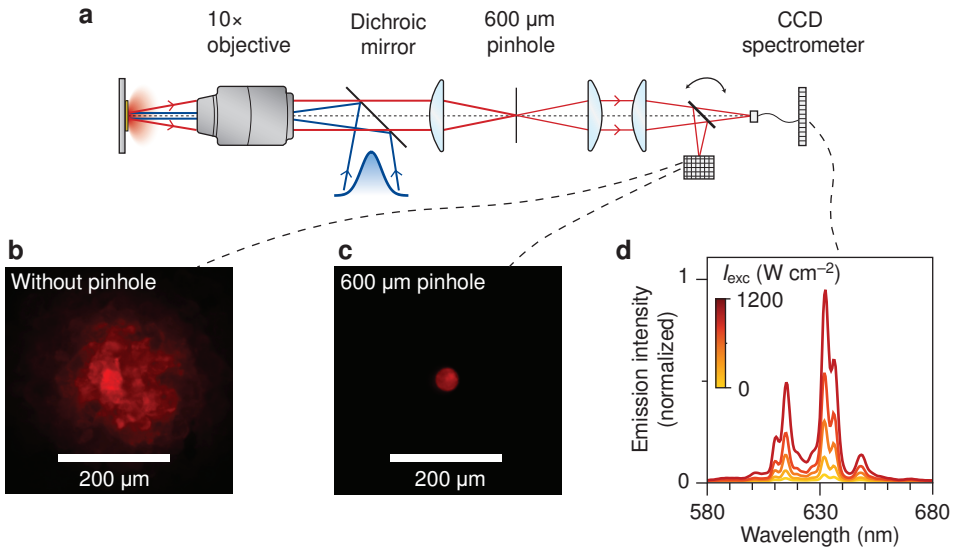

Figure 3.3 | Saturation measurements set-up. (**a**) Schematic of the optical setup used for our saturation experiments. The 460 nm excitation light is weakly focused on the back-focal plane of the objective to excite the powder with a spot size of ~200 µm in diameter. The luminescence image is magnified by a factor 10 onto a pinhole that transmits a part to a spectrometer. (**b**) Image of the phosphor luminescence. (**c**) Same as in panel b, but with a 600-µm-diameter pinhole in the detection path. (**d**) Emission spectra of the 0.1%-doped sample as a function of excitation intensity I_{exc}.

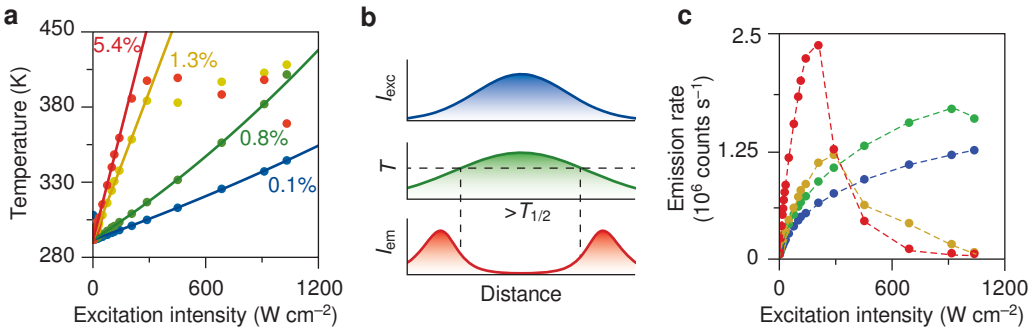

Figure 3.4 | Simultaneous saturation and in situ thermometry measurements. (**a**) Temperature of the 0.1%- (blue), 0.8%- (green) 1.3%- (yellow), and 5.4%-doped sample (red), calculated using the measured anti-Stokes/Stokes ratio and the calibration of **Figure 3.1b**, as a function of I_{exc}. Solid lines: empirical second-order polynomial fits that include only datapoints below 390K. (**b**) Schematic explaining the discrepancy between actual and apparent temperature due to thermal quenching. A Gaussian excitation spot (top) produces an approximately Gaussian temperature profile (middle). Regions where the temperature exceeds the quenching temperature (bottom) are dark. The apparent temperature is therefore weighted towards the colder regions. (**c**) Total emission intensity as a function of I_{exc} for the same doping concentrations as in panel **a**. We excluded any influence of material degradation by verifying that changes in emission intensity with I_{exc} were reversible. Dashed lines are drawn through the datapoints as a guide to the eye.

At each excitation intensity, we convert the anti-Stokes/Stokes emission intensity ratio (I_{aS}/I_S) in the recorded spectrum to a temperature, using our calibration (**Figure 3.2b**; Equation 3.2) with a small correction for differences in scattering and detection efficiency between samples (Section S3.5 in the Supporting Information).[22] The resulting temperatures for the differently doped samples (**Figure 3.4a**) reveal gradual illumination-induced heating, likely caused in large part by the Stokes shift. The temperature of the 0.1%- and 0.8%-doped samples increases approximately linearly with excitation intensity at a rate of 6 and 9°C/(100 W cm^{-2}), respectively. The temperature of the 1.3%- and 5.4%-doped sample increases much more rapidly—at a rate of 37- and 55°C/(100 W cm^{-2}) respectively—which is expected considering the stronger absorption of the blue excitation light. It is noteworthy that the heating rates do not increase linearly with Mn^{4+} concentration, which we attribute to differences in heat transport and excited volume, caused by e.g. powder packing. The observed temperature levels off around 400 K and then does not increase any further. This observation might be counterintuitive, but is a consequence of thermal quenching (schematically shown in **Figure 3.4b**). As the center of the illumination spot heats up to the quenching temperature ($T_{1/2}$ = 453 K), it will stop emitting. The dominant signal that we then record, originates from the edges of the illumination spot where the temperature remains just below the quenching temperature. The apparent temperature from luminescence thermometry can thus not exceed the quenching temperature. We assume for our further analysis, that the actual temperature in the center of the spot (in contrast to the apparent temperature) continues to increase for all I_{exc} following the heating rate observed at temperatures lower than 390 K. We use an empirical quadratic model for the heating as a function of I_{exc}, which makes physical sense as non-radiative processes become more dominant at elevated I_{exc}.[23]

In **Figure 3.4c**, the emission intensity is plotted as a function of I_{exc} for the different Mn^{4+} doping concentrations. The dependence is approximately linear for I_{exc} < 50 W cm^{-2}, with a steeper slope for the higher doped samples. Saturation, i.e. a sublinear increase of emission intensity with I_{exc},

becomes apparent at $I_{exc} > 50$ W cm^{-2} for both the 0.1- and 0.8%-doped samples. In the 1.3- and 5.4%-doped samples, the emission intensity has a maximum between $I_{exc} = 208–287$ W cm^{-2} and drops for higher I_{exc}. These maxima coincide with the I_{exc} where the temperature reaches 400 K (**Figure 3.4a**). If we extrapolate the temperature fits of the 1.5- and 5.4%-doped samples to $I_{exc} = 600$ W cm^{-2}, the sample temperature would be 517 K and 626 K, respectively, where thermal quenching is severe (**Figure 3.2b**). Clearly, the drop in emission intensity at high I_{exc} has a significant contribution from thermal quenching.

While the influence of thermal quenching on droop is obvious in **Figure 3.3d**, the contributions of other processes are more difficult to distinguish. Absorption bleach and Auger quenching would both result in gradual saturation of the emission intensity as I_{exc} increases. Simultaneously, illumination-induced heating comes with increasing radiative decay rates (**Figure 3.2a, b**), reducing the steady-state excited-state population and thereby counteracting droop, as previously realized by Beers et al.[18] Quantitative modeling of the excited-state relaxation pathways, based on saturation measurements, in situ thermometry, and pulsed experiments, is necessary to disentangle the various potential contributions to droop.

We first analyze the 0.1%-doped sample, where we assume that contributions from Auger quenching are negligible (large distance between Mn^{4+} ions will prevent energy transfer) so that we can quantify the absorption bleach. Under CW excitation the phosphor reaches a steady-state situation. In the absence of Auger quenching, the steady state excited-state population p_{ss}, i.e. the fraction of Mn^{4+} ions in the excited state, is given by[17]

$$p_{ss} = \frac{\sigma_{abs} I_{exc}/h\omega}{\sigma_{abs} I_{exc}/h\omega + k_{decay}(T)} \tag{3.4}$$

Here, σ_{abs} is the absorption cross-section for photons of energy $\hbar\omega$ and $k_{decay}(T)$ is the temperature-dependent decay rate of the ^{2}E state. A derivation can be found in Section S3.6 of the Supporting Information. The experimental count rate as measured by the CCD spectrometer in the saturation experiments scales as

$$I_{em} = A k_{rad}(T) p_{ss} \tag{3.5}$$

where $k_{rad}(T)$ is the temperature-dependent radiative decay rate of the ^{2}E state and A is a prefactor that accounts for various experimental factors such as the detection efficiency of the set-up, the amount of material investigated, or the doping concentration. We do not consider the role of excited-state absorption as our model does not explicitly account for penetration of the blue excitation light into the phosphor, so excited-state absorption has no influence on the observed count rate. We fit Equation 3.5 to the experimental saturation curve of the 0.1%-doped sample (blue line, **Figure 3.4c**), neglecting Auger quenching by using Equation 3.4 for the excited-state population. The temperature at each excitation density (**Figure 3.3d**) determines $k_{rad(}T)$ and $k_{nonrad}(T)$ following our calibration (**Figure 3.2b**). We find $\sigma_{abs} = 3.1\times10^{-19}$ cm^2, which is close to literature values found for the $^4A_2 \rightarrow {}^4T_2$ absorption transition in Mn^{4+} ($1.5–7.0\times10^{-19}$ cm^2)[17,18] and the isoelectronic ion Cr^{3+} (1.7×10^{-19} cm^2).[24]

Based on the analysis of the saturation curve of the 0.1%-doped sample, we can calculate the contribution of absorption bleach and the beneficial effect of illumination-induced heating. Dividing out the experimental prefactor A from the saturation curve yields the emission rate per ion as a function of I_{exc} (**Figure 3.5a**). For reference, we have added the theoretical situation without any

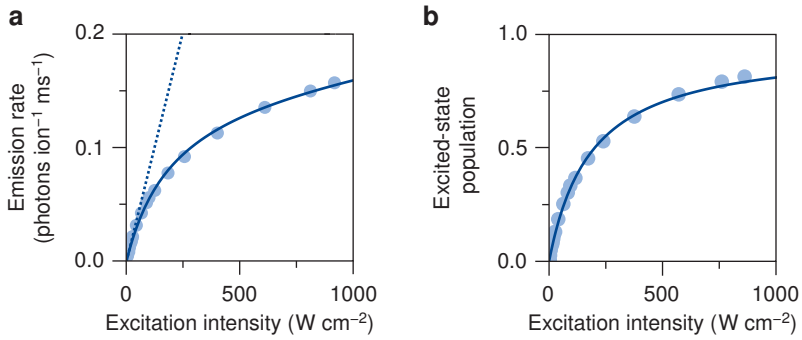

Figure 3.5 | Saturation at low doping concentration. (**a**) Saturation measurement of K_2TiF_6:Mn^{4+} (0.1%) (**Figure 3.4c**) converted to the emission rate per ion as a function of excitation intensity I_{exc}. Solid line: fit using the I_{exc}-dependent temperatures from luminescence thermometry experiments in **Figure 3.4a**. Dashed line: theoretical emission rate without droop effects. (**b**) Same as in panel **a**, but now converted to the excited-state population, i.e. the steady-state fraction of Mn^{4+} centers that is in the ^2E excited state.

droop effects as a dashed line. Further dividing out $k_{rad}(T)$ yields the excited-state population pss as a function of I_{exc} (**Figure 3.5b**). See Section S3.6 in the Supporting Information for further explanation on these conversion procedures. The emission rate per ion approaches the radiative decay rate (**Figure 3.3a**) and the excited-state population reaches almost 80% at the highest I_{exc} considered here (**Figure 3.5b**). The 80% excited-state population corresponds with an 80% absorption bleach. This alone is sufficient to explain the droop (**Figure 3.4c**). Illumination-induced heating has a small beneficial effect:[19] the emission rate per ion reaches 163 s^{-1} at I_{exc} = 1200 W cm^{-2} including heating to 362 K, but would be 140 s^{-1} if the temperature were fixed at 293 K. This results in a 81% absorption bleach at I_{exc} = 1200 W cm^{-2} including heating, compared to 84% absorption bleach without heating (**Figure 3.5b**). Note that our measurements and analysis are blind to excited-state absorption because we measure only luminescence.

The significant excited-state populations at the excitation intensities used in our experiments could cause Auger quenching (**Figure 3.6a**). Indeed, a recent paper highlighted the issue of Auger quenching in K_2SiF_6:Mn^{4+}, a phosphor similar to ours.[18] CW saturation experiments are however not ideal for the quantification of Auger quenching rates, because Auger quenching and absorption bleach are difficult to distinguish; both manifest as a gradual decrease of the slope of the saturation curve.

We use ns-pulsed experiments on our highest-doped sample, with 5.4% Mn^{4+}, to quantify Auger quenching. The high doping concentration ensures short distances between dopants, making Auger quenching more prominent, while ns-pulsing the excitation laser limits heating and gives a good time resolution to probe excited state dynamics. The photoluminescence decay (**Figure 3.6b**) shows an increasingly prominent fast component (at t < 2 ms) at increasing excitation fluence. This is indicative of Auger quenching, as a higher excitation fluence results in more possibilities for interactions between excited Mn^{4+} ions in close proximity. The time evolution of the anti-Stokes/Stokes ratio reveals negligible laser-induced heating even shortly after the laser pulse and for the highest fluence (**Figure 3.6c**). We fit the photoluminescence decay of the highest excitation fluence of J_{exc} = 2.2 J cm^{-2} with a kinetic Monte Carlo model. We achieve a good match with the experimental data if we assume dipole–dipole interaction between excited Mn^{4+} ions, with a quenching rate scaling as:

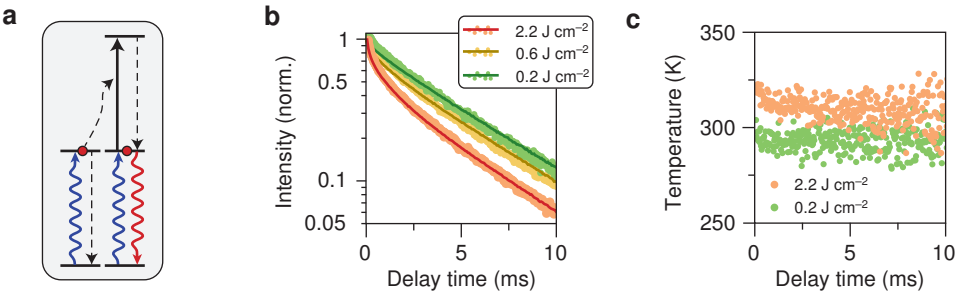

Figure 3.6 | Auger quenching upon ns-pulsed excitation. (**a**) Schematic of Auger quenching by energy-transfer upconversion between Mn^{4+} ions in the ^2E excited state. One excited Mn^{4+} ion transfers its energy to another excited Mn^{4+} ion. The donor ion thereby returns to the $^4A_2$ ground state, while the acceptor ion is raised to the $^4T_1(^4P)$ excited state and quickly relaxes back to the ^2E state. The net effect is the loss of one excited state. (**b**) Photoluminescence decay curves of K_2TiF_6 doped with 5.4% Mn^{4+} excited with 5-ns pulses at high fluences of 0.2 (green), 0.6 (yellow), and 2.2 J cm^{-2} (red). Solid lines: fit to our kinetic Monte Carlo model with C_{Auger} = 657 nm^6 s^{-1}. (**c**) Temperature as a function of delay time after pulsed excitation, determined from the time evolution of the ratio of two separate photoluminescence decay measurements of the ν_6 peaks of the anti-Stokes and Stokes emission.

$$k_{Auger} = \frac{C_{Auger}}{R^6} \tag{3.6}$$

where C_{Auger} is the Auger strength and R is the distance between the ions. We assume that an Auger event quenches one of the ions involved, while the other returns to the ^2E emitting state (**Figure 3.6a**). The model accounts for the discrete lattice of the KTF crystal. We initiate the model with an excited-state population of $1 - \exp(-\sigma_{abs}I_{exc}/\hbar\omega) = 0.802$ and then track the fate of discrete excited states. Details are given in Section S3.7 in the Supporting Information. C_{Auger} = 657 nm^6 s^{-1} yields the best fit to the experimental data at J_{exc} = 2.2 J cm^{-2} and also provides a good match to the data at lower fluences (**Figure 3.6b**). This corresponds to an Auger quenching rate of $k_{Auger} = 64\times10^3$ s^{-1} between nearest-neighbor (R = 4.66 Å) excited Mn^{4+} ions, more than two orders of magnitude faster than radiative decay.

Now that we have separately studied thermal quenching, absorption bleach, and Auger quenching, we can combine these to model the full droop behavior of our phosphors. We use a kinetic Monte Carlo algorithm to simulate CW excitation. The model uses the excitation rate $k_{exc} = \sigma_{abs}I_{exc}/\hbar\omega$ from the value found for σ_{abs} (**Figure 3.5a**), accounts for temperature-dependent radiative and nonradiative decay (**Figure 3.2b**) by using the temperatures from in situ luminescence thermometry (e.g., **Figure 3.3d**) as input, and includes Auger quenching (**Figure 3.6**). The algorithm continues until a steady-state population p_{ss} is reached. The results from a series of simulations at different I_{exc} can be matched to the experimental saturation curves using Equation 3.5 by optimizing only the prefactor A.

Figure 3.7a–d compares the results of the Monte Carlo model to the experimental saturation curves. The overall match is good, especially because a single value for σ_{abs} and a single value for C_{Auger} are used to match all four curves. Deviations are apparent around the I_{exc} where thermal quenching sets in. This is likely the result of temperature gradients in the phosphor powder. Indeed, luminescence thermometry provides an in situ average sample temperature but is blind to locations where the temperature exceeds the quenching temperature. Such temperature hotspots

would decrease the emission intensity and could be caused by, for example, a phosphor grain with high defect concentration that acts as a source of heat. Future studies may be able to characterize temperature inhomogeneities in phosphor powders in more detail, perhaps by combining intensity-ratio and lifetime thermometry.

Based on our Monte Carlo model, **Figure 3.7e–h** show the contributions of thermal quenching, absorption bleach, and Auger quenching to droop at different Mn^{4+} doping concentrations and as a function of I_{exc}. Absorption bleach leads to transmission (or backscattering) of excitation light and is the dominant droop mechanism in the lowest-doped phosphors. Auger quenching becomes more important at higher doping concentration, which is a consequence of the strong distance dependence of the Auger quenching rate (Equation 3.6). The contributions of absorption bleach and Auger quenching are equally strong in the highest-doped sample with 5.4% Mn^{4+}. Losses due to thermal quenching completely dominate the droop behavior in the high-doped samples at high I_{exc}.

Clearly, illumination-induced heating is a key factor to control the droop characteristics of a Mn^{4+}-doped fluoride phosphor. Mildly elevated temperatures are beneficial for the light output of the phosphor (**Figure 3.5**). However, one should prevent that the temperature increases above the thermal quenching threshold. The optimal temperature for the maximum light output is just below the quenching temperature, around 350–400 K for KTF:Mn^{4+}, where the radiative decay rate is maximum but thermal quenching is negligible. Careful heat management is thus critical when designing devices that hit exactly this optimal phosphor temperature. The absolute light output increases with increasing Mn^{4+} doping concentration (**Figure 3.4c**), but the higher doping concentrations are also more sensitive to illumination-induced heating (**Figure 3.2a**). These considerations would have to be carefully balanced, depending on the heat management. The tolerance for heating-induced illumination may be increased, allowing for higher phosphor operating temperatures, by choosing the right host material of Mn^{4+}. For example, the quenching temperature of K_2SiF_6:Mn^{4+} ($T_{1/2}$ = 558 K) is higher than that of K_2TiF_6:Mn^{4+} ($T_{1/2}$ = 453 K) used in this work.

The present results are highly relevant for the commercial application of Mn^{4+}-doped phosphors for general lighting. Typical doping concentrations for commercial phosphors are 5–10%, required to reach sufficient absorption of blue light. The results in **Figure 3.7** show that at these doping concentrations and typical excitation densities of 100 W cm^{-2} in w-LEDs, Auger quenching contributes substantially to droop. It is evident that in lighting applications the high I_{exc} unavoidably lead to high excited-state populations, determined by the balance between absorption and emission rates (Equation 3.4). Auger quenching due to interactions between excited Mn^{4+} ions can be minimized by lowering the doping concentration, as apparent from **Figure 3.7e–h**. This solution may however come at the cost of a larger amount of required phosphor material in a device. Auger quenching could be further reduced by incorporation of Mn^{4+} in a fluoride host where the nearest-neighbor Mn^{4+}–Mn^{4+} distance is large (>10 Å) and radiative decay can outcompete Auger quenching even in nearest neighbor pairs. Alternatively, one could reduce excited-state populations, thus reducing both Auger quenching and absorption bleach, by increasing the decay rate of the excited state (k_{decay} in Equation 3.4). Available tuning knobs are the choice of host material (e.g., k_{decay} = 0.167 ms^{-1} for K_2TiF_6:Mn^{4+} at room temperature versus 0.115 ms^{-1} for K_2SiF_6:Mn^{4+}), temperature management, and finally (nano)photonic design. (Nano)photonic structures, such as waveguides or antennas, can in principle increase radiative decay rates by orders of magnitude. Fabrication and embedding of the phosphor will however be increasingly challenging and costly for real-live devices and applications.

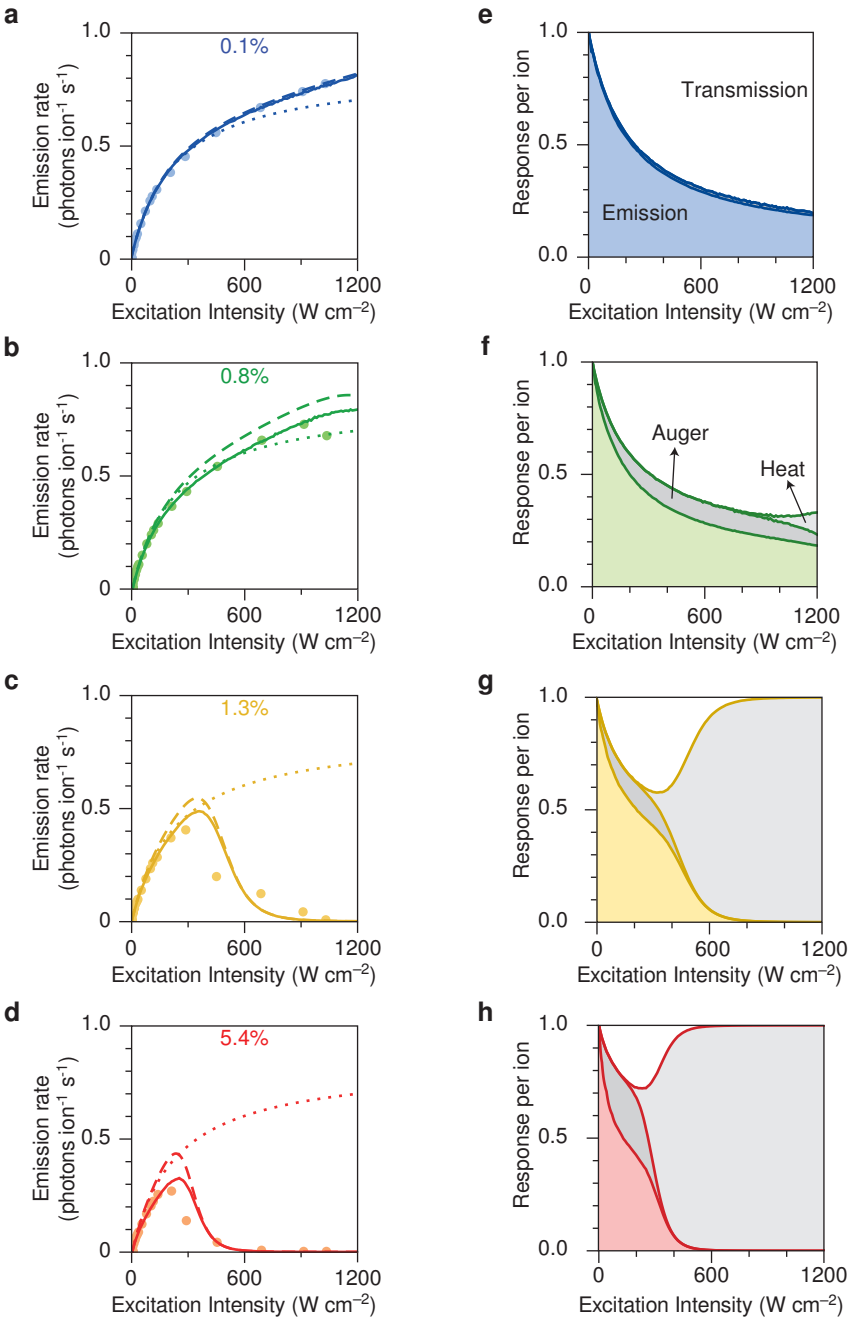

Figure 3.7 | Different contributions to phosphor droop. (**a–d**) Saturation curves of K_2TiF_6 doped with (**a**) 0.1% Mn^{4+}, (**b**) 0.8% Mn^{4+}, (**c**) 1.3% Mn^{4+}, and (**d**) 5.4% Mn^{4+}. Solid lines: fits to our kinetic Monte Carlo model for continuous-wave excitation, using the temperatures measured by luminescence thermometry and parameter values based on the reference measurements of **Figures 3.1**, **3.5**, **3.6**. Dotted lines: theoretical emission rate including only the effect of absorption bleach. Dashed lines: emission rate including the effect of heating but without Auger quenching. (**e–h**) Different contributions to phosphor droop as a function of excitation intensity and for the same four samples as in panels **a–d**.

Conclusion

In summary, we have quantified the contributions of absorption bleach, Auger quenching, and thermal quenching to the droop of four different K_2TiF_6 phosphor samples with different Mn^{4+} doping concentrations. All three processes contribute to the droop, to amounts depending on the continuous-wave excitation intensity up to 1200 W cm^{-2} and on the doping concentration. Follow-up work could aim at including scattering and temperature inhomogeneities into the analysis and modeling. Additionally, the effect of excited-state absorption on the transmission of blue LED light was beyond the scope of this work but is important to consider for the performance of a complete device. Our work highlights the unique temperature-dependent optical properties of Mn^{4+}-doped fluorides, which provides opportunities for new LED architectures with improved performance. An interesting engineering challenge would be to operate a Mn^{4+}-based phosphor at the temperature sweet spot where excited-state decay is accelerated but the luminescence is not yet quenched. We show that a combination of Mn^{4+} doping concentration, excitation intensity and heat regulation could determine the optimal operating conditions. Our results and modeling will contribute to the development of these and other strategies to mitigate droop of Mn^{4+}-based phosphors for high-power warm-white lighting.

Supporting Information

S3.1 Methods

Synthesis: The samples synthesized by Senden et al.[20] were used in this investigation. All Mn^{4+}-doping concentrations were experimentally determined with ICP-OES measurements and are given in mol% Mn^{4+} with respect to Ti^{4+}. Further details about the procedure and chemicals can be found there.

Characterization: The procedures of the temperature-dependent optical measurements are described by Senden et al.[20] The steady-state saturation measurements were performed with a Coherent Genesis CX-460 CW laser and an AvaSpec-HSC 1024×58 TEC-EVO CCD spectrometer equipped with an optical fiber. The blue light intensity was modulated with the Standa 10MVAA motorized attenuator and measured with a Thorlabs S405C thermal power sensor. The pulsed Auger quenching experiments were performed with an Ekspla NT342B OPO laser at a repetition rate of 10 Hz and a pulse width of 5 ns as excitation source. Its emission profile was measured with a 1280×1024 CMOS camera and the pulse energy was recorded with a Thorlabs ES111C pyroelectric sensor. The emission was recorded with a TRIAX 550 monochromator combined with a H74220-60 PMT. The decay curves were recorded using a PicoQuant TimeHarp 260 computer card.

S3.2 Temperature-dependent lifetime and anti-Stokes–Stokes ratio

Three vibrational modes of energies $h\nu_6 = 216\ \mathrm{cm}^{-1}$, $h\nu_4 = 325\ \mathrm{cm}^{-1}$, and $h\nu_3 = 630\ \mathrm{cm}^{-1}$ dominate the emission of KTF:Mn^{4+}. The occupation $n_i(T)$ of a phonon mode with energy $h\nu_i$ depends on temperature:

$$n_i(T) = \frac{1}{e^{h\nu_i/k_B T} - 1}. \tag{S3.1}$$

Here, we show that the combined contribution of three phonon modes $h\nu_i$ (with i = 6, 4, 3) to the temperature-dependent radiative decay rate and the temperature-dependent anti-Stokes–Stokes ratio can be approximated as the effect of a single phonon mode with an effective energy $h\nu_{\mathrm{eff}}$. The Stokes emission lines are at energies $E_{S,i} = E_0 - h\nu_i$ and anti-Stokes emission lines at energies $E_{aS,i} = E_0 + h\nu_i$, where E_0 is the zero-phonon-line energy. We assume that the three Stokes emission lines have equal transition rates $k_{S,4}(0) = 0.6\ k_{S,6}(0)$ and $k_{S,3}(0) = 0.2\ k_{S,6}(0)$ at $T = 0$ K. The transition rates of the Stokes lines at higher temperature are then

$$k_{S,i}(T) = k_{S,i}(0)\left[n_i(T) + 1\right], \tag{S3.2}$$

while the transition rates of the anti-Stokes lines are

$$k_{aS,i}(T) = \left(\frac{E_{aS,i}}{E_{S,i}}\right)^3 k_{S,i}(0) n_i(T). \tag{S3.3}$$

The prefactors $(E_{aS,i}/E_{S,i})$ are larger than unity and account for the different densities of optical states at the anti-Stokes emission energies compared to the Stokes emission energies.

The radiative lifetime of Mn^{4+} is the inverse of the sum of radiative transition rates:

$$\tau_{\mathrm{rad}}(T) = \left[k_{aS,3}(T) + k_{aS,4}(T) + k_{aS,6}(T) + k_{S,6}(T) + k_{S,4}(T) + k_{S,3}(T)\right]^{-1}. \tag{S3.4}$$

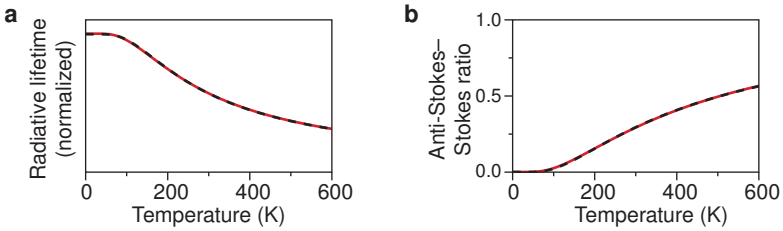

Figure S3.1 | Comparison of three-phonon to one-phonon models. (**a**) The temperature-dependent radiative lifetime $\tau_{\mathrm{rad}}(T)$ according to the three-phonon model (Equation S3.4; red solid line) and fitted with the approximate one-phonon model (Equation S3.5; black dashed line). The effective phonon energy fitted is $h\nu_{\mathrm{eff}} = 270\ \mathrm{cm}^{-1}$. (**b**) Same, but for the temperature-dependent anti- Stokes–Stokes ratio. The full model is Equation S3.6; the approximate model is Equation S3.7. We fit $h\nu_{\mathrm{eff}} = 271\ \mathrm{cm}^{-1}$.

Figure S3.1a shows that the full lifetime model (Equation S3.4) is well matched with an approximate model of a single effective phonon energy that neglects the correction due to density of optical states,

$$\tau_{\mathrm{rad}}(T) \approx \left[k_{\mathrm{aS,eff}}(T) + k_{\mathrm{S,eff}}(T)\right]^{-1} = k_{\mathrm{S,eff}}^{-1}(0)\left[2n_{\mathrm{eff}}(T)+1\right]^{-1} = k_{\mathrm{S,eff}}^{-1}(0)\coth(h\nu_{\mathrm{eff}}/2k_{\mathrm{B}}T)\,. \tag{S3.5}$$

The anti-Stokes–Stokes ratio is the ratio of the sum anti-Stokes and the sum of Stokes transition rates:

$$\frac{I_{\mathrm{aS}}}{I_{\mathrm{S}}}(T) = \frac{k_{\mathrm{aS},6}(T) + k_{\mathrm{aS},4}(T) + k_{\mathrm{aS},3}(T)}{k_{\mathrm{S},6}(T) + k_{\mathrm{S},4}(T) + k_{\mathrm{S},3}(T)}. \tag{S3.6}$$

Figure S3.1b shows how also Equation S3.6 is approximated well by a model of a single effective phonon mode,

$$\frac{I_{\mathrm{aS}}}{I_{\mathrm{S}}}(T) \approx \frac{k_{\mathrm{aS,eff}}(T)}{k_{\mathrm{S,eff}}(T)} = A\frac{n_{\mathrm{eff}}(T)}{n_{\mathrm{eff}}(T)+1} = A\mathrm{e}^{-h\nu_{\mathrm{eff}}/k_{\mathrm{B}}T}, \tag{S3.7}$$

where A is a prefactor that accounts for the differences in density of optical states at different emission energies and potential differences in detection efficiencies of different emission wavelengths.

We see that, while the approximate one-phonon models match the three-phonon models, the effective phonon energy fitted on the temperature-dependent lifetime is larger than that we need to match the experimental data on Mn^{4+}. The experimental effective phonon energy is in fact nearly equal to the lowest phonon $h\nu_6$. The origin of this inconsistency is not clear to us.

S3.3 Calibrating the excitation intensity

The weakly focused 460-nm excitation light creates an approximately Gaussian spot on the top surface of the powder sample (**Figure S3.2**):

$$I_{\mathrm{exc}}(r) = \frac{P_{\mathrm{exc}}}{2\pi\sigma^2}\mathrm{e}^{-r^2/2\sigma^2}, \tag{S3.8}$$

where P_{exc} is the excitation power, r is the distance from the center of the spot, and $\sigma = \mathrm{fwhm}/2\sqrt{2\ln(2)} = 71$ µm. A pinhole in our optical setup (**Figure 3.3a** in the main text) transmits only signal from a circular area of radius $R = 30$ µm in the center of the spot to the detectors. From this model of the excitation spot, we want to calculate average excitation intensity $\langle I_{\mathrm{exc}}\rangle_{\mathrm{det}}$ integrated over the detected area and weighted by the signal strength from a location. We neglect that the signal strength recorded from a particular location depends on local saturation of the phosphor, instead approximating that the local signal strength scales with the local excitation intensity:

$$\langle I_{\mathrm{exc}}\rangle_{\mathrm{det}} = \frac{\int_0^R I_{\mathrm{exc}}(r)^2\,2\pi r\,\mathrm{d}r}{\int_0^R I_{\mathrm{exc}}(r)\,2\pi r\,\mathrm{d}r} = \frac{P_{\mathrm{exc}}}{4\pi\sigma^2}\left(1+\mathrm{e}^{-R^2/2\sigma^2}\right). \tag{S3.9}$$

The x-axes of our saturation plots show this parameter $\langle I_{\mathrm{exc}}\rangle_{\mathrm{det}}$, calculated using Equation S3.9. The powers P_{exc} are calculated from the measured laser power and the transmission of neutral-density filters used.

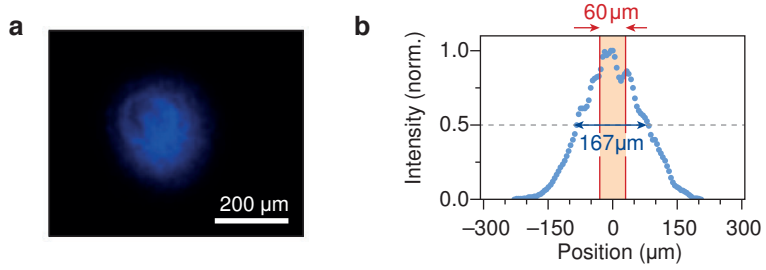

Figure S3.2 | The excitation spot. (**a**) Direct image of the weakly focused excitation spot of the at the exact same position of the sample holder used for the power-dependent saturation experiments. (**b**) Cross-cut through the center of the spot, highlighting the fwhm of 167 µm. The red vertical lines denote the circular area from which the signal is measured in our optical setup. Because the objective has a 10x magnification, the 600 µm pinhole selects a circular area with a diameter of 60 µm at the image plane.

The variation of the excitation intensity over the detected area,

$$\frac{\sigma_{I_{\mathrm{exc}}}}{\langle I_{\mathrm{exc}}\rangle_{\mathrm{det}}} = \frac{\sqrt{\langle I_{\mathrm{exc}}^2\rangle_{\mathrm{det}} - \langle I_{\mathrm{exc}}\rangle_{\mathrm{det}}^2}}{\langle I_{\mathrm{exc}}\rangle_{\mathrm{det}}} = \frac{1}{\sqrt{3}}\tanh\left(\frac{R^2}{4\sigma^2}\right), \tag{S3.10}$$

is as small as 2.6%.

S3.4 Emission spectra of K_2TiF_6:*x* % Mn^{4+} (x = 0.8, 1.3, 5.4) as a function of excitation power

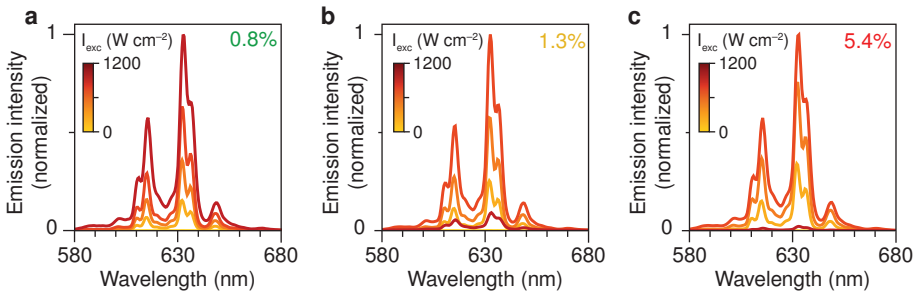

Figure S3.3 | Emission spectra of the (a) 0.8%-, (b) 1.3%-, and (c) 5.4%-doped K2TiF6 samples as a function of excitation intensity. For the 0.8 % doped sample the emission intensity keeps increasing, while for the 1.3%- and 5.4%-doped samples the emission intensity decreases at the highest excitation intensities.

S3.5 In situ measurements of phosphor temperature

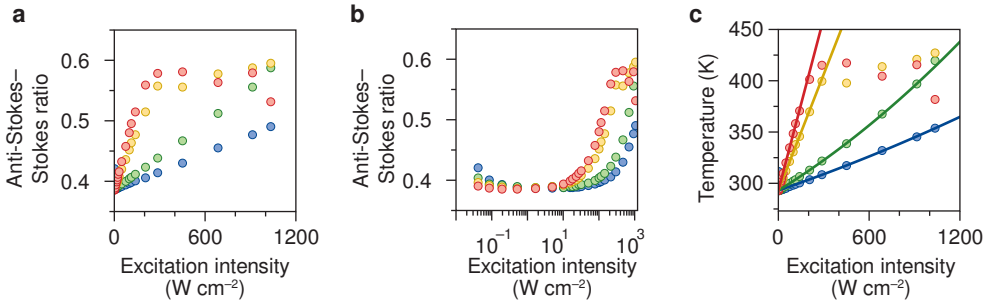

Figure S3.4 | In situ measurements of the phosphor temperature. (**a**) The anti-Stokes–Stokes intensity ratio of the Mn^{4+} emission as a function of excitation intensity for different Mn^{4+} doping concentrations of 0.1% (blue), 0.8% (green), 1.3% (yellow), and 5.4% (red). The Stokes intensity was integrated on the emission wavelength range between 575 and 624 nm; the anti-Stokes intensity between 624 and 690 nm. The anti-Stokes–Stokes ratio increases with excitation intensity, because of illumination-induced heating, but appears to saturate at a value of approximately 0.58. This saturation does not reflect a maximum illumination-induced temperature but is rather an artefact due to thermal quenching. As the temperature in the center of the illumination spot exceeds the thermal quenching temperature at 400–450 K, the center turns dark. The dominant emission signal then originates from the edges of the illumination spot, which are still at approximately 400 K and show the corresponding anti-Stokes–Stokes ratio (**Figure 3.3d**) in the main text). (**b**) The same data as in panel **a** but now plotted with a logarithmic x-axis. This reveals higher anti-Stokes–Stokes ratio at the lowest (k_{exc} ≈ 0.1 W cm^{-2}) compared to intermediate (k_{exc} ≈ 1 W cm^{-2}) excitation intensities. This increased anti-Stokes–Stokes ratio is likely due to difficulties in the background subtraction at low signal strengths and does not reveal an actually higher temperature at the lowest excitation powers. (**c**) The phosphor temperature as a function of excitation intensity, calculated from the data in panel a using the calibration presented in the main text (**Figure 3.1b**). The solid lines are fits to an empirical model of a second-order polynomial. Only data at temperatures <390 K are included in the fit, so that we can use it to extrapolate the temperature in the center of the illumination spot.

S3.6 Derivation of the emission rate per ion under continuous-wave excitation

Blue light excites Mn^{4+} to the $^4T_2$ level, after which relaxation to the emitting ^2E level occurs on timescales much faster than any other decay process. From the ^2E level Mn^{4+} transitions back to the ground state. Mn^{4+} thus has only two relevant energy levels that must be explicitly considered in a kinetic model: the excited ^2E and the $^4A_2$ ground state. The rate constant for excitation $k_{exc} = \sigma_{abs} I_{exc}/h\omega$ depends on the absorption cross-section $\sigma_{abs} = 3.1 \times 10^{-19}$ cm^2 at photon energy $h\omega = 4.32 \times 10^{-19}$ J (460 nm). A rate constant for relaxation k_{decay} includes radiative decay and nonradiative cross-over, which are both temperature-dependent, with rates $k_{rad}(T)$ and $k_{nr}(T)$ (**Figure 3.2b** in the main text). In addition, a Mn^{4+} ion may relax to the ground state by Auger energy transfer to a neighbor that is already in the ^2E excited state. This last type of decay depends on the crystal geometry, doping concentration, and excitation power. We model this with Monte Carlo procedure (see Section S3.7).

Continuous-wave excitation creates a steady-state population pss in the Mn^{4+} excited state, determined by the balance between excitation and the various decay pathways. The steady-state photon emission rate per ion ϕ (i.e. number of photons emitted per unit of time) is proportional to the steady-state population:

$$\phi = k_{rad} p_{ss}. \tag{S3.11}$$

The count rate I_{em} in our saturation experiments (**Figure 3.4c** in the main text) scales with the emission rate per ion as well as with various experimental factors such as the detection efficiency of the setup, the amount of material investigated, or the doping concentration:

$$I_{em} = A\, k_{rad} p_{ss}, \tag{S3.12}$$

where A accounts for all experimental factors affecting the absolute count rate. To model our saturation experiments, we extract the temperature ftrom the Mn^{4+} emission spectrum (**Figure 3.3d** in the main text), which then determines the radiative and nonradiative recombination rates $k_{rad}(T)$ and $k_{nr}(T)$. The full model, including Auger quenching, relies on the Monte Carlo algorithm described in the next section to calculate p_{ss}. Alternatively, for the determination of σ_{abs} from the low-doping sample and for the simulations without Auger quenching, we can use an approximate model. k_{exc} and k_{decay} are then the only relevant processes and a simple rate equation model for the excited-state population,

$$\frac{dp}{dt} = k_{exc}(1 - p) - k_{decay} p, \tag{S3.13}$$

yields as the steady-state solution

$$p_{ss} = \frac{k_{exc}}{k_{exc} + k_{decay}}. \tag{S3.14}$$

Auger quenching makes the steady-state population deviate from Equation S3.14 as another decay pathway becomes available at high blue excitation intensity. Using Equation S3.12 to fit the experimental saturation data, we can convert the experimental data in units of emission counts per unit of time to photons emitted per Mn^{4+} ion per unit of time or photons emitted per unit of phosphor volume per unit of time.

For the plots of **Figure 3.7e–h** in the main text we compare the calculated steady-state emission rate per ion $\phi = k_{rad} p_{ss}$ in different scenarios. The maximum emission rate per ion $\phi(\max) = k_{exc}$ is in a hypothetical case of no absorption bleach (i.e., infinitely fast radiative decay) and no quenching. The scenarios considered are:

(**I**) Reality: all processes are active, including absorption bleach, thermal quenching, and Auger quenching. We calculate p_{ss} using the procedure described below in Section S3.7.
(**II**) Neglecting Auger quenching. pss is then given by Equation S3.14 using $k_{decay} = k_{rad}(T) + k_{nr}(T)$.
(**III**) Neglecting both Auger quenching and thermal quenching. p_{ss} is then given by Equation S3.14 using $k_{decay} = k_{rad}(T)$.

For each scenario we normalize the calculated emission intensity. The normalized emission intensity of scenario i is $\Phi(i)_{em} = \phi(i) = \phi(\max)$. From bottom to top, the lines in each of the **Figure 3.7e–h** in the main text (i.e., the boundaries between the shaded areas) are plots of Φ_{em}(I), Φ_{em}(II), and Φ_{em}(III).

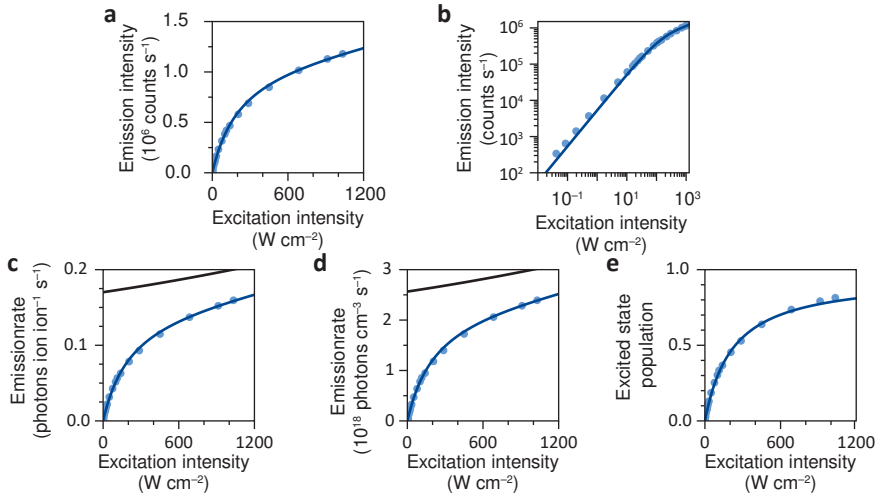

Figure S3.5 | Saturation at low Mn^{4+} concentration. (**a**) The photon count rate in a saturation experiment on K_2TiF_6:Mn^{4+} (0.1%) after correction for background signal and the transmission of the neutral-density filter in the detection path. From the spectra we extract the phosphor temperature as a function of excitation intensity (**Figure 3.3d** in the main text). Solid line: fit to Equation S3.12, using the known dependence of k_{rad} and k_{nr} on temperature (**Figure 3.2b** in the main text) and neglecting any Auger quenching. The fit parameters are A and σ_{abs}. (**b**) Same as in panel **a** but plotted on a double-logarithmic scale. (**c**) The experimental data of panel **a** scaled by the fitted factor A to obtain the photon emission rate per ion ϕ as a function of the excitation intensity. Blue solid line: fitted model from panel a scaled by a factor A. Black solid line: maximum possible photon emission rate $\phi_{max} = k_{rad}$. (**d**) The photon emission rate per ion (panel **c**) converted to a photon emission rate per unit of phosphor volume, by multiplication with the doping concentration and with the density of tetravalent cation sites in the material. (**e**) The steady-state population Equation S3.14 as a function of excitation intensity, obtained by dividing the data and the model of panel **c** by k_{rad}.

S3.7 Monte Carlo simulations of Auger quenching

To calculate the contribution of Auger quenching at high excited-state population, we perform Monte Carlo simulations. We build a box of $5 \times 5 \times 5$ K_2TiF_6 unit cells (edge lengths $a = b = 5.7354$ Å, $c = 4.6635$ Å; angle $\gamma = 120°$; one lattice site at the origin of each unit cell) with periodic boundary conditions. Each Ti^{4+} lattice site has a probability of x to be occupied by a Mn^{4+} center. The code keeps track which Mn^{4+} centers are in their ground and which in their excited state. At $t = 0$ each Mn^{4+} center is randomly initiated in its excited state with probability P. For the fit model that describes the pulsed experiments, we use $P = \sigma J_{exc}/h\omega$, where σ is the Mn^{4+} absorption cross-section at photon energy $h\omega = 4.32 \times 10^{-19}$ J and J_{exc} is the pulse fluence. For the saturation simulations, we choose $P = (\sigma I_{exc}/h\omega)/(\sigma I_{exc}/h\omega + k_{decay})$, where Iexc is the excitation intensity and kdecay is the sum of the rate constants for radiative and nonradiative decay.

At each step in the simulation procedure, various decay and excitation processes may be possible in the crystal. We calculate the total rate of change $k_{tot,}$ which is the sum of the rates of all possible processes. Each center in the ground state contributes an amount $k_{exc} = \sigma I_{exc}/h\omega$; each center in the excited state contributes an amount k_{decay}; and each pair of centers in the excited state contribute an amount $k_{Auger,ij} = C_{Auger}/r^6_{ij}$, where r_{ij} is the distance between the two centers and C_{Auger} is the Auger interaction strength. For the simulation of the pulsed experiments, we determine kdecay by fitting a single exponential model to the photoluminescence decay curve at delay times 10–15 ms at the doping concentration of interest. For the simulation of the continuous-wave experiments, k_{decay} is set to the radiative and nonradiative decay rates of Mn^{4+} (**Figure 3.2b** in the main text) at the temperature extracted from the spectrum (**Figure 3.3d** in the main text).

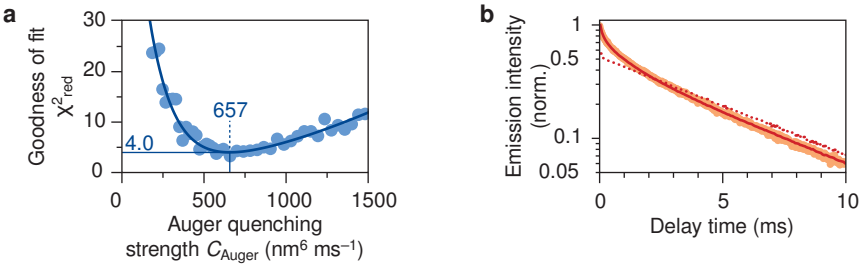

Figure S3.6 | Determining the Auger quenching strength C_{Auger}. We fit the output of the Monte Carlo simulations to the experimental photoluminescence decay of K_2TiF_6:Mn^{4+}(5.4%) at an excitation pulse fluence of J_{exc} = 2.2 J cm^{-2}. (**a**) The reduced χ^2 statistics for the fit as a function of the Auger quenching strength C_{Auger}. The procedure further optimizes a scaling factor A between the experimental and the simulated curve and takes into account that both the experimental data and the simulation output contain Poissonian noise:

$$\chi^2_{red} = \frac{1}{N-2}\sum_i^N \frac{[y_i - Af(t_i)]^2}{y_i + A^2 f(t_i)}, \tag{S3.15}$$

where y_i and $f(t_i)$ are the experimental and simulated counts at time t_i, respectively, and N is the number of histogram bins in the photoluminescence decay curve. The simulation is integrated over 200 different doping realizations in the box of 125 unit cells and 5000 excitation pulses for each realization. (**b**) The best match between the experimental data and Monte Carlo simulation (solid line), at C_{Auger} = 657 nm^6 s^{-1}. An alternative model with only nearest-neighbour Auger quenching (dashed line) produces biexponential decay with a weak fast component, inconsistent with the data. See **Figure 3.6b** in the main text for the decay curves for lower excitation fluences of J_{exc} = 0.6 J cm^{-2} (yellow) and J_{exc} = 0.2 J cm^{-2}, simulated with the fixed C_{Auger} value determined in panel **a**. For the different Mn^{4+} doping concentrations, we average the steady-state under CW excitation count rates simulated with the Monte Carlo algorithm over 37500, 7500, 3000, or 1000 different doping realizations in the box of 125 unit cells, respectively. In order to further suppress noise on the simulation output, the average steady-state count rates are corrected for the actual number of dopants that occurred in the simulations. Effectively, this yields a simulated value for $k_{rad}p_{ss}$ in Equation S3.12, including the effect of Auger quenching on p. The simulated count rate per dopant as a function of excitation intensity is then matched to the experimental data with the single scaling factor A as the sole fit parameter.

References

[1] T. Takahashi, S. Adachi, *J. Electrochem. Soc.* **2008**, 155, E183.
[2] S. Nishiura, S. Tanabe, K. Fujioka, Y. Fujimoto, *Opt. Mater.* **2011**, 33, 688.
[3] M. A. van de Haar, J. Werner, N. Kratz, T. Hilgerink, M. Tachikirt, J. Honold, M. R. Krames, *Appl. Phys. Lett.* **2018**, 112, 132101.
[4] X. Piao, K. Machida, T. Horikawa, H. Hanzawa, Y. Shimomura, N. Kijima, *Chem. Mater.* **2007**, 19, 4592.
[5] R.J. Xie, N. Hirosaki, T. Takeda, T. Suehiro, *ECS J. Solid State Sci. Technol.* **2013**, 2, R3031.
[6] K. Uheda, N. Hirosaki, Y. Yamamoto, A. Naito, T. Nakajima, H. Yamamoto, *Electrochem. Solid-State Lett.* **2006**, 9, H22.
[7] H. Zhu, C. C. Lin, W. Luo, S. Shu, Z. Liu, Y. Liu, J. Kong, E. Ma, Y. Cao, R.-S. Liu, *Nat. Commun*. **2014**, 5, 4312.
[8] H. F. Sijbom, R. Verstraete, J. J. Joos, D. Poelman, P. F. Smet, *Opt. Mater. Express* **2017**, 7, 3332.
[9] D. Chen, Y. Zhou, J. Zhong, *RSC Adv.* **2016**, 6, 86285.
[10] M. J. Lee, Y. H. Song, Y. L. Song, G. S. Han, H. S. Jung, D. H. Yoon, *Mater. Lett.* **2015**, 141, 27.
[11] F. Garcia-Santamaria, J. E. Murphy, A. A. Setlur, S. P. Sista, *ECS J. Solid State Sci. Technol.* **2018**, 7, R3030.
[12] E. Song, Y. Zhou, X.-B. Yang, Z. Liao, W. Zhao, T. Deng, L. Wang, Y. Ma, S. Ye, Q. Zhang, *ACS Photonics* **2017**, 4, 2556.
[13] M. Kim, W. B. Park, J.-W. Lee, J. Lee, C. H. Kim, S. P. Singh, K.-S. Sohn, *Chem. Mater.* **2018**, 30, 6936.
[14] Y. Zhou, C. Yu, E. Song, Y. Wang, H. Ming, Z. Xia, Q. Zhang, *Adv. Opt. Mater.* **2020**, 8, 2000976.
[15] O. B. Shchekin, P. J. Schmidt, F. Jin, N. Lawrence, K. J. Vampola, H. Bechtel, D. R. Chamberlin,R. Mueller-Mach, G. O. Mueller, *Phys. Status Solidi RRL* **2016**, 10, 310.
[16] W. W. Beers, D. Smith, W. E. Cohen, A. M. Srivastava, *Opt. Mater.* **2018**, 84, 614.
[17] M. A. Van De Haar, M. Tachikirt, A. C. Berends, M. R. Krames, A. Meijerink, F. T. Rabouw, *ACS Photonics* **2021**, 8, 1784.
[18] R. A. Osborne, N. J. Cherepy, Z. M. Seeley, S. A. Payne, A. D. Drobshoff, A. M. Srivastava, W. W. Beers, W. W. Cohen, D. L. Schlagel, *Opt. Mater.* **2020**, 107, 110140.
[19] H. F. Sijbom, J. J. Joos, L. I. D. J. Martin, K. Van den Eeckhout, D. Poelman, P. F. Smet, *ECS J. Solid State Sci. Technol.* **2015**, 5, R3040.
[20] T. Senden, R. J. A. van Dijk-Moes, A. Meijerink, *Light Sci. Appl.* **2018**, 7, 8.
[21] B. Henderson, G. F. Imbusch, *Optical Spectroscopy of Inorganic Solids*, Oxford University Press, **2006**.
[22] T. P. Van Swieten, T. Van Omme, D. J. Van Den Heuvel, S. J. W. Vonk, R. G. Spruit, F. Meirer, H. H. P. Garza, B. M. Weckhuysen, A. Meijerink, F. T. Rabouw, *ACS Appl. Nano Mater.* **2021**, 4, 4208.
[23] C. Hoelen, P. Antonis, D. de Boer, R. Koole, S. Kadijk, Y. Li, V. Vanbroekhoven, P. Van De Voorde, in *Sixt. Int. Conf. Solid State Light. LED-Based Illum. Syst.*, Vol 10378, SPIE, **2017**, 74.
[24] I. Nikolov, X. Mateos, F. Güell, J. Massons, V. Nikolov, P. Peshev, F. Diaz, *Opt. Mater.* **2004**, 25, 53.

Chapter 4

Luminescence and formation of cubic and hexagonal $(K,Rb)_2SiF_6:Mn^{4+}$

Based on:

A.J. van Bunningen[§], J.W. de Wit[§], S. Wakui, A. Meijerink, Luminescence and formation of cubic and hexagonal $(K,Rb)_2SiF_6:Mn^{4+}$, *ACS Applied Materials & Interfaces* 16 (1), 1044–1053, **2023**

§ These authors contributed equally

Abstract

The efficient red emitting phosphor $K_2SiF_6:Mn^{4+}$ (KSF) is widely used for low-power LED applications. The saturated red color and sharp line emission are ideal for application in backlight LEDs for displays. However, the long excited-state lifetime lowers the external quantum yield (EQY) at high photon flux, limiting the application in (higher-power-density) lighting. Here we report on the synthesis of a new crystalline phase: hexagonal $(K,Rb)SiF_6:Mn^{4+}$ (h-KRSF). Due to the lower local symmetry the Mn^{4+} emission in this new host material shows a pronounced zero-phonon line (ZPL), different from Mn^{4+} in the cubic KSF. The lower symmetry reduces the excited-state lifetime and thus the loss of EQY under high photon fluxes and the spectral change also increases the lumen/W output. Temperature-dependent emission and lifetime measurements reveal a high luminescence quenching temperature of ~500 K, similar to KSF. The formation mechanism of h-KRSF was studied in situ by measuring the emission spectra of the precipitate in solution over time. Initially nanocrystalline cubic KRSF (c-KRSF) is formed which transforms into the microcrystalline hexagonal precipitate with a surprising exponential increase in transformation rate with time. The stability of the new phase was studied by temperature-dependent XRD and an irreversible transition back to the cubic phase was seen upon heating to temperatures above 200°C.

Introduction

In the field of lighting and displays, the discovery of the blue light-emitting diode (LED) marks the beginning of a revolution. Converting part of the blue LED output to longer-wavelength light (green, yellow, orange or red) by a luminescent material (a phosphor) makes it possible to realize compact and efficient white-light sources with a great flexibility in spectral distribution. The desired characteristics of a phosphor depend on the application. Lighting requires white LEDs (wLEDs) with a high efficacy (lumen/W output) and a high color rendering index (CRI). The high brightness of wLEDs can only be realized using phosphors with emitters that have a high turnover rate (photons/s). In addition, the luminescence quenching temperature has to be high as the device locally heats up to 150 °C. In displays brightness is lower and this sets less stringent requirements on turnover rate and stability. However, phosphors with saturated colors with emission at specific wavelengths are preferred to extend the color gamut while remaining efficient.

A successful red-emitting phosphor, especially for displays, is $K_2SiF_6:Mn^{4+}$ (KSF). The Mn^{4+} ion has the $3d^3$ configuration and in fluorides it shows sharp line emission around 620 nm due to vibronic $^2E \rightarrow {}^4A_2$ transitions. The narrow spectral distribution is ideal for displays. The luminescence of KSF was reported already back in 1973 but it was not until 2006 that the potential in LED lighting and displays was realized.[1,2] The spectral properties are superior to those of other red LED phosphors such as $CaAlSiN_3:Eu^{2+}$ (CASN). The broadband red Eu^{2+} emission extends towards the NIR where the eye sensitivity is low. This reduces the lumen/W output. The narrow line emission around 620 nm of Mn^{4+} helps to extend the color gamut in displays. Unfortunately, for higher-power applications KSF is less suitable as the long emission lifetime (~10 ms) for the parity- and spin-forbidden $^2E \rightarrow {}^4A_2$ transition limits the turnover rate to ~100 photons/s per Mn^{4+} ion and thus lowers the external quantum yield (EQY) at higher photon fluxes.

The popular KSF phosphor has a cubic crystal structure and the Mn^{4+} ion is in a centrosymmetric octahedral coordination of fluoride ions. The inversion symmetry makes the parity selection rule strict and it can only be lifted by coupling with odd-parity vibrations. As a result, the sharp emission lines observed are vibronic lines corresponding to ungerade vibrations that induce odd-parity crystal field components. The strictly forbidden zero-phonon line (ZPL) is not observed and that

luminescence lifetime of the ^2E state is long. Later other Mn^{4+}-doped fluoride hosts were found with a hexagonal or trigonal crystal structures.[3–5] The lower local symmetry for the Mn^{4+} ion results in the appearance of a ZPL (induced by static odd-parity crystal-field components) in addition to vibronic lines. The emission lifetime for Mn^{4+} in these hosts is shorter and the higher eye sensitivity at the ZPL wavelength is also beneficial for the efficacy. Unfortunately, for all of these hosts the luminescence quenching temperature and/or stability were low and they could not replace KSF, in spite of the superior spectral properties.

There has been a search for Mn^{4+} phosphors similar to KSF but with a lower-symmetry crystal structure to decrease the lifetime and induce a ZPL. Such a phosphor is reported here: hexagonal $(K,Rb)SiF_6:Mn^{4+}$ (h-KRSF:Mn^{4+}). Normally K_2SiF_6 and Rb_2SiF_6 as well as their solid solutions form a cubic phase. Yet, here we show that under specific reaction conditions the mixed solid solutions can form in a stable hexagonal phase. Interestingly, the existence of the hexagonal crystal structure for KSF or KRSF has sporadically been reported. The crystal structure was described by Kolditz and Preiss in 1963[6], referring back to earlier reports from 1904.[7] In the mineralogy of fumaroles, grains of 0.3 mm have been reported with the chemical formula K_2SiF_6 and hexagonal symmetry[8] while in 1952 hexagonal KSF was found when analyzing chemicals of a decommissioned chimney that was used to drain sulfuric acid and hydrogen fluoride gases.[9] There are also a few recent examples on the hexagonal form of KSF. In 2015 the luminescence of KSF:Mn^{4+} was measured at increasing pressure. Between 9 and 13 kbar a strong ZPL arises which does not disappear after decompression. This could be due the formation of nanocrystalline hexagonal KSF, but XRD measurements after decompression did not indicate a cubic-to-hexagonal phase transformation.[10] In 2014 hexagonal KSF:Mn^{4+} was synthesized, but no luminescence was observed.[11] So far no reports have been made that measured and verified Mn^{4+} in hexagonal KSF. For h-KRSF there is one patent that reports the existence and luminescence of this phase and describes the synthesis of h-KRSF:Mn^{4+} as a phosphor.[12]

In this chapter we describe the reproducible synthesis of h-KRSF doped with Mn^{4+}. We report the improved luminescence properties induced by the lower site symmetry for Mn^{4+} in the hexagonal phase and evaluate the advantageous properties such as a shorter luminescence decay time and a strong ZPL increasing the efficacy of the phosphor. We follow the formation of h-KRSF by measuring the Mn^{4+} emission to probe the phase transition from cubic to hexagonal and show how after a long induction period h-KRSF starts to form and the transformation rate of h-KRSF increases exponentially with time. Finally we determine the temperature stability of h-KRSF by measuring the back transformation to the cubic KRSF via temperature-dependent XRD and luminescence measurements.

Results and Discussion

To investigate the crystal structure and phase purity of the different materials, after synthesis the dry powders were checked by measuring the x-ray diffractograms. In **Figure 4.1a** the diffractograms of the different microcrystalline powders are shown with their respective reference underneath.

In **Figure 4.1a** we can see that for all samples there is good agreement with the reference diffraction patterns. This shows that the different synthesis methods result in phase-pure crystalline materials. For cubic KSF and RSF the crystal structure is well established and the reference diffractograms are well-known. For cubic KRSF the diffraction lines are at angles in between KSF and RSF, as expected for a solid solution. A good agreement with the experimentally observed positions of diffraction lines was obtained by assuming an increase of 2% in lattice distances compared to the KSF reference. A slight increase is expected by the replacement of K by Rb as the ionic radius of Rb^+ (1.72 Å) is bigger than of K^+ (1.64 Å) causing a small expansion of the unit cell.[15]

The reference pattern of h-KRSF is based on earlier work on hexagonal KSF. In ref. [8] the XRD pattern for h-KSF is reported and used to derive lattice parameters a = 5.67 Å and c = 9.24 Å and identify two differently sized M^+ sites (M1 and M2). The diffraction pattern obtained here for KRSF is very similar. A good match is obtained for slightly larger lattice parameters a = 5.78 Å and c = 9.42 Å, providing convincing evidence for the formation of hexagonal $KRbSiF_6$:Mn^{4+}. The powder XRD data does not allow to make a distinction between the ordering of Rb^+ and K^+ on the M1 and M2 site. Single-crystal data can provide valuable information about the ordering of K^+ and Rb^+ in future work.

To evaluate the particle size and particle size distribution, SEM images were made of the final product. The SEM image in **Figure 4.1b** shows that the synthesis procedure used results in a homogeneous particle size distribution with an average particle size of ~30 µm.

Optical properties To study the optical properties of Mn^{4+} in the new h-KRSF both PL and PLE spectra were measured for low-doped samples (0.1–0.5% Mn^{4+}). For comparison the spectra of Mn^{4+} in cubic KRSF, KSF and RSF were measured as well. In **Figure 4.2a** it is observed that all the PLE spectra have two relatively strong and broad excitation bands around 360 nm and 460 nm.

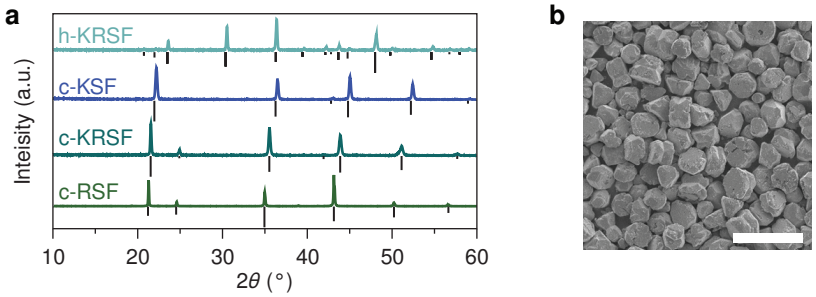

Figure 4.1 | X-ray diffractograms of Mn^{4+}-doped fluorides and SEM of h-KRSF. (**a**) From top to bottom the diffractograms of h-KRSF, cubic K_2SiF_6, cubic $KRbSiF_6$ and cubic Rb_2SiF_6 doped with 0.5% Mn^{4+} are shown. Below the experimental patterns, the reference patterns are plotted.[8,13,14] Note that these diffractograms are recorded using a Co X-ray source. (**b**) SEM image of synthesized h-KRSF:1.8% Mn^{4+}. The average particle size is ~30 µm. The scale bar at the bottom is 100 µm.

The 460 nm band shows some sharp lines around 470 nm. These can be ascribed to Xe-lamp lines that are visible in spite of correcting the spectra for variations in the Xe-lamp intensity. A zoom-in for the area between 560 and 625 nm shows a multitude of weak and narrow excitation lines (**Figure 4.2b**). The PLE spectra of the four samples are very similar with one exception: there is sharp extra peak at 621.5 nm for Mn^{4+} in h-KRSF. In the PL spectra (**Figure 4.2c**) again all spectra are very similar showing sharp emission lines at the same positions, with small shifts of ~0.5 nm to longer wavelengths from KSF to RSF. Again there is one exception: an extra peak at 621.5 nm for Mn^{4+} in the hexagonal form of KRSF.

Based on the Tanabe–Sugano diagram for $3d^3$ ions in octahedral symmetry, the excitation bands at 360 and 460 nm in the PLE spectra are assigned to the $^4A_2 \rightarrow {}^4T_1$ and $^4A_2 \rightarrow {}^4T_2$ transitions, respectively. In the zoom-in spectra, **Figure 4.2b**, the peaks observed from 560 to 595 nm are assigned to the vibronic lines of the $^4A_2 \rightarrow {}^2T_1$ transition and from 600 to 625 nm to vibronic excitation lines of the $^4A_2 \rightarrow {}^2E$ transition in the cubic modifications. For Mn^{4+} in inversion symmetry, all $3d^3 \rightarrow 3d^3$ transitions are parity forbidden and coupling with odd-parity vibrations is required to partly lift the parity selection rule resulting in the observation of vibronic excitation and emission lines. In h-KRSF the Mn^{4+} ion is in a site with lower symmetry and static odd-parity crystal-field components allow for breaking the parity selection rule. As a result, also the purely electronic zero-phonon transition can be observed. For the $^4A_2 \rightarrow {}^2E$ transition in h-KRSF this zero-phonon line (ZPL) is at 621.5 nm and is identical in the excitation and emission spectra. The positions of the vibronic emission lines in KSF (**Figure 4.2c**) are 597, 608, 613, 630, 635 and 648 nm, in agreement with earlier reports. The lines at 630, 635 and 648 nm are Stokes vibronic lines due to coupling with

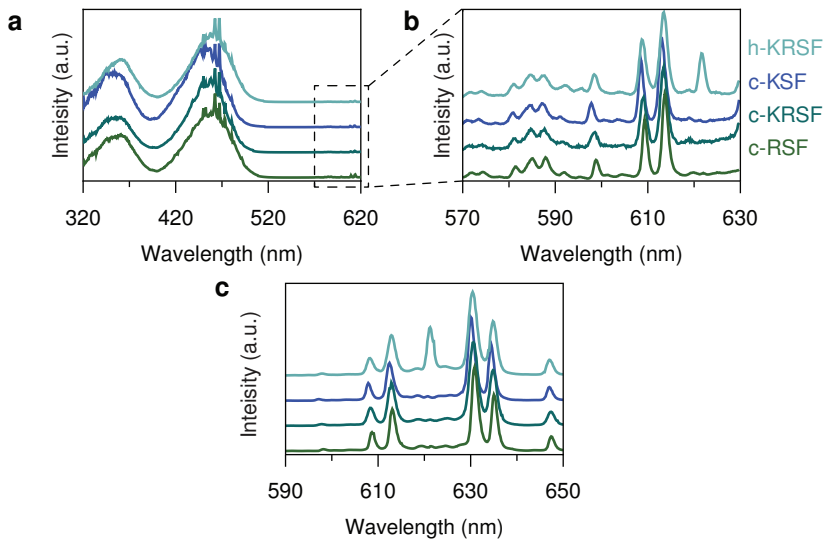

Figure 4.2 | Photoluminescence excitation (PLE) and photoluminescence (PL) spectra of h-KRSF and cubic M_2SiF_6 (M = K and/or Rb) doped with 0.1–0.5% Mn^{4+}. (**a**) PLE spectra recorded at λ_{em} = 630 nm that show two spin-allowed $^4A_2 \rightarrow {}^4T_2$ and $^4A_2 \rightarrow {}^4T_1$ excitation bands centered at 460 and 360 nm respectively. (**b**) PLE spectra recorded for 648 nm emission, showing the spin-forbidden, vibronic $^4A_2 \rightarrow {}^2T_1$ and ^2E excitation lines. Multiple vibronic excitations are visible for both $^4A_2 \rightarrow {}^2E$ excitation (range 598–619 nm) and the $^4A_2 \rightarrow {}^2T_1$ excitation (570–596 nm) (**c**) PL spectra of the $^2E \rightarrow {}^4A_2$ transition excited at 450 nm. Only for the hexagonal $KRbSiF_6$ samples the ZPL is clearly present at 621.5 nm, in excitation and emission.

ν_6, ν_4 and ν_3 vibrations. The lines at 597, 608 and 613 nm are anti-Stokes vibronics at the same energy differences from the ZPL (that is hardly observed, except for h-KRSF) as the Stokes lines.

The change in local symmetry around the tetravalent ion in cubic KSF to hexagonal KSF is key for understanding the appearance of the ZPL. In the cubic phase the Si^{4+} atom (or the Mn^{4+}) is symmetrically surrounded by 6 equidistant fluorine ligands at 1.677 Å. In ref [8], a Rietveld refinement on the diffraction pattern of the hexagonal phase of KSF shows there is a slight distortion of the octahedron: 3 ligands are at a distance of 1.681 Å while the others are at a distance of 1.688Å.[8,13] The same deviation from inversion symmetry for Mn^{4+} can be expected in h-KRSF and explains why for the hexagonal phase a zero-phonon line is observed and not for the cubic phases. Again, single-crystal XRD data could provide valuable information about deviations in the $[MnF_6]^{2-}$ octahedron that result in the ZPL

The enhanced ZPL is beneficial for the performance. The additional emission at ~620 nm where the eye sensitivity is higher increases the efficacy. The luminous response function has its maximum at 550 nm and drops to 1% of the maximum at 680 nm. A higher fraction of the emission spectrum towards longer wavelengths reduces the efficacy. If we compare c-KRSF to h-KRSF, a smaller fraction of the emission is from the Stokes emission lines of 630, 636 and 648 nm. The additional emission intensity at ~620 nm results in an efficacy increase of 2.9% for h-KRSF compared to c-KRSF (see Supporting Information Section S4.2, Figure S4.1). In addition, deviation from inversion symmetry also increases the $^4A_2 \rightarrow {}^4T_2$ absorption strength for the blue excitation wavelength at 450 nm as a result of the relaxation of the parity selection rule. The increased absorption strength at 450 nm is experimentally observed to be ~34% by comparing the emission intensity of c-KRSF with h-KRSF under the same excitation intensity (see Supporting Information Section S4.2, Figure S4.2). To evaluate the efficiency of the new h-KRSF phosphor quantum yield measurements were done. A sample with 1.8 mole% Mn incorporated had an internal quantum yield of 91%. We consider this value to be very high as little effort was put into optimizing the synthesis.

For practical applications a wLED phosphor needs to be resilient to high temperatures and a humid atmosphere. To test the stability the luminescence of h-KRSF was measured after synthesis and this was compared to the luminescence after 48 h exposure to 85% humidity at 85°C. A KSF phosphor was measured simultaneously. For the h-KRSF a decrease in luminescence was seen of 16% which is considerably worse than the KSF which showed a loss of 1 to 2%. The relatively fast degradation of h-KRSF compared to KSF we attribute to the incorporation of Rb. Rb compounds tend to be more hygroscopic than K compounds, thus enhancing the degradation.[16] For practical application the stability needs to be improved e.g. by post-synthesis treatment, overcoating and/or encapsulation in a protective matrix using strategies that have also been explored for KSF.[17,18] Reducing the Rb-content from 50% to 20% (a Rb concentration for which the hexagonal phase can still be obtained, vide infra) may also enhance the stability. Further optimization is required to explore the potential of h-KRSF as a new LED phosphor. An initial test with h-KRSF phosphor in a wLED shows promising results with a performance that is similar to a wLED with KSF (see Supporting Information Section S4.3).

Concentration-dependent luminescence The 450 nm absorption by Mn^{4+} in the $^4A_2 \rightarrow {}^4T_1$ absorption band involves a spin-allowed but parity-forbidden transition. As discussed above, the deviation from inversion symmetry in h-KRSF is expected to make the absorption stronger than

in c-KRSF or KSF but this absorption is still much weaker than for fully allowed transitions such as the $4f^n \rightarrow 4f^{n-1}5d^1$ transition in Ce^{3+} or Eu^{2+}. A high Mn^{4+} concentration is thus beneficial to reduce the amount of phosphor that is required to absorb sufficient blue LED light in a wLED. At the same time, a high dopant concentration can lead to concentration quenching. Energy transfer between neighboring ions will cause migration of the excitation energy over the dopant sublattice. Especially above the percolation point (where a 3D connected lattice of dopant ions is realized) the migrating excitation energy can probe a large volume in which there is a high probability to encounter a defect or impurity quenching site causing concentration quenching. Investigating the concentration dependence of the luminescence efficiency is therefore important and a concentration series of h-KRSF:Mn^{4+} x% (x = 0.1 to 10) was synthesized (See Supporting Information Section S4.4 for the XRD patterns). It is important to realize that the fraction of Mn^{4+} in the synthesis mixture is not the same as the fraction incorporated in the h-KRSF. Indeed, after evaporating the EtOH out of the reaction mixture darker-colored spots are visible within the dry powder. Washing with H_2O_2 removes these spots. Probably these spots were compounds with a high concentration of Mn that dissolve in H_2O_2. This also means that the fraction of Mn^{4+} incorporated in h-KRSF is lower than the nominal concentration. To check the actual Mn concentration, inductively coupled plasma optical emission spectroscopy (ICP-OES) measurements were done. The measurements show that 16 to 60% of the added Mn is actually incorporated (see Supporting Information Section S4.5). The concentrations mentioned below always refer to actual concentrations in the phosphors as determined with ICP-OES.

To study the concentration-dependent optical properties both emission spectra and luminescence decay curves were measured for samples with Mn^{4+} concentrations varying between 0.1 and 10 mole%. In **Figure 4.3a** the emission spectra of samples with different Mn concentrations are shown under 450 nm excitation. The samples were diluted 10× (wt%) with optically inactive $BaSO_4$ to limit the pathlength of light through the h-KRSF phosphor and reduces saturation effects in blue light absorption. It can be seen that the intensity increases with increasing Mn concentration. The integrated intensities as function of Mn^{4+} concentration (**Figure 4.3b**) show a rapid increase at low concentrations (up to 1% Mn^{4+}) after which it levels off. This non-linear increase at highdopant concentrations has been observed before and is explained by saturation of blue light absorption. The integrated emission intensities of the undiluted phosphors show an even

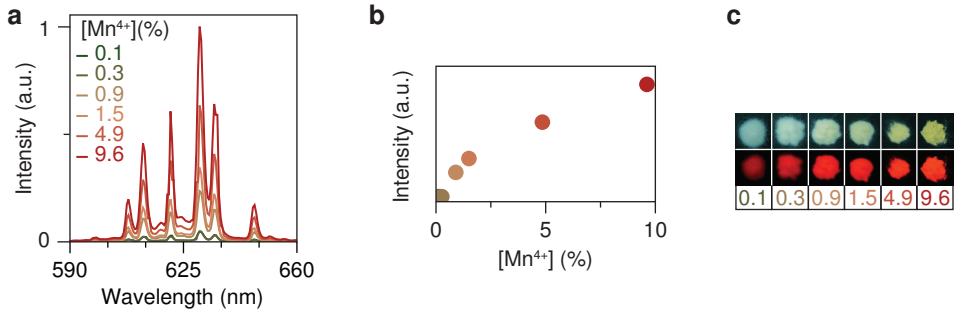

Figure 4.3 | Optical properties of h-KRSF at different Mn^{4+}-doping concentrations. (**a**) Emission spectra of h-KRSF for different doping concentrations that range from 0.1–9.6 mole% with respect Si^{4+} (λ_{exc} = 450 nm). All samples are diluted 10× (wt%) with $BaSO_4$. (**b**) Integrated intensity of the emission spectra in panel **a**. The sublinear increase of emission intensity with [Mn^{4+}] is ascribed to saturation in the absorption of the blue excitation light. (**c**) Photographs of the undiluted KRSF samples under flashlight (top row) and 360 nm UV (bottom row) illumination.

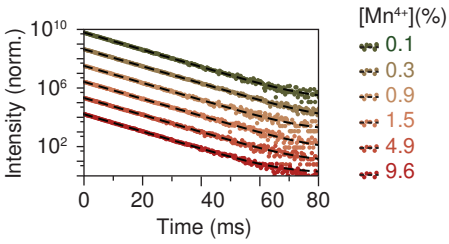

Figure 4.4 | Photoluminescence decay curves of h-KRSF at different Mn^{4+}-doping concentrations. Decay curves are recorded using ns pulsed excitation at 450 nm and emission at 630 nm. An offset between the datasets was added for clarity. The dashed lines show the single-exponential fit to the experimental data.

stronger leveling off with increasing Mn^{4+} concentration (Supporting Information Section S4.6). As the Mn^{4+} concentration increases a substantial part of the blue light is absorbed and the fraction of absorbed light no longer increases linear with Mn^{4+} concentration as is also evident from Lambert-Beers' law. Only for a low value of εcl (molar extinction coefficient × concentration × path length) the fraction of absorbed light increases linearly with concentration. This makes it difficult to determine if concentration quenching occurs based on concentration-dependent emission intensities.

A better method to study concentration quenching is measuring luminescence lifetimes. In case of non-radiative loss processes as a result of concentration quenching, the emission lifetime will decrease. Luminescence decay curves of the 630 nm emission after pulsed 450 nm excitation are shown in **Figure 4.4**. A single-exponential decay is observed for all concentrations and the decay times are constant ~6.2 ms. The single-exponential decay curves and constant decay time indicates that no concentration quenching occurs up to at least 10% Mn^{4+}.

Temperature-dependent luminescence The temperature stability of luminescence is an important aspect of wLED phosphors. Heat is generated by the LED chip and also by heat dissipation inherent to the conversion of a higher-energy blue photon to green or red photons. The local temperature of a phosphor in wLEDs can easily reach 150 °C. The thermal quenching behavior is therefore crucial. Indeed, previously Mn^{4+}-doped fluorides have been found where the lower local symmetry also resulted in the desired observation of a strong ZPL and shorter emission life time but the poor thermal quenching behavior made these phosphors unfit for application in wLEDs.[3,5,19] The thermal quenching behavior of h-KRSF: 0.1% Mn^{4+} was therefore measured and compared with that of cubic KRSF: 0.1% Mn^{4+} and KSF: 0.5% Mn^{4+}. The temperature-dependence of the integrated emission intensities in the relevant high temperature region 373–700 K is shown in **Figure 4.5**. The corresponding emission spectra at different temperatures of the three samples are shown in the Supporting Information Section S4.7. When the temperature increases, the emission intensity remains constant until 450 K above which it starts to decrease.

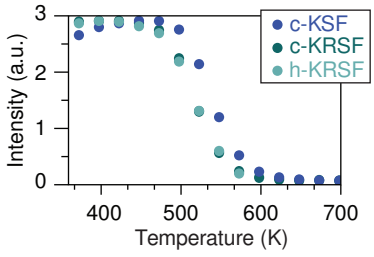

Figure 4.5 | Integrated emission intensity as a function of temperature for c-KSF and c-KRSF and h-KRSF doped with 0.1% Mn^{4+}. The integration range is from 580 nm to 680 nm.

Measuring emission intensity as a function of temperature to probe thermal quenching can be complicated by intensity variations not related to thermal quenching, for example when the oscillator strength of the absorption transition is temperature-dependent. In addition, practical aspects such as changes in alignment, collection efficiency or excitation source intensity can give rise to intensity variations not related to thermal quenching. A fast and reliable method to determine the thermal quenching temperature is measuring the emission lifetime as a function of temperature. As non-radiative decay sets in, the emission lifetime shortens as the lifetime is the inverse of the sum of radiative and non-radiative decay rates. Therefore also lifetimes were measured as function of temperature for h-KRSF: 0.1% Mn^{4+} and c-KRSF: 0.1% Mn^{4+} and KSF: 0.5% Mn^{4+} and are shown in **Figure 4.6a**. All the decay curves are single-exponential. The lifetimes of the Mn^{4+} emission in the three different host lattices is shown as a function of temperature in **Figure 4.6b**. For all three host matrices it can be seen that the lifetime decreases slowly up till 450–480 K after which the lifetime drops sharply, consistent with the temperature-dependent intensity measurements.

Before discussing the luminescence quenching temperature it is interesting to discuss differences in lifetimes for Mn^{4+} emission in the three compounds: the lifetime is longer for KSF and c-KRSF than for h-KRSF. As discussed above, the perfect octahedral coordination in the two cubic lattices imposes a strict parity selection rule. This does not only prevent the observation of a ZPL but also reduces the overall transition probability as the ZPL transition is forbidden. The room-temperature emission lifetime is ~6 ms for Mn^{4+} in h-KRSF vs. ~8 ms in the cubic lattices. The shorter lifetime in h-KRSF is beneficial for application in wLEDs. As mentioned in the introduction, the long emission lifetime is a limiting factor in the total light output and prevents the application of KSF in high-brightness wLEDs. The 25% shorter lifetime helps to improve the performance of h-KRSF in higher-brightness sources although the lifetime is still long compared to that for emission in other wLED phosphors relying on d–f emission from Ce^{3+} (~40–80 ns) or Eu^{2+} (~1–2 µs).

In **Figure 4.5** it is observed that the luminescence intensity is constant up until 450 K while the lifetime decreases gradually with temperature between 100 and 400 K (**Figure 4.6b**). This is an indication that the change in emission lifetime is not caused by temperature quenching. This is

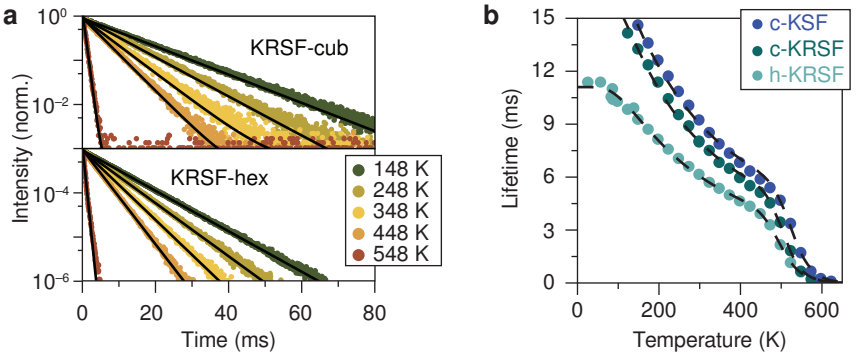

Figure 4.6 |Temperature-dependent photoluminescence decay properties of KSF and KRSF. (**a**) Integrated emission intensity as a function of temperature for cubic KSF and cubic and hexagonal KRSF doped with 0.1% Mn^{4+}. (**b**) PL decay measurements of Mn^{4+} emission in cubic (top) and hexagonal (bottom) KRSF, single-exponential fits to the data are shown in black. (**c**) Emission lifetime of the Mn^{4+} emission as a function of temperature in c-KSF, c-KRSF and h-KRSF. All samples were excited at 450 nm and luminescence decay was recorded at 631 nm (c-KSF and c-KRSF) or 621 nm (h-KRSF).

generally observed for ^2E emission of Mn^{4+} and explained by an increase in vibronic transition probabilities induced by a higher phonon occupation number n. It is well-established that the transition probability for Stokes vibronics scales with $(n + 1)$ and anti-Stokes vibronics with n.[19] The corresponding change in radiative lifetime as a function of temperature is described by:

$$\tau_r(T) = \frac{\tau_r(0)}{\coth(h\nu/2k_BT) - 1} \tag{4.1}$$

Here $\tau_r(T)$ is the radiative lifetime at temperature T, hν is the effective phonon energy and k_B is the Boltzmann constant. This equation describes the emission lifetime before temperature quenching sets in at 450 K. Temperature quenching for Mn^{4+} has been shown to occur via the $^4T_2$ state with an activation energy ΔE. Together with temperature dependence for the radiative decay time $\tau_r(T)$ from Equation 4.1 the expression for the lifetime as a function of temperature is:

$$\tau(T) = \frac{\tau_r(T)}{1 + \frac{\tau_r(T)}{\tau_{nr}} e^{-\Delta E/k_BT}} \tag{4.2}$$

where τ_{nr} is the non-radiative decay time which is typically in the order of picoseconds, the time scale of vibrations. We can now use Equations 4.1 and 4.2 to find the quenching temperature $T_{1/2}$, defined as the temperature at which $\tau(T)$=½ $\tau_r(T)$. The $T_{1/2}$ temperatures determined in this way for c-KSF, c-KRSF and h-KRSF were found to be 530, 510 and 503 K, respectively. All temperatures are sufficiently high to prevent thermal quenching in wLEDs. There is a small decrease in $T_{1/2}$ from KSF to both cubic and hexagonal KRSF. The thermal luminescence quenching mechanism has been shown to occur by thermal crossover from the ^2E to the $^4A_2$ state via the $^4T_2$ state. The lower the energy of the $^4T_2$ state, the lower the quenching temperature will be. The slightly lower $T_{1/2}$ values for KRSF are consistent with a small red shift (from 452 nm in KSF to ~458 nm in c-KRSF) of the $^4T_2$ excitation band. The small redshift may be related to slightly larger distances to the F^- ligands in compounds with increasing Rb content which lowers the crystal field splitting.[19]

Formation mechanism The formation mechanism of the h-KRSF is intriguing. The method was found serendipitously: the addition of extra aqueous HF to dissolve the initial precipitate followed by the addition of ethanol (EtOH) was meant to precipitate a random mixed-phase Rb/K system to investigate the role of disorder in a more distant cation (K/Rb) coordination sphere on the Mn^{4+} luminescence. Interestingly, the absence of a ZPL in c-KRSF shows that deviations from inversion symmetry by disorder in the second (K/Rb) coordination sphere are too small to effectively relax the parity selection rule, as was the original goal of the research project. When the EtOH addition did not result in precipitation, the solution was left to evaporate for several days and the new h-KRSF phase was found. It is interesting to obtain better insight in the formation mechanism of h-KRSF. Therefore, to follow the formation of h-KRSF emission spectra were recorded during the evaporation process. A 445-nm laser was used to illuminate the reaction beaker (as shown in the Supporting Information Section S4.8) while the emission spectra were recorded at regular time intervals over a period of days by a simple fiber-coupled CCD spectrometer. The results are shown in **Figure 4.7**.

Immediately after pouring the reaction mixture in the EtOH the solution shows emission spectra typical of the cubic phase with vibronic Stokes and anti-Stokes emission lines, but no ZPL. No precipitation is observed, however, blue excitation shows that much of the c-KRSF immediately concentrates in the lower part of the beaker. The presence of the typical Mn^{4+} spectrum without a ZPL in the initially formed clear solution indicates that

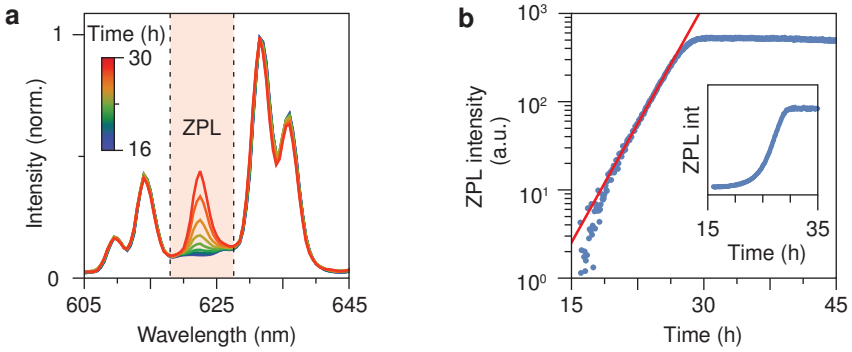

Figure 4.7 | In situ emission spectroscopy measurements to follow h-KRSF:Mn^{4+} formation. (**a**) A selection of emission spectra recorded between 16 and 30 hours after pouring the precursor mixture into EtOH. During this time the ZPL intensity increases strongly, indicating the transition from c-KRSF to h-KRSF. (**b**) Logarithmic plot of the integrated emission intensity of the ZPL peak, corrected for "background" signal as recorded before 16 h. The integration limits are indicated by the highlighted area in panel **a**. A single-exponential function is fitted to the data between 16 and 26 hours after mixing and is plotted in red. The inset shows the corrected ZPL intensity between 15 and 35 hours in a linear plot.

nanocrystalline c-KRSF is formed and based on the higher concentration at the bottom of the beaker the particle size is estimated to be 50–100 nm. The characterization and optical properties of nanocrystalline KRSF (and KSF) deserves further study but is beyond the scope of this work. Stabilizing the KRSF nanocrystals may be interesting for applications where nanocrystalline KSF offers advantages over the conventional microcrystalline material.

To follow the transformation from cubic to hexagonal KRSF, the emission spectra as recorded over time are shown in **Figure 4.7a**. The formation of h-KRSF is probed by monitoring the intensity of the ZPL. No ZPL is present in the cubic phase and by integrating the 618-to-627-nm range the ZPL intensity is measured by subtracting the background measured in spectra recorded immediately after the addition to EtOH. The integrated ZPL intensity increases over time and shows a peculiar time dependence. There is a delay in the formation and only after ~15 h the transformation to h-KRSF starts and a small ZPL appears. The relative intensity of the ZPL increases, first slowly and then rapidly until all c-KRSF is transformed into h-KRSF. The rapidly increasing transformation rate can be well-described by exponential growth: when plotted on a logarithmic scale vs. time the ZPL intensity increase is linear. This behavior is consistently observed, also when reaction conditions are changed. There is always a delay time (induction period) before the formation of h-KRSF starts and after that the ZPL intensity increases exponentially with time. The reaction conditions were varied by changing the Rb/K ratio and the alcohol used. The minimum fraction of Rb required to form the hexagonal phase is 20% for the synthesis procedure followed, resulting in part hexagonal and part cubic KRSF. For all the different alcohols used (from methanol to butanol) formation of h-KRSF was observed. The induction period varied and was longer for a lower Rb content. A detailed discussion about the influence of these and other parameters on the stability and formation of h-KRSF can be found in Supporting Information Section S4.9.

Before discussing the formation mechanism, it is good to evaluate the thermodynamic stability of the hexagonal vs. cubic phase. To test this, first temperature-dependent XRD was used. Diffractograms over the range 2θ = 17.5–24.0° were measured. This range was chosen because in this area

there are peaks that distinctively belong to either the cubic or hexagonal KRSF. After each measurement the sample was heated by 10 K and the next diffractogram was measured. The results between 2θ = 18–19° are shown in **Figure 4.8** and the full pattern (17.5 to 24.0°) is shown in the Supporting Information Section S4.10. Upon heating above 500 K the peaks at 18.85° and 20.1° (from h-KRSF) diminish and then disappear while the peaks at 18.4° and 21.2° (from c-KRSF) increase in intensity and then remain constant above 570 K. After cooling down to RT the peaks at 18.85° and 20.1° do not reappear.

The transformation from hexagonal to cubic indicates that at higher temperatures the cubic phase is the most stable phase. The observation that the peaks at 18.85° and 20.1° do not reappear upon cooling shows that the transformation is irreversible. Note that this is different from K_2MnF_6 for which the cubic phase is not stable at RT. Heating hexagonal K_2MnF_6 to 440 °C transformed the crystals to the cubic phase but after storing the crystals at room temperature they transformed back to the hexagonal phase.[20] To test whether c-KRSF transforms back to h-KRSF at lower temperatures several experiments were done: in one experiment h-KRSF was kept for months at 253 K and RT, in another c-KRSF was heated for one month at 373 K. We also heated and then slowly cooled h-KRSF from 573 to 435 K in 90 hours. In all cases, no XRD peaks of h-KRSF were found in any of the diffractograms recorded afterwards indicating that c-KRSF is the stable phase around and above RT. The XRD results were confirmed by luminescence measurements which showed no ZPL at 621.5 nm and only the emission spectra typical of c-KRSF

Based on the observations so far one can only speculate on the formation mechanism of h-KRSF. Initially, when the aqueous solution is added to the EtOH nanosized c-KRSF particles are formed. Precipitation at the bottom of the beaker occurs gradually during the evaporation and it is difficult to estimate whether differences in solubility between KSF and RSF influence this process. Possibly, the decreased alcohol content destabilizes the nanocrystals and induces particle growth. At the same time it can destabilize the surface of the nanoparticles. It is known that differences in solvent composition changes the surface–solvent interaction and can affect the obtained crystal structure of polymorphic materials.[21,22] A high surface area may induce the transformation to a structure with a higher density and thus less surface area.[23] This can explain the transformation to h-KSF, as h-KSF has a higher reported density than c-KSF (2.87 vs. 2.746 g/cm^3).[6] Once particles transform to the hexagonal phase these can serve as seeds that grow at the expense of dissolving c-KRSF nanoparticles and give rise to an exponential increase of the fraction of h-KRSF

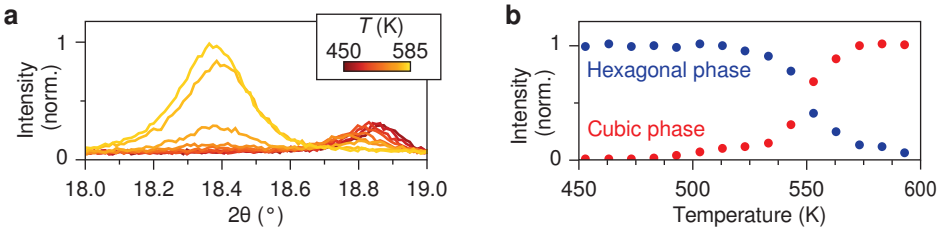

Figure 4.8 | Monitoring the stability of h-KRSF with temperature-dependent XRD measurements. (**a**) Selection of diffractograms measured between 450 and 585 K. The peak at 18.85° corresponds to the hexagonal phase ((002) reflection) and the peak at 18.4° corresponds to the cubic phase ((111) reflection). (**b**) Integrated intensity underneath the peaks corresponding to the hexagonal (blue) and cubic (red) phase of h-KRSF with temperature intervals of 10 K. Note that for recording these diffractograms a Cu Kα (λKα = 1.5418 Å) X-ray source is used.

over c-KRSF with time. A similar rapid increase in conversion rate was recently observed in the transformation of cubic (α-phase) $NaYF_4$ nanocrystals to larger hexagonal (β-phase) $NaYF_4$ nanocrystals.[24] We were able to model this transformation by taking into account a distribution in reaction (dissolution/growth) rates for nanoparticles, first resulting in a bimodal size distribution followed by an increasingly rapid transformation to large and monodisperse β-phase crystallites with time, similar to what is observed in **Figure 4.8**

To obtain better insight in and evidence for a formation mechanism, further studies such as combined in situ WAXS and SAXS measurements are required to follow particle size and crystallinity in time and relate these to the time-dependent luminescence properties. Indeed, also other mechanisms have been reported where an induction period is followed by a rapidly increasing transformation rate, for example the transformation of ferrihydrite to goethite or hematite nanocrystals.[25] Alternatively, autocatalysis can explain an exponential growth of the phase transformation rate. This mechanism has been extensively studied in for example the transformation of α- to β-Sn.[26]

A final challenge is the formation of hexagonal KSF free of Rb, especially since the presence of Rb can be linked to a lower stability of the phosphor under the extreme conditions experienced in wLEDs. To lower the amount of Rb, the synthesis of h-KRSF was done with different Rb/K ratios. Lowering the Rb fraction resulted in longer induction periods and slower formation of h-KRSF. For 40% and 30% Rb still a complete transformation to h-KRSF was observed. For 20% Rb there was no complete transformation (For details, see Supporting Information Section S4.10) while for 10% and 0% Rb, no formation of h-K(R)SF could be observed (no increase in ZPL intensity). However, based on earlier reports on the synthesis of h-KSF by Kolditz in 1963 and Gossner in 1904,[6,7] and the observation of h-KSF in Refs. [10] and [11] it is evident that h-KSF can be obtained and it is worthwhile pursuing a synthesis method to realize the synthesis of h-KSF doped with Mn^{4+} with superior performance as a wLED phosphor.

To understand the role of the Rb in the formation of h-KRSF DFT calculations were done to determine the formation energy of cubic and hexagonal Rb_2SiF_6, $KRbSiF_6$, and K_2SiF_6. The results and a more extensive discussion are provided in the Supporting Information Section S4.11. In h-KRSF there are (in contrast with c-KRSF) two non-equivalent M^+ sites. The calculations show that the lowest-energy configuration of h-KRSF is obtained when K^+ ions occupy the smaller M1 site and Rb^+ ions occupy the larger M2 site. If the ordering of the monovalent cations during crystal growth is indeed responsible for the formation of the (thermodynamically favorable) hexagonal phase, this could trigger the chain reaction among the other crystals we observe. Single-crystal XRD data could provide further information about the location of the Rb and K ions in the lattice and test this hypothesis. To quantify how stable the hexagonal phase is compared to the cubic phase, the formation energy of the hexagonal phase was subtracted from the cubic phase. The calculations show that in all cases the cubic phase is more stable. However, it can be seen that K_2SiF_6 and Rb_2SiF_6 have a much stronger preference for the cubic phase as the energy difference between the cubic and the hexagonal phase is 43 meV and 71 meV per unit cell respectively, while it is only 9 meV for the $KRbSiF_6$. This confirms that for the mixed K/Rb composition it is easier to form the hexagonal phase.

Conclusion

The luminescence of Mn^{4+} in a new hexagonal phase of $KRbSiF_6$ is reported. The optical properties have clear advantages over those for Mn^{4+} in the cubic KSF. The deviation from inversion symmetry allows for the observation of a strong zero-phonon line and shortens the luminescence lifetime for Mn^{4+}. This improves the lumen/W efficacy, increases the absorption strength and reduces saturation at high blue photon fluxes. The quenching temperature of the Mn^{4+} luminescence in the hexagonal phase is very high and comparable to that in the cubic phase (>500K). High quantum yields (>90%) are realized without synthesis optimization but the stability is lower, probably due to the large fraction of Rb. The h-KRSF is synthesized by adding precursors dissolved in water to an excess volume of ethanol followed by slow evaporation of the ethanol. The formation mechanism is intriguing and was studied by continuously measuring luminescence spectra of the (nano)particles in the reaction volume. After an induction period of ~15 hours the precipitate started to transform to the hexagonal phase with an exponentially increasing transformation rate. After 8 hours it was fully transformed. The stability of the hexagonal phase was tested by temperature-dependent XRD and luminescence measurements showing that above 200 ^{0}C h-KRSF transforms back to c-KRSF. The higher efficacy, shorter luminescence lifetime and high quenching temperature make the hexagonal phase superior to cubic KSF, especially if a Rb-free synthesis route for pure h-KSF can be found to match the stability of c-KSF.

Supporting Information

S4.1 Method

Synthesis: The synthesis procedure for h-KRSF is inspired by previously reported methods for KSF. As Mn-precursor K_2MnF_6 was used. As this is not commercially available because of the low stability, it was synthesized as described by Roesky.[27] Other chemicals used were 48% HF and 30% H_2SiF_6 solutions from Sigma Aldrich, KHF_2 from Strem Chemicals and RbF from Chempur.

For the typical synthesis of h-KRSF: 0.5% Mn^{4+}, 12 mg K_2MnF_6, 0.391 g KHF_2, and 0.523 g RbF were dissolved in 1.5 ml aqueous HF (48 vol%). In a second beaker, 1.5 ml of aqueous 30 wt% H_2SiF_6 was combined with 5 ml 48% HF. Upon combining the two solutions some turbidity was observed. To regain full dissolution of all precursors, ~20 ml aqueous HF was added until a clear solution was obtained. This solution was added to four times its volume of EtOH (~100ml). No precipitate was visible by naked eye but under illumination with a handheld violet laser (405 nm) the solution showed red luminescence. This indicates the formation of nano-sized KRSF particles. The aqueous EtOH solution was left to evaporate for two days to a week in the fume hood. The amount of precipitate gradually increases during evaporation. After all the liquid has evaporated the solid material was washed with 3% H_2O_2 aqueous solution and subsequently with EtOH, after which it was dried at 100°C for 1 to 2 hours. The hexagonal KRSF (h-KRSF) synthesized through this procedure contained 20 to 50 mole% of Rb. The K, Rb and Mn concentrations in the samples discussed below were measured with ICP-OES and values can be found in the Supporting Information Section S4.

For comparison also cubic KRSF (c-KRSF) was synthesized. Two different methods were employed. One involved immediate separation by decantation of the precipitate formed directly after the addition of H_2SiF_6 in the synthesis method described above. The second method was heating the hexagonal KRSF to 400 °C for 30 minutes.

Characterization: The powders were examined by using powder X-ray diffraction to determine phase purity. A Bruker D2 PHASER X-ray diffractometer with a Co source ($\lambda K\alpha$ = 1.7902 Å) was used at 30 kV operating voltage and 10 mA current. The temperature-dependent X-ray diffraction measurements were performed with a Malvern Panalytical Aeris Research diffractometer equipped with an Anton Paar BTS 500 heating stage and a Cu radiation source ($\lambda K\alpha$ = 1.5418 Å).

The K, Rb and Mn concentration in the phosphors were examined with inductively coupled plasma optical emission spectroscopy (ICP-OES). All measurements were performed on a Perkin Elmer Optima 8300DV spectrometer (Mn λ_{em}=257.610 nm, Rb λ_{em}=780.023 nm, and K λ_{em}=766.490 nm). Aqua regia was used to dissolve the phosphors.

Optical spectroscopy: Photoluminescence (PL) and PL excitation (PLE) spectra were recorded using an Edinburgh Instruments FLS 920 spectrofluorometer equipped with a 450 W Xe lamp as excitation source and a Hamamatsu R928 photomultiplier tube (PMT) detector. PL decay curves were recorded using a tunable optical paramagnetic oscillator (OPO) Opotek Opolette HE 355II giving ~1-5 mJ pulses in the visible or near-infrared (pulse width: 10 ns; repetition rate: 20 Hz) as excitation source and the multi channel scaling (MCS) capabilities included in the Edinburgh spectrofluorometer. For temperature dependent studies a temperature-controlled stage from Linkam Scientific (THMS600) was built in the spectrofluorometer for measurements in a –190 °C to 450 °C temperature range. Measurements down to 4 K were performed with an Oxford Instruments liquid-He cold-finger cryostat

The in situ monitoring of the cubic-to-hexagonal phase transformation was performed with a custom build optical set-up. In short, the beaker containing the reaction mixture was illuminated from above with an OBIS LX 445 nm 45 mW laser with a fiber pigtail output. An AvaSpec-HSC 1024×58 TEC-EVO CCD spectrometer equipped with an optical fiber and a 472 nm longpass filter was used to collect the red emission on the side of the beaker to measure emission spectra at regular time intervals during the formation (for up to several days).

DFT calculations: To assess the stability of the cubic vs. hexagonal phase for KSF, RSF and KRSF, first-principles

total energy calculations[28] were performed based on density functional theory (DFT)[29,30] using the Projector Augmented Wave (PAW) as implemented in Vienna ab-initio simulation package.[31,32] Frozen core approximation was combined with PAW and the valence electron configurations are $3s^2 3p^6 4s^1$ for K, $4s^2 4p^6 5s^1$ for Rb, $3s^2 3p^2$ for Si, $2s^2 2p^5$ for F. Exchange and correlation were treated with the generalized gradient approximation.[33] The wave functions were expanded in a plane-wave basis set with kinetic energy cut off of 600eV. 8×8×8 and 6×6×4 Monkhorst-pack *k*-points mesh were used for the integration in *k* space in the Brillouin zone for the cubic and hexagonal unit cell, respectively. The structural optimization were performed until each component of the interatomic force became less than 1.0×10^{-3} eV/Å.

S4.2 Luminous efficacy and increase of absorption strength

The luminous efficacy *K* (Lm/W) of c-KRSF, h-KRSF, and c-KSF are calculated and compared with each other. The spectra of these materials are shown in **Figure S4.1** and are normalized with respect to their integral. In the same figure the photopic eye responsivity curve is plotted in black, highlighting the advantage of Mn^{4+}-doped fluorides and h-KRSF:Mn^{4+} in particular. In the CCD spectrometer and PMT detectors used in our research, the number of counts as a function of wavelength is proportional to the number of photons that are registered by the detector. As energy is proportional to $1/\lambda$ the measured intensity needs to be converted into energy by dividing all measured intensities by its corresponding wavelength. With the corrected spectrum, the luminous efficacy K of the Mn-doped fluorides is calculated between 580 and 680 nm:

$$K = \frac{\int_{580\text{nm}}^{680\text{nm}} V(\lambda)\Phi_\lambda d\lambda}{\int_{580\text{nm}}^{680\text{nm}} \Phi_\lambda d\lambda} \tag{S4.1}$$

Where $V(\lambda)$ is the eye responsivity curve and Φ_λ is the radiant flux in W/nm. The numerator of the fraction describes the luminous flux and the denominator describes the radiant flux. Based on this calculation the luminous efficacy of h-KRSF is determined to be 1.2 % higher than for c-KSF and 2.9 % higher than for c-KRSF.

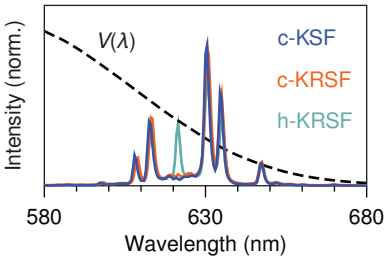

Figure S4.1 | Normalized emission spectra of c-KSF, c-KRSF and h-KRSF plotted with the eye responsivity curve *V*(λ). Because the emission redshifts a little going from KSF to KRSF, the luminous efficacy improvement is slightly larger for h-KRSF to c-KRSF than for h-KRSF to c-KSF.

In order to quantify the increase in absorption strength caused by the relaxation of the parity selection rule, we measure the room temperature emission spectrum of h-KRSF and c-KRSF. The c-KRSF used for these measurements is obtained by heating h-KRSF to 698 K for 15 min, after which it will be fully transformed into c-KRSF. In terms of measurement conditions, there are no changes between the c-KRSF and h-KRSF measurement. We assume that the QY of both the cubic and hexagonal KRSF are the same after the phase transition. Because the h-KRSF will inherently emit more photons in the wavelength region of 580 to 680 nm, we omit the area under the ZPL peak (518 to 526 nm). Dividing the resulting integral values shows an increase in the absorption strength at 450 nm of 34% going from c-KRSF to h-KRSF. See **Figure S4.2** for the emission spectra.

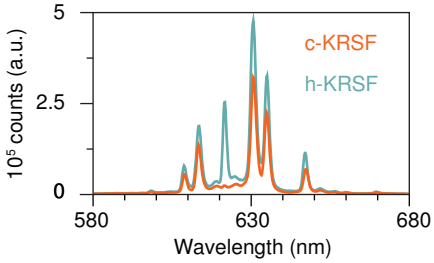

Figure S4.2 | Room temperature emission spectra of h-KRSF and c-KRSF formed after heating h-KRSF. After heating the h-KRSF to 698 K and cooling it down to RT, it has fully transformed into c-KRSF. A comparison of the integral of the two emission spectra reveals that (assuming the same QY) the absorption strength of the h-KRSF is 34% higher than that of the c-KRSF.

S4.3 Performance of h-KRSF in a wLED phsophor

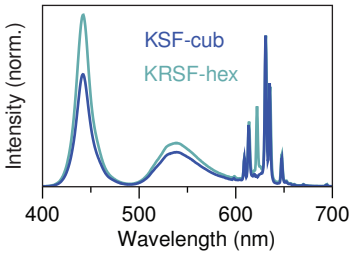

Figure S4.3 | Comparison of wLED performance of a blue LED coated with β-SiAlON:Eu^{2+} and KSF or h-KRSF. Both LED spectra are normalized with respect to the most intense v_6 emission peak around 630 nm. Note the additional ZPL peak around 620 nm for the h-KRSF sample.

S4.4 XRD patterns with KRSF:Mn^{4+} doped with different [Mn^{4+}]

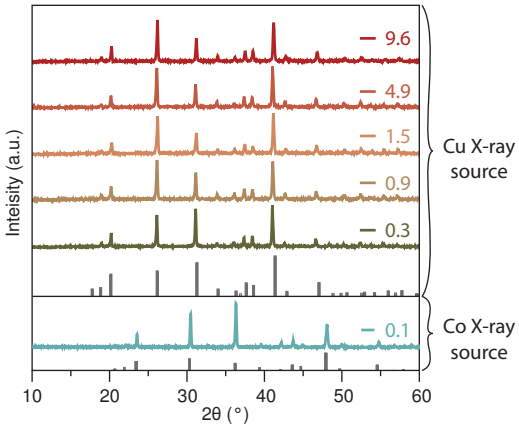

Figure S4.4 | XRD patterns for hexagonal $KRbSi_{(100-x)/100}Mn_{(x/100)}F_6$. The XRD patterns were recorded with the Malvern Panalytical Aeris Research diffractometer and a Cu source. The Mn^{4+} concentrations are determined with ICP-OES, exact concentrations of K, Rb and Mn can be found in Section S4.5.

S4.5 Determination of [K], [Rb] and [Mn] with ICP-OES and incorporation rate of [Mn^{4+}]

The concentration of Mn^{4+} in the KRSF host material is determined with respect to the combined K^+ and Rb^+ concentration. Because these three elements were all present in a single multi-element calibration solution, only one calibration curve had to be prepared. Therefore, the (K+Rb)/Mn ratio was used to determine the actual doping concentration of Mn^{4+}. The results are presented in Table S4.1. Note that when a high [Mn^{4+}] of 40% was used, the actual incorporated [Mn^{4+}] was only 6.49 %. Because of the lower incorporated Mn^{4+} concentration than for the 20% doped sample, the sample was omitted from the concentration-dependent measurement series.

Feed [Mn] (%)	[K]	[Rb]	[Mn] (%)
0.5	1.10	0.90	0.13
1	1.14	0.86	0.14
2	1.17	0.83	0.27
5	1.26	0.74	0.90
7	1.27	0.73	1.50
10	1.29	0.71	4.86
20	1.43	0.57	9.61
40	1.62	0.38	6.49

Table S4.1 | The concentration of K, Rb and Mn in hexagonal $K_{2-y}RbySi_{(100-x)/100}Mn_{(x/100)}F_6$ as determined with ICP-OES. The concentration of K, Rb and Mn are determined at λ_{em} = 766.490 nm, λ_{em} = 780.023 nm and λ_{em} = 257.610 nm respectively. Note that the concentration of K increases with increasing Mn doping concentrations because the Mn precursor is K_2MnF_6.

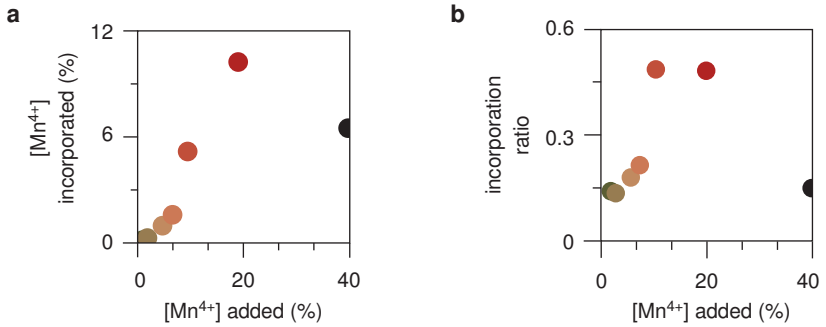

Figure S4.5 | Incorporation of Mn^{4+} in h-KRSF. (**a**) Incorporation into the host lattice as a function of feed concentration. (**b**) Incorporation ratio as a function of feed concentration. The black datapoint represents the sample with a 40% feed [Mn^{4+}], which results in an actual incorporated [Mn^{4+}] of 6.49%.

S4.6 Emission intensity as a function of [Mn^{4+}] – diluted and undiluted

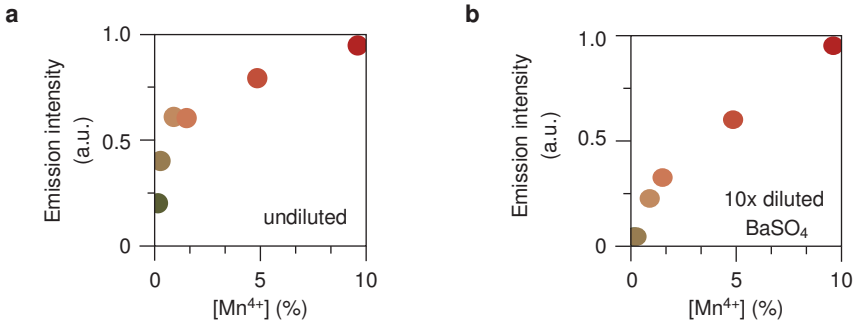

Figure S4.6 | Emission intensity as a function of [Mn^{4+}]. (**a**) Integrated emission intensity between 580–680 nm as a function of [Mn^{4+}] in h-KRSF. (**b**) Same as in panel **a**, but for samples that are diluted (weight dilution) 10× with $BaSO_4$ in order to reduce the effect of blue light extinction on the measured emission intensity. Even though in both measurements the emission intensity does not increase linearly as a function of [Mn^{4+}], the behavior becomes much more linear by diluting the samples. This observation, in addition to the constant lifetime as a function of [Mn^{4+}] (**Figure 4.4** in the main text) shows that concentration quenching does not play an important role up to 10 % Mn^{4+}.

S4.7. Temperature-dependent emission spectra

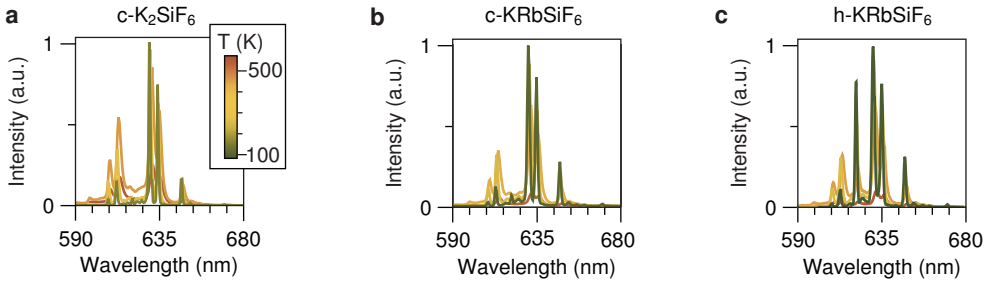

Figure S4.7.1 | Temperature-dependent emission spectra for c-KSF, c-KRSF and h-KRSF between 100 and 650 K. (**a**–**c**) A selection of emission spectra between 100 and 600 K for c-KSF, cKRSF and h-KRSF.

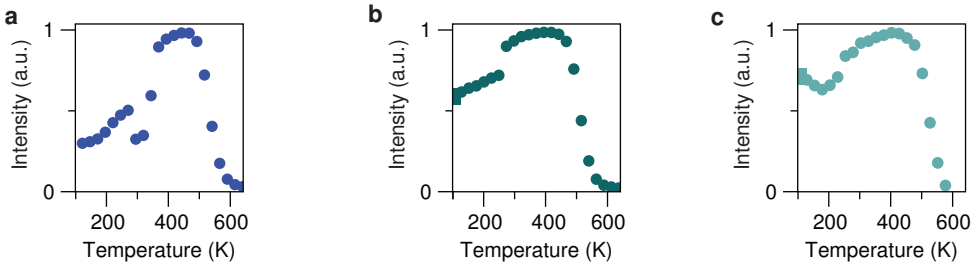

Figure S4.7.2 | Temperature-dependent integrated emission intensities for c-KSF, c-KRSF and h-KRSF between 100 and 650 K. (**a**–**c**) Integrated intensity of the spectra between 590 and 680 nm. Note that the temperature range for hexagonal h-KRSF does not extend beyond 600 K, as it is fully converted into c-KRSF at that temperature.

S4.8 Experimental set-up in situ emission

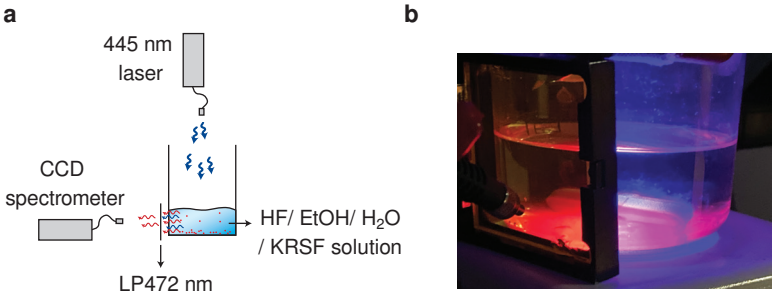

Figure S4.8 | Schematic and photographic depiction of the experimental set-up for tracking the growth of h-KRSF. (**a**) Schematic depiction of the optical set-up. (**b**) photograph of the set-up with the fiber-coupled spectrometer visible on the left hand side, after the 472nm LP filter.

S4.9 Influence of K/Rb ratio and other investigated parameters influencing the h-KRSF phase formation

We have attempted to synthesize pure h-KSF by reducing the Rb concentration. However, below 20% Rb concentration no phase pure h-KRSF was obtained using the synthesis protocol described in the methods section. With the 20% Rb sample, we obtained mixed phase h-KRSF and c-KRSF (**Figure S4.9a**). The 20% Rb sample was therefore used to check which parameters tip the reaction in favor of obtaining phase pure h-KRSF.

The first investigated parameter is the amount of EtOH used in the synthesis. Using double the amount of EtOH does result in phase pure h-KRSF for the 20% Rb sample (**Figure S4.9b**). The reaction took much longer to complete for the 20% Rb sample. The excess EtOH probably facilitates a prolonged reaction time, because of which the full conversion can take place. To further investigate the influence of reaction time, we used the same 20% Rb sample and tracked the growth in different antisolvents: MeOH, EtOH, extra EtOH, iso-PrOH and BuOH. We monitored these experiments in situ by tracking de rise of the ZPL peak intensity at 4 points in time (**Figure S4.9c**). The green line indicates the synthesis with extra EtOH and its ZPL intensity indicates a full conversion to h-KRSF. It is noteworthy that the full conversion in extra EtOH takes much longer for the 20% Rb synthesis (~120h) than for the 50% Rb sample (~8h). Indicating that an equal presence of K and Rb increases the rate of the autocatalytic process. For the other alcohols, the amount of antisolvent was 200 ml, like in the standard synthesis. Even though the evaporation rate decreased (BP_{MeOH} = 78 °C and BP_{BuOH} = 117 °C), the prolonged reaction time did not result in full conversion to h-KRSF in e.g. iso-PrOH and BuOH. Possibly the

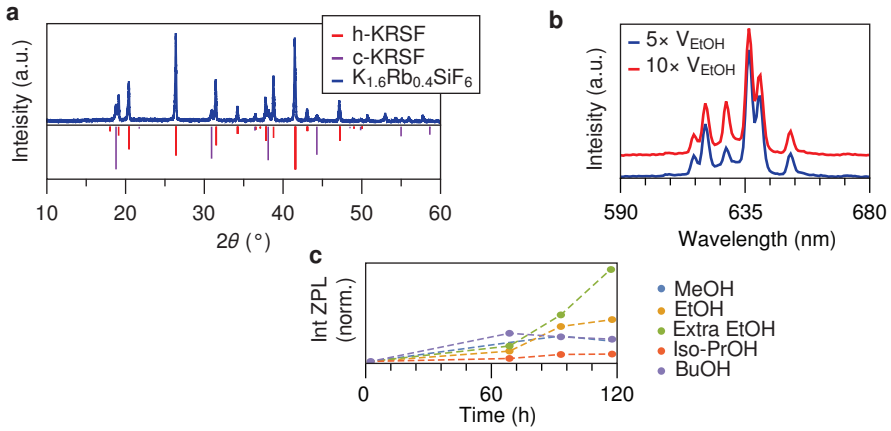

Figure S4.9 | Influence of the K/Rb ratio and the choice of antisolvent on the formation of h-KRSF. (**a**) XRD pattern of $K_{1.6}Rb_{0.4}SiF_6$ doped with 0.1% Mn^{4+}, synthesized with the protocol described in the methods section. The XRD pattern matches with both the cubic and hexagonal phase of KRSF. (**b**) Upon pouring the K/Rb = 0.2 reaction mixture into extra EtOH, the full cubic-to-hexagonal transformation takes place again (red spectrum). Using the "standard" amount of EtOH does not result in a full conversion (blue spectrum). (**c**) The conversion from the cubic to the hexagonal phase for $K_{1.6}Rb_{0.4}SiF_6$ takes place over a time period that is roughly 5 times longer than that of the K/Rb = 1 synthesis. If the regular amount (5× excess) of EtOH is used no full conversion is obtained. The effect of other alcohols was investigated as well. All tested alcohols other than EtOH performed worse in terms of the cubic-to-hexagonal phase transformation for the $K_{1.6}Rb_{0.4}SiF_6$.

fact that these liquids are not as miscible with water plays a role. It could be interesting to further investigate the role of the liquid evaporation by (partly) covering the reaction beaker.

Some other systems that show a phase transformation at a certain temperature, are induced by the presence of nucleation points.[34] A notable example is the conversion from β-Sn to α-Sn below −13 °C.[26] In this material α-Sn seeds are the nucleation points for the phase transformation. In our synthesis this nucleation point could be the hexagonal Mn^{4+} precursor K_2MnF_6. However, upon doing a h-KRSF synthesis without adding hexagonal K_2MnF_6, the pure h-KRSF phase still forms.

S4.10 Temperature-dependent XRD measurements

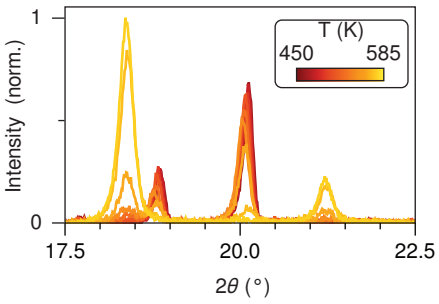

Figure S4.10 | Full range T-dependent XRD pattern. The peak intensity values shown in **Figure 4.8b** in the main text are determined based on both the cubic and the hexagonal peaks in this pattern.

S4.11 Ab-initio DFT calculations on phase stability in hexagonal and cubic KSF, KRSF and RSF

DFT calculations were performed to calculate the formation energies of different crystal structures. For h-KRSF there are 4 positions for K/Rb within the unit cell, 2 smaller M1 (2b) sites and 2 larger M2 (2a) sites. The fractional coordinates of the sites along with their symmetry are shown in **Table S4.2a**. Of these positions two are

occupied by K and two by Rb in our calculations. The number of possible placements is $\binom{4}{2} = 6$, which can be reduced to 4 because of the symmetry. For h-KRSF, 4 calculations are performed with different occupations of the 4 sites. The lowest energy configuration is obtained when K occupies the smaller M1 sites and Rb the larger M2 sites. The energy of this configuration is chosen as the energy of h-KRSF (**Table S4.2b**).

The DFT calculations indicate an ordering in the h-KRSF crystal where the small M1 site is occupied by K and the larger M2 site by Rb. In the cubic phase, there is only one M1 site. It could be that the placement of the Rb and the K on the large and small site respectively is the driving force of the hexagonal phase transformation. This thermodynamically more stable phase is never obtained under alternative (faster) synthesis conditions because of the kinetically favored random placements of cations.

Our hypothesis is that as the sample heats up (above 200°C), this ordering is lost and the h-KRSF reverts to the cubic phase. As mentioned in the main text, we have performed a few control measurements to check if the hexagonal phase could be obtained from the cubic phase after it had formed:

- Cool c-KRSF to 253 K for 2 months
- Heat c-KRSF to 373 K for 3 months
- Heat c-KRSF to 573 K and cool down to 435 K over the course of 90h

Table S4.2 | Atomic positions of M^+ sites in h-KRSF and total energies at different K^+ and Rb^+ placements. (**a**) Fractional coordinates of the different sites within the primitive cell for h-KRSF. Note that the Wyckoff symbols are different, indicating a different coordinating polyhedron. (**b**) Total energy of h-KRSF for different K an Rb configurations. The energy (bold) for the K, K, Rb, Rb placement is lowest and that there are two energetically equivalent placements possible (bottom rows).

a

site	*a*1	*a*2	*a*3	wyck. symb.
1	2/3	1/3	0.0875	2*b*
2	1/3	2/3	0.5875	2*b*
3	0	0	0.8122	2*a*
4	0	0	0.3122	2*a*

b

Configuration on site 1, 2, 3, 4	E_{tot} (eV)
Rb, Rb, K, K	–92.8130
K, K, Rb, Rb	–93.0058
Rb, K, Rb, K (K, Rb, K, Rb)	–92.9090
K, Rb, Rb, K (Rb, K, K, Rb)	–92.9382

All these experiments failed in obtaining h-KRSF, unfortunately neither confirming nor disproving the hypothesis that the ordering of the K and Rb ions is indeed responsible for the formation of the hexagonal phase. Single crystal XRD measurements on h-KRSF could provide valuable further insights on the ordering of K and Rb ions in the lattice.

Finally, we compared the formation energies of cubic KSF, KRSF and RSF with their hexagonal and trigonal counterparts. The results are shown in **Figure S4.11**. The primitive unit cell is used for the calculation of cubic phase. The primitive vectors are (0, *a*/2, *a*/2), (*a*/2, 0, *a*/2), (*a*/2, *a*/2, 0). In the case of the cubic cell, there are 2 equivalent positions for K, where one is for K and the other for Rb. So, for c-KRSF only one structure is calculated. The calculated formation energies of each cubic compound are subtracted by the formation energies of the hexagonal compound. The resulting energy difference is in all cases negative (favorable to form cubic MSF), but smallest for h-KRSF.

	$Fm\bar{3}m$	$P6_3mc$	$P\bar{3}m1$	E ($Fm\bar{3}m$ – $P6_3mc$)
KSF	–46.643	–46.600	–46.522	–0.043
KRSF	–46.511	–46.502	-	–0.009
RSF	–46.443	–46.372	–46.278	–0.071

Values in eV.

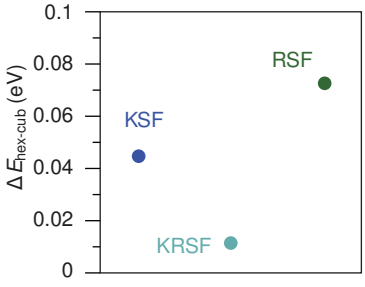

Figure S4.11 | Results for DFT calculations for the formation energy per unit cell of cubic, hexagonal and trigonal KSF, KRSF and RSF. Note that the total energy of the h-KRSF is halved with respect to the values in Table S4.2 because there are 2 unit cells are used in the calculations.

References

[1] A. G. Paulusz, J. *Electrochem. Soc.* **1973**, 120, 942.
[2] E. Radkov, L. Grigorov, A. Setlur, A. Srivastava, US Pat. 7,497,973 B2, **2010**.
[3] S. Yan, ECS J. *Solid State Sci. Technol.* **2020**, 9, 106004.
[4] Y. K. Xu, S. Adachi, *J. Appl. Phys.* **2009**, 105.
[5] S. Adachi, *J. Lumin.* **2018**, 197, 119.
[6] L. Kolditz, H. Preiss, *J. Inorg. Gen. Chem.* **1963**, 325, 245.
[7] B. Gossner, *Zeitschrift für Krist. - Cryst. Mater.* **1904**, 38, 110.
[8] C. M. Gramaccioli, I. Campostrini, *Can. Mineral.* **2007**, 45, 1275.
[9] M. E. Denaeyer, D. Ledent, *Bull. Soc. Fr. Minéral, Cristallogr.* **1952**, 75, 231.
[10] A. Lazarowska, S. Mahlik, M. Grinberg, C. C. Lin, R. S. Liu, *J. Chem. Phys.* **2015**, 143, 134704.
[11] L. Lv, X. Jiang, S. Huang, X. Chen, Y. Pan, *J. Mater. Chem. C* **2014**, 2, 3879.
[12] V. Weiler, P. J. Schmidt, W. Schnick, M. A. Seibald, US9422471B2, **2014**.
[13] J. H. Loehlin, *Acta Crystallogr. Sect. C* **1984**, 40, 570.
[14] J. Rienmüller, J. Bandemehr, F. Kraus, *Zeitschrift fur Naturforsch. - Sect. B J. Chem. Sci.* **2021**, 76, 559.
[15] R. D. Shannon, *Acta Crystallogr. Sect. A* **1976**, 32, 751.
[16] B. H. W. S. de Jong, H. T. J. Supèr, R. M. Frijhoff, A. L. Spek, G. Nachtegaal, *Zeitschrift fur Krist.* **2000**, 215, 397.
[17] H. D. Nguyen, C. C. Lin, R. S. Liu, *Angew. Chemie - Int. Ed.* **2015**, 54, 10862.
[18] Y. Y. Zhou, E. H. Song, T. T. Deng, Q. Y. Zhang, *ACS Appl. Mater. Interfaces* **2018**, 10, 880.
[19] T. Senden, R. J. A. Van DIjk-Moes, A. Meijerink, *Light Sci. Appl.* **2018**, 7, 1.
[20] H. F. Sijbom, R. Verstraete, J. J. Joos, D. Poelman, P. F. Smet, *Opt. Mater. Express* **2017**, 7, 3332.
[21] H. Chu, X. Li, G. Chen, W. Zhou, Y. Zhang, Z. Jin, J. Xu, Y. Li, *Cryst. Growth Des.* **2005**, 5, 1801.
[22] C. Stoica, P. Verwer, H. Meekes, P. J. C. M. Van Hoof, F. M. Kaspersen, E. Vlieg, *Cryst. Growth Des.* **2004**, 4, 765.
[23] D. Croker, B. K. Hodnett, *Cryst. Growth Des.* **2010**,10, 6, 2808–2816.
[24] P. T. Prins, J. C. van der Bok, T. P. van Swieten, S. O. M. Hinterding, A. J. Smith, A. V. Petukhov, A. Meijerink, F. T. Rabouw, *Angew. Chemie - Int. Ed.* **2023**, 62.
[25] S. Das, M. J. Hendry, J. Essilfie-Dughan, *Environ. Sci. Technol.* **2011**, 45, 268.
[26] B. Cornelius, S. Treivish, Y. Rosenthal, M. Pecht, *Microelectron. Reliab.* **2017**, 79, 175.
[27] H. W. Roesky, *Efficient Preparations of Fluorine Compounds*, Wiley Online Library, **2012**.
[28] M. Bockstedte, A. Kley, J. Neugebauer, M. Scheffler, *Comput. Phys. Commun.* **1997**, 107, 187.
[29] R. Nityananda, P. Hohenberg, W. Kohn, *Resonance* **2017**, 22, 809.
[30] W. Kohn, L. J. Sham, *Phys. Rev.* **1965**, 140, A1133.
[31] D. Joubert, *Phys. Rev. B - Condens. Matter Mater. Phys.* **1999**, 59, 1758.
[32] G. Kresse, J. Furthmüller, *Phys. Rev. B - Condens. Matter Mater. Phys.* **1996**, 54, 11169.
[33] J. P. Perdew, K. Burke, M. Ernzerhof, *Phys. Rev. Lett.* **1996**, 77, 3865.
[34] P. T. Cardew, R. J. Davey, *Proc. R. Soc. London. A. Math. Phys. Sci.* **1985**, 398, 415.

Chapter 5

Shedding light on host-to-Yb^{3+} energy transfer in $Cs_2AgBiBr_6$:Yb^{3+} (nano)crystals

Based on:

J.W. de Wit, L.L. Sonneveld, A. Meijerink, Shedding light on host-to-Yb^{3+} energy transfer in $Cs_2AgBiBr_6$:Yb^{3+} (nano)crystals, *Chemistry of Materials* 36 (6), 2857–2866, **2024**

Abstract

The optical properties of $Cs_2AgBiBr_6$ double perovskite nanocrystals have attracted considerable attention as a lead-free alternative to lead halide perovskites. A promising strategy to create additional flexibility in emission color is doping lanthanide ions into $Cs_2AgBiBr_6$. Incorporating Yb^{3+} in the lattice has been shown to give rise to near-infrared (NIR) emission but the energy-transfer mechanism remained unclear. Here we report on the luminescence and sensitization mechanism of Yb^{3+} in $Cs_2AgBiBr_6$ nano- and microcrystals. We observe that the incorporation of Yb^{3+} in the host lattice does not strongly affect the broadband red emission of the $Cs_2AgBiBr_6$ host but does give rise to an additional and characteristic ~1000 nm NIR line emission from Yb^{3+}. Temperature-dependent and time-resolved photoluminescence studies on undoped and Yb-doped $Cs_2AgBiBr_6$ reveal that the energy transfer does not take place through the red emissive state of the $Cs_2AgBiBr_6$ host. Instead, there is a competition between relaxation to the red-emitting state and trapping of photoexcited charge carriers on Yb^{3+}. Trapping on Yb^{3+} subsequently results in a charge transfer state that relaxes to the $^2F_{5/2}$ excited state of Yb^{3+}, followed by NIR narrow-line f–f emission to the $^2F_{7/2}$ ground state.

Introduction

Lanthanide-doped nanocrystals (NCs) find diverse applications because of their efficient and narrow-line emission across the UV, visible, and (N)IR spectral ranges. Due to the shielding provided by the 5s and 5p orbitals, the energy levels of 4f–4f transitions remain unaffected by the local coordination and give rise to characteristic luminescence properties. Narrow line emission is of particular interest for example for color conversion phosphors in blue-LED-based displays where a high color purity helps to expand the color gamut. However, a disadvantage of lanthanides is that intra-configurational f–f transitions are forbidden according to the parity selection rule and therefore absorb light weakly. This creates a challenge in many phosphor applications that require strong broadband absorption. To address this issue, a stronger absorbing species is typically introduced to transfer its energy non-radiatively to the emitting lanthanide ion, which is known as sensitization. Traditionally, strongly absorbing luminescent ions such as Ce^{3+} or Eu^{2+} have been co-doped as sensitizers of lanthanide ions showing the characteristic f–f line emission of the desired color.

A promising alternative approach is to use semiconductor nanocrystals (NCs) as a sensitizer for lanthanide luminescence and combine their strong, broadband, and size-tunable absorption with the desired lanthanide line emission. In recent years lanthanides have been doped in several semiconductor NC systems, among others CdSe[1] and InP/YF_3 core/shell[2] and $PbIn_2S_4$ NCs.[3] However, it is difficult to incorporate large, trivalent lanthanide ions in lattices that have only cation sites with coordination number (CN) of 4, which is the case for the traditional II/VI and III/V colloidal quantum dots having wurtzite- or zincblende-type structures, as lanthanides require coordination numbers of 6 or higher. The doping of Yb^{3+} in the perovskite $CsPbCl_3$ NCs on Pb^{2+} sites with CN = 6 has been successful and resulted in spectacular near-infrared (NIR) quantum yields (QYs) of almost 200% caused by a quantum cutting process.[4,5] Research efforts directed at incorporation of other lanthanides in $CsPbCl_3$ have emerged and demonstrated incorporation of both Er^{3+} and Yb^{3+}.[6] Claims for the incorporation of many other lanthanides (including Ce^{3+}, Sm^{3+}, Eu^{3+}, Tb^{3+}, Dy^{3+}) have also been made but have so far been difficult to reproduce.[7] More recently, elpasolite (or double perovskite) NCs have emerged as a promising host material. In this host two divalent ions of the perovskite are replaced by a monovalent and trivalent ion arranged in an ordered manner. This offers the possibility to replace the large

six-coordinated trivalent ion by a trivalent lanthanide and allows for doping without charge compensation and offers a new family of hosts for semiconductor-to-Ln^{3+} energy transfer.[8] The cubic elpasolite structure is of the $A_2^+M^+M^{3+}X_6^-$ form, with $Cs_2AgBiBr_6$ as a well-studied workhorse material.[9] Similar to perovskite NCs, the optical properties can be adjusted by changing their chemical composition, while also being free of toxic lead.[10] The class of materials is not novel. In the 1970s, insulator elpasolite microcrystals and single crystals became notable as hosts for luminescent lanthanide ions because of their highly symmetrical trivalent cation site. The Richardson's group, among others, utilized the nearly perfect octahedral symmetry of Cs_2NaYCl_6:Ln^{3+}, a wide-bandgap insulator material, for gaining theoretical understanding on intra-configurational lanthanide transitions.[11,12] More recently, doping various lanthanide ions into different elpasolite NCs has opened up many new prospects for sensitizing lanthanide emission with the absorption of semiconductor NCs.[13]

There is ongoing debate about the energy-transfer process from semiconductor host NCs to lanthanide dopants. In perovskite $CsPbCl_3$ NCs doped with Yb^{3+} QYs close to 200% have been achieved through quantum cutting.[4] Here the mechanism involves the formation of a trapped-exciton state at the lattice distortion where the two Yb^{3+} ions replace three Pb^{2+} ions. Cooperative energy transfer from the exciton state excites both Yb^{3+} ions and explains the almost 200% quantum yield.[14,15] In the case of $Cs_2(Ag,Na)(In,Bi)(Cl,Br)_6$ micro- and nanocrystals the results are less conclusive. There is evidence that Bi co-doping is required to enable energy transfer from the $Cs_2Ag_{1-x}Na_xInCl_6$ elpasolite host to various lanthanides.[16,17] Photoluminescence excitation measurements of NIR-emitting Er^{3+} in these crystals confirm that the lanthanide luminescence is sensitized via Bi^{3+} $^1S_0 \rightarrow {}^1P_{0,\,1}$ transitions which involve localized transitions in this host.[18] Excitation measurements on $Cs_2AgBiBr_6$ NCs doped with Yb^{3+} and Mn^{2+} show that both host and lanthanide emission are sensitized by the excitonic absorption band resulting from delocalized conduction band (CB) states (which still have considerable Bi^{3+} 6p character[19]).[20] For Yb^{3+}-doped double perovskites a mechanism similar to that for Yb-doped perovskites has been proposed where energy transfer occurs from the red-emitting self-trapped exciton (STE) state to (a single) Yb^{3+} ion.[21] Alternatively, direct energy transfer from the host to Yb^{3+} has been depicted.[22] In recent research on $Cs_2AgBiBr_6$:Yb^{3+} very high NIR QYs of more than 80% were reported for thin films fabricated with physical vapor deposition.[22,23] For these Yb-doped thin films, the sensitization mechanism is not discussed in detail. In an earlier study on thin film $Cs_2AgBiBr_6$:Yb^{3+} based on room temperature spectroscopy and DFT calculations, the proposed energy transfer mechanism involves trapping of a CB electron by Yb^{3+} followed by releasing the electron to the CB, leaving Yb^{3+} behind in the excited state.[24] To gain deeper insight in the host-to-Yb^{3+} energy transfer mechanism here we report temperature-dependent and time-resolved spectroscopy studies on Yb^{3+}-doped $Cs_2AgBiBr_6$. Previous variable-temperature studies on undoped $Cs_2AgBiBr_6$ have shown that the broad red host emission experiences strong thermal quenching at room temperature. Hence, temperature-dependent emission and time-resolved emission measurements could aid in differentiating between different energy transfer mechanisms.

We synthesized both undoped and Yb^{3+}-doped $Cs_2AgBiBr_6$ NCs and microcrystals (MCs), and conduct temperature-dependent emission and time-resolved emission spectroscopy measurements down to 4 K. The Yb incorporation is monitored with luminescence spectroscopy and ICP-OES measurements. Interestingly, while the red host emission shows its previously reported thermal quenching, the Yb-emission intensity increases with increasing temperature. This shows that direct energy transfer from the red-emitting host state to Yb^{3+} is not the operative transfer mechanism.

Based on our findings we propose that a photoexcited electron–hole pair can either relax to the self-trapped state responsible for the red host emission or, and in competition with, the electron can localize on Yb^{3+}, thereby reducing it to Yb^{2+}. Subsequent capturing of the photogenerated hole by Yb^{2+} results in the formation of Yb^{3+} in the excited $^2F_{5/2}$ state through a charge transfer state. The interesting increase of the Yb^{3+} emission intensity with temperature is a result of the increased hole mobility. At elevated temperatures, the hole mobility increases the probability for relaxation via electron and hole capture by Yb^{2+},[25] resulting in higher Yb^{3+} emission intensity.

Results and Discussion

First we present and discuss the general structural and optical characteristics of undoped $Cs_2AgBiBr_6$ and $Cs_2AgBiBr_6$:Yb^{3+} NCs that were synthesized using a previously reported hot-injection method.[26] The XRD patterns (**Figure 5.1a**) demonstrate that both the doped and undoped NCs adopt a cubic structure with the $Fm\bar{3}m$ space group, with the (200) and (400) lattice plane reflections being the most prominent. Reflections from other lattice planes are weaker than expected based on the reference pattern, likely due to the preferential ordering of the NCs on a low-background Si wafer. The weaker reflections are also present (Supporting Information Section S5.2) and show that the $Cs_2AgBiBr_6$ NCs with the elpasolite structure have formed. TEM images show that the doped and undoped NCs are monodisperse in size and cubic in shape (**Figure 5.1b,c**). These properties, and also the average NC edge length of 9.0 ± 0.4 nm are in good agreement with those of NCs in earlier reports.[20,26] ICP-OES measurements were conducted to verify the incorporation of Yb^{3+} into the host lattice, which resulted in a 0.23% Yb^{3+} doping concentration relative to Bi^{3+} ($[Yb^{3+}]=[Yb^{3+}]/([Yb^{3+}]+[Bi^{3+}])$). The fraction of Yb^{3+} incorporated is much lower than the 5% Yb-to-Bi feeding ratio. The challenge in incorporating lanthanides is consistent with prior studies. Incorporation is especially difficult in NCs, as impurities can be easier removed or be prevented from incorporation by staying in solution. The harder Lewis acid nature of Yb^{3+} makes that it binds stronger to oleic acid than the softer Lewis acid Bi^{3+}.[27] Because of the higher energy needed to dissociate Yb^{3+} from the ligands it is not unexpected that the incorporated fraction of Yb^{3+} into the $Cs_2AgBiBr_6$ NCs is well below the concentration in the reaction mixture.

Figure 5.2a shows the room-temperature absorption, emission and excitation spectra of the undoped $Cs_2AgBiBr_6$ NCs. The absorption spectrum reveals a peak at 430 nm that has a gradually increasing and weak absorption onset starting around 520 nm. The strong excitonic peak and

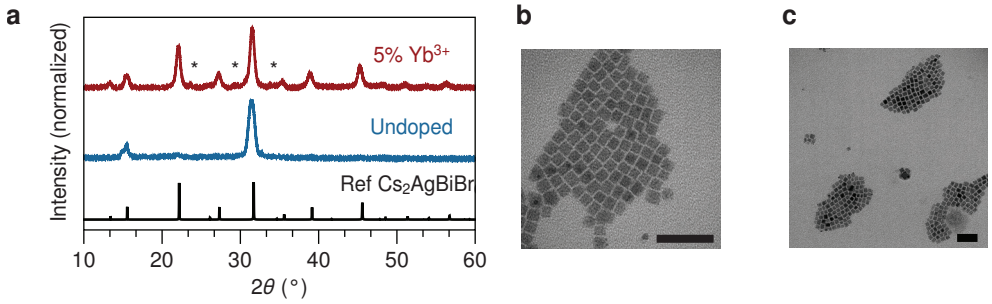

Figure 5.1 | XRD patterns and TEM photographs of the undoped and Yb-doped $Cs_2AgBiBr_6$ NCs. (**a**) XRD patterns show that the doped and undoped NCs crystallize in the cubic phase. The asterisks indicate a small impurity phase, that could be attributed to a ternary Cs-Bi-Br impurity.[26] The reference pattern has ICSD collection code 239874. TEM images of (**b**) $Cs_2AgBiBr_6$ NCs and (c) $Cs_2AgBiBr_6$: 0.23% Yb^{3+} NCs. The scale bar is 50 nm in both images.

weak absorption onset are typically associated with a direct- and indirect-bandgap transition, respectively.[28] See Supporting Information Section S2 for a Tauc analysis of the absorption spectrum. At shorter wavelengths the absorption drops beyond the first excitonic transition and then significantly increases at wavelengths shorter than 380 nm. Upon excitation in the exciton peak at 420 nm weak, broadband emission centered around 690 nm is observed, in agreement with earlier work.[29] The excitation spectrum of the red emission (λ_{em} = 660 nm) recorded from to 300 to 600 nm shows that the excitation and absorption spectra overlap until 350 nm, in good agreement with an indirect and direct excitonic transition. At shorter wavelengths, the excitation intensity is lower in comparison to the absorption spectrum. Such differences between absorbance and excitation intensity is sometimes attributed to physical properties of luminescent materials, which has also been reported for $Cs_2AgBiBr_6$ and has for example been explained by the neutral character of the exciton state which would less effectively populate the emissive state.[22,24,28] Instead we attribute this to artefacts related to absorption saturation and/or competing absorption in the ultraviolet. Because the emission of $Cs_2AgBiBr_6$ NCs is weak at room temperature, a high NC concentration is often used to achieve a good signal-to-noise ratio. For high concentrations strong absorption effects can cause distortions of the excitation spectra by complete absorption of the excitation light in a thin layer of sample. Deeper penetration of the excitation light at wavelengths with less absorption can thus lead to an overall stronger detected emission signal. It is not unusual to even observe a dip at the peak wavelength for strongest absorption due to this effect as stronger absorption leads to less detected emission. To demonstrate the effect of concentration on experimentally observed excitation spectra, we conducted excitation measurements on a dilution series (for details see Supporting Information Section S3). The series reveals a redshift of the absorption maximum for higher concentration and the presence of an excitation dip around the absorption maximum. However, for the strongest dilution the excitation spectrum closely resembles the absorption spectrum showing that the change in shape of the excitation spectrum is not caused by physical properties (such as a variation in the efficiency of trapped exciton generation depending on the excitation energy) of the luminescent nanocrystals and that the true excitation spectrum closely follows the absorption spectrum, as expected and in line with earlier observations, including those for the analogous system $CsPbCl_3$:Yb^{3+}.[30]

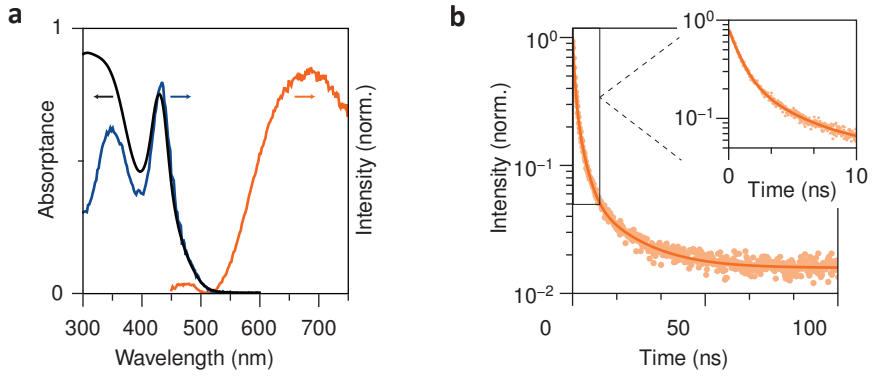

Figure 5.2 | Optical properties of undoped $Cs_2AgBiBr_6$ NCs at room temperature. (**a**) Absorption (black line), emission (orange) and excitation (blue) spectra of the undoped $Cs_2AgBiBr_6$ NCs, with λ_{exc} = 420 nm and λ_{em} = 650 nm (**b**) Photoluminescence decay curve of the host emission, excited at 374 nm and recorded at 660 nm. The inset shows the fast initial decay component. The data is fitted with an exponential function containing three exponents, from which the weighted average lifetime is calculated with $\tau_{ave} = \Sigma_i A_i \tau_i / \Sigma_i A_i$.

Continuing our analysis, luminescence decay curves of the host emission were recorded at room temperature and show a fast ns decay that is best fitted with three exponents. (**Figure 5.2b**). Based on this fit, the calculated average decay time ($\tau_{ave} = \Sigma_i A_i \tau_i / \Sigma_i A_i$) is 2 ns. The multi-exponential decay, in addition to the presence of a fast sub-ns component (inset **Figure 5.2b**) is explained by a combination of thermal quenching and quenching caused by surface defects in $Cs_2AgBiBr_6$ NCs.[26] The radiative decay time for the STE emission is expected to be in the µs range (and is indeed observed at low temperatures[31]) but a combination of thermal quenching and surface quenching causes the luminescence decay curves to be non-exponential with ns components. The origin of the strongly redshifted photoluminescence in $Cs_2AgBiBr_6$ NCs is often ascribed to the formation of self-trapped excitons[32,33] or color centers[28] after photoexcitation. Upon direct bandgap photoexcitation of an electron from the valence band (VB) to conduction band (CB), within ps a trapped exciton state is formed giving rise to broadband red emission.[34] At very short times weak direct-bandgap emission in the blue has also been observed that decays on a ps time scale giving evidence for the fast relaxation from the direct-bandgap exciton state.[32,33] One conceivable scenario for the rapid capture of charge carriers involves the localization of a VB hole on a $[AgBr_6]^{5-}$ cluster, leading to lattice relaxation.[34] The propensity of Ag^+ to act as hole acceptors has been observed in other semiconductor systems like CdSe doped with Ag^+.[35] A self-trapped exciton forms if the trapped hole binds a photoexcited electron. Radiative recombination from this self-trapped exciton state to the ground state is characterized by a large lattice relaxation and offset between the ground- and excited-state parabola. As a result, the emission spectrum consists of a broad band with a large Stokes shift. Because of the local differences in coordination of the self-trapped state, decay curves are typically multi-exponential.[25] As a result of the large Stokes shift, semiconductor elpasolites often display thermal quenching around or below room temperature due to thermally assisted crossover from the excited-state to ground-state parabola.[31,36]

Next, we focus on the optical properties of the Yb-doped $Cs_2AgBiBr_6$ NCs and compare these with the undoped NCs. There is no variation in the absorption and host emission spectra with respect to the undoped NCs (**Figure 5.3a**, Supporting Information Section S4). Due to the low efficiency of the host emission at room temperature, it is difficult to estimate the effect of Yb^{3+}

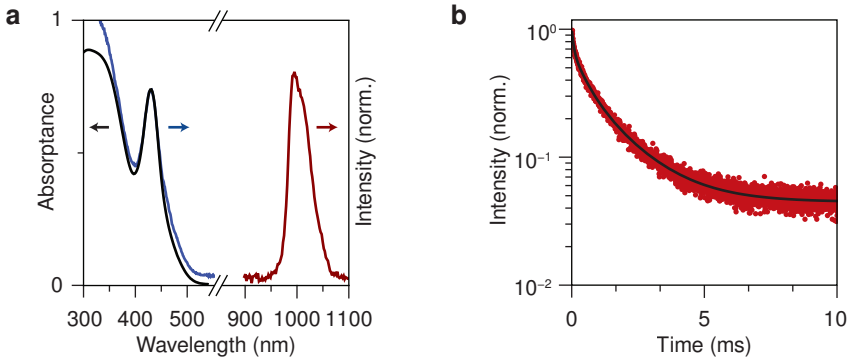

Figure 5.3 | Optical properties of $Cs_2AgBiBr_6$:0.23% Yb^{3+} NCs at room temperature. (**a**) Absorption and near-IR emission and excitation spectra of the $Cs_2AgBiBr_6$:Yb^{3+} NCs, with λ_{exc} = 350 nm and λ_{em} = 1000 nm. The host emission is still observable but not shown in the graph. (**b**) Photoluminescence decay curve of the Yb^{3+} $^2F_{5/2} \rightarrow {}^2F_{7/2}$ emission (λ_{exc} =374 nm, λ_{em} = 1000 nm), fitted with two exponents (black).

incorporation on the intensity of the host PL. In the near-IR emission spectrum, a sharp peak is observed around 1000 nm for the Yb^{3+}-doped sample, which we assign to the $^2F_{5/2} \rightarrow {}^2F_{7/2}$ transition of Yb^{3+}. Upon recording an excitation spectrum of the NIR emission band, the spectrum very closely matches the host absorption spectrum and this proves that the Yb-emission is excited through the $Cs_2AgBiBr_6$ host and that energy transfer from the host to Yb^{3+} occurs. Time-resolved measurements of the Yb emission show that it has a multi-exponential decay that can be fitted with a bi-exponential decay function (**Figure 5.3b**). The weighted average decay time is 1.5 ms. A ms lifetime is typical for parity forbidden f–f transitions of lanthanides. The lifetime is however notably faster than the radiative lifetime of Yb^{3+} in bulk elpasolites (6.3 ms in Cs_2NaYF_6: 10% Yb^{3+} and 2.7 ms in $Cs_2AgInCl_6$ microcrystals[37,38]), but comparable to previous work on Yb-doped $Cs_2AgBiBr_6$ NCs.[20] We explain the multi-exponential and relatively fast decay by quenching of emission for near-surface Yb^{3+} ions. An additional washing step with acetonitrile was performed to verify whether there is surface absorbed Yb^{3+} that contributes to the faster decay but extra washing did not lead to a significant decrease in Yb emission. The Yb^{3+} luminescence is therefore assigned to Yb^{3+} incorporated in the $Cs_2AgBiBr_6$ NCs. High-energy (~3000 cm^{-1}) C-H vibrations of the oleic acid capping and toluene solvent molecules can quench the Yb^{3+} emission for Yb^{3+} ions close to the surface by multi-phonon relaxation, as 3 or 4 vibrations can bridge the energy gap between the $^2F_{5/2}$ excited state and $^2F_{7/2}$ ground state of Yb^{3+}. The distribution of Yb^{3+} through the NCs gives rise to Yb^{3+} ions with longer lifetimes for ions in the center and shorter lifetimes for Yb^{3+} near the surface and thus explains the non-exponential decay.

Before comparing the temperature-dependent optical properties of the doped and undoped $Cs_2AgBiBr_6$ NCs, we first discuss the temperature-dependent optical properties of the undoped $Cs_2AgBiBr_6$ NCs. **Figure 5.4a** shows the host emission at room temperature (RT) and at 4 K. As the temperature increases from 4 K to RT the emission peak redshifts by ~50 meV, which is typically observed for semiconductor materials and described empirically by the Varshni equation.[39] The redshift is accompanied by pronounced peak broadening, exhibiting a full width at half maximum (fwhm) of 200 meV at 4 K and 600 meV at RT. With increasing temperature, we observe a large decrease in the emission intensity caused by thermal quenching. A similar but smaller peak broadening (fwhm of 125 meV at 4 K and 175 meV at RT) is observed for the absorption spectrum,

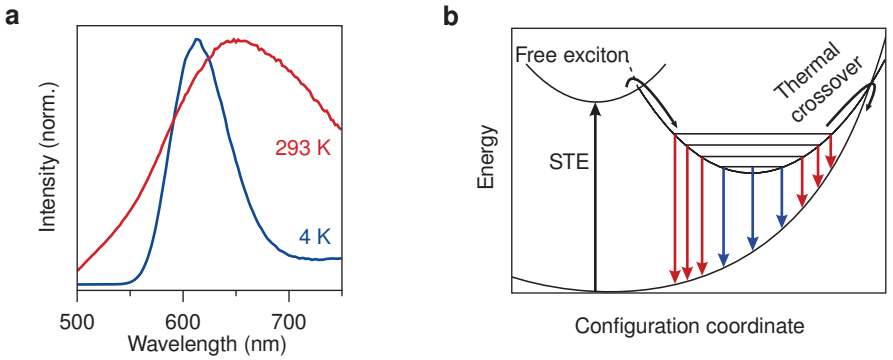

Figure 5.4 | STE emission at room temperature and cryogenic temperature. (**a**) Emission spectra of $Cs_2AgBiBr_6$ NCs at 4 K and room temperature excited with 374 nm light. (**b**) Configuration coordinate diagram showing thermal crossover quenching of the STE state and emission from the different vibrational levels. The colors of the emission arrows correspond to the spectra in panel **a**.

indicating the much stronger coupling to the lattice of the self-trapped exciton state[34]. At 4 K, only the lowest vibrational levels of the STE parabola are occupied, which has two effects (**Figure 5.4b**): First, crossover to the ground-state parabola does not occur as the wavefunctions of the lowest vibrational levels of the excited state have a close to zero overlap with high vibrational levels of the ground state. Secondly, emission only occurs from the lowest vibrational states of the excited state, resulting in a relatively narrow emission peak, indicated by the blue arrows. The absence of a zero-phonon line and vibronic fine structure at 4 K can be attributed to and is typical for optical transitions with very large electron–phonon coupling.[40,41] At higher temperatures, higher vibrational states are populated and emission occurs from these levels, leading to a broadening of the emission peak and ultimately, thermally activated quenching. It is noteworthy that at 4 K, we do not observe free- or bound-exciton recombination close to the absorption band, which indicates that the energy barrier between the free exciton state and the STE state is very small. This finding is in line with the recently observed barrier-free and fast (< ps) charge-carrier localization in vapor-deposited thin-film $Cs_2AgBiBr_6$.[34]

As discussed above, several mechanisms have been proposed for the energy transfer from the $Cs_2AgBiBr_6$ host to Yb^{3+} dopants including transfer from the direct bandgap exciton state or STE state or electron trapping by Yb^{3+}(forming Yb^{2+}) followed by release of the electron to the conduction band leaving Yb^{3+} in the excited $^2F_{5/2}$ state.[24] In the discussion of our results we focus on two plausible mechanisms for the energy transfer process: (1) After photoexcitation, the CB electron is trapped by Yb^{3+} ion reducing it to Yb^{2+} ion. Alternatively, the electron may be trapped near the Yb^{3+} site due to a local lattice deformation. Subsequent charge recombination with a hole results in Yb^{3+} remaining in the excited state.[20,33] Note that in the mechanism suggested in ref. [24] it is unclear how release of the Yb^{2+} trapped electron back to the CB would leave Yb^{3+} in the excited state. (2) Photoexcitation creates an exciton that rapidly relaxes to the red-emitting STE state.[42] Subsequently, the localized STE state transfers its energy to a nearby Yb^{3+} ion. Both possibilities have been suggested in the literature for lanthanide-doped elpasolite (nano)crystals. A third mechanism where transfer occurs from the unrelaxed direct-exciton state seems unlikely as ps-relaxation occurs and there is no resonant excited state of Yb^{3+} to which energy transfer can occur given the fact that the $^2F_{5/2}$ state is the only intra $4f^{13}$ excited state of Yb^{3+}.

To distinguish between the different mechanisms, temperature-dependent luminescence and time-resolved spectroscopy experiments were conducted. **Figure 5.5** presents the temperature-dependent emission spectra of the Yb^{3+}-doped $Cs_2AgBiBr_6$ NCs. The temperature-dependence of the host emission in **Figure 5.5a** shows the same trend with increasing temperature as the undoped sample (**Figure 5.4a**, Supporting Information Section S5) and is almost completely quenched at room temperature. Interestingly, the Yb^{3+} emission intensity – shown in **Figure 5.5b** – increases when the temperature increases. Also, because of line narrowing at low temperature, multiple sharp emission lines due to the crystal field splitting of the $^2F_{5/2}$ and $^2F_{7/2}$ levels becomes visible in the low-temperature emission spectra around 1000 nm. To accurately determine the intensity of the Yb emission at low temperatures, the background of the host emission band has to be subtracted as the host emission band becomes more intense with decreasing temperatures and the tail overlaps with the Yb^{3+} line emission. The procedure for background correction is described in detail in Supporting Information Section S6. The temperature dependence of the integrated intensities of both host and Yb emission are summarized in **Figure 5.5c**, where the normalized and background-corrected emission integrals of both the host and Yb emission bands are plotted.

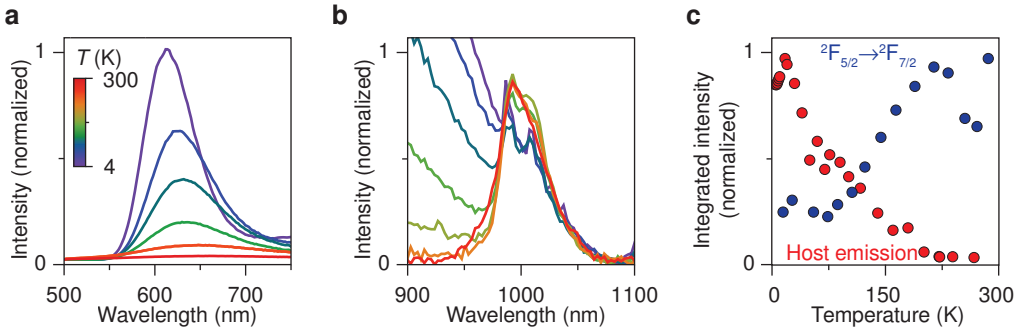

Figure 5.5 | Temperature-dependent emission spectra of Yb^{3+}-doped $Cs_2AgBiBr_6$ NCs. (**a**) Temperature-dependent emission spectra of the host emission intensity measured between 4 and 267 K. Upon increasing the temperature the emission band redshifts, becomes broader and gets increasingly quenched. (**b**) Temperature-dependent Yb^{3+} emission measurements from 7 to 300 K. Note that that red tail of the host emission band starts overlapping with the Yb emission at lower temperatures. (**c**) Temperature dependence of the integrated host emission intensity and Yb^{3+} emission intensity.

The red host emission (originating from the STE state) increases in intensity from 4 K up to 20 K, after which it strongly quenches due to thermally activated non-radiative processes. The intensity of the Yb band increases 4-fold going from 50 K to 250 K, after which the intensity drops by about 30% up to 300 K. These results strongly suggest that the STE state does not act as a sensitizer in the energy transfer (ET) process as in mechanism (2). If energy transfer would occur via the STE state, the Yb emission intensity is expected to experience similar thermal quenching. Instead, the opposite is observed.

Because of the presence of surface quenching sites at NC surfaces, it is instructive to compare the properties of nanocrystalline $Cs_2AgBiBr_6$:Yb^{3+} with that of its microcrystalline analogue (XRD in Supporting Information Section S7). Therefore, we synthesized and measured Yb-doped $Cs_2AgBiBr_6$ MCs with a 5% Yb feed concentration (with respect to Bi^{3+}), and measured their temperature-dependent emission spectra (**Figure 5.6**). The exciton Bohr radius in perovskites and elpasolites is typically smaller than 5 nm and the effect of quantum confinement on the host emission is very limited for ~10 nm NCs.[43,44] Indeed, the similar host emission band energy at

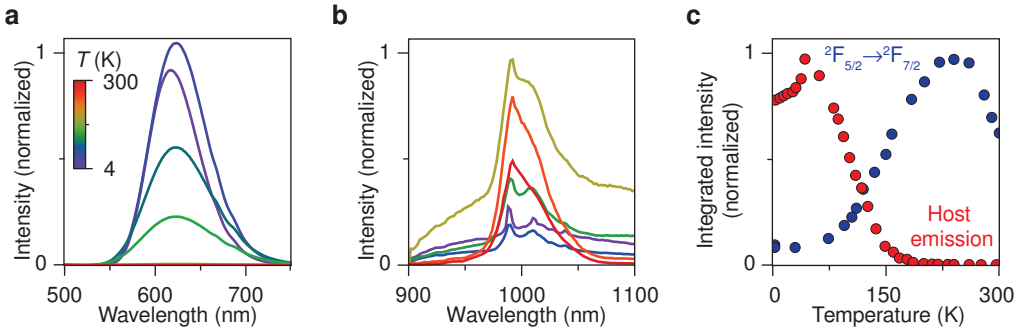

Figure 5.6 | Temperature-dependent emission spectra of Yb^{3+}-doped $Cs_2AgBiBr_6$ NCs MCs. Temperature-dependent (**a**) visible and NIR (**b**) emission spectra of $Cs_2AgBiBr_6$:Yb^{3+} MCs. (**c**) Integrated intensity of the visible and NIR emission of $Cs_2AgBiBr_6$:Yb^{3+} MCs as a function of temperature. The excitation wavelength for all experiments was 374 nm.

4 K for the doped NCs and MCs (**Figure 5.6a**) indicate no role of confinement effects. In that situation the sensitization mechanism in NCs and MCs is expected to be the same. The temperature-dependent red host emission and Yb^{3+} NIR emission presented in **Figure 5.6b** show a similar trend and features as in the NCs. After an initial increase at low temperatures the host emission strongly drops between 50 and 200 K while the Yb^{3+} NIR emission increases by a factor 13 in that same temperature range. For the MCs underneath the Yb-emission band a broad emission band is present that also varies in intensity with temperature (details in Supporting Information Section S8). The emission intensity related to Yb^{3+} was determined by a background-correction procedure similar to that discussed for **Figure 5.5b**. The origin of the broad emission band is unclear and this NIR emission is not observed in the $Cs_2AgBiBr_6$ NCs. Cu-doped $Cs_2AgBiBr_6$ single crystals did show a similar broad NIR emission peak with the same temperature dependence suggesting that Cu-impurities may be the origin.[45] In **Figure 5.6c**, we again compare the integrated emission intensities of both the MC host and Yb-related emission as a function of temperature and observe very similar characteristics as in the NCs. There is an increase in emission intensity above 4 K in both the $Cs_2AgBiBr_6$ NCs (to 20 K) and MCs (to 40 K) followed by strong thermal quenching, which we will discuss together with the time-resolved measurements below. In the MCs, the PL intensity of the Yb emission shows a similar temperature dependence as in the NCs. These results highlight that the Yb sensitization mechanism is the same in NCs and MCs.

To further investigate the energy transfer pathway from the host to Yb^{3+}, we performed variable temperature PL lifetime measurements from 4 K to 100 K on both doped and undoped NCs (**Figure 5.7a–b**). Because of the large changes in decay time the decay curves are shown up to 200 µs, even though at 4 K this does not capture the complete luminescence decay behavior. Full decay curves and further details about the fitting procedure and presence of a fast component can be found in the Supporting Information Section S9. Similar to the room-temperature decay curves discussed above, the luminescence decay of the undoped NCs is multi-exponential, revealing the presence of multiple decay pathways.[46] In order to determine decay times, a three-exponential fit procedure was used to calculate the weighted average lifetime. The resulting average lifetimes are shown in **Figure 5.8**.

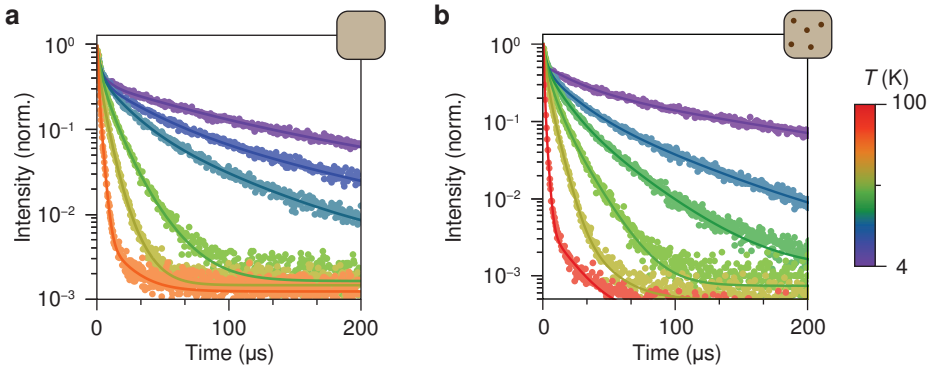

Figure 5.7 | Temperature-dependent photoluminescence decay measurements of the host emission of doped and undoped $Cs_2AgBiBr_6$ NCs. (**a**) Photoluminescence decay measurements of undoped $Cs_2AgBiBr_6$ NCs between 6 and 80K. (**b**) Host emission lifetime of Yb-doped $Cs_2AgBiBr_6$ NCs from 4 to 100 K. The excitation wavelength for both measurements is 374 nm and the emission wavelength is shifted with the emission peak maximum. In order to capture the increasingly fast decay with increasing temperature various laser repetition rates between 400 Hz–10 kHz were used to record the decay curves.

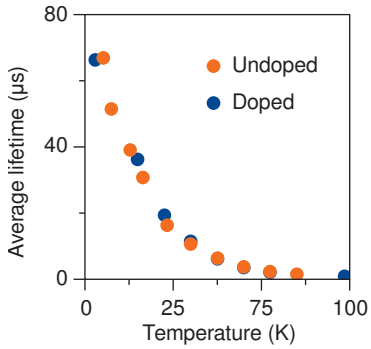

Figure 5.8 | Temperature-dependent weighted average of the STE luminescence lifetime as a function of temperature for Yb-doped and undoped $Cs_2AgBiBr_6$ NCs.

To obtain insight in the role of direct energy transfer from the STE to Yb^{3+}, the host emission lifetime of the doped and undoped NCs are compared. We observe no difference between the average lifetime of the host emission for the doped and undoped $Cs_2AgBiBr_6$ NCs, which provides further evidence that the energy transfer mechanism does not involve the STE state as an intermediary. If energy transfer would occur from the STE state, a shorter emission decay time is expected for the STE emission in the Yb-doped NCs as energy transfer is an additional decay pathway.

The rapid drop in STE emission lifetime between 4 K and ~50 K from 65 µs to 5 µs cannot be explained by thermal quenching as in this temperature regime there is even an increase in emission intensity. A plausible explanation is the spin-forbidden nature of emission from the lowest energy high-spin STE dark state. Upon raising the temperature, thermal population of the low-spin bright state makes the emission allowed and this gives rise to faster radiative decay. This is generally observed for (trapped) exciton emission.[47,48] The strong rise in radiative decay rate can also explain the increase in emission intensity in the low temperature regime. If there are non-radiative decay pathways with no or weak temperature dependence, at elevated temperature faster radiative rates will favor radiative decay over non-radiative decay and the emission intensity increases. Above 50 K thermal quenching of the STE emission starts and a rapid decrease in emission intensity and further decrease of the emission decay time to 2 ns at room temperature is observed. The thermal quenching of STE emission from $Cs_2AgBiBr_6$ has been observed before and the present results are in line with previous observations.[31]

Based on in the temperature-dependent luminescence properties and decay dynamics for undoped and Yb^{3+}-doped $Cs_2AgBiBr_6$ NCs and MCs, we can construct a mechanism for the host-mediated photoexcitation of Yb^{3+} in $Cs_2AgBiBr_6$ NCs and MCs (**Figure 5.9a**). Initially, direct-bandgap absorption of a photon promotes a VB electron to the CB, creating an electron–hole pair. The hole subsequently localizes on a $[AgBr_6]^{5-}$ on a ps timescale,[34] while the electron remains delocalized in the NC (or MC). The subsequent trapping of the electron can take place in multiple ways, but a recent photoconductivity study showed that almost all electrons do localize on trap sites on a sub-ns timescale.[49] Upon doping $Cs_2AgBiBr_6$ NCs and MCs with Yb^{3+}, a competing pathway for electrons is trapping by Yb^{3+}, forming Yb^{2+}, or an Yb^{3+} impurity trapped electron state. Recombination with a trapped hole results in Yb^{3+} in the excited $^2F_{5/2}$ state followed by the characteristic sharp line emission from Yb^{3+} around 1000 nm corresponding to the $^2F_{5/2} \rightarrow {}^2F_{7/2}$ f–f transition. The negative thermal quenching behavior of the Yb^{3+} emission provides support for this mechanism.

It is well-known that as the temperature increases, the mobility of trapped carriers in $Cs_2AgBiBr_6$ (and for example also AgCl) increases.[34,50,51] The higher hole mobility increases the probability for recombination at an Yb^{2+} site, thereby leaving the Yb^{3+} ion in the excited state and an increase of the characteristic $^2F_{5/2} \rightarrow {}^2F_{7/2}$ emission intensity (**Figure 5.9b**). A similar mechanism has been proposed and experimentally validated for Yb^{3+} emission in InP thin films.[52,53] In this model, the subsequent decrease in Yb^{3+} emission intensity at even higher temperatures, above 250 K, can be explained by thermally activated relaxation from the $^2F_{5/2}$ state to the $^2F_{7/2}$ ground state via the charge transfer state.

Finally it is interesting to consider the nature of the trapped electron state, specifically whether Yb^{2+} is formed or electron trapping occurs as a result of a lattice distortion near the Yb^{3+} impurity. A similar discussion is valid for Yb^{3+}-doped perovskite halides where the energy transfer mechanism to Yb^{3+} is also the topic of debate.[6,30] The position of the Yb^{2+} ground state relative to the conduction band minimum is relevant. Often the energetic position of Yb^{2+} relative to the valence band is estimated from the energy of the charge transfer (CT) absorption band.[54] Indeed, the CT absorption corresponds to excitation of a valence band electron to Yb^{3+}. The maximum of the CT absorption band for Yb^{3+} in bromides is typically 3 to 3.5 eV[54–56] which would suggest that the Yb^{2+} ground state cannot be situated in the forbidden gap in $Cs_2AgBiBr_6$ as the bandgap energy is only 2.4 eV. However, one has to realize that the CT absorption band maximum corresponds to a transition to a very high vibrational level in the CT excited state. Charge-transfer transitions are characterized by strong lattice relaxation giving rise to broad emission and excitation bands and large Stokes shifts, typically around 2 eV for Yb^{3+} CT transitions.[57] The position of the Yb^{2+} ground state in the energy-band diagram corresponds to the relaxed state and not the energy of the CT absorption-band maximum. Stabilization of the Yb^{2+} CT state

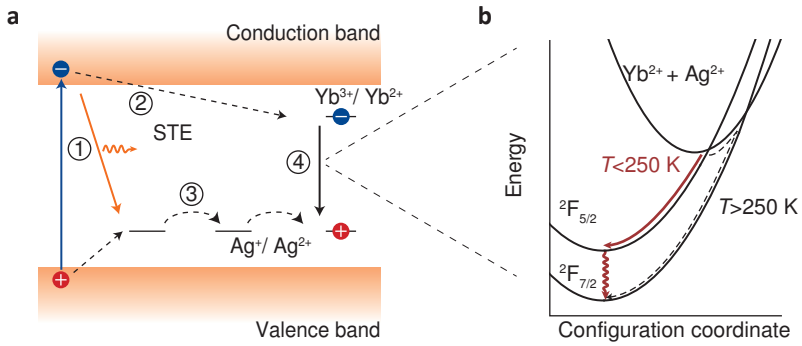

Figure 5.9 | Schematic representation of the emission mechanism of Yb^{3+}-doped $Cs_2AgBiBr_6$ NCs and MCs. (**a**) Band diagram of $Cs_2AgBiBr_6$ with all the transitions leading to Yb^{3+} emission marked with arrows. Formation of an STE state is in competition with trapping on Yb^{3+}. Red STE luminescence is denoted by the orange arrow. (1) Indicates the absorption of blue light leading to the generation of charge carriers. (2) The CB electron traps on Yb^{3+} and reduces it to Yb^{2+}. (3) The VB hole can localize on a $[AgBr_6]^{2-}$ cluster effectively oxidizing Ag^+ into Ag^{2+}. The trapped hole can migrate through the lattice though a temperature activated process. (4) Recombination of a trapped hole and electron happens through the $Yb^{2+} + Ag^{2+} \rightarrow Yb^{3+} + Ag^+$ charge transfer. (**b**) Configuration coordinate diagram of the Yb^{3+} on a Bi^{3+} site. The upper parabola represents a charge-transfer state where Yb^{3+} is reduced to oxidation state (II) accompanied by a hole that localizes on an Ag^+ site. The charge-transfer step between Yb^{2+} and Ag^{2+} leaves the Yb^{3+} in the $^2F_{5/2}$ excited state after which relaxation to the $^2F_{7/2}$ ground state takes place. With increasing temperature (roughly above 250 K) there is a diminishing probability of forming Yb^{3+} in the excited $^2F_{5/2}$ state after the charge transfer step.

as the system relaxes to the new equilibrium distances has to be taken into account (but is often forgotten in band diagram pictures that do not allow for depicting lattice relaxation). The lattice relaxation in the excited CT state is about half the Stokes shift, around 1 eV for $Yb^{2+/3+}$ and thus the position of the Yb^{2+} trapped electron level may very well be positioned in the forbidden gap of $Cs_2AgBiBr_6$, just below the conduction-band minimum. Further research is needed to pinpoint the nature of the trapped electron state.

Conclusion

To conclude, we have investigated the optical properties of undoped and Yb^{3+}-doped $Cs_2AgBiBr_6$ NCs and MCs at variable temperatures down to 4 K. Both broadband trapped-exciton emission around 690 nm and near-infrared Yb^{3+} line emission around 1000 nm are observed. The Yb^{3+} emission can be successfully excited through $Cs_2AgBiBr_6$ host absorption, as confirmed with excitation spectroscopy. Surprisingly, the Yb-emission intensity as a function of temperature shows negative thermal quenching in both $Cs_2AgBiBr_6$ NCs and MCs while the red trapped-exciton emission shows strong thermal quenching above 50 K. Temperature-dependent emission and time-resolved spectroscopy confirm that the STE emission is not strongly affected by the incorporation of Yb. These results can be explained by a host-to-Yb energy-transfer mechanism in $Cs_2AgBiBr_6$ that does not take place via the red-emitting trapped exciton state, but by electron trapping on Yb^{3+} in competition with forming a STE state. The subsequent recombination of Yb^{2+} with a trapped hole results in Yb^{3+} in the excited $^2F_{5/2}$ state and characteristic Yb^{3+} sharp line emission around 1000 nm due to the $^2F_{5/2} \rightarrow {}^2F_{7/2}$ 4f–4f transition. Thermally activated hole mobility explains the negative thermal quenching of the Yb^{3+}-emission. Based on these results we provide evidence for host-to-Yb energy transfer in $Cs_2AgBiBr_6$ by charge carrier trapping on Yb^{3+} and not through the STE state.

Supporting information

S5.1 Methods

Synthesis: The $Cs_2AgBiBr_6$ NCs were synthesized using the hot injection method based on the publication of Creutz et al.[26] Typically, Cs_2CO_3 (0.355 mmol), CH_3COOAg (0.5 mmol, $(CH_3CO_2)_3Bi$ (0.5 mmol), oleylamine (0.5 g), oleic acid (2.5 g) and octadecene (10 mL) were added to a 50 mL 3-neck flask connected to a Schlenk line. The solution was then degassed for 45 minutes under vacuum. During degassing, the solution turned from colorless to yellow to dark brown. Then, the temperature was increased to 145 °C under nitrogen atmosphere and TMS-Br (0.34 mL) was swiftly injected into the reaction mixture under vigorous stirring. A yellow precipitate immediately formed. After 15 seconds, the reaction vessel was submerged in an ice-water bath to quench the reaction. The cooled mixture was collected and centrifuged for 10 minutes at 4000 rpm (RCF = 3112 *g*). The dark brown supernatant was thoroughly drained and the yellow precipitate was dispersed in toluene (5 mL) with sonication (10 minutes). The solution was centrifuged again for 10 minutes at 4000 rpm. The orange supernatant containing the NCs was collected for further characterization. Doping the $Cs_2AgBiBr_6$ NCs with Yb^{3+} was done by adding 0.025 mmol $Yb(CH_3CO_2)\cdot 6H_2O$ to the reaction mixture.

The $Cs_2AgBiBr_6$ MCs were synthesized based on a protocol for $Cs_2AgInCl_6$ microcrystals.[37] The MCs were typically prepared by combining $BiBr_3$ (0.5 mmol), AgBr (0.5 mmol) and $YbCl_3\cdot 6H_2O$ (0.2 mmol) and dissolving this in 4 ml HBr (9M).[37] The solution was heated to ~70 °C until complete dissolution. Then 1 mmol of CsBr was added to the solution, after which an orange precipitate immediately formed. This solution was heated for 20 more minutes before decanting the solution. The powder was washed twice with ethanol and dried in an oven (70 °C) before being stored in a nitrogen filled glovebox.

Characterization: XRD measurements were performed on a Panalytical Aeris diffractometer with Cu Kα radiation at 40 kV. The NC measurements were done by dropcasting a NC solution on a low background Si-wafer until a thin film had formed. Measurements on microcrystals (MCs) were performed by placing the powder on a solid state sample holder. TEM images were taken on a FEI T120C 100keV microscope by dropcasting dilute NCs solutions on a carbon coated copper grid. The elemental analysis was carried out with a Perkin Elmer ICP-OES (Optima 8300) after the NCs were completely dissolved in concentrated (65%) nitric acid. To ensure accurate measurements of only incorporated Yb and not surface or dissolved Yb, the NCs were washed with acetonitrile prior to the measurement.

Samples for optical characterization were prepared by diluting the nanocrystal stock solution 300 times (300 times dilution yields an absorbance of 0.07 at 430 nm) in toluene in a 10×10 mm quartz cuvette. Absorption spectra were measured on a Perkin Elmer Lambda 950 UV/VIS/IR spectrometer. Photoluminescence emission and excitation spectra on both NCs and MCs were measured on an Edinburgh Instruments FS920 spectrometer with a 450 W xenon light source. Luminescence spectra in the 400–850 nm range were recorded using a Hamamatsu R928 photomultiplier tube while 800–1600 nm spectra were recorded using a liquid-nitrogen cooled Hamamatsu R5509 photomultiplier tube. For the optical measurements on NCs a quartz cuvette was used, while for the MCs a thin layer of powder was mounted in a holder. Room temperature photoluminescence decay measurements were performed using an OBIS LX 375 nm diode laser with pulse period of 200 ns and a Hamamatsu H74422-40 photomultiplier tube. For temperature-dependent photoluminescence decay curves we used an OBIS LX 375 nm laser module operated with a pulse generator with varying pulse widths and repetition rates. The temperature-dependent measurements on NCs down to 4 K were carried out with an Oxford Instruments liquid-He cryostat and a home-made liquid quartz cell to contain the NCs in solution. The low temperature measurements on microcrystals were performed with an Oxford Instruments cold-finger liquid-He cryostat.

S5.2 XRD patterns of doped and undoped $Cs_2AgBiBr_6$ NCs

The XRD patterns for the undoped (**Figure S5.1a**) NCs only reveals all $Cs_2AgBiBr_6$ reflections upon zooming in, in contrast to the XRD pattern recorded for the $Cs_2AgBiBr_6$: 0.23% Yb^{3+} NCs (Figure S5.1b). The difference originates from the change in recording settings. The pattern of the undoped sample was recorded with a recording time of 12 min. The XRD pattern of the Yb-doped NCs were recorded with a recording time of 11 h.

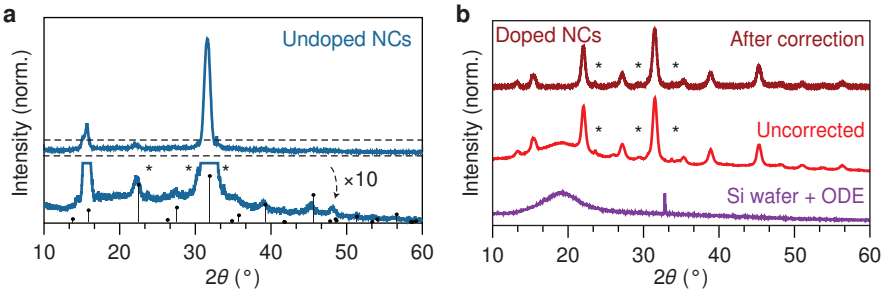

Figure S5.1 | XRD patterns of the doped and undoped $Cs_2AgBiBr_6$ NCs. XRD patterns for the (**a**) $Cs_2AgBiBr_6$ and (**b**) $Cs_2AgBiBr_6$:0.23% Yb^{3+} NCs. A significant amount of material from one NC synthesis was used for obtaining an XRD measurement with sufficient signal. In order to have a high concentration of NCs, only the standard purification steps were performed, not washing with acetonitrile. This results in a higher concentration of ODE in the solution and gives rise to an additional broad band around 19° (see reference pattern from ODE). In the corrected XRD pattern this background is subtracted. The asterisks denote minor impurities in the sample that originate from a ternary Cs-Bi-Br impurity.[26]

S5.3 Tauc plot analysis of $Cs_2AgBiBr_6$ NCs

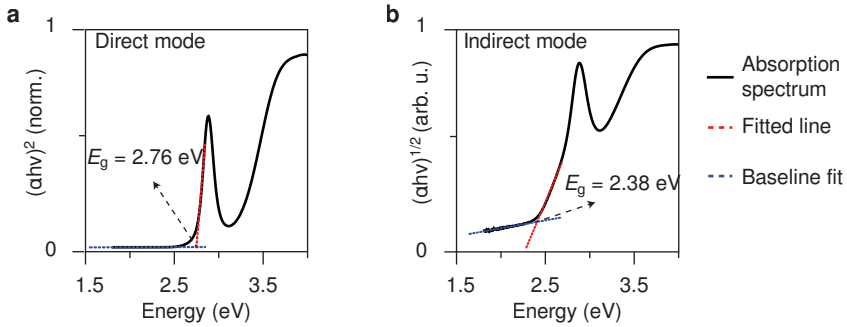

Figure S5.2 |Tauc plot analysis of the absorption spectrum of undoped $Cs_2AgBiBr_6$ NCs[58] (**a**) Plot of $(\alpha h\nu)^2$ vs. E to determine the direct bandgap at the crossing point between the baseline (fitted between 1.5 and 2.5 eV) and slope between 2.75 and 2.85 eV. (**b**) Tauc analysis of the indirect bandgap from the plot of $(\alpha h\nu)^{0.5}$ vs. E. Again the crossing point between the background and slope (fitted between 2.4 and 2.68 eV) is determined and gives the indirect bandgap energy.

S5.4 The effect of NC concentration on $Cs_2AgBiBr_6$ excitation spectra

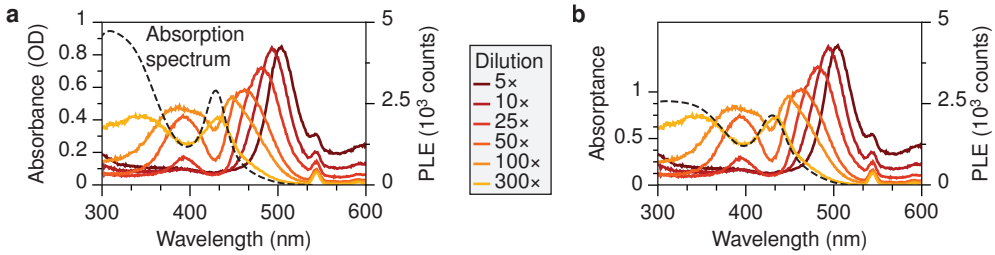

Figure S5.3 | Absorbance (a) and absorptance (b) plotted with photoluminescence excitation (PLE) spectra for different dilutions of the $Cs_2AgBiBr_6$:0.23% Yb^{3+} NCs. To illustrate the difference, we plot both the absorbance ($A = -\log(T)$) and the absorptance ($\alpha = 1 - T - R$, where T is the transmittance and R is the reflectance). The PLE intensity scales with absorptance (linear) instead of absorbance (logarithmic).[59] Differences between

absorptance spectra and excitation spectra thus reflect absorption processes that do not give rise to (detected) emission of photons. Excitation spectra for emission at 650 nm were recorded for decreasing concentrations of the NCs in solution, up to a factor 300. The effect of NC concentration on the excitation spectrum can clearly be seen. Only at a dilution of 300× with respect to the concentrated stock solution the excitonic peak of the excitation spectrum aligns with the absorption/absorptance spectrum. The red shift and distortions (e.g. dip at maximum absorption) at higher concentrations are explained by saturation effects and the excitation spectrum for the highest dilution represents the true excitation spectrum. Note that also for this strongly diluted sample at wavelengths < 360 nm the PLE intensity is lower than expected based on the absorptance. One possible explanation is that the high absorptance (>0.8) causes additional artefacts, like discussed in the supporting information of ref [30]. It can also be because of competing UV absorption by other molecules formed during the reaction which does not lead to 650 nm emission. The peak around 540 nm is a Raman peak. This was checked by shifting the recording emission wavelength. This resulted in a similar shift (in energy) of the peak around 540 nm in the excitation spectrum. The energy difference between the 540 nm peak and the detection wavelength of 650 nm is 3000 cm^{-1}, consistent with C-H stretching vibrations and confirms that this is a Raman peak.

S5.5 Host emission spectrum of doped and undoped $Cs_2AgBiBr_6$ NCs

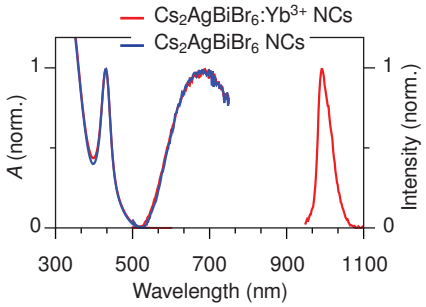

Figure S5.4 | Normalized room temperature absorption and emission of Yb-doped (red) and undoped (blue) $Cs_2AgBiBr_6$ NCs. Emission spectra were recorded with 430 nm excitation at room temperature.

S5.6 Temperature-dependent emission spectra of doped and undoped $Cs_2AgbiBr_6$ NCs

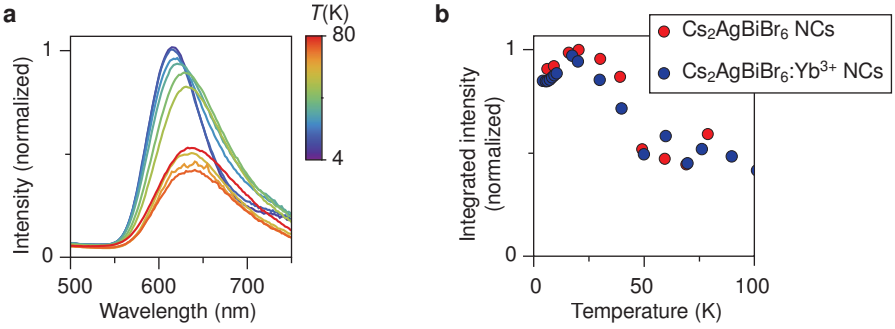

Figure S5.5 | Temperature-dependent emission of doped and undoped $Cs_2AgBiBr_6$ NCs between 4 and 80 K. (**a**) Emission spectra were recorded with 374 nm excitation. (**b**) Integrated intensity plotted as a function of temperature. The comparison with the emission intensity measured for the $Cs_2AgBiBr_6$:Yb^{3+} NCs shows that the quenching behavior is the same for both materials.

S5.7 Background correction for temperature-dependent NIR emission spectra of $Cs_2AgBiBr_6$:Yb^{3+} NCs

The NIR emission band of Yb-doped $Cs_2AgBiBr_6$ NCs overlaps with the host emission band at increasingly low temperatures. To be able to evaluate the temperature dependence of the emission intensity of the Yb-ions the underlying emission band is fitted with a polynomial function of the form $p(x)= a +bx + cx^2 + dx^3 + ex^4$, where *a*, *b*, *c*, *d,* and *e* are free parameters to determine the background. The integral for the Yb-emission that is shown in **Figure 5.5c** ion the main text, is taken between 950 and 1050 nm after subtraction of this background.

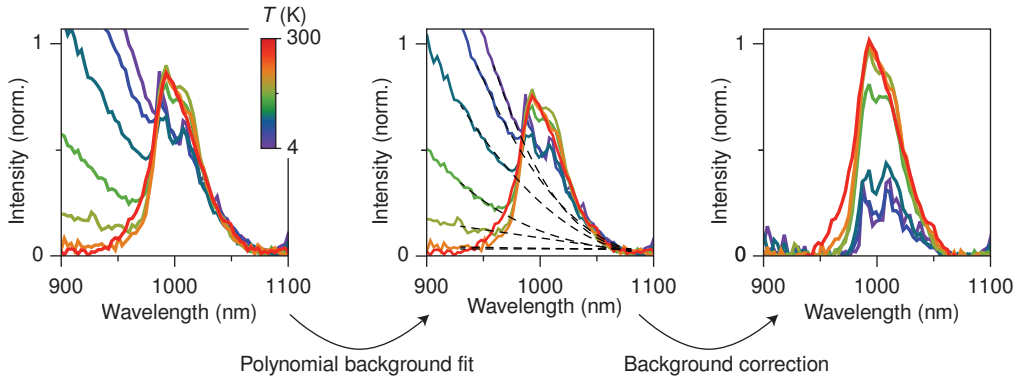

Figure S5.6 | Polynomial background correction of the T-dependent NIR emission spectra of Yb-doped $Cs_2AgBiBr_6$ NCs. (left) Original spectra with only the noise of the detector subtracted. (middle) Spectra along with the polynomial background fits. The spectral regions to which the polynomial was fitted are 900–940 nm and 1090–1100 nm. (right) Yb^{3+} emission spectra after subtraction of the area underneath the polynomial fit, based on which the integral values for the Yb emission intensity of **Figure 5.5c** in the main text are determined.

S5.8 XRD patterns of $Cs_2AgBiBr_6$ and $Cs_2AgBiBr_6$:Yb^{3+} MCs

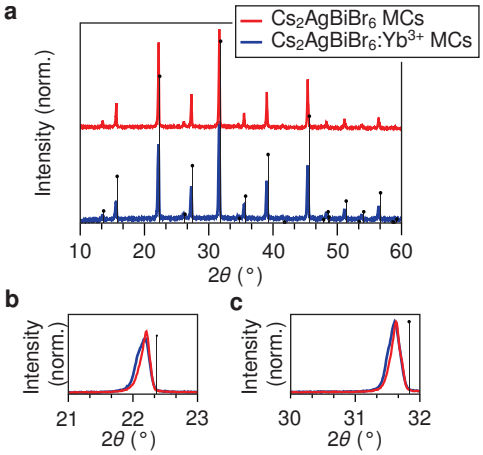

Figure S5.7 | XRD patterns of $Cs_2AgBiBr_6$ and $Cs_2AgBiBr_6$:Yb^{3+} MCs. (a) XRD patterns of doped and undoped $Cs_2AgBiBr_6$. The reference pattern is calculated using VESTA and based on the ICSD collection code 239874. Note that there is a small offset between the peaks of the reference pattern and our experimental data. The offset is probably the result of a small misalignment of the z-height of the measurement stage. (**b**) and (**c**) Zoom-ins on the two main reflections of both doped and undoped $Cs_2AgBiBr_6$ MCs. The peak position of the $Cs_2AgBiBr_6$:Yb^{3+} MCs shows a small shift to smaller angles, which is contrary to what one would expect based on the smaller ionic radius of Yb^{3+} (VI: 0.868 Å) than of Bi^{3+} (VI: 1.03 Å).[60] We therefore conclude that this is a consequence of small differences in z-stage alignment. In the zoom-ins, a small asymmetry is visible in the Yb-doped sample, indicative of increased disorder in the crystal structure.

S5.9 Background correction for temperature-dependent NIR emission spectra of $Cs_2AgBiBr_6:Yb^{3+}$ MCs

For the NIR emission spectra of the MCs, the background consists of a broad emission band that stretches from roughly 900 to 1500 nm. To determine the temperature dependence of the Yb^{3+} emission a similar procedure as for the NCs was used. The broad band was fitted with a polynomial function of the form $p(x)= a +bx + cx^2 + dx^3 + ex^4$, where a, b, c, d, and e are free parameters to determine the background. The integral for the Yb-emission that is shown in **Figure 5.6c**, is taken between 950 and 1050 nm after subtraction of this background.

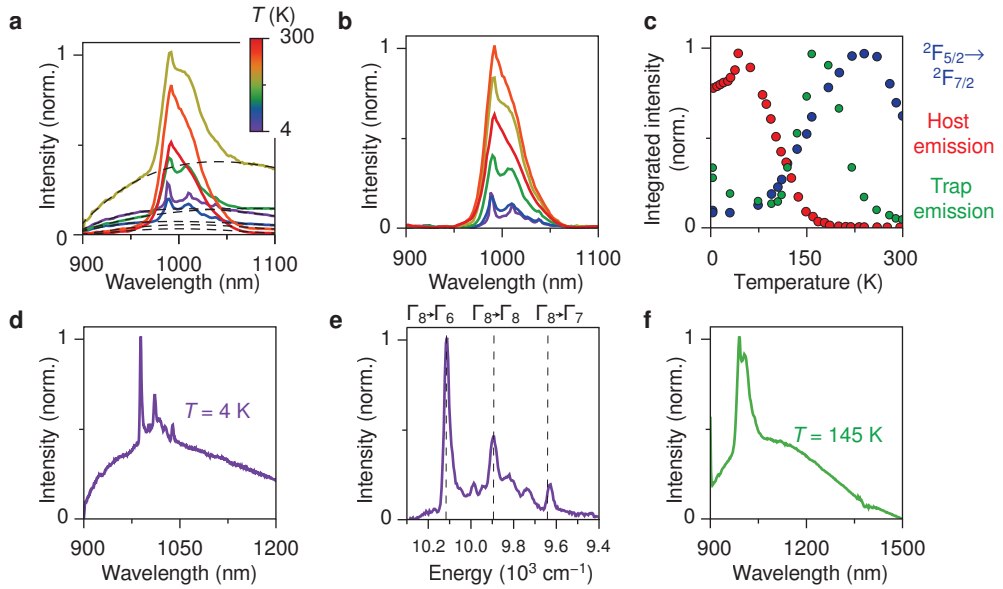

Figure S5.8 | Temperature-dependent emission spectra of $Cs_2AgBiBr_6:Yb^{3+}$ MCs. (**a**) Emission spectra with only the noise of the detector subtracted and the polynomial fits added. The spectral regions to which the polynomial was fitted are 900–940 and 1090–1100 nm. (**b**) Spectra corrected by subtracting the fits from panel **a**. (**c**) Integrated intensities of the host emission (**Figure 5.6c**, main text), Yb-emission and integrated area underneath the polynomial fits (trap emission). Note that the NIR trap emission intensity peaks around 170 K. (**d**) Higher spectral resolution NIR emission spectrum at 4 K without background correction. (**e**) NIR emission spectrum at 4 K with background correction and peaks assigned to the different crystal field components of Yb^{3+}, the transition energies are obtained from Yb^{3+} in Cs_2NaYCl_6.[61] (**f**) NIR emission spectrum at 4 K without background correction and a wider spectral range (900–1500 nm), indicating that the trap emission band stretches far into the NIR.

S5.10 Temperature-dependent lifetime measurements of doped and undoped $Cs_2AgBiBr_6:Yb^{3+}$ NC

The temperature-dependent time-resolved STE emission measurements on both $Cs_2AgBiBr_6$ and $Cs_2AgBiBr_6:Yb^{3+}$ NCs are shown in the figures **Figure S5.9** and **Figure S5.10**. As the excitation source an OBIS LX-375nm diode laser with a pulse period of 200 ns and its excitation wavelength at 374 nm was used. At the end of a laser pulse, the fall time at the end is specified to be 5 ns. Therefore, analyzing decay processes faster than 5 ns in these measurements is not feasible. After a decay curve is measured, we fit the data with three exponents and a constant (background) to fully capture the multi-exponential decay. The results of the weighted average are plotted in **Figure 5.8** of the main text.

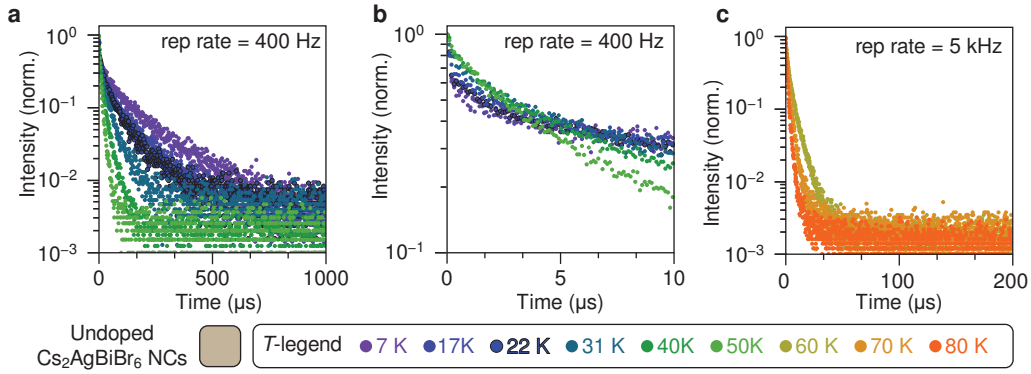

Figure S5.9 | Temperature-dependent luminescence decay curves of undoped $Cs_2AgBiBr_6$ NCs. (**a**) Decay curves recorded between 4 and 50 K, with a repetition rate of 400Hz for excitation at 374 nm and emission at the maximum of the broad red emission band. Note that on this timescale there is a fast component visible at the beginning of each decay curve. (**b**) Zoom-in on the first 10 µs, revealing a fast initial component present at lower temperature. Previous results in $Cs_2AgBiBr_6$ single crystals showed similar results upon lowering the temperature down to 4 K. (**c**) Decay curves recorded between 60 and 80 K and with a repetition rate of 5 kHz. All measurements were conducted with 374 nm excitation, while the emission wavelength was at the peak of the emission spectra.

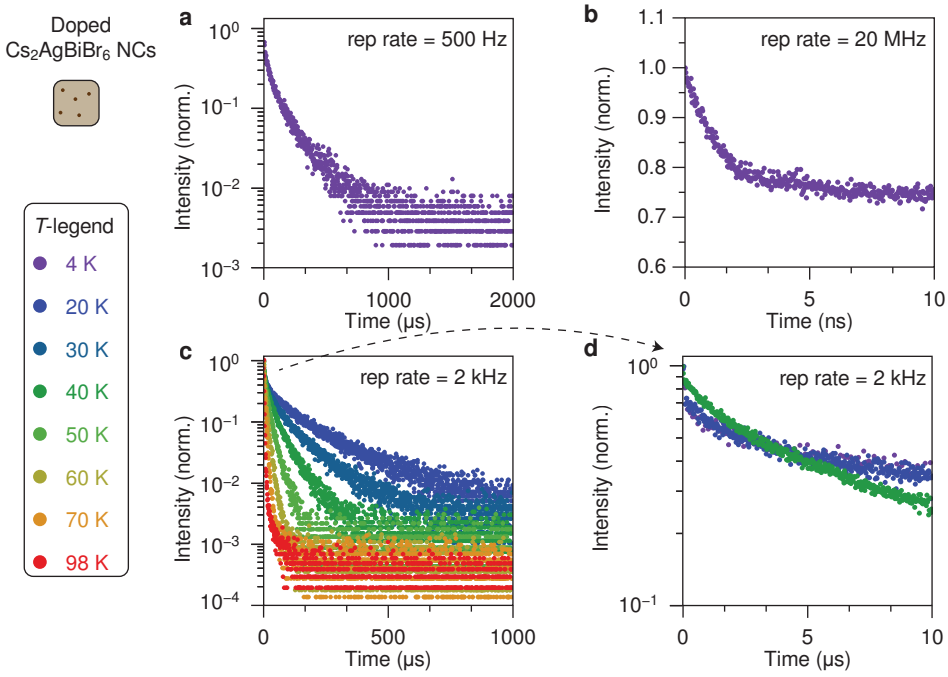

Figure S5.10 | Temperature-dependent luminescence decay curves of Yb^{3+}-doped $Cs_2AgBiBr_6$ NCs. (**a**) Decay curve recorded at 4 K, with a repetition rate of 500 Hz for excitation at 374 nm and emission at 690 nm. Note that, like for the undoped samples, on this timescale there is a fast component visible at the beginning of each decay curve. (**b**) Luminescence decay measurement with a faster laser (PicoQuant, λ_{exc} = 374 nm, pulse width = 54 ps, repetition rate 20 MHz) to capture the fast initial decay. (**c**) Overview of decay measurements recorded between 20 and 98 K, with a repetition rate of 2 kHz. (**d**) A zoom-in of the first 10 µs.

References

[1] R. Martín-Rodríguez, R. Geitenbeek, A. Meijerink, *J. Am. Chem. Soc.* **2013**, 135, 13668.
[2] J. K. Swabeck, S. Fischer, N. D. Bronstein, A. P. Alivisatos, *J. Am. Chem. Soc.* **2018**, 140, 9120.
[3] S. E. Creutz, R. Fainblat, Y. Kim, M. C. De Siena, D. R. Gamelin, *J. Am. Chem. Soc.* **2017**, 139, 11814.
[4] T. J. Milstein, D. M. Kroupa, D. R. Gamelin, *Nano Lett.* **2018**, 18, 3792.
[5] D. M. Kroupa, J. Y. Roh, T. J. Milstein, S. E. Creutz, D. R. Gamelin, *ACS Energy Lett.* **2018**, 3, 2390.
[6] M. Zeng, F. Artizzu, J. Liu, S. Singh, F. Locardi, D. Mara, Z. Hens, R. Van Deun, *ACS Appl. Nano Mater.* **2020**, 3, 4699.
[7] G. Pan, X. Bai, D. Yang, X. Chen, P. Jing, S. Qu, L. Zhang, D. Zhou, J. Zhu, W. Xu, B. Dong, H. Song, *Nano Lett.* **2017**, 17, 8005.
[8] R. Marin, D. Jaque, *Chem. Rev.* **2021**, 121, 1425.
[9] H. Lei, D. Hardy, F. Gao, *Adv. Funct. Mater.* **2021**, 31, 2105898.
[10] N. R. Wolf, B. A. Connor, A. H. Slavney, H. I. Karunadasa, *Angew. Chemie - Int. Ed.* **2021**, 60, 16264.
[11] F. S. Richardson, *Rare Earths Mod. Sci. Technol.* **1982**, 147.
[12] T. R. Faulkner, J. P. Morley, F. S. Richardson, R. W. Schwartz, *Mol. Phys.* **1980**, 40, 1481.
[13] H. Tang, Y. Xu, X. Hu, Q. Hu, T. Chen, W. Jiang, L. Wang, W. Jiang, *Adv. Sci.* **2021**, 3, 1.
[14] D. E. Sommer, D. R. Gamelin, S. T. Dunham, *Phys. Rev. Mater.* **2022**, 6, 25404.
[15] K. T. Kluherz, S. T. Mergelsberg, D. E. Sommer, J. Y. D. Roh, S. A. Saslow, D. Biner, K. W. Krämer, S. T. Dunham, J. J. De Yoreo, D. R. Gamelin, *Phys. Rev. Mater.* **2022**, 6, 74601.
[16] C. Y. Wang, P. Liang, R. J. Xie, Y. Yao, P. Liu, Y. Yang, J. Hu, L. Shao, X. W. Sun, F. Kang, G. Wei, *Chem. Mater.* **2020**, 32, 7814.
[17] H. Arfin, J. Kaur, T. Sheikh, S. Chakraborty, A. Nag, *Angew. Chemie - Int. Ed.* **2020**, 59, 11307.
[18] S. Jin, R. Li, H. Huang, N. Jiang, J. Lin, S. Wang, Y. Zheng, X. Chen, D. Chen, *Light Sci. Appl.* **2022**, 11, 52.
[19] E. T. McClure, M. R. Ball, W. Windl, P. M. Woodward, *Chem. Mater.* **2016**, 28, 1348.
[20] N. Chen, T. Cai, W. Li, K. Hills-Kimball, H. Yang, M. Que, Y. Nagaoka, Z. Liu, D. Yang, A. Dong, C. Y. Xu, R. Zia, O. Chen, *ACS Appl. Mater. Interfaces* **2019**, 11, 16855.
[21] G. Zhang, Y. Wei, P. Dang, H. Xiao, D. Liu, X. Li, Z. Cheng, J. Lin, *Dalt. Trans.* **2020**, 49, 15231.
[22] M. N. Tran, I. J. Cleveland, J. R. Geniesse, E. S. Aydil, *Mater. Horizons* **2022**, 9, 2191.
[23] M. N. Tran, I. J. Cleveland, E. S. Aydil, *ACS Appl. Electron. Mater.* **2022**, 4, 4588.
[24] F. Schmitz, K. Guo, J. Horn, R. Sorrentino, G. Conforto, F. Lamberti, R. Brescia, F. Drago, M. Prato, Z. He, U. Giovanella, F. Cacialli, D. Schlettwein, D. Meggiolaro, T. Gatti, *J. Phys. Chem. Lett.* **2020**, 11, 8893.
[25] R. T. Williams, K. S. Song, *J. Phys. Chem. Solids* **1990**, 51, 679.
[26] S. E. Creutz, E. N. Crites, M. C. De Siena, D. R. Gamelin, *Nano Lett.* **2018**, 18, 1118.
[27] R. T. Myers, *Inorg. Chem.* **1974**, 13, 2040.
[28] S. J. Zelewski, J. M. Urban, A. Surrente, D. K. Maude, A. Kuc, L. Schade, R. D. Johnson, M. Dollmann, P. K. Nayak, H. J. Snaith, P. Radaelli, R. Kudrawiec, R. J. Nicholas, P. Plochocka, M. Baranowski, *J. Mater. Chem. C* **2019**, 7, 8350.
[29] M. R. Filip, S. Hillman, A. A. Haghighirad, H. J. Snaith, F. Giustino, *J. Phys. Chem. Lett.* **2016**, 7, 2579.
[30] J. Y. D. Roh, M. D. Smith, M. J. Crane, D. Biner, T. J. Milstein, K. W. Krämer, D. R. Gamelin, *Phys. Rev. Mater.* **2020**, 4.
[31] L. Schade, A. D. Wright, R. D. Johnson, M. Dollmann, B. Wenger, P. K. Nayak, D. Prabhakaran, L. M. Herz, R. Nicholas, H. J. Snaith, P. G. Radaelli, *ACS Energy Lett.* **2019**, 4, 299.
[32] A. Dey, A. F. Richter, T. Debnath, H. Huang, L. Polavarapu, J. Feldmann, *ACS Nano* **2020**, 14, 5855.
[33] A. Schmitz, L. Leander Schaberg, S. Sirotinskaya, M. Pantaler, D. C. Lupascu, N. Benson, G. Bacher, *ACS Energy Lett.* **2020**, 5, 559.
[34] A. D. Wright, L. R. V. Buizza, K. J. Savill, G. Longo, H. J. Snaith, M. B. Johnston, L. M. Herz, *J. Phys. Chem. Lett.* **2021**, 12, 3352.
[35] H. D. Nelson, S. O. M. Hinterding, R. Fainblat, S. E. Creutz, X. Li, D. R. Gamelin, *J. Am. Chem. Soc.* **2017**, 139, 6411.
[36] S. Yakunin, B. M. Benin, Y. Shynkarenko, O. Nazarenko, M. I. Bodnarchuk, D. N. Dirin, C. Hofer, S. Cattaneo, M. V. Kovalenko, *Nat. Mater.* **2019**, 18, 846.
[37] Y. Mahor, W. J. Mir, A. Nag, *J. Phys. Chem. C* **2019**, 123, 25

[38] P. A. Loiko, N. M. Khaidukov, J. Méndez-Ramos, E. V. Vilejshikova, N. A. Skoptsov, K. V. Yumashev, *J. Lumin.* **2016**, 175, 260.
[39] Y. P. Varshni, *Physica* **1967**, 34, 149.
[40] J. A. Steele, P. Puech, M. Keshavarz, R. Yang, S. Banerjee, E. Debroye, C. W. Kim, H. Yuan, N. H. Heo, J. Vanacken, A. Walsh, J. Hofkens, M. B. J. Roeffaers, *ACS Nano* **2018**, 12, 8081.
[41] R. Kentsch, M. Scholz, J. Horn, D. Schlettwein, K. Oum, T. Lenzer, *J. Phys. Chem. C* **2018**, 122, 25940.
[42] Y. Liu, X. Rong, M. Li, M. S. Molokeev, J. Zhao, Z. Xia, *Angew. Chemie - Int. Ed.* **2020**, 59, 11634.
[43] J. Butkus, P. Vashishtha, K. Chen, J. K. Gallaher, S. K. K. Prasad, D. Z. Metin, G. Laufersky, N. Gaston, J. E. Halpert, J. M. Hodgkiss, *Chem. Mater.* **2017**, 29, 3644.
[44] J. C. Dahl, W. T. Osowiecki, Y. Cai, J. K. Swabeck, Y. Bekenstein, M. Asta, E. M. Chan, A. P. Alivisatos, *Chem. Mater.* **2019**, 31, 3134.
[45] B. I. Ito, E. K. Tekelenburg, G. R. Blake, M. A. Loi, A. F. Nogueira, *J. Phys. Chem. Lett.* **2021**, 12, 10444.
[46] S. Yue, Y. Zhou, S. Zou, L. Wang, H. Liu, S. S. Wong, *Adv. Opt. Mater.* **2017**, 5, 1.
[47] C. De Mello Donegá, M. Bode, A. Meijerink, *Phys. Rev. B - Condens. Matter Mater. Phys.* **2006**, 74, 85320.
[48] M. Szymura, M. Duda, M. Karpińska, T. Kazimierczuk, R. Minikayev, K. Sobczak, M. Parlińska-Wojtan, Ł. Kłopotowski, *J. Phys. Chem. C* **2023**, 127, 6768.
[49] V. M. Caselli, J. Thieme, H. J. Jöbsis, S. A. Phadke, J. Zhao, E. M. Hutter, T. J. Savenije, *Cell Reports Phys. Sci.* **2022**, 3.
[50] C. L. Marquardt, R. T. Williams, M. N. Kabler, *Solid State Commun.* **1971**, 9, 2285.
[51] E. Laredo, W. B. Paul, L. Rowan, L. Slifkin, *Phys. Rev. B* **1983**, 27, 2470.
[52] M. A. J. Klik, T. Gregorkiewicz, I. V. Bradley, J. P. R. Wells, *Phys. Rev. Lett.* **2002**, 89, 227401.
[53] P. S. Whitney, K. Uwai, H. Nakagome, K. Takahei, *Appl. Phys. Lett.* **1988**, 53, 2074.
[54] P. Dorenbos, A. Josef, J. T. M. de Haas, K. W. Krämer, *J. Lumin.* **2019**, 208, 463.
[55] J. L. Ryan, *J. Phys. Chem.* **1966**, 70, 2845.
[56] X. Zhou, M. F. Reid, M. D. Faucher, P. A. Tanner, *J. Phys. Chem. B* **2006**, 110, 14939.
[57] L. Van Pieterson, A. Meijerink, *Mater. Sci. Forum* **1999**, 315–317, 446.
[58] P. Makuła, M. Pacia, W. Macyk, *J. Phys. Chem. Lett.* **2018**, 9, 6814.
[59] D. Tonti, F. Van Mourik, M. Chergui, *Nano Lett.* **2004**, 4, 2483.
[60] R. D. Shannon, *Acta Crystallogr. Sect. A* **1976**, 32, 751.
[61] P. A. Tanner, *Mol. Phys.* **1986**, 58, 317.

Chapter 6

New insights in luminescence and quenching mechanisms of Ag_2S NCs through temperature-dependent spectroscopy

Based on:

J.W. de Wit, I. Zabala-Gutierrez, R. Marin, S. Melle, O. G. Calderon, J. Marques-Hueso, D. Jaque, J. Rubio-Retama, A. Meijerink, New insights in luminescence and quenching mechanisms of Ag_2S nanocrystals through temperature-dependent spectroscopy, *submitted*

Abstract

Bright near-infrared emitting Ag_2S nanocrystals are promising candidates for in vivo bioimaging and also temperature sensing relying on a reversible variation in intensity and luminescence lifetime in the physiological temperature regime. Here, we investigated the temperature-dependent luminescence of ~9 nm dodecanethiol (DDT) and polyethylene glycol (PEG) capped Ag_2S nanocrystals (NCs) down to 10 K to gain insight in the luminescence and quenching mechanisms. Interestingly, both emission and lifetime measurements reveal similar and strong thermal quenching from 200 to 300 K, indicating an intrinsic quenching process that limits the quantum yield to ~15% at room temperature. The low thermal quenching temperature, broadband emission and multi-exponential μs decay behavior suggest the optical transition involves strong lattice relaxation consistent with recombination of an Ag^+-trapped hole with a delocalized conduction band electron. Cooling down below 200 K, the emission intensity remains constant while the luminescence lifetime shortens until 50 K, followed by a lengthening of the lifetime upon further cooling to 10 K. We explain these unexpected results in terms of multiple thermally coupled excited states, with a lowest-energy dark state, a higher bright state followed by dark states at even higher energies. Our findings offer valuable insights for understanding the optical properties of Ag_2S NCs and the thermal quenching mechanism underlying its temperature sensing capabilities.

Introduction

Semiconductor nanocrystals (NCs) are attractive for in vivo bioimaging and optical biosensing due to their small size and tunable optical properties.[1,2] Particularly near-infrared (NIR) emitting NCs are interesting candidates because of the deep penetration depths for this wavelength region and NIR excitation does not result in background autofluorescence. Ag_2S NCs have emerged as a promising candidates for these applications, offering low (cyto)toxicity,[3,4] and temperature-dependent optical properties from room temperature (RT) to ~60°C enabling accurate luminescence thermometry.[5–7] Additionally, Ag_2S has strong absorption in the first biological window (750–900 nm),[8] and its emission band falls within the second biological window (1000–1700 nm).[9] However, the low photoluminescence quantum yields (QY) reported for Ag_2S NCs (typically below 1%) limit their performance.

Since the first reports on fluorescent Ag_2S NCs in 2010,[10] efforts to enhance the QY of Ag_2S NCs have focused on improving the quality of the Ag_2S core material and on implementing effective surface treatments.[11–13] Generally, Ag_2S NCs in organic media are synthesized in a single-pot synthesis with Ag-diethyldithiocarbamate (Ag-DDTC) as the silver and sulfur precursor and dodecanethiol (DDT) and oleylamine acting as both solvent and capping ligand. Tuning reaction parameters like ligand ratios and reaction temperature improved the QY to roughly 2% by making more stoichiometric Ag_2S NCs.[14] Further improvements were realized by post-synthetic sonochemical or fs laser irradiation treatments in chloroform. The sonication results in the formation of small amounts of HCl that causes surface etching and gives rise to fewer surface quenching sites, while during the fs laser treatment a protective AgCl shell is formed.[15,16] Both procedures result in QYs of up to 10% and the name superdots was coined for these bright Ag_2S NCs. Despite these extensive efforts and impressive improvement in efficiency, the QY of Ag_2S NCs still lags behind that of other NIR emitting NCs such as PbSe (QY~40%).[17]

To gain more insight into the limitations and possibilities of Ag_2S NCs, it helps to better understand the origin of the NIR emission and the quenching mechanism. For small (<4.5 nm) Ag_2S NC, a size dependence of the emission maximum was observed, based on which the exciton Bohr

radius for Ag_2S was calculated to be around 1.2–2.2 nm.[18,19] For NC sizes larger than 4.5 nm, the emission maximum stabilizes at ~1200 nm, which is at a slightly lower energy than the bulk Ag_2S bandgap energy of about 1.1 eV.[10,20] In the description of the absorption spectrum different observations are reported, where some do observe excitonic features [20–22] while others do not.[18,19] It is not clear what causes the presence or absence of excitonic features in Ag_2S NCs but there appears to be no correlation with NC monodispersity. In ref [18], sub-µs luminescence lifetimes were reported for a series of NCs with sizes ranging between 2.2 and 7 nm. Even though the emission maximum did not redshift above a size of 4.5 nm, the average lifetime lengthened.[18] The current understanding of the luminescence properties of Ag_2S is primarily based on optical measurements between 0 °C and 60 °C where strong temperature quenching and a redshift of the emission maximum are typically observed.

It is surprising that in the analyses of the luminescence properties for Ag_2S NCs so far there have only been a few reports that have included temperature-dependent optical measurements below 0°C. Pereplitsa et al. observed a 40-fold decrease in PL intensity going from 80 to 300 K in 2.2-nm silica-coated Ag_2S NCs, but do not explain its origin.[21] They also observed different intensity-temperature curves upon cooling and heating. It cannot be excluded that the hysteresis is an experimental artefact caused by a delay in the sample reaching the set temperature rather than a physical effect. Temperature-dependent and time-resolved spectroscopy down to 10 K has, to the best of our knowledge, not yet been reported even though this can provide valuable information about the emission and quenching mechanisms.

In this chapter we report on the photoluminescence properties of bright Ag_2S NCs between 10 and 300 K. Both photoluminescence intensity and time-resolved spectroscopy show that between 200 and 300 K strong and reversible quenching occurs for both thiol- and PEG-capped Ag_2S NCs. This indicates an intrinsic quenching mechanism which limits the RT QY to about 15% and is also responsible for the reproducible temperature dependence of emission intensity and lifetime that is utilized in temperature sensing with Ag_2S NCs. Upon further cooling below 200 K a remarkable temperature dependence of the average emission lifetime is observed and attributed to the thermal population of multiple dark and bright exciton states existing in Ag_2S. These results contribute to a better understanding of the optical properties of Ag_2S NCs and can aid in further optimizing Ag_2S NCs for bioimaging and sensing applications.

Results and discussion

We synthesized Ag_2S nanocrystals (NCs) using a thermal decomposition synthesis and subjected them to a sonication step to enhance the quantum yield (QY), following the procedure outlined by Gutierrez et al.[15] This procedure results in dodecanethiol-terminated NCs (Ag_2S-DDT) or, after a ligand exchange procedure also outlined in Ref. [15], in similarly sized polyethylene-glycol-capped NCs (Ag_2S-PEG). **Figures 6.1a,b** shows electron microscope images of both types of Ag_2S nanocrystals, with a diameter of 9.0 ± 1.2 nm for the Ag_2S-PEG NCs and 9.1 ± 1.7 nm for the Ag_2S-DDT NCs. In order to make Ag_2S NCs biocompatible, they are often capped with PEG. We investigate and compare the properties of both Ag_2S-PEG and Ag_2S-DDT NCs to be able to distinguish effects related to the capping layer from intrinsic luminescence properties of the Ag_2S cores. To avoid differences due to solvent effects, all measurements on the Ag_2S NCs are performed in chloroform ($CHCl_3$).

In **Figure 6.1c** the RT absorption and emission spectra of Ag_2S-DDT and Ag_2S-PEG NCs are shown. The absorption spectrum consists of a featureless broad band with an onset around 1200

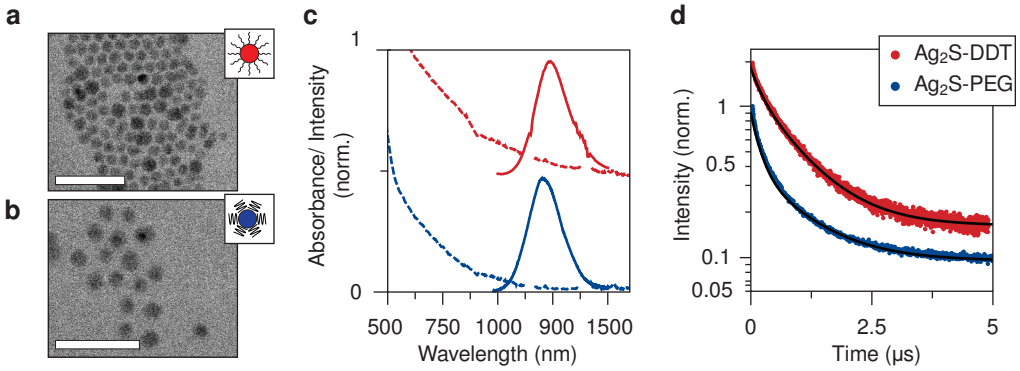

Figure 6.1 | TEM images and room temperature optical properties of Ag_2S NCs capped with DDT and PEG. (**a**) Electron microscopy image of Ag_2S-DDT NCs and (**b**) Ag_2S-PEG NCs. Both scale bars are 50 nm. (**c**) Absorption (dashed) and emission spectrum (full, λ_{exc} = 520 nm) of Ag_2S-DDT NCs and Ag_2S-PEG NCs. (**d**) Luminescence decay curves of Ag_2S-DDT NCs (λ_{exc} = 520 nm, λ_{em} = 1205 nm) and Ag_2S-PEG NCs (λ_{exc} = 520 nm, λ_{em} = 1205 nm), recorded at 289 K and 293 K, respectively. They are fitted with a double-exponential function represented by the black lines. The offset between the absorption/ emisson spectra in panel **c** and the decay curves in panel **d** is added for clarity.

nm. Chloroform C-H vibrational overtone absorptions around 1150 nm and 1400 nm are left out for clarity but are shown in the full spectra in Figure S6.1. No excitonic features are observed, which are typically present for semiconductor quantum dots in the quantum confinement regime. Specifically, a distinct band is usually observed for the first excitonic transition. The absence is in line with the expectation that the ~10 nm Ag_2SNCs are not affected by quantum confinement effects, based on the exciton Bohr radius for Ag_2S (~2 nm).[18,19] Upon excitation at 520 nm, very similar emission spectra are observed with maxima around 1220 nm (for Ag_2S-DDT NCs) and 1200 nm (for Ag_2S-PEG NCs) and full width at half maximum (fwhm) of 140 meV (Ag_2S-PEG NCs) and 150 meV (Ag_2S-DDT NCs). The RT QY of these samples is 5.1 ± 0.7% for the Ag_2S-DDT NCs and 1.6 ± 0.2% for the Ag_2S-PEG NCs (details about the QY measurements can be found in Supporting Information Section S3). The lower QY for the Ag_2S-PEG NCs has been ascribed to a poorer surface passivation, resulting in increased quenching caused by surface related traps.[15]

To gain further insight in the RT optical properties, we recorded luminescence decay curves on both types of Ag_2S NCs (**Figure 6.1d**). Both show non-exponential decay indicating the presence of multiple decay pathways. Decay curves were fitted with a bi-exponential function which results in an average lifetime ($\tau_{ave} = \Sigma_i A_i \tau_i / \Sigma_i A_i$) of 0.63 µs for the Ag_2S-DDT NCs and 0.46 µs for the Ag_2S-PEG NC. The observation of non-exponential decay is in line with previous reports.[15,16] The origin of non-exponential decay has been explained by quenching of the emission by surface traps. It is interesting to observe that even for the most efficient Ag_2S super dots the decay is non-exponential. The decay times show a clear correlation with the quantum yield. While for the super dots a ~2 µs average lifetime was observed at RT, the decay curves for less efficient Ag_2S NCs is much shorter, in the ~100 ns time range.[16] The lifetimes measured here for the Ag_2S NCs are shorter than 2 µs, in agreement with a lower QY than for the best superdots. The shorter average lifetime of the Ag_2S-PEG vs. Ag_2S-DDT NCs is in line with the lower QY values but it is also evident that there is no linear dependence between QY and average lifetime. The faster decay for less efficient Ag_2S NCs can be qualitatively explained by additional non-radiative (surface)

quenching in NCs with a lower QY. The absence of quantitative agreement reflects that the luminescence decay curves do not capture all non-radiative processes. For example, very fast direct quenching lowers the QY but can be hidden in a lower intensity for the first data point of decay curves. In summary, the optical properties of both the PEG- and DDT-capped bright Ag_2S NCs are in agreement with what can be expected based on luminescence and lifetime measurements reported in earlier publications and the high QYs of the Ag_2S-DDT vs. Ag_2S-PEG NCs.[5,13,16]

Previously reported temperature-dependent behavior above RT shows strong and reversible quenching resulting in a drop in both luminescence intensity and decay time.[5] To better understand the quenching, we investigated the temperature-dependent emission spectra of Ag_2S NCs in the temperature range 10 to 310 K. With decreasing temperature, the Ag_2S-PEG NCs emission peak position blueshifts from 1200 nm at RT to 1080 nm at 16 K, corresponding to a peak maximum shift of 120 meV for the Ag_2S-PEG NCs (**Figure 6.2a**, Figure S6.2a). A similar peak shift of 125 meV is observed for the Ag_2S-DDT NCs (**Figure 6.2b**, Figure S6.3a). This is typical Varshni behavior observed in semiconductors, but the peak shift is larger than observed in

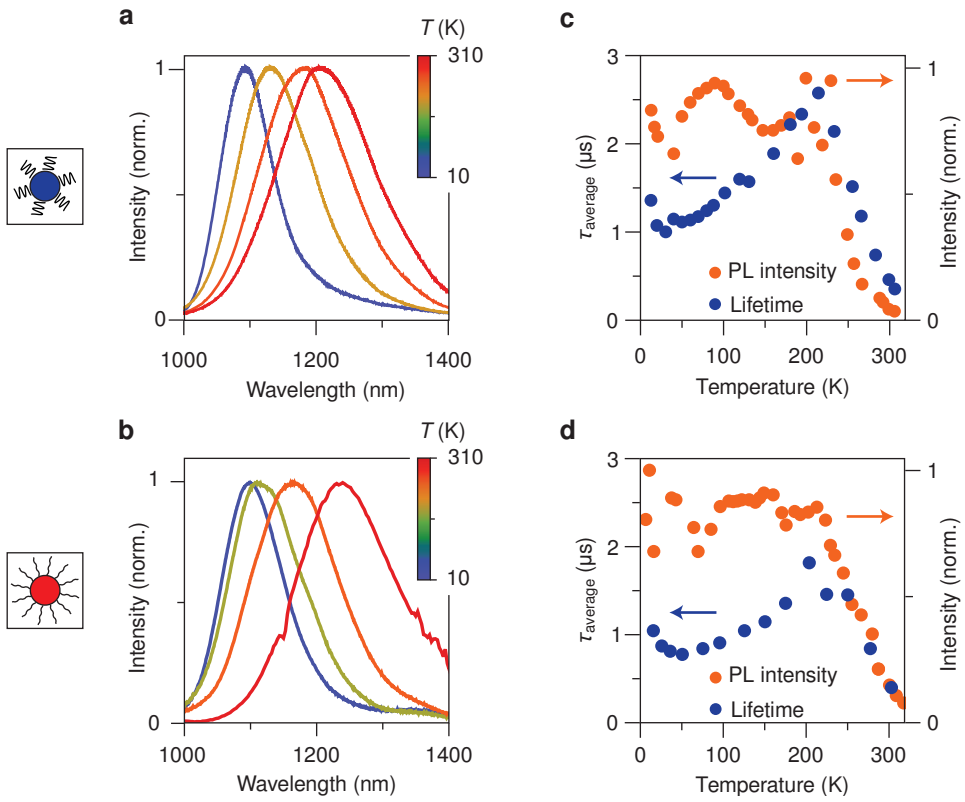

Figure 6.2 | Temperature-dependent emission spectroscopy on of Ag_2S NCs. (**a**) Emission spectra of Ag_2S-PEG NCs recorded at (blue to red) 13, 128, 220 and 289 K. (**b**) Emission spectra of Ag_2S-DDT NCs recorded at 16, 120, 175 and 293 K. (**c**) Integrated photoluminescence intensity plotted as a function of temperature (orange) together with the average lifetime as a function of temperature (blue) for Ag_2S-PEG NCs. (**d**) Sames as in panel **c** but for Ag_2S-DDT NCs. All spectra and decay curves were recorded with λ_{exc} = 520 nm, the emission maximum was used to record the decay curves.

e.g. CdSe NCs (70 meV) and $CuInS_2$ (50 meV).[23][24] In addition to the blueshift, the emission bands also narrow with decreasing temperature, showing a fwhm reduction to about 100 meV for both the Ag_2S-PEG (Figure S6.2a) and Ag_2S-DDT NCs (Figure S6.3a). The fwhm at 10 K is considerably larger than bandwidths observed for II-VI or IV-VI QDs. For example, for CdSe QDs the fwhm is reduced to ~40-80 meV and depends on the polydispersity of particle size as a result of the variation of emission wavelength for QDs with size due to quantum confinement effects. For single dots extremely narrow emission lines (< 1 meV) are observed at 10 K which is expected for recombination of a delocalized conduction band (CB) electron and valence band (VB) hole. Because of the delocalized nature of both charge carriers, the lattice relaxation involved in the optical transition is small resulting in narrow emission lines (weak electron-phonon coupling). For 10 nm Ag_2S NCs there is no influence of quantum confinement and narrow-band emission is expected at the bandgap energy for CB electron with VB hole recombination. The large fwhm for the Ag_2S emission at 10 K suggests a much larger electron–phonon coupling. The broad emission band can be explained by a luminescence mechanism where fast hole trapping occurs by Ag^+. This results in the formation of Ag^{2+}, with a formal 2+ charge of Ag but in fact involving a charge redistribution, including the S^{2-} ligands, and a shortening of the Ag–S distance. Hole trapping is followed by radiative recombination with a CB electron, resulting emission involving strong local lattice relaxation.[25] A similar mechanism has been reported for broadband emission for various Ag and Cu doped and Cu-based semiconductor nanocrystals.[26]

The emission spectra in **Figure 6.2a,b** are plotted after normalization to be able to more clearly observe the peak shift and changes in bandwidth. To determine the temperature dependence of the emission intensity, the integrated peak areas were determined and are plotted in **Figure 6.2c,d** for the DDT and PEG capped Ag_2S NCs as a function of temperature. For both we observe a sharp increase of intensity upon cooling from 300 to 200 K. For the PEG capped NCs a 15-fold increase is observed, while for the DDT capped NCs it is 9-fold. Below 200 K the intensity remains constant for both samples. Because the measurements are performed on Ag_2S NC dissolved in chloroform we have to correct for the intensity offset caused by the solidification of chloroform around 210 K. Details about the correction, including a plot for temperature dependence of the uncorrected intensity integrals can be found in the Supporting information Section S6.4. The fluctuations in intensity are relatively large between 10 and 200 K. We do not attribute this to real variations in intensity but to artefacts related to changes in sample alignment and some condensation on the cryostat windows.

Recording the emission intensity as a function of temperature to study thermal quenching can be complicated by intensity fluctuations unrelated to thermal quenching. Changes in alignment, excitation-source intensity, collection efficiency, temperature-dependent absorption strength or, specifically in this case, the phase transition in the solvent contribute to intensity variations unrelated to thermal quenching.[27] A complimentary and insightful approach for investigating thermal quenching involves measuring the emission lifetime as a function of temperature. For a constant radiative decay rate, quenching through thermally activated non-radiative decay will give shortening of the emission lifetime along with a drop in emission intensity. Therefore also luminescence lifetimes were measured as a function of temperature for the Ag_2S-PEG and Ag_2S-DDT NCs between 10 K and 310 K. At all temperatures non-exponential decay curves were recorded. In **Figure 6.3** a selection of decay curves recorded at different temperatures in the maximum of the emission band is shown. The decay curves were fitted with bi-exponential functions to determine the average decay time τ_{ave} (*vide supra*). Upon cooling from RT to 200 K the average

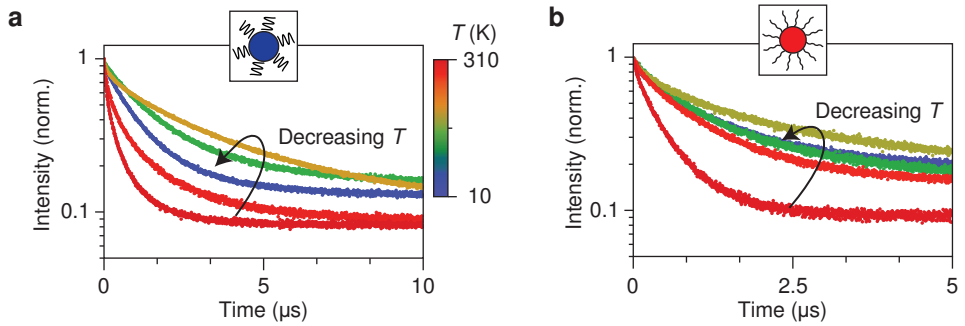

Figure 6.3 | Temperature-dependent luminescence decay of Ag_2S NCs. (**a**) Luminescence decay curves of Ag_2S-PEG NCs at (blue to red) 20, 131, 195, 284 and 307 K. (**b**) Decay curves for Ag_2S-DDT NCs recorded at 15, 131, 195, 285 and 308 K with excitation at 520 nm and emission at the maximum of the emission band.

lifetime increases sharply and closely follows the increase in emission intensity for both samples (blue dots, **Figure 6.2c,d**). For the Ag_2S-PEG NCs τ_{ave} increases from 0.46 µs at 300 K to 2.6 µs at 215 K, while for Ag_2S-DDT NCs τave increases from 0.63 µs to 1.87 µs at 203 K. This corresponds to a 5.6-fold and 3-fold increase of the average lifetime in this temperature range. The steep and consistent drop in lifetime and emission intensity between 200 and 300 K for both Ag_2S-DDT and Ag_2S-PEG NCs shows that the temperature dependence of emission lifetime and intensity that is used for luminescence thermometry is based on an intrinsic luminescence quenching process that starts at 200 K and continues above RT.[15] The large ~10-fold decrease in intensity and ~5-fold decrease in decay time upon heating from 200 to 300 K shows that the emission is already strongly quenched at 300 K and we can estimate the maximum RT QY to be around 15%, not much higher than the 10% QY reported for the best Ag_2S superdots. The strong intrinsic quenching at RT shows that the QY realized for these superdots cannot be significantly improved. The observation of quenching at relatively low temperatures can be explained by an optical transition with strong electron-phonon coupling, consistent with the mechanism for the emission proposed above, *viz.* recombination of a trapped hole with a delocalized CB electron.

To further corroborate the mechanism for NIR emission from Ag_2S NCs the shape of the luminescence decay curves is considered. A representative selection in **Figures 6.3a** and **6.3b** depicts decay curves down to 10 K. More decay curves with overlaid fits can be found in Figure S6.4. Similar to the measurement at RT and decay curves reported in the literature, the decay curves remain non-exponential. This observation suggests that, in addition to thermal quenching above ~200 K, the presence of multiple decay rates is characteristic for emission from Ag_2S NCs. This phenomenon may arise from variations in non-radiative decay rates because of differences in (surface) defects quenching the emission. However, similar temperature-invariant multi-exponential decay has been observed for $CuInS_2$ NCs and Ag-doped semiconductors like CdSe.[23] Depending on the exact location for trapping of the hole by Ag^+, the overlap with the delocalized electron wavefunction will vary. Faster recombination is expected for a hole trapped in the center of the NC and slower recombination for trapping at the edge, where the electron wavefunction has a lower amplitude resulting in a lower recombination probability. This is an additional explanation for the non-exponential behavior that is consistent with a luminescence mechanism of recombination of a trapped hole and a CB electron.

Surprisingly, as we cool down below 200 K, the average lifetime for both Ag_2S-PEG and Ag_2S-DDT NCs shortens down to ~50 K, where the average lifetime of Ag_2S-PEG NCs drops to 1 μs and for Ag_2S-DDT NCs to 0.8 μs. While the average lifetime decreases, the emission intensity remains constant. This suggests that, in contrast to the thermal quenching above 200 K, there is no change in the efficiency of the non-radiative process; instead, there is a change in radiative decay rates. Further reducing the temperature from 50 to ~10 K reveals another increase in the average lifetime to 1.4 μs and 1.1 μs for Ag_2S-PEG NCs and Ag_2S-DDT NCs, respectively. It is noteworthy that despite differences in the observed average lifetime between Ag_2S-PEG and Ag_2S-DDT NCs, the thermal quenching (>200 K), lifetime shortening (50–200 K), and lifetime lengthening (<50 K) ranges are consistent for the two types of Ag_2S NCs.

The unusual shortening in emission lifetime upon cooling below 200 K and the increase in lifetime below 50 K can be explained by the presence of thermally coupled excited states from which radiative decay is possible. These states are a lowest energy dark state, a higher energy bright state and again a dark state at even higher energies. In **Figure 6.4**, we schematically illustrate the behavior of this thermally coupled energy level system at various temperatures. In Figure S6.5, we divide the temperature-lifetime plot into temperature regions corresponding to the three situations depicted in **Figure 6.4**. The lengthening of the lifetime upon cooling from 50 to 0 K is commonly observed in (chalcogenide) semiconductor such as CdSe, PbSe and $CuInS_2$ NCs and is attributed to freezing in all population in a lowest energy 'dark' exciton state separated by ΔE_1 from a higher energy bright state.[23,28] Decay from this dark state is characterized by a longer radiative lifetime due to its spin-forbidden nature. For CdSe and PbSe QDs the slow (μs) decay component is determined by the weighted average population of the dark and bright state and has a single exponential character and an increasing decay rate (shorter lifetime) is observed upon raising the temperature. [29,30] The temperature dependence of the decay rates makes it possible to determine ΔE_1 and the lifetime of the low-energy dark state. Unfortunately, the inherent non-exponential decay in Ag_2S NCs makes it difficult to quantitatively analyze the decay curves to determine ΔE_1. The increase in lifetime between 50 and 200 K is unusual, as luminescence lifetimes typically decrease with temperature due to thermally activated non-radiative decays. The significant lengthening of the emission lifetime can be explained by the presence of

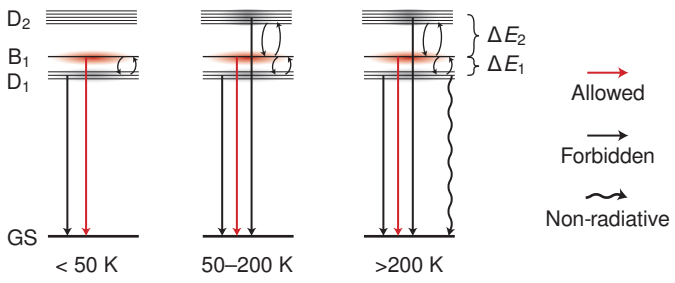

Figure 6.4 | Proposed electronic structure of the emissive excited states in Ag_2S NCs. At 0 K, only the lowest dark D_1 excited state is populated with slow decay because of the forbidden nature of the emission transition. At 50 K, the B_1 bright state is thermally populated as $k_BT > \Delta E_1$ giving rise to faster decay from bright state B*1*. Upon further raising the temperature, the higher energy dark state D*2* is populated and the forbidden nature of this transition causes lengthening of the emission lifetime until it rapidly drops because of thermal quenching (> 200 K).

additional higher energy dark states (D_2), which become increasingly populated at elevated temperatures. In the proposed energy level structure, the higher lying energy state would need to have a higher degeneracy than the bright state to explain the strong increase in decay time. Additional experiments and excited-state DFT calculations could offer further insights into the electronic structure of excitons in Ag_2S NCs, to confirm the current explanation for the unusual increase in lifetime observed between 50 and 200 K. It is noteworthy that a lengthening of decay time has also been observed for CdSe quantum dots just above RT and is consistent with theoretical energy level calculations showing a lowest energy dark state, a higher energy bright state followed by even higher energy dark states, analogous to the energy level scheme in **Figure 6.4**.[31–33]

Conclusion

The luminescence and quenching mechanism for Ag_2S NCs with a diameter of ~9 nm and capped with either DDT or PEG were investigated. At room temperature a featureless absorption band starting in the NIR and a broad emission band around 1220 nm are observed, in line with earlier reports on these bright NIR emitting NCs. For the first time, the temperature-dependent photoluminescence properties of Ag_2S NCs are reported in the temperature range 10 K to 310 K. Both temperature-dependent emission and time-resolved spectroscopy reveal strong and reversible thermal quenching between 200 and 300 K in both PEG and DDT capped Ag_2S NCs. This intrinsic luminescence quenching is held responsible for the previously reported temperature sensing capabilities for Ag_2S NCs between RT and 60°C based on a decrease in intensity and shortening of emission lifetime with temperature. It also limits the RT quantum yield of Ag_2S NCs to ~15%. Below 200 K the emission intensity remains constant, while the average lifetime initially shortens upon cooling down to 50 K before lengthening again for further cooling below 50 K. To explain the remarkable variation in luminescence lifetime with temperature, we propose an energy level scheme for Ag_2S NCs with three thermally coupled excited states. Finally, based on the characteristic broad emission band, μs radiative lifetime, low thermal luminescence quenching temperature, Stokes shifted emission and multi-exponential decay, even at 10 K, we propose that the NIR emission originates from recombination of a delocalized conduction band electron with a hole localized on Ag^+, similar to the recombination mechanism proposed for Ag-doped CdSe and $CuInS_2$ NCs.

Supporting Information

S6.1. Methods

Chemicals: Silver nitrate (99.9%), sodium diethyldithiocarbamate (NaDDTC) (ACS reagent grade), oleylamine (70%) (OLAM), 1-DDT (≤98%), and toluene (99.5%) were purchased from Sigma-Aldrich. Heterofunctional methoxy PEG thiol (HS-PEG-OMe) with molecular weight M_W = 750 g·mol^{-1} were acquired from RAPP Polymere and used without further purification. Chloroform ($CHCl_3$, 99.6%) and ethanol absolute pure (99.8%) were purchased from PanReac AppliChem. Anhydrous tetrachloroethylene (TCE) (>99%) were obtained from Sigma Aldrich.

Synthesis: The synthesis of Ag_2S-DDT NCs: The Ag_2S NCs were synthesized based on a protocol described in ref [1]. In brief, AgDDTC was prepared by combining 200 ml of 0.125M $AgNO_3$ with 200 ml of 0.125 M NaDDTC. The AgDDTC precipitate was collected and vacuum dried at 60°C. For a typical synthesis, 25 mg AgDDTC, 2.5 ml OLAM and 2.5ml DDT were combined in a 2-neck flask and degassed under vacuum and sonication. The flask was then filled with N_2 atmosphere and heated to 185°C using a preheated oil bath. After heating for 1 h at 185°C the flask was left to cool down, after which ethanol was added and the mixture was centrifuged at 10 000 g for 10 min to precipitate the Ag_2S NCs. This washing step was repeated twice before the NC were stored in 10 ml $CHCl_3$ with a final concentration of ~1mg/ml.

Sonication procedure: The sonication procedure is also described in ref [1]. For the sonication step a Branson Sonifier 250 was used at 20 W operating power with a duty cycle of 10%. The horn was placed in a 10 ml vial containing 5 ml of a 0.3 mg ml^{-1} Ag_2S NC in $CHCl_3$ solution. The vial was placed in an ice bath to avoid heating up.

Ligand exchange to Ag_2S-PEG NCs: For the ligand exchange, 2 mg of PEG was added to 1 mg of sonicated Ag_2S NCs dispersed in 1 ml $CHCl_3$. The reaction was stirred vigorously for 30 min after which hexane was added to destabilize the dispersion. The precipitate was collected and redispersed in $CHCl_3$.

Characterization and optical spectroscopy: Transmission electron micrographs were recorded on a Talos L120C from Thermo Fischer Scientific. The grids consisted of a Cu mesh covered with a carbon-coated polymer film. Optical absorption measurements were performed with a PerkinElmer Lambda 950 UV-Vis/IR spectrometer in a cuvette with a 1 cm pathlength. The stock samples were diluted ~30 times. Photoluminescence measurements were carried out on a Edinburgh Instruments FS920 spectrometer equipped with a 450 W Xe lamp or an OBIS 520 nm LX 40 mW laser as the excitation source. The emitted light was spectrally dispersed in a 0.22 m monochromator with a liquid nitrogen cooled R5509 photon multiplier tube. The time-resolved measurements were performed using a pulsed OBIS 520 nm LX 40 mW laser as the excitation source and the liquid nitrogen cooled R5509 photon multiplier tube as the detector. For the measurements down to 4 K, an Oxford Instruments liquid He cryostat equipped with a quartz liquid cell sample holder was used. The same excitation sources and detectors as mentioned above were used in addition to an Andor Kymera 328i IR CCD detector for recording NIR emission spectra.

QY measurements: A calibrated spectrofluorometer (Edinburgh Instruments, FLS920) was used for spectral measurements, equipped with a 102 mm inner diameter integrating sphere (Jobin-Yvon). For detection a liquid nitrogen cooled NIR photon multiplier tube was used. For the excitation a CW 808 nm laser from Roithner Lasertechnik GmbH was used. Temperature controlling and sensing capabilities were incorporated into the integrating sphere using a temperature controlling chip (W1209), heating element, sample holder thermistor, and sample thermistor.

S6.2 Absorption for Ag_2S-DDT and Ag_2S-PEG NCs

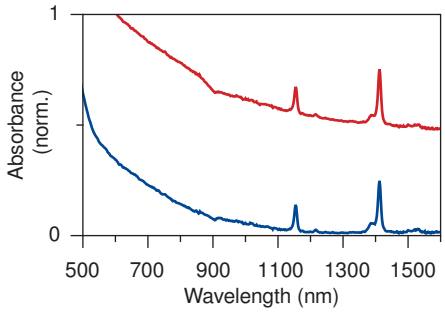

Figure S6.1 | Absorption spectra of Ag_2S-PEG (blue) and Ag_2S-DDT NCs (red). Absorption spectra of both samples of Ag_2S NCs dissolved in tetrachloroethylene with small amounts of $CHCl_3$ left in the solution. The asterisks indicate overtone C-H absorptions originating from the $CHCl_3$.

S6.3 Photoluminescence quantum yield measurements on Ag_2S NCs

The photoluminescence quantum yield (PLQY) is defined by Equation S6.1: [34]

$$\mathrm{PLQY} = \frac{\#\,\text{photons emitted}}{\#\,\text{photons absorbed}} = \frac{I_{\text{sample}}}{E_{\text{reference}} - E_{\text{sample}}}. \tag{S6.1}$$

Where I_{sample} is the Emission intensity, $E_{\text{reference}}$ is the intensity of excitation light for a non-absorbing reference and E_{sample} is the intensity of excitation light not absorbed by the sample. Three measurements for emission and scattering were taken for a cuvette inside of the integrating sphere and the average is reported. The standard deviation was used for the reported errors. The results of the PLQY measurements are detailed below in **Table S6.1.**

Table S6.1 | PLQY values for Ag_2S-DDT and Ag_2S-PEG NCs at room temperature.

Sample	Temperature (°C)	PLQY (%)
Ag2S-DDT	24.1	5.1 ± 0.7
Ag2S-PEG	23.8	1.6 ± 0.2

Section S6.4 Temperature-dependent emission spectra of Ag_2S NCs

Figure 6.2a and **Figure 6.2b** show the temperature-dependent normalized emission spectra of Ag_2S-PEG NCs and Ag_2S-DDT NCs. Based on these emission spectra, we determined the peak position and fwhm for the Ag_2S-PEG NCs (**Figure S6.2a**) and Ag_2S-DDT NCs (**Figure S6.3a**). The integrated emission intensities as function of temperature for the Ag_2S-PEG NCs are shown in **Figure S6.2b**. Around 210 K, a discontinuity is

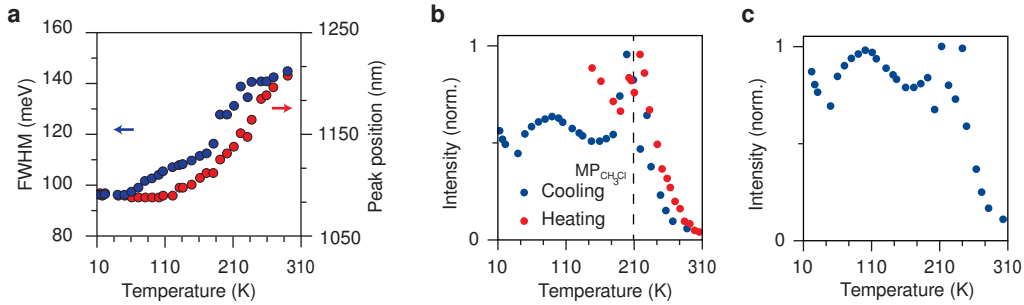

Figure S6.2 | Temperature-dependent emission spectroscopy on Ag_2S-PEG NCs. (**a**) Plot of the fwhm and the peak position as a function of temperature for the Ag_2S-PEG NCs. (**b**) Integrated photoluminescence intensity plotted as a function of temperature recorded while cooling down (blue) and while warming up (red). The dashed line marks the melting temperature of $CHCl_3$. (**c**) Same as in panel **b** but corrected for the intensity jump created by the solidification of $CHCl_3$.

observed in the integrated intensity for both samples. This temperature coincides with the melting point of the $CHCl_3$ in which the NCs are dispersed (dashed black line). To verify the intensity jump was caused by a phase transition induced change in the collection efficiency, we also recorded spectra while warming up. During warming up, the intensity jump takes place at a slightly lower set temperature, indicating that a (delayed) phase transition is indeed responsible for the jump in emission intensity. To correct the data, we took the average intensity of the datapoints in the temperature range 13 to 200 K and subtracted that from all datapoints above 210 K (**Figure S6.2c).** The same procefure as applied to the temperature-dependent data for the Ag2S-DDT NCs (**Figure S6.3b, c**).

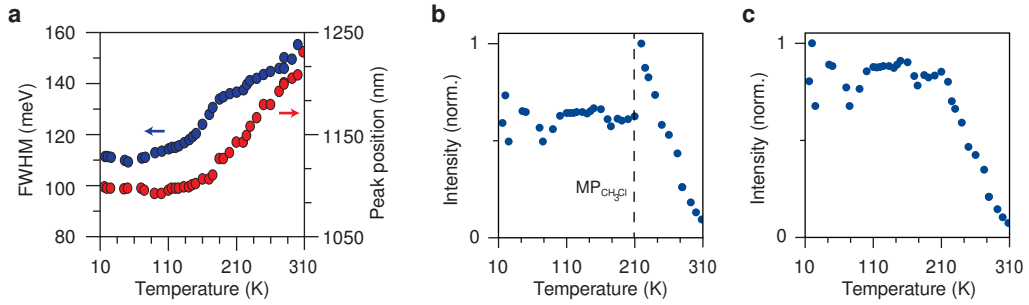

Figure S6.3 | Temperature-dependent emission spectroscopy on Ag_2S-DDT NCs. (**a**) Plot of the fwhm and the peak position as a function of temperature for the Ag_2S-DDT NCs (**b**) Integrated photoluminescence intensity plotted as a function of temperature recorded while cooling down (blue) and while warming up (red). The dashed line marks the melting temperature of $CHCl_3$. (**c**) Same as in panel **b** but corrected for the intensity jump created by the solidification of $CHCl_3$.

Section 6.5 Temperature-dependent decay measurements

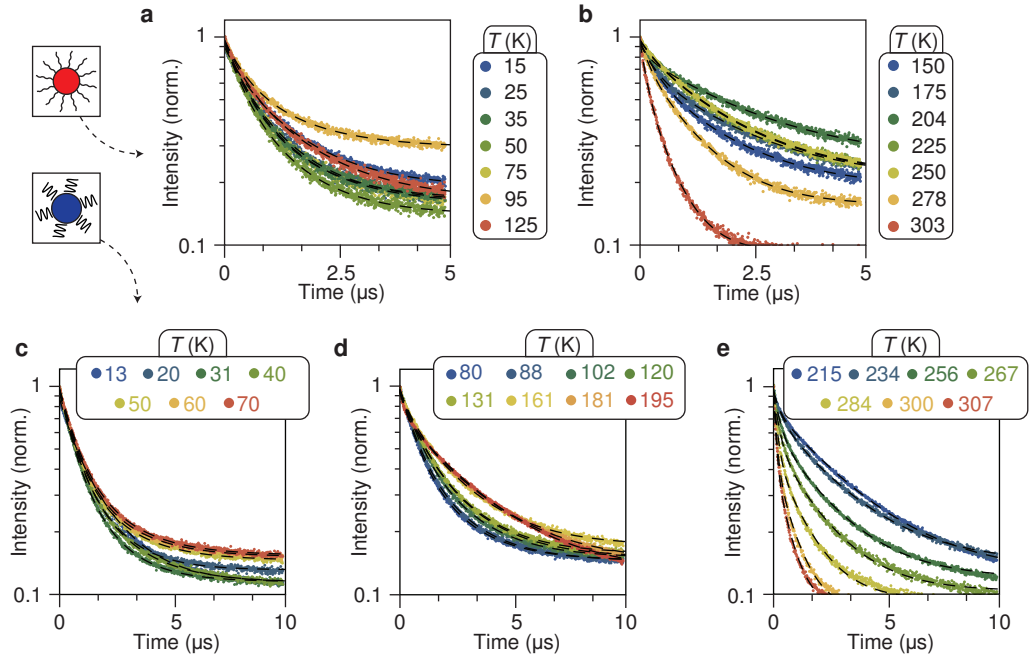

Figure S6.4 | Overview of temperature-dependent time-resolved emission measurements for the Ag_2S-PEG and Ag_2S-DDT NCs. (**a**) Temperature-dependent decay curves of Ag_2S-DDT NCs between 15 and 125 K

including fits. (**b**) Same as in **a**, but between the 150 and 303 K. (**c**) Temperature-dependent decay curves of Ag_2S-PEG NCs between 15 and 70 K including fits. (**d**) Same as in **c**, but between the 80 and 195 K. (**e**) Same as in **c** and **d**, but between the 215 and 307 K.

Section 6.6 Temperature-dependent lifetime and proposed model

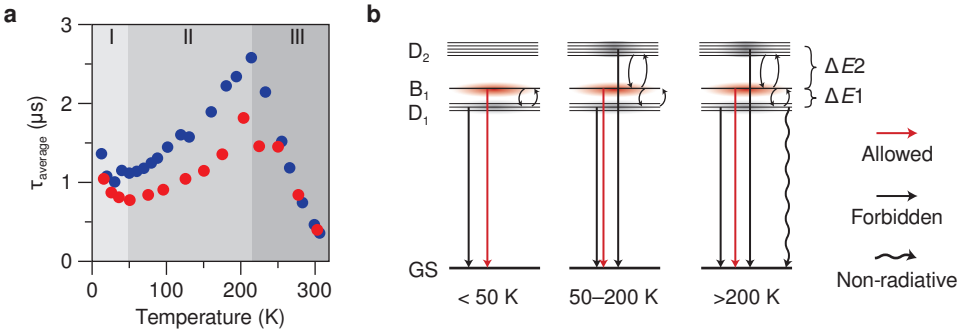

Figure S6.5 | Temperature-dependent lifetime of Ag_2S NCs and the proposed three-level excited state model for Ag_2S. (**a**) Plot of the average lifetime as a function of temperature for the Ag_2S-PEG NCs (blue) and the Ag_2S-DDT NCs (red). At 0 K only the lowest dark state (D_1) is populated and all emission takes place from there. With increasing temperature, the lifetime becomes shorter because increasingly, the bright B_1 excited state is thermally populated. Upon increasing the temperature above 50 K (region II), the higher energy excited dark state D_2 is populated which lengthens the average observed lifetime. In region III non-radiative process increasingly dominate the observed decay time and quench the emission. (**b**) Same plot as in **Figure 6.4** in the main text showing the temperatures at which the different states become thermally occupied and corresponding to the Regions I, II and III in panel **a**.

References

[1] T. Yang, Y. Tang, L. Liu, X. Lv, Q. Wang, H. Ke, Y. Deng, H. Yang, X. Yang, G. Liu, Y. Zhao, H. Chen, *ACS Nano* **2017**, 11, 1848.

[2] L. Ming, I. Zabala-Gutierrez, O. G. Calderon, S. Melle, E. Ximendes, J. Rubio-Retama, R. Marin, *Opt. Mater.* **2023**, 141, 113940.

[3] M. P. Hirsch, *Environ. Toxicol. Chem.* **1998**, 17, 601.

[4] D. Asik, M. B. Yagci, F. Demir Duman, H. Y. Acar, *J. Mater. Chem. B* **2016**, 4, 1941.

[5] D. Ruiz, B. del Rosal, M. Acebrón, C. Palencia, C. Sun, J. Cabanillas-González, M. López-Haro, A. B. Hungría, D. Jaque, B. H. Juarez, *Adv. Funct. Mater.* **2017**, 27, 1604629.

[6] H. D. A. Santos, D. Ruiz, G. Lifante, C. Jacinto, B. H. Juarez, D. Jaque, *Nanoscale* **2017**, 9, 2505.

[7] Y. Shen, H. D. A. Santos, E. C. Ximendes, J. Lifante, A. Sanz-Portilla, L. Monge, N. Fernández, , C. Jacinto, C. D. S. Brites, L. D. Carlos, A. Benayas, M. C. Iglesias-de la Cruz, D. Jaque, *Adv. Funct. Mater.* **2020**, 30, 2002730.

[8] V. M. Huxter, T. Mirkovic, P. S. Nair, G. D. Scholes, *Adv. Mater.* **2008**, 20, 2439.

[9] Z. Feng, T. Tang, T. Wu, X. Yu, Y. Zhang, M. Wang, J. Zheng, Y. Ying, S. Chen, J. Zhou, X. Fan, D. Zhang, S. Li, M. Zhang, J. Qian, *Light Sci. Appl.* **2021**, 10, 197.

[10] Y. Du, B. Xu, T. Fu, M. Cai, F. Li, Y. Zhang, Q. Wang, *J. Am. Chem. Soc.* **2010**, 132, 1470.

[11] M. Yarema, S. Pichler, M. Sytnyk, R. Seyrkammer, R. T. Lechner, G. Fritz-Popovski, D. Jarzab, K. Szendrei, R. Resel, O. Korovyanko, M. A. Loi, O. Paris, G. Hesser, W. Heiss, *ACS Nano* **2011**, 5, 3758.

[12] Y. Zhang, G. Hong, Y. Zhang, G. Chen, F. Li, H. Dai, Q. Wang, *ACS Nano* **2012**, 6, 3695.

[13] C. Ding, Y. Huang, Z. Shen, X. Chen, *Adv. Mater.* **2021**, 33, 2007768.

[14] A. Ortega-Rodríguez, Y. Shen, I. Zabala Gutierrez, H. D. A. Santos, V. Torres Vera, E. Ximendes, G. Villaverde, J. Lifante, C. Gerke, N. Fernández, O. G. Calderón, S. Melle, J. Marques-Hueso, D. Mendez-Gonzalez, M. Laurenti, C. M. S. Jones, J. M. López-Romero, R. Contreras-Cáceres, D. Jaque, J. Rubio-Retama, *ACS Appl. Mater. Interfaces* **2020**, 12, 12500.

[15] I. Z. Gutierrez, C. Gerke, Y. Shen, E. Ximendes, M. M. Silvan, R. Marin, D. Jaque, O. G. Calderón, S. Melle, J. Rubio-Retama, *ACS Appl. Mater. Interfaces* **2022**, 14, 4871.

[16] H. D. A. Santos, I. Zabala Gutiérrez, Y. Shen, J. Lifante, E. Ximendes, M. Laurenti, D. Méndez-González, S. Melle, O. G. Calderón, E. López Cabarcos, N. Fernández, I. Chaves-Coira, D. Lucena-Agell, L. Monge, M. D. Mackenzie, J. Marqués-Hueso, C. M. S. Jones, C. Jacinto, B. del Rosal, A. K. Kar, J. Rubio-Retama, D. Jaque, *Nat. Commun.* **2020**, 11, 2933.

[17] O. E. Semonin, J. C. Johnson, J. M. Luther, A. G. Midgett, A. J. Nozik, M. C. Beard, *J. Phys. Chem. Lett.* **2010**, 1, 2445.

[18] Y. Zhang, Y. Liu, C. Li, X. Chen, Q. Wang, *J. Phys. Chem. C* **2014**, 118, 4918.

[19] S. Lin, Y. Feng, X. Wen, P. Zhang, S. Woo, S. Shrestha, G. Conibeer, S. Huang, *J. Phys. Chem. C* **2015**, 119, 867.

[20] W. J. Mir, A. Swarnkar, R. Sharma, A. Katti, K. V. Adarsh, A. Nag, *J. Phys. Chem. Lett.* **2015**, 6, 3915.

[21] A. S. Perepelitsa, M. S. Smirnov, O. V. Ovchinnikov, A. S. Kotko, A. I. Zvyagin, A. N. Latyshev, L. Y. Leonova, *Russ. J. Phys. Chem. B* **2018**, 12, 611.

[22] M. S. Smirnov, O. V. Ovchinnikov, *J. Lumin.* **2020**, 227, 117526.

[23] K. E. Knowles, H. D. Nelson, T. B. Kilburn, D. R. Gamelin, *J. Am. Chem. Soc.* **2015**, 137, 13138.

[24] A. Al Salman, A. Tortschanoff, M. B. Mohamed, D. Tonti, F. Van Mourik, M. Chergui, *Appl. Phys. Lett.* **2007**, 90.

[25] H. D. Nelson, S. O. M. Hinterding, R. Fainblat, S. E. Creutz, X. Li, D. R. Gamelin, *J. Am. Chem. Soc.* **2017**, 139, 6411.

[26] K. E. Knowles, K. H. Hartstein, T. B. Kilburn, A. Marchioro, H. D. Nelson, P. J. Whitham, D. R. Gamelin, *Chem. Rev.* **2016**, 116, 10820.

[27] S. Yan, *ECS J. Solid State Sci. Technol.* **2023**, 12, 016001.

[28] M. Nirmal, D. J. Norris, M. Kuno, M. G. Bawendi, A. L. Efros, M. Rosen, *Phys. Rev. Lett.* **1995**, 75, 3728.

[29] C. De Mello Donegá, M. Bode, A. Meijerink, *Phys. Rev. B - Condens. Matter Mater. Phys.* **2006**, 74, 1.

[30] M. S. Gaponenko, A. A. Lutich, N. A. Tolstik, A. A. Onushchenko, A. M. Malyarevich, E. P. Petrov, K. V. Yumashev, *Phys. Rev. B - Condens. Matter Mater. Phys.* **2010**, 82, 1.

[31] S. A. Crooker, T. Barrick, J. A. Hollingsworth, V. I. Klimov, *Appl. Phys. Lett.* **2003**, 82, 2793.

[32] Y. Zhao, C. Riemersma, F. Pietra, R. Koole, C. De Mello Donegá, A. Meijerink, *ACS Nano* **2012**, 6, 9058.

[33] G. Morello, M. De Giorgi, S. Kudera, L. Manna, R. Cingolani, M. Anni, *J. Phys. Chem. C* **2007**, 111, 5846.

[34] C. M. S. Jones, N. Panov, A. Skripka, J. Gibbons, F. Hesse, J.-W. G. Bos, X. Wang, F. Vetrone, G. Chen, E. Hemmer, J. Marques-Hueso, *Opt. Express* **2020**, 28, 22803.

Chapter 7

Summary & Outlook

For luminescent materials competition between radiative decay (emission of photons, light) and non-radiative decay (conversion of excited state energy to heat) is crucial for their performance. This battle between light and darkness is the topic in this thesis for a selection of materials that (may) find application in displays, lighting and optical sensing. New insights are presented for different types of materials (insulator or semiconductor, doped or undoped), activator ions (transition metal or lanthanide) and size (micro- or nanocrystalline) and contribute to a brighter future.

7.1 Understanding and improving the luminescence of Mn^{4+}-doped phosphors at higher powers

In the first part of this thesis the red-emitting Mn^{4+}-doped fluorides were investigated. In commercial applications, the high blue-to-red conversion efficiency of ~100% contributes to their success, as well as their sharp emission lines in the red part of the spectrum where the eye sensitivity is still high. The sharp emission lines create the additional benefit of being able to generate colors in displays with high purity for a wider color gamut. Despite the success of K_2SiF_6:Mn^{4+} as a red display phosphor, at higher photon fluxes the slow radiative rate of Mn^{4+} emission in fluorides (~ms^{-1}) causes droop i.e. decreasing performance at increasing power. This limits its applicability for high-power applications, including white-light LEDs. In **Chapter 3** we provide a unified picture of all the processes that contribute to droop, while in **Chapter 4** we discuss the synthesis and characteristics of a novel Mn^{4+}-doped fluoride that can alleviate some of the identified causes of saturation.

In **Chapter 3** of this thesis, we investigate droop in the red-emitting phosphor K_2TiF_6:Mn^{4+} (KTF) on a custom built set-up that allows for a wide range of (high-)power excitation densities. Previous studies have identified Auger quenching, absorption bleach and heating as causes of droop in Mn^{4+}-doped fluorides but have not unified these in a single model.[1–3] The challenge in creating a unified picture stems from the fact that the effect of Auger quenching, thermal quenching and absorption bleach are difficult to separate experimentally: Auger quenching and absorption bleach result in the same sublinear increase in the emission output with increasing excitation intensity, while thermal quenching at high temperatures causes a drop in the emission intensity. We constructed a model with a few input parameters: an experimental fit parameter, the temperature-dependent radiative and non-radiative decay rates during our measurements, the absorption cross-section of Mn^{4+} ions, and the Auger rate between neighboring Mn^{4+} ions, both in the excited state.

We used the unique temperature-dependent emission spectrum of KTF:Mn^{4+} and calibrated it for use as an in situ thermometer during our continuous-wave excitation intensity versus emission intensity measurements. Based on these results we were able to measure the temperature and thus determine the non-radiative and radiative decay rates during our saturation experiments. The absorption cross-section of Mn^{4+} can be extracted from the saturation curve of a low-doped sample (0.1%) under the assumption that Auger losses play a negligible role at this low doping concentration. We determined the Auger rate in a separate experiment by performing ns-pulsed measurements on a highly doped sample (5.4%) at different excitation intensities. We used a 'shell model' that takes into account discrete distances between Mn^{4+} ions to explain and fit the faster decay component observed at increasing excitation powers and used this to determine the contribution of Auger quenching.[4]

After having quantified the impact of heating, absorption bleach and Auger quenching separately, we employed kinetic Monte Carlo modeling to simulate the droop behavior of KTF:Mn^{4+} at different Mn^{4+} concentrations. The results are in good agreement with our experimental data and we find that at the lowest Mn^{4+} concentration (<2%) absorption bleach is the largest contributor to droop. For the (commercially relevant) higher doped (>2%) samples, heat formation and Auger quenching become more important. We conclude that, especially at higher dopant concentrations, heat control and a faster radiative rate are required to improve the performance of Mn^{4+}-doped fluorides under higher excitation power.

To further refine the model explaining droop in Mn^{4+}-doped fluorides and provide even stronger experimental evidence for the quantitative contribution of several quenching paths, we see several research directions. To more accurately determine the impact of absorption bleach on the droop behavior in Mn^{4+} doped fluorides, transparent ceramic samples can be very useful for future research. Because of light scattering in our powder samples, we could not measure the fraction of our excitation light that was absorbed by Mn^{4+} and converted into red light. Therefore, our value for the absorption cross-section σ_{abs} is probably a slight overestimation because blue excitation light could scatter throughout the sample multiple times instead of just passing through once. This is a challenge in general for estimating the quantum efficiency of powdered phosphor materials. If a powder can be transformed into a transparent ceramic, as demonstrated to be feasible in ref [2], the amount of absorbed and transmitted light follows Lambert–Beer's law. An additional benefit of using ceramic based phosphors could be the improved heat transport to help reduce thermal quenching.[2,5]

Another direct technique for investigating the effect of Auger quenching and identify the role of excited state absorption is the use of transient absorption (TA) spectroscopy. This technique is very useful in establishing the rates of "dark" processes like excited-state absorption and Auger quenching. We tried to measure the TA spectrum of KTF:Mn^{4+} and concluded that the bright emission of Mn^{4+} around 630 nm obscures any differential signals in that region. To find out more about the role and nature of the Auger upconversion, it is useful to perform intensity-dependent luminescence lifetime measurements on several Mn^{4+}-doped hosts with a varying crystal field strength. The shift in energy of the $^4T_1$ level with crystal-field strength is expected to impact the Auger quenching rate as the spectral overlap for the Auger energy-transfer process will depend on the position of the higher energy $^4T_1$ excited state, without shifting the position of the ^2E energy levels from the desired 630 nm.

Our work clearly identifies which droop mechanisms are dominant with increasing blue excitation power and at different Mn^{4+} concentrations. The long ms lifetime of Mn^{4+} ions causes the buildup of population of Mn^{4+} ions in the excited state at high excitation powers. To extend the applicability of Mn^{4+}-doped fluorides to higher power applications the radiative lifetime should be shortened. Available tuning knobs to realize this are the choice of host material, temperature management, and (nano)photonic design.

In **Chapter 4**, we discuss the discovery and characterization of a new crystalline phase which can partly mitigate the droop in Mn^{4+}-based phosphors under high power density excitation: hexagonal (K,Rb)SiF_6:Mn^{4+} (h-KRSF). Due to the lower local symmetry around the Mn^{4+} ion the emission in this new host material has a 25% faster emission rate than for cubic K_2SiF_6:Mn^{4+} (KSF). The deviation from inversion symmetry in the first F^- coordination sphere around Mn^{4+}

gives rise to a distinct zero-phonon line (ZPL) at a wavelength where the eye sensitivity is higher, thus contributing to an enhanced lumen/W output. Stronger absorption, also related to a deviation from inversion symmetry, decreases the blue excitation power needed to achieve an equivalent level of human-perceived "red" in lighting. We further characterized the novel phosphor and compared it with commercial KSF. Temperature-dependent emission and lifetime measurements reveal a high luminescence-quenching temperature of ~500 K for h-KSRF, similar to KSF. In addition, emission and luminescence lifetime measurements show that up to ~10% Mn^{4+} doping, concentration quenching does not affect the quantum yield of the material. Temperature-dependent XRD shows that above ~500 K a phase transformation back to cubic KRSF (c-KRSF) takes place. This is well above the operating temperature in wLEDs around ~373 K. We were not able synthesize pure KSF:Mn^{4+} in the hexagonal modification indicating an important role for Rb in the formation of h-KSRF.

The discovery of h-KRSF was serendipitous and a consequence of our attempts to shorten the lifetime of Mn^{4+} emission by mixing various alkaline cations M like Na, K, Rb and Cs in solid solutions with composition M_2SiF_6. The idea was to create disorder in the second coordination sphere and thus shorten the lifetime of Mn^{4+} emission and induce a ZPL in the emission spectrum. After several failed attempts, one mixture containing K and Rb ions was left in the fume hood to release toxic HF for about a week, only to have transformed into h-KRSF upon our return. To our advantage, the synthesis protocol leading to h-KSRF involved an almost transparent reaction mixture that allowed us to monitor the formation mechanism of h-KRSF in situ. This was achieved by measuring the rise of the ZPL in the emission spectra of the precipitate in solution over time. Initially nanocrystalline c-KRSF is formed which transforms into the microcrystalline hexagonal precipitate while the ethanol/water/HF solvent evaporates. After an induction period of ~15 hours, the transformation takes place with a surprising exponential increase in transformation rate that is finished after roughly 10 hours.

The attractive properties of our new h-KRSF phase are not described in academic literature, but have been mentioned in a 2014 patent.[6] What is still lacking is Mn^{4+}-doped pure h-K_2SiF_6. Even though the (undoped) hexagonal phase has been reported for KSF a few times in the last century[7–9] and was observed near the opening of an active volcano,[10] we have not been able to synthesize pure-phase hexagonal KSF. With our synthesis protocol it is uniquely possible to track the influence of reaction parameters on the cubic-to-hexagonal KRSF phase transformation process. Our hypothesis, that the hexagonal phase is the thermodynamically more stable phase but is kinetically never obtained under normal reaction conditions, can be further investigated by varying reaction parameters such as temperature, choice of (anti)-solvent and reactant concentrations.

The slow transformation to the h-KSRF phase is possibly related to two different crystallographic positions for the M^+ ion the hexagonal crystal structure. DFT calculations showed an energetic preference for the distribution where smaller K^+ ions locate on smaller M1 lattice sites, while the Rb^+ ions locate exclusively on the larger M2 site. Single-crystal XRD measurements could reveal more about the actual location of the K and Rb ions within the hexagonal lattice. Such an ordering could also reveal information about the cubic-to-hexagonal transformation. Perhaps the slow growth process could be driven by the sequential incorporation of K and Rb ions in solution, similar to what has been reported for the growth of the dolomite mineral $CaMg(CO_3)_2$.[11]

7.2 Energy transfer from semiconductor $Cs_2AgBiBr_6$ to Yb^{3+}

Semiconductor nanocrystals (NCs) doped with lanthanides can be used to kill two birds with one stone: they typically have very strong (tunable) absorption in the blue while lanthanides have narrow line emission, ideal for achieving high color purity in displays. In this context, we investigated various (double) perovskite NCs and doped them with different lanthanide ions, including Eu^{3+} (red), Tb^{3+} (green) and Yb^{3+} (near-infrared). While doping with Yb^{3+} does not have direct implications for display applications, it is an ideal candidate for investigating the host-to-Ln^{3+} energy transfer mechanism because of its simple energy level structure with only one excited state at ~10 000 cm^{-1} above the ground state (see Dieke diagram in **Figure 2.9**). Incorporating Yb^{3+} in halide (double) perovskite or elpasolite lattices has been shown to give rise to near-infrared (NIR) emission but the energy-transfer mechanism is still under debate. [12,13]

In **Chapter 5**, we present a detailed investigation into the luminescence and sensitization mechanism of Yb^{3+} within elpasolite $Cs_2AgBiBr_6$ nano- and microcrystals (NCs and MCs) by means of temperature-dependent emission and time-resolved spectroscopy between 4 K and room temperature. Our findings show that the incorporation of Yb^{3+} in the host lattice has a minimal impact on the $Cs_2AgBiBr_6$ host's broadband red emission, while introducing an additional ~1000 nm NIR line emission from Yb^{3+}. Surprisingly, the Yb-emission intensity as a function of temperature shows negative thermal quenching in both $Cs_2AgBiBr_6$ NCs and MCs up to 250 K while the red, self-trapped exciton (STE) emission shows strong thermal quenching above 50 K. To investigate the energy-transfer mechanism, we recorded temperature-dependent luminescence decay curves of the host emission in both doped and undoped $Cs_2AgBiBr_6$ NCs. Our measurements revealed no difference between the two samples, thereby ruling out the possibility of energy transfer through the self-trapped state.

Instead, we propose that the host-to-Yb energy transfer takes place by trapping a conduction band electron on Yb^{3+}, which is in competition with forming a STE state that is responsible for the red host emission band. A charge-transfer recombination (CT) of Yb^{2+} with a trapped hole yields Yb^{3+} in the excited $^2F_{5/2}$ state, which results in sharp line emission around 1000 nm due to the $^2F_{5/2} \rightarrow {}^2F_{7/2}$ transition. Up to 250 K, the negative thermal quenching of the Yb^{3+} emission is explained by thermally activated hole mobility, increasing the probability of CT recombination of a hole with Yb^{2+}. The decrease in Yb^{3+} emission intensity above 250 K can be explained by thermally activated crossover from the CT state to the $^2F_{7/2}$ ground state instead of populating the $^2F_{5/2}$ excited state.

The evidence we provide for the Yb^{3+} sensitization mechanism by electron trapping is based on measuring thermal quenching, relying on the temperature dependence of both the emission intensity and luminescence decay times. The observations clearly show that energy transfer does not proceed via the STE state of the host but there is no direct evidence for electron trapping by Yb^{3+}. Optically stimulated deexcitation could provide direct evidence similar to what has been reported for Yb^{3+} doped in InP.[14] In the case of optically stimulated deexcitation one uses sequential excitation by two different lasers. The first pulsed laser is used to excite Yb^{3+} through $Cs_2AgBiBr_6$ bandgap excitation and a second pulsed, tunable (near-)infrared laser is used to optically deexcite the electron trapped on Yb^{3+} at variable delay times after the first pulse. If, at a given photon energy, the Yb^{3+} emission intensity decreases one can experimentally determine both the optical trap depth and dynamics of the electron on Yb^{3+} with respect to the conduction-band minimum and provide more direct evidence for electron trapping by Yb^{3+}. Experiments in which Eu^{3+} or Tb^{3+}

Tb^{3+} were doped into $Cs_2AgBiBr_6$ NCs and MCs failed to show red Eu^{3+} or green Tb^{3+} emission following host lattice excitation. It is not clear why. Possibly, emission from the higher energy $4f^n$ states is quenched via charge-transfer states. It remains a challenging field of research to dope visible-light-emitting lanthanides into semiconductor NCs and combine strong semiconductor-host absorption with efficient green or red narrow-line emission.

7.3 Thermal quenching in Ag_2S NCs

Semiconductor nanocrystals do not only hold great promise for lighting and display technologies, but have also established themselves as workhorses in the biomedical field. Notably, the use of bright near-infrared (NIR) emitting Ag_2S nanocrystals (NCs) holds great promise for applications like in vivo imaging, cancer therapy and temperature sensing. This is particularly promising because of their low (cyto)toxicity in comparison with NIR emitting alternatives like CdSe and PbSe NCs. Temperature sensing using Ag_2S NCs relies on the reversible variation in both emission intensity and luminescence lifetime within the physiological temperature regime. Despite Ag_2S NCs being a focal point of research for over a decade, the quantum yield (QY) lags behind that of e.g. PbSe NCs (~10% vs. 40%) and the origin of temperature-dependent optical properties remained elusive.

In **Chapter 6**, we report on the photoluminescence of bright dodecanethiol (DDT) and polyethylene glycol (PEG) capped Ag_2S NCs between 10 and 300 K. Cooling both types of Ag_2S NCs down from room temperature to 10 K results in a large blueshift of the emission band (~120 meV), which is typical Varshni behavior for semiconductors. The full width at half maximum (fwhm) of the emission band for both Ag_2S NCs remains large, around 100 meV at 10 K, and suggests strong electron–phonon coupling given the absence of quantum confinement effects in ~10 nm Ag_2S NCs. Between 200 and 300 K, we observe strong and reversible emission intensity quenching in both DDT and PEG capped Ag_2S NCs, which is confirmed by variable-temperature time-resolved spectroscopy. These results show that the temperature-dependent emission intensity and decay time, which are used for temperature sensing, originate from an intrinsic thermal-quenching process that already starts at 200 K. It also means the maximum quantum yield of bright Ag_2S NCs at room temperature is around 15%.

Cooling Ag_2S NCs further down, below 200 K, does not affect the emission intensity, but does result in a 2.5 fold (PEG) and 2 fold (DDT) decrease in the average lifetime at 50 K. Below 50 K the average lifetime lengthens again. These results are explained by the existence of thermally coupled excited states in Ag_2S from which radiative decay is possible. The highest-energy excited state is a dark state characterized by slow spin-forbidden decay, at lower energy there is a bright state from which fast decay is possible and at the lowest energy, there is again a dark state which freezes in population below 50 K resulting in a lengthening of the average lifetime with temperature.

Finally, our results for Ag_2S NCs are consistent with a luminescence mechanism of recombination of a trapped hole and a conduction-band electron, resulting in emission involving a strong local lattice relaxation. First, between 10 K and 300 K all decaycurves are multi-exponential. This could be a consequence of the presence of variations in the non-radiative decay rate because of differences in (surface) defects but non-exponential decay is observed even for the most efficient Ag_2S NCs and down to 10 K. A similar temperature-invariant multi-exponential decay has been observed for e.g. $CuInS_2$ NCs and is ascribed to hole trapping on different Cu^+ sites resulting in inherently different radiative rates since the decay rate will depend on the wavefunction overlap

between the hole and delocalized CB electron.[15,16] For holes trapped in the center of the NC this overlap will be larger than for holes trapped in the outer rings of the NCs. Second, the low thermal-quenching temperature and large fwhm are characteristic of an optical transition with strong electron–phonon coupling and a large offset between the ground state and excited state parabola. Such characteristics are in line with recombination processes involving a trapped charge carrier, giving rise to significant local lattice reorganization. Emission originating from recombination of delocalized charge carriers has a narrow fwhm, especially at low temperatures.

There are several strategies to gather evidence for the presence of multiple, thermally coupled excited states. Firstly, excited-state DFT or tight-binding calculations can provide insight in the energy level structure of Ag_2S and provide detailed understanding of the nature of specific energy levels, their positions, and associated degeneracies in Ag_2S. Secondly, conducting analogous temperature-dependent optical studies on Ag_2S NCs with sizes below 4 nm are expected to reveal a larger splitting between the energy levels as a result of quantum confinement.[17]

Further research can also help to support the emission mechanism in Ag_2S NCs (recombination of a delocalized electron with a trapped hole), like $CuInS_2$. Especially promising are single-NC measurements at cryogenic temperatures. Recombination of an electron with a trapped hole in Ag_2S would still result in broad emission bands because of the strong lattice relaxation (electron–phonon coupling) and multi-exponential decay because of different recombination rates caused by variations in electron–hole overlap depending on the location for hole trapping.[18] These characteristics will be very different from narrow line emission and single-exponential decay expected for recombination of a delocalized CB electron and VB hole as typically observed for semiconductor nanocrystals such as CdSe, CdTe and PbSe.

In this thesis I have provided new insights in processes giving rise to emission of light or non-radiative relaxation for a variety of luminescent materials that are closely linked to applications in lighting, displays, optical imaging and sensing. At the same time the research raises new questions. Applications of light-emitting materials continue to expand and to go beyond the traditional fields of lighting and displays and can benefit from the knowledge presented here.

References

[1] M. A. Van De Haar, M. Tachikirt, A. C. Berends, M. R. Krames, A. Meijerink, F. T. Rabouw, *ACS photonics* **2021**, 8, 1784.
[2] R. A. Osborne, N. J. Cherepy, Z. M. Seeley, S. A. Payne, A. D. Drobshoff, A. M. Srivastava, W. W. Beers, W. W. Cohen, D. L. Schlagel, *Opt. Mater.* **2020**, 107, 110140.
[3] H. F. Sijbom, J. J. Joos, L. I. D. J. Martin, K. Van den Eeckhout, D. Poelman, P. F. Smet, *ECS J. Solid State Sci. Technol.* **2016**, 5, R3040.
[4] T. Senden, F. T. Rabouw, A. Meijerink, *ACS Nano* **2015**, 9, 1801.
[5] Y. Zhou, C. Yu, E. Song, Y. Wang, H. Ming, Z. Xia, Q. Zhang, *Adv. Opt. Mater.* **2020**, 8, 2000976.
[6] V. Weiler, P. J. Schmidt, W. Schnick, M. A. Seibald, US9422471B2, **2014**.
[7] B. Gossner, *Zeitschrift für Krist. - Cryst. Mater.* **1904**, 38, 110.
[8] L. Kolditz, H. Preiss, *Z. Anorg. Allg. Chem.* **1963**, 325, 245.
[9] M. E. Denaeyer, D. Ledent, *Bull. Soc. Fr. Minéral, Cristallogr.* **1952**, 75, 231.
[10] C. M. Gramaccioli, I. Campostrini, *Can. Mineral.* **2007**, 45, 1275.
[11] J. Kim, Y. Kimura, B. Puchala, T. Yamazaki, U. Becker, W. Sun, *Science* **2023**, 382, 915.
[12] M. N. Tran, I. J. Cleveland, E. S. Aydil, *ACS Appl. Electron. Mater.* **2022**, 4, 4588.
[13] N. Chen, T. Cai, W. Li, K. Hills-Kimball, H. Yang, M. Que, Y. Nagaoka, Z. Liu, D. Yang, A. Dong, C. Y. Xu, R. Zia, O. Chen, *ACS Appl. Mater. Interfaces* **2019**, 11, 16855.
[14] M. A. J. Klik, T. Gregorkiewicz, I. V. Bradley, J. P. R. Wells, *Phys. Rev. Lett.* **2002**, 89, 227401.
[15] K. E. Knowles, K. H. Hartstein, T. B. Kilburn, A. Marchioro, H. D. Nelson, P. J. Whitham, D. R. Gamelin, *Chem. Rev.* **2016**, 116, 10820.
[16] K. E. Knowles, H. D. Nelson, T. B. Kilburn, D. R. Gamelin, *J. Am. Chem. Soc.* **2015**, 137, 13138.
[17] C. De Mello Donegá, M. Bode, A. Meijerink, *Phys. Rev. B - Condens. Matter Mater. Phys.* **2006**, 74, 1.
[18] S. O. M. Hinterding, M. J. J. Mangnus, P. T. Prins, H. J. Jöbsis, S. Busatto, D. Vanmaekelbergh, C. De Mello Donega, F. T. Rabouw, *Nano Lett.* **2021**, 21, 658.

Chapter 8

Nederlandse samenvatting

Introductie

Luminescente materialen vormen tegenwoordig een onmisbare schakel in vele moderne technologieën. Het is een van de stille technologische hoogstandjes die zo goed werken, dat je nooit stilstaat bij de positieve impact die ze hebben op je leven. Denk aan verlichting nadat de zon is ondergegaan en de schermen waarmee je met de wereld om je heen communiceert.

In dit proefschrift zijn bestaande en nieuwe fotoluminescente materialen onderzocht. Voor de duidelijkheid, dit zijn materialen die licht van een bepaalde kleur absorberen om daarna een andere kleur uit te zenden. Echter, dit vervalproces (licht uitzenden) ervaart vaak concurrentie van niet-stralend verval (omzetten energie in warmte). Vandaar de titel van dit proefschrift: Licht of Donker. Tijdens het onderzoek hebben we ons gericht op twee typen luminescente materialen: (i) Mangaan-gedoteerde kristallen die al veel in (telefoon)schermen worden toegepast en (ii) Halfgeleider nanokristallen, die veel potentie hebben maar nog mondjesmaat in de praktijk worden gebruikt.

Voordat we fotoluminescentie bespreken is het nuttig om even stil te staan bij hoe licht kan worden beschouwd. Licht bestaat uit massaloze elementaire deeltjes genaamd fotonen, waarvan de eigenschappen ook kunnen worden beschreven met golven. Wanneer we praten over de golflengte van licht, beschrijven we eigenlijk de afstand tussen opeenvolgende punten op een lichtgolf: hoe korter de golflengte, hoe hoger de energie van een foton. In **Figuur 7.1** kun je zien dat zichtbaar licht golflengtes heeft tussen de 400 (violet) en 700 (rood) nanometer, een nanometer is een miljardste van een meter. Blauw licht heeft een kortere golflengte dan rood licht, en heeft daarom een hogere fotonenergie.

Fotoluminescentie voor verlichting

Om toch wat context te geven over hoe ver we al zijn gekomen in termen van efficiëntie en flexibiliteit, ga ik terug naar het begin. De eerste menselijke pogingen om kunstmatig licht te creëren waren gebaseerd op verhitting, of specifieker, op verbranding. Pas sinds het begin van de 20ste eeuw heeft de gecontroleerde elektrische verhitting van wolfraamdraadjes in gloeilampen ervoor gezorgd dat kunstmatige verlichting op steeds grotere schaal beschikbaar werd. Net als in de zon, of in roodgloeiende kooltjes, zorgt de hoge temperatuur van het wolfraamdraadje ervoor dat de lamp licht uitzendt van het zichtbaar tot ver in het infrarood. Het lampspectrum van een gloeilamp is weergegeven in **Figuur 7.2a**. In hetzelfde figuur is de menselijke ooggevoeligheid geplot als een stippellijn. Hieruit blijkt dat het gros van het uitgezonden licht van een gloeilamp niet door mensen kan worden waargenomen.

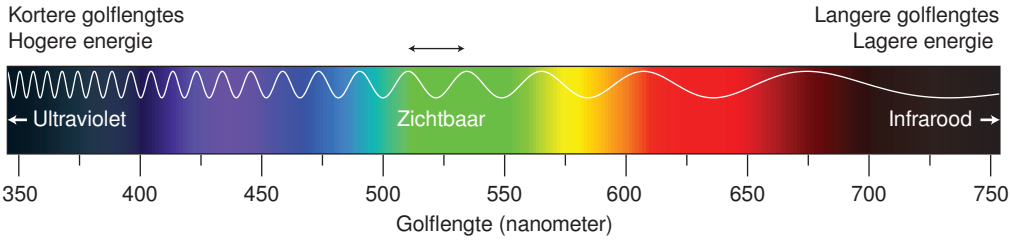

Figuur 7.1 | Het spectrum van zichtbaar licht uitgedrukt in golflengte. Licht kan worden beschreven als een golf in de ruimte, de afstand tussen twee maxima is dan de golflengte λ. Licht met een kortere golflengte heeft hogere fotonenergie dan licht met een langere golflengte.

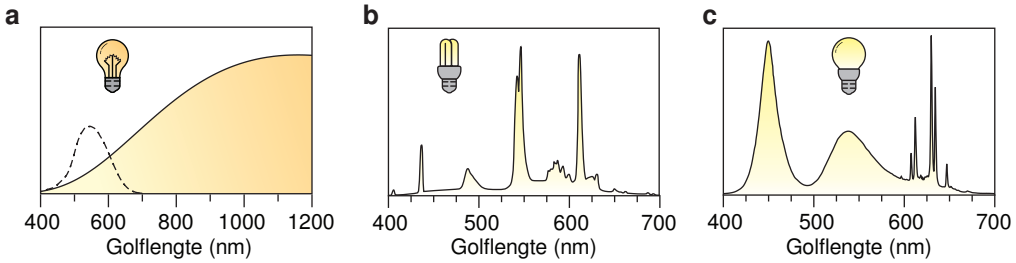

Figuur 7.2 | Oude en nieuwe lichtbronnen en hun emissiespectra. (**a**) Spectrum van een gloeilamp. De wolfraamdraad in een gloeilamp zendt licht uit omdat het tot ~2500 °C wordt verwarmd. Hierdoor zendt het naast zichtbaar licht, net als de zon, ook veel infrarood licht uit. Ter illustratie: de piek van dit spectrum ligt pas rond de 1150 nm. De stippellijn geeft de menselijke ooggevoeligheid weer. (**b**) Spectrum van een spaarlamp gevuld met kwikdamp en voorzien van een fosforcoating met daarin de optisch actieve lanthaniden europium (Eu) en terbium (Tb). (**c**) Emissie spectrum van een witte LED lamp die vaak wordt gebruikt als backlight in beeldschermen. Van links naar rechts horen de pieken bij de blauwe LED, een Eu-gedoteerde fosfor en de scherpe emissie pieken aan de rechterkant (rond 630 nm) zijn het gevolg van een mangaan (Mn) gedoteerde fosfor.

Aangezien er bij gloeilampen 95% van de energie verloren gaat in de vorm van warmte, heeft de zoektocht naar een hogere lichtopbrengst geleid tot de ontdekking en intrede van de TL buis (Frans: *tube luminescent*), gevolgd door de spaarlamp van Philips rond 1980. Hierin wordt door een elektrische stroom gasvormig kwik in de buis geïoniseerd, waarna het UV straling uitzendt. De wanden van de TL buis of spaarlamp zijn gecoat met dunne poederlagen (bestaande uit fosforen) die het voor ons onzichtbare UV licht absorberen en omzetten in blauw, groen en rood licht. Dit blauwe, groene en rode licht maken samen wit licht. In **Figuur 7.2b** is het spectrum van een veel voorkomende fluorescentielamp geplot als functie van golflengte. De scherpe pieken zijn een combinatie van luminescentie van het kwik (Hg) en de lanthaniden Terbium (Tb) en Europium (Eu). Nog los van het giftige kwik, heeft ook dit type lamp zo zijn nadelen: het elektrische circuit is relatief ingewikkeld, kwikionisatie kost veel energie en doordat UV fotonen (hoge energie) worden omgezet in zichtbare fotonen (lage energie) neemt de elektriciteit-naar-licht opbrengst af tot ~25% voor de meest efficiënte spaarlampen.

Begin jaren 90 is het na veel onderzoek gelukt om een zeer efficiënte blauw emitterende light-emitting diode (LED) te ontwikkelen. Hierin wordt elektriciteit direct omgezet in blauw licht. Initieel was het plan om deze blauwe LEDs te combineren met de bestaande rode en groene LEDs, maar dit bleek te ingewikkeld en duur voor massaproductie en wordt tegenwoordig alleen in enkele duurdere niche producten zoals de veelkleurige Philips Hue verlichting gebruikt. In plaats daarvan werden wederom fosforen om de blauwe LED gecoat, die een gedeelte van het blauwe licht omzetten in groen en rood licht om zo het gewenste witte licht te krijgen (**Figuur 7.2c**). Door de samenstelling van de fosforlaag te veranderen kan de 'warmte' van het licht worden aangepast van koud of klinisch (ziekenhuis) naar warm (sfeerverlichting). Vanwege de hoge efficiëntie, lange levensduur, en de lage prijs is de blauwe LED-fosfor combinatie inmiddels niet meer weg te denken uit de hedendaagse verlichting en beeldschermtechnologie. Deze innovatie heeft een enorme bijdrage geleverd aan een energiezuinigere wereld.

De werking en verbetering van rode fosforen

De combinatie blauwe LED en fosforen is eigenlijk vrij simpel, er zit namelijk een epoxy laag met fosforen boven op de blauwe LED. Je hebt dit gele laagje vast wel eens zien zitten bij een witte

LED lamp. Als we inzoomen op de fosforlaag vlak boven de blauwe LED, bestaat die uit losse deeltjes van enkele micrometers (**Figuur 7.3**), feitelijk niet meer dan een zeer fijn, vastgezet poeder. Meestal bestaat het fosformengsel uit een geel of groen en rood emitterende fosfor. Als we nog verder inzoomen tot op de atomaire schaal van fosforen, bestaan deze uit positief (kation) en negatief (anion) geladen atomen die volgens een bepaalde, nauwkeurig gedefinieerde kristalstructuur geordend zijn. In het rechterpaneel van **Figuur 7.3** is een schematisch 2D voorbeeld gegeven van ionen in een hexagonale pakking. De optische eigenschappen van de fosfor zijn het gevolg van toevoegingen in het kristal: sommige kationen zijn vervangen door optisch actieve kationen. Op basis van het luminescente kation en het omringende kristal kan een fosfor de gewenste optische eigenschappen krijgen. Het doelbewust toevoegen van optisch actieve ionen in een kristal heet doteren. Een vergelijkbaar proces vindt plaats in bijvoorbeeld robijnen: de diep rode kleur ontstaat doordat een gedeelte van de aluminium ionen in het Al_2O_3 kristalrooster is vervangen door chroom (Cr). Deze optisch actieve ionen kunnen een lichtpakketje met een bepaalde energie (één foton) absorberen en vervolgens een foton uitzenden met een lagere energie. Enkele bekende voorbeelden van optisch actieve elementen zijn de lanthaniden cerium (Ce) en Europium (Eu) en sommigen transitiemetalen zoals mangaan (Mn) en chroom (Cr).

De hierboven beschreven gedoteerde fosforen vormen een belangrijk deel van het onderzoek beschreven in dit proefschrift. Zo hebben we onderzoek gedaan naar de eigenschappen van mangaan wanneer het is ingebouwd in een kristal dat bestaat uit kalium, titanium en fluor (geschreven als: K_2TiF_6:Mn). De resultaten hiervan zijn beschreven in **Hoofdstuk 3**. Dit type materiaal wordt commercieel veel gebruikt als rode fosfor in (telefoon)schermen, maar nauwelijks in witte lampen. Dit komt door een proces dat verzadiging wordt genoemd. Bij hoge helderheid (blauwe lichtintensiteit) daalt de efficiëntie van blauw-naar-rood omzetting in de fosfor. Dit gaat als volgt: nadat een Mn-ion een blauw foton heeft opgenomen duurt het een tijdje voordat het een rood foton uitzendt en kan het niet nog een blauw foton absorberen. Dus neemt de absorptie van blauw licht af. Daarnaast zorgen opwarming en de koppeling van twee naburige Mn-ionen in de aangeslagen toestand ervoor dat de efficiëntie van blauw-naar-rood omzetting verder afneemt bij hoge lichtintensiteit. Wat dit materiaal uniek maakt is dat de opwarming als gevolg van belichting kan worden gemeten door het emissiespectrum te meten: een luminescente thermometer dus. Met behulp van experimenten en modellen hebben we kwantitatief laten zien hoe absorptiereductie, opwarming en koppeling tussen Mn-Mn buren het verzadigingsgedrag bepalen en bijdragen aan het verlagen van de efficiëntie.

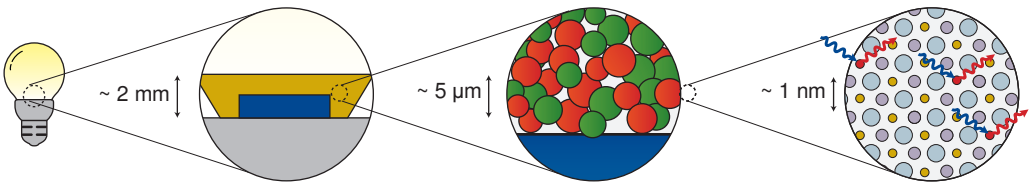

Figuur 7.3 | De werking van fosforen van groot naar klein. In een lamp zit een blauwe LED omringd met fosforkorrels van enkele micrometers, ingebed in een hars. Deze korrels absorberen een deel van het blauwe licht en zetten dit om in groen en rood licht. Als we nog verder inzoomen tot op het niveau van de kristalstructuur, zien we een regelmatige ordening van anionen (blauw) en kationen (paars) met enkele optisch actieve kationen die blauwe fotonen absorberen en heruitzenden als rode fotonen. De absorptie (blauw) en emissie (rood) van fotonen zijn in het rechterpaneel aangegeven met golvende pijlen.

In navolging op bovenstaand werk hadden we een plan bedacht om verzadiging in dit type materiaal tegen te gaan. Dit hield in dat we de helft van het kalium (K) door rubidium (Rb) vervingen in het zeer vergelijkbare K_2SiF_6, waarin Si voor silicium staat. Door wanorde in het kristalrooster als gevolg van ofwel K ofwel Rb op roosterplaatsen rond Mn wordt de omringing van het Mn kation minder symmetrisch. Het idee was dat Mn-ionen hierdoor na absorptie van een blauw foton sneller een rood foton uit zouden zenden en er dus minder snel verzadiging zou optreden. Na vele mislukte pogingen zo snellere rode emissie te realiseren, hebben we een reactiemengsel een week laten staan voor het op te ruimen. Ondanks het ogenschijnlijk mislukte experiment hebben we het reactiemengsel toch gereinigd en gemeten, waarna bleek dat we per ongeluk $KRbSiF_6$ met een hexagonale in plaats van de gebruikelijke kubische kristalstructuur hadden gevormd. In **Hoofdstuk 4** beschrijven we deze synthese en eigenschappen van dit op basis van toeval gevonden materiaal $KRbSiF_6$. Het materiaal heeft niet alleen een snellere uitzending van rode fotonen (minder verzadiging), maar heeft ook een extra emissiepiek in het gebied waar de ooggevoeligheid hoger is (hogere lichtopbrengst). Deze extra piek stelde ons ook in staat om de bijzonder trage omzetting van kubisch $KRbSiF_6$ naar hexagonaal $KRbSiF_6$ door middel van het emissiespectrum te volgen en bestuderen in het reactiemengsel.

De emissie van halfgeleider nanokristallen

Naast gedoteerde microkristallen hebben we ook halfgeleider nanokristallen onderzocht in dit proefschrift. Dit is een relatief nieuw soort fotoluminescent materiaal dat sinds begin jaren 90 steeds meer wordt onderzocht. In 2023 hebben drie wetenschappers in dit vakgebied zelfs de Nobelprijs voor de scheikunde ontvangen voor hun bijdrage aan het onderzoek naar halfgeleider nanokristallen. De fotoluminescentie in deze halfgeleider nanokristallen is fundamenteel anders dan in de gedoteerde kristallen: in plaats van dat er een dotering moet worden geïntroduceerd, zijn deze materialen van zichzelf luminescent. De grootte en compositie van het nanokristal bepalen bij welke golflengte er licht wordt geabsorbeerd en uitgezonden. Deze nanokristallen bestaan uit veel minder atomen (10^3–10^4) dan de hierboven beschreven microkristallen (>10^8), wat ervoor zorgt dat de schaal waarop nanokristallen kunnen worden toegepast veel kleiner is (zie **Figuur 7.4a**). Voorbeelden hiervan zijn microLEDs voor een nieuwe generatie beeldschermen en het afbeelden en het gericht meten van de temperatuur op celniveau (**Figuur 7.4b,c**).

Energie overdracht van halfgeleiders naar lanthaniden

Traditionele gedoteerde fosforen, bestaande uit micrometerkorrels, zijn helaas niet geschikt voor microLEDs vanwege hun te grote omvang. Het is mogelijk om deze fosforen op nanometerschaal te produceren, maar ze hebben doorgaans de eigenschap dat ze te weinig licht absorberen om al het blauwe licht van de microLED effectief om te zetten in groen of rood licht. Halfgeleidende nanokristallen vertonen een veel sterkere lichtabsorptie en worden daarom onderzocht als potentiële fosforlaag voor microLEDs.

Een alternatieve benadering is om halfgeleidende nanokristallen te doteren met optisch actieve elementen. Na sterke lichtabsorptie door het halfgeleidende nanokristal kan de energie worden overgedragen aan de gedoteerde kationen. We hebben deze veelbelovende methode onderzocht door cesiumzilverbismutbromide ($Cs_2AgBiBr_6$) nanokristallen te doteren met rood (europium, Eu), groen (terbium, Tb) en infrarood (ytterbium, Yb) emitterende lanthaniden. Ons werk heeft laten zien dat alleen het infrarood emitterende ytterbium via de halfgeleider in een aangeslagen toestand kon worden gebracht.

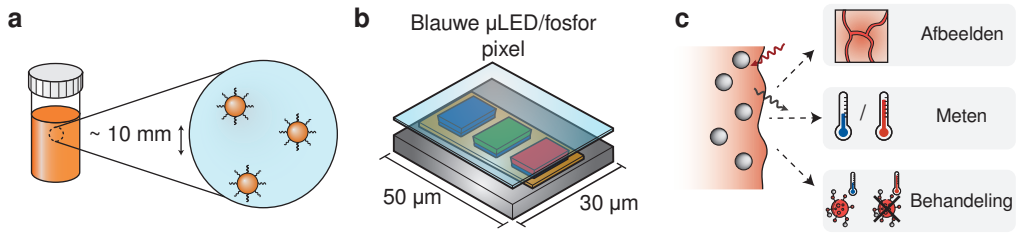

Figuur 7.4 | Halfgeleider nanokristallen en toepassingen. (**a**) Het is gangbaar om halfgeleider nanokristallen als een stabiele colloïdale oplossing te bewaren. Energetisch is het gunstiger als ze samensmelten tot een groter kristal, maar dat wordt belet door een laagje moleculen aan het nanokristal oppervlak die ze in oplossing houdt. Dit klinkt ingewikkeld maar bijvoorbeeld melk is ook een stabiele colloïdale oplossing. (**b**) Een microLED scherm bestaat uit pixels waarvan elke subpixel (blauw, rood, groen) afzonderlijk kan worden uitgezet of aangezet. Hierdoor kan het contrast veel hoger worden dan in traditionele schermen. De rode en groene pixel bestaan in dit ontwerp uit een blauwe microLED gecoat met een dun (rood of groen luminescerend) fosforlaagje. Gezien de zeer kleine schaal werken fosforen op de micrometer schaal niet meer en worden (gedoteerde) nanokristallen hiervoor onderzocht. (**c**) Luminescente nanokristallen kunnen ook worden ingezet om processen te volgen of zelfs beïnvloeden die op de micrometer of nanoschaal plaatsvinden. Een voordeel van nanokristallen is dat het oppervlak ervan kan worden aangepast zodat ze specifiek aan bepaalde cellen of tumoren kunnen binden. In dat kader hebben wij het emissie mechanisme van zilver sulfide nanokristallen onderzocht die gebruikt worden voor het op afstand meten van temperatuur.

Hoewel we geen nieuw interessant microLED-fosfor hebben geproduceerd, bood deze benadering ons de mogelijkheid om het overdrachtsmechanisme van het nanokristal naar ytterbium te onderzoeken. In **Hoofdstuk 5** bespreken we het mechanisme waardoor na absorptie van licht door $Cs_2AgBiBr_6$ ytterbiumemissie kan worden waargenomen. Op basis van temperatuurafhankelijke metingen is het duidelijk dat de energieoverdracht naar Yb plaatsvindt voor en concurreert met relaxatie naar een lagere aangeslagen en licht emitterende toestand van het nanokristal zelf. Dit onderzoek biedt aanknopingspunten voor het doteren van andere lanthaniden en overgangsmetalen in $Cs_2AgBiBr_6$ en andere halfgeleider nanokristallen.

De oorsprong van thermische doving in Ag_2S nanokristallen

Sommige nanokristallen zijn ook interessant om biologische processen mee te volgen. Een voorbeeld hiervan zijn zilversulfide (Ag_2S) nanokristallen. Zowel de absorptie als emissie van deze nanokristallen liggen tussen de 800 en 1300 nm in het infrarood. Deze golflengtes vallen in het zogenoemde optische biologische venster: golflengtes waar de absorptie door organisch weefsel relatief zwak is waardoor deze straling dieper kan binnendringen. Eerder werk heeft aangetoond dat de emissie van deze Ag_2S nanokristallen sterk (en voorspelbaar) afneemt en naar langere golflengtes verschuift tussen de 0 °C en 60 °C. Hierdoor kan het (net als mangaan) als luminescente thermometer worden ingezet: door de emissie van de Ag_2S nanokristallen te meten met een microscoop kan lokaal de temperatuur worden uitgelezen.

Echter, de oorsprong van deze temperatuur-gerelateerde vermindering van de emissie was nog niet opgehelderd in de literatuur. Daarom hebben wij onderzoek gedaan naar de emissie van Ag_2S nanokristallen tussen de −270°C en 30°C. In **Hoofdstuk 6** bespreken we de resultaten hiervan. We hebben aangetoond dat de afname van de luminescentie al begint bij −70°C, wat de maximale emissie-efficiëntie bij kamertemperatuur beperkt tot ongeveer 15%. Met behulp van deze kennis kan gericht worden gezocht naar verbeteringen van het materiaal om de efficiëntie te verhogen.

Hoe nu verder?

Voor luminescente materialen blijft de concurrentie tussen stralend verval (emissie van fotonen, licht) en niet-stralend verval (omzetting naar warmte) cruciaal voor hun prestaties. Deze strijd tussen licht en donker is het onderwerp van dit proefschrift voor een selectie van materialen die mogelijk worden toegepast in displays, verlichting en optische sensoren. Op al deze vlakken wordt voortdurend geïnnoveerd om lichtbronnen feller, efficiënter en kleiner te maken, naargelang een (toekomstige) toepassing dat vereist. Hopelijk dragen de verworven inzichten beschreven in dit proefschrift bij aan betere luminescente materialen in de toekomst.

Appendix

Publications in this thesis

1. **Increasing the power: absorption bleach, thermal quenching, and auger quenching of the red-emitting phosphor K_2TiF_6: Mn^{4+}**
   J.W. de Wit, T.P. van Swieten, M.A. van de Haar, A. Meijerink, F.T. Rabouw
   Advanced Optical Materials 11(9), **2023**

2. **Luminescence and formation of cubic and hexagonal $(K,Rb)_2SiF_6$:Mn^{4+}**
   A.J. van Bunningen[§], J.W. de Wit[§], S. Wakui, A. Meijerink
   ACS Applied Materials & Interfaces 16(1), 1044, **2024**

3. **Shedding light on host-to-Yb^{3+} energy transfer in $Cs_2AgBiBr_6$:Yb^{3+} (nano)crystals**
   J.W. de Wit, L.L. Sonneveld, A. Meijerink
   Chemistry of Materials 36(6), 2857, **2024**

4. **New insights in luminescence and quenching mechanisms of Ag_2S NCs through temperature-dependent spectroscopy**
   J.W. de Wit, I. Zabala-Gutierrez, R. Marin, S. Melle, O. G. Calderon, J. Marques-Hueso, D. Jaque, J. Rubio-Retama, A. Meijerink
   Submitted

Other publications

1. **Sizing curve, absorption coefficient, surface chemistry, and aliphatic chain structure of PbTe nanocrystals**
   J.L. Peters, J.W. de Wit, D.A.M. Vanmaekelbergh
   Chemistry of Materials 31(5), 1672, **2019**

2. **Alkyl Phosphonic Acids Deliver $CsPbBr_3$ Nanocrystals with High Photoluminescence Quantum Yield and Truncated Octahedron Shape**
   Chemistry of Materials 31(21), 9140, **2019**

3. **Two-Dimensional CdSe-PbSe Heterostructures and PbSe Nanoplatelets: Formation, Atomic Structure, and Optical Properties**
   B.B.V. Salzmann[§], J.W. de Wit[§], C. Li, D. Arenas-Esteban, S. Bals, A. Meijerink, D.A.M. Vanmaekelbergh
   The Journal of Physical Chemistry C 126(3), 1513, **2022**

4. **Highly luminescent Gd_2O_2S: Er^{3+}, Yb^{3+} upconversion microcrystals obtained by a time- and energy-saving microwave-assisted solid-state synthesis**
   I.P. Machado, J.W. de Wit, A.J. van Bunningen, C.C.S. Pedroso, L.C.V. Rodrigues, H.F. Brito, A. Meijerink
   Journal of Alloys and Compounds 942, 169083, **2023**

§ These authors contributed equally

5. **High-throughput characterization of single-quantum-dot emission spectra and spectral diffusion by multiparticle spectroscopy**
   M.J.J. Mangnus, J.W. de Wit, S.J.W. Vonk, J.J. Geuchies, W. Albrecht, S.Bals, A.J. Houtepen, F.T. Rabouw
   ACS Photonics 10(8), 2688, **2023**

6. **Cation Exchange and Spontaneous Crystal Repair Resulting in Ultrathin, Planar CdS Nanosheets**
   M.M. van der Sluijs, J.F. Vliem, J.W. de Wit, J.J. Rietveld, J.D. Meeldijk, D.AM. Vanmaekelbergh
   Chemistry of Materials 35(19), 8301, **2023**

Conference contributions

1. **Unusual photoluminescence temperature dependence in Ag_2S NCs**
   Presentation
   The 20th International Conference on Luminescence, **2023**, Paris

2. **Visualising latent fingerprints by labelling with InP/ZnSe core/shell quantum dots**
   Poster
   Light Conference Week, **2023**, Changchun

3. **Luminescence and formation of hexagonal $(K,Rb)_2SiF_6$: Mn^{4+}**
   Presentation (Best paper award)
   Light Conference Week, **2023**, Changchun

4. **Energy transfer in $Cs_2AgBiBr_6$ nanocrystals doped with Yb^{3+}**
   Presentation
   1st International Conference on Dynamical Processes in Excited States of Solids, **2022,** Wroclaw

5. **Photoluminescence saturation and heating effects in Mn^{4+}-doped K_2TiF_6**
   Presentation
   *6th International Conference on the Physics of Optical Materials and Devices & the 5th International Workshop of Persistent and Photostimulable Phosphors, **2022**,* Belgrade

6. **2D CdSe-PbSe heterostructures and PbSe nanoplatelets: formation and optical properties**
   Poster
   GRC Colloidal Semiconductor Nanocrystals, **2022,** Les Diablerets

7. **Saturation and heating effects in Mn^{4+}-Doped K_2TiF_6**
   Presentation (Best young presenter award)
   The 19th International Conference on Luminescence (online), **2021**, Changchun

About the author

Jur de Wit was born in Eindhoven, the Netherlands, on May 22 1993. In 2011 he graduated from the Pleincollege Vanmaerlant in Eindhoven. In 2012 he started the bachelor Science and Innovation management at Utrecht University. After obtaining his bachelor degree in 2015 he followed a premaster so he could start the Nanomaterials Science master in 2016 at Utrecht University. During his master, he wrote a thesis under the supervision of Daniel Vanmaekelbergh about the optical properties of PbTe nanocrystals in a colloidal solution and their oriented attachment. He continued his studies with a 5-month research internship at the Isitituto Italiano di Tecnologia (IIT) in Genua. His work there focused on the synthesis and colloidal stabilisation of perovskite nanocrystals with a new type of ligand and was supervised by Liberato Manna. He received his masters degree in 2018.

In July 2019, Jur started as a PhD researcher in the Condensed Matter & Interfaces group under the supervision of Andries Meijerink and later also Freddy Rabouw. The main results of his work are described in this thesis, have been published in peer-reviewed academic journals and presented at international conferences. Jur was awarded the award for best young presenter at the (online) ICL conference in Changchun in 2021 and the best paper award during the ICL in 2023, also in Changchun. During his PhD Jur assisted in several chemistry courses, supervised 12 students and arranged and hosted the weekly group meeting.